Mapping Galaxy Components with Kinematics

Dynamical models with stellar and gaseous kinematics

Meng Yang

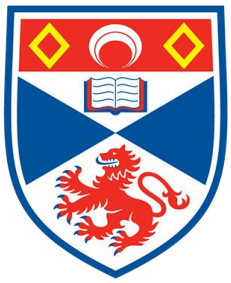

University of
St Andrews

This thesis is submitted in partial fulfilment for the degree of

Doctor of Philosophy (PhD)

at the University of St Andrews

August 2020

Candidate's declaration

I, Meng Yang, do hereby certify that this thesis, submitted for the degree of PhD, which is approximately 30,000 words in length, has been written by me, and that it is the record of work carried out by me, or principally by myself in collaboration with others as acknowledged, and that it has not been submitted in any previous application for any degree.

I was admitted as a research student at the University of St Andrews in August 2016.

I received funding from an organisation or institution and have acknowledged the funder(s) in the full text of my thesis.

Date Signature of candidate

19 August 2020

Supervisor's declaration

I hereby certify that the candidate has fulfilled the conditions of the Resolution and Regulations appropriate for the degree of PhD in the University of St Andrews and that the candidate is qualified to submit this thesis in application for that degree.

Date Signature of supervisor

19 August 2020

Permission for publication

In submitting this thesis to the University of St Andrews we understand that we are giving permission for it to be made available for use in accordance with the regulations of the University Library for the time being in force, subject to any copyright vested in the work not being affected thereby. We also understand, unless exempt by an award of an embargo as requested below, that the title and the abstract will be published, and that a copy of the work may be made and supplied to any bona fide library or research worker, that this thesis will be electronically accessible for personal or research use and that the library has the right to migrate this thesis into new electronic forms as required to ensure continued access to the thesis.

I, Meng Yang, confirm that my thesis does not contain any third-party material that requires copyright clearance.

The following is an agreed request by candidate and supervisor regarding the publication of this thesis:

Printed copy

No embargo on print copy.

Electronic copy

No embargo on electronic copy.

Date Signature of candidate

19 August 2020

Date Signature of supervisor

19 August 2020

Underpinning Research Data or Digital Outputs

Candidate's declaration

I, Meng Yang, understand that by declaring that I have original research data or digital outputs, I should make every effort in meeting the University's and research funders' requirements on the deposit and sharing of research data or research digital outputs.

Date Signature of candidate

19 August 2020

Permission for publication of underpinning research data or digital outputs

We understand that for any original research data or digital outputs which are deposited, we are giving permission for them to be made available for use in accordance with the requirements of the University and research funders, for the time being in force.

We also understand that the title and the description will be published, and that the underpinning research data or digital outputs will be electronically accessible for use in accordance with the license specified at the point of deposit, unless exempt by award of an embargo as requested below.

The following is an agreed request by candidate and supervisor regarding the publication of underpinning research data or digital outputs:

No embargo on underpinning research data or digital outputs.

Date Signature of candidate

19 August 2020

Date Signature of supervisor

19 August 2020

Abstract

Mapping galaxy mass distribution is an important means of understanding galaxy morphology and the nature of dark matter haloes, and therefore build up our knowledge of galaxy formation and evolution. Analytical and numerical dynamical models are powerful methods to model galaxy mass distributions based on galaxy stellar kinematics, and are strengthened by including gaseous kinematics.

In this thesis, I start my research with using descriptive analytical models to identify thin-disc components in galaxies. I kinematically classify the sample into disc-dominated, non-disc-dominated and disc-free galaxies and measure the dynamical mass for disc-dominated galaxies to study their mass budget. I find a dichotomy of lenticular galaxies in my classification, which is explained by the deficiency of molecular gas. Realising the limitation of analytical models, I continue my research with numerical models. I develop an orbit-based method with stellar kinematics modelled by the Schwarzschild technique, and cold gas (H I) assumed as a thin disc aligned with stars. The application of this method to early-type galaxy NGC 2974 shows that including extended cold gas kinematics significantly narrows down the measurement of the dark matter inner slope. I then further generalise this method to be adapted for galaxies with misaligned stellar and gas discs and apply the generalised method to early-type NGC 3626. The results suggest that with very extended cold gas discs out to 10 $R_{\rm e}$, there is a chance to determine the overall shape of dark matter halo and even distinguish between different halo models. I finally model a larger sample of galaxies which have two-aperture stellar kinematics using the Schwarzschild technique to study their orbital components and dark matter profiles across a wider mass range. The dark matter fraction is typically 40%-70% at 3 $R_{\rm e}$, and I find no clear trends between the dark matter fraction and stellar mass.

Acknowledgements

General acknowledgements

I would like to thank my supervisor Dr Anne-Marie Weijmans, who has always been an excellent example as an independent and collaborative researcher, for being supportive during my entire postgraduate study. The success of this project benefits from the regular inspiring discussions with Anne-Marie and the collaborations that she helps me to establish. I also start to participate in public engagement under her influence, in which I contribute to the society and enjoy myself. Last but not least, her continuous encouragements play an important role in improving my confidence and now I have more courage than ever to face any challenge in the future. Looking back on my four years in St Andrews, I will always feel lucky for Anne-Marie being my supervisor.

This thesis is completed with abundant help from many people, and I thank all of them gratefully. I thank Matthew Bershady, Michael Merrifield, Nicholas Boardman and Niv Drory for their valuable comments on identifying thin discs in MaNGA galaxies. I thank Kyle Wesfall for the discussion about the measurements of kinematic position angles and inclinations, and together with David Law for sharing their internal discussion about the line spread function issue of MaNGA DAP data. I also thank people in the SDSS collaboration for their interests, discussion and comments in SciCons, meetings and conferences. I appreciate the important support from Ling Zhu, Glenn van de Ven and Nicholas Boardman for developing orbit-based models, especially Ling for the continually discussions about technical problems while applying the orbit-based models. I thank Raffaella Morganti and Tom Oosterloo for providing neutral hydrogen data with detailed data description.

I feel honoured to work with excellent colleagues in the School of Physics and Astronomy. I thank every person in the galaxy group for our daily communication, and I mention Chris Duckworth and Yirui Zheng particularly for the frequent scientific discussions inside office. I thank Nicole Schanche, Tatiana Pavlidou and Suinan Zhang for their kindness. I thank all the members working on the Planetarium, especially Lisa Lehmann and Oliver Herbort for the organising work. I thank Ian Taylor along with the staff members in the PC Clinics of the university for the solution to technical problems. I thank Vivienne Wild for the discussion

about personal choice, which is of great importance to me.

I would like to thank my family and friends for being with me all the way through. I would like to express my gratitude to my mother Guiying Meng and my fiancé Xiang Zhu, for being supportive and encouraging to me. I thank my friends, especially my flatmates Zhen Yao and Jiazhu Hu, for sharing my happiness and sadness during my postgraduate study.

This thesis is dedicated to the memory of my dad, Ziran Yang, who had always believed in my ability and encouraged me to pursue my dream.

Funding

My postgraduate study was supported by the China Scholarship Council [File No. 201603780010].

My research in this thesis received grant from the Scottish Universities Physics Alliance [Postdoctoral and Early Career Researcher Exchange Program]; the Royal Astronomical Society [RAS Small Grants Scheme]; and the International Astronomical Union [IAU Symposium No. 353].

Research Data/Digital Outputs access statement

- Research data underpinning Chapter 2 are available at https://doi.org/10.17630/71cd0f94-5758-4fcc-8e68-fdcd0ff19f7d.
- Research data underpinning Chapter 4 are available at https://doi.org/10.17630/5f7160c0-813d-4504-9ed6-f6e61e876426.
- The MaNGA data are available at https://www.sdss.org/dr15/manga/.
- The Atlas^{3D} data are available at http://www-astro.physics.ox.ac.uk/atlas3d/.
- The Mitchell data are available at https://doi.org/10.17630/43b4e7fb-2f2c-4867-a4d5-21599299c9d9.

Contents

List of Figures

List of Tables

1

Introduction to galaxies

Galaxies are gravitationally bound systems of stars and interstellar medium formed in dark matter haloes. Galaxies of various morphologies are widely distributed in the Universe, tracing the structure of the Universe. The mass distribution is one of the most fundamental properties in galaxies, which hold important clues to the formation and evolution history of galaxies. Among all kinds of galaxy data obtained with the development of observational techniques, galaxy stellar and gaseous kinematics are of great importance, because they not only reveal the internal dynamics of galaxies, but also provide an important method to measure the mass distributions of the stellar components and dark matter haloes.

In this thesis, I will present my work of mapping galaxy components with stellar and gaseous kinematics for galaxies with various morphologies, to study the formation and evolution of their stellar components and dark matter haloes. For a better understanding of this thesis, I make an introduction to galaxies in this section as follows: I will first introduce the galaxy morphology and classification schemes as a background. I then introduce some observational technologies which are used to obtain the data in this thesis. I also make an overview

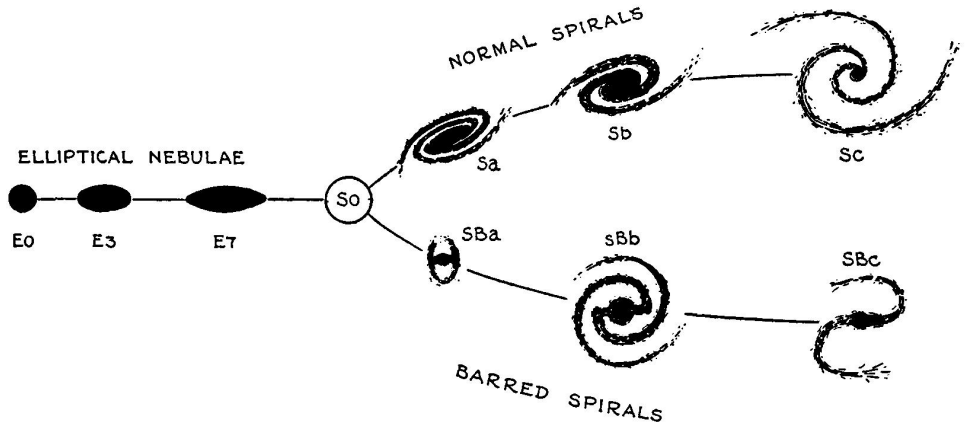

Figure 1.1: The Hubble tuning fork diagram (credit: Hubble, 1936). Galaxies are arranged according to their apparent shapes. Elliptical galaxies are one the left of the tuning fork, and from left to right the shapes are more flattened. There are two branches of spiral galaxies on the right of the tuning fork: the upper branch is unbarred spirals and the lower branch is barred galaxies.

of stellar populations and dark matter in galaxies, respectively. Lastly, I review the some important results about galaxy evolution in regards to the scope of this thesis.

1.1 Galaxy morphology and classification

Galaxy classification is a fundamental topic for galaxy research, because classifying galaxies into populations with common intrinsic features is the prerequisite of understanding them. Therefore, establishing galaxy classification schemes which can reflect the internal physics of galaxies is of great importance.

Hubble (1926) first invented a morphological classification scheme now called the Hubble sequence, which arranges regular galaxies into a tuning fork according to their visual appearance (see Figure 1.1). On the left of the tuning fork are the elliptical galaxies with smooth and featureless light distribution, indicated by the letter E followed by an integer n. n is conventionally 10 times of galaxy ellipticity $\epsilon = 1-b/a$ rounded to the closest integer, where a and b stand for the semi-major and semi-minor axes. Therefore, E0s stand for spherical shapes and E7s are highly flattened. The lenticular galaxies (or S0 galaxies) lie in the middle of the tuning fork, consisting of a bright central bulge surrounded by disc structures. S0 galaxies connect two branches of spiral galaxies: bar galaxies with a central bar-shaped structure are denoted by SB, and galaxies without a bar are denoted by S, followed by a lower-case letter (a, b or c) describing how tightly the spiral arms are wound and the brightness and size of the bulge, in

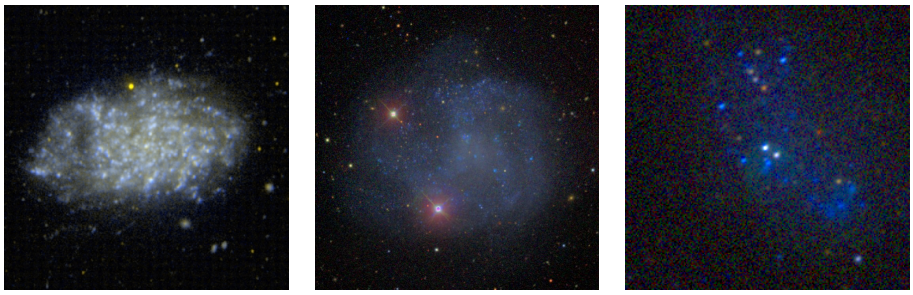

(a) NGC 7793 (Sd) (b) IC 4182 (Sm) (c) DDO 155 (Im)

Figure 1.2: The images of Sd galaxy NGC 7793 (de Paz et al., 2007), Sm galaxy IC 4182 and Im galaxy DDO 155 (Baillard et al., 2011).

which Sa (SBs) galaxies have most tightly wounded spiral arms and most bright bulges.

The Hubble sequence was then complemented by the de Vaucouleurs system (de Vaucouleurs, 1959), with more detailed definitions for spirals and irregular galaxies. Sd (SBd) is introduced to describe galaxies with very diffuse spiral arms and a faint central bulge. Sm (SBm) is introduced for irregular, bulgeless spirals and Im stands for highly irregular galaxies. I show images for Sd, Sm and Im galaxies in Figure 1.2. This morphological classification scheme includes structural components such as bulges, discs, bars and spiral arms. It is important to understand the definitions and descriptions of these components before studying their features and formation processes. Bulges (classical) are the spherical bright component at galaxy centres. They have similar surface brightness distribution to elliptical galaxies, which can be modelled empirically by the de Vaucouleurs profile (de Vaucouleurs, 1953) or a more generalised Sérsic profile (Sérsic, 1968)

$$I(R) = I_{\rm e} \exp\left\{-b_n\left[\left(\frac{R}{R_e}\right)^{1/n} - 1\right]\right\}, \tag{1.1}$$

where $I_{\rm e}$ is the intensity at the effective radius R_e (or half-light radius, defined as the radius within which half of the luminosity of a galaxy is contained), n is the Sérsic index and b_n is approximately $2n - 0.33$. $n = 4$ indicates the de Vaucouleurs profile. Discs are extended components usually surrounding the bulge following an exponential profile, and the surface brightness of spiral galaxies can be decomposed with a bulge and a disc (Freeman, 1970). Spiral arms are a typical feature of spiral galaxies, and bars are discovered in one thirds of disc galaxies (e.g. de Vaucouleurs et al., 1991; Masters et al., 2011).

Based on the recognition of galaxy structural components, the de Vaucouleurs system is

widely used as collected in galaxies catalogues (e.g. de Vaucouleurs et al., 1964, 1976, 1991). To deal with large amounts of galaxies observed by sky surveys, other techniques are introduced. For example, the Galaxy Zoo project (e.g. Lintott et al., 2008; Willett et al., 2013) involves amateur volunteers to do visual classification for galaxies instead of professionals through a web interface, significantly enhancing the efficiency of classification. The popular Deep Learning algorithms also have a great advantage of handling large amounts of data and have been successfully applied in morphological classifications (e.g. Gravet et al., 2015; Domínguez Sánchez et al., 2018).

However, it has been argued that morphological classification schemes are purely descriptive and not physical enough to distinguish galaxies by their evolution modes. Physical classification schemes are therefore constructed, such as classifications according to the dominant stellar populations of galaxies (e.g. Morgan, 1958; Morgan & Osterbrock, 1969). Conselice (2003) developed a CAS classification system adopting three nonparametric diagnostics: the concentration (C), asymmetry (A), and clumpiness (S) of a galaxy. Principal component analysis (PCA) is also used for building physical classification schemes using nonparametric diagnostics (e.g. the ZEST by Scarlata et al., 2007; Peth et al., 2016).

Galaxy kinematics, which provides information of intrinsic kinematic states of galaxies, also show a strong potential in building galaxy classification schemes linking to galaxy evolution modes. Using well-defined parameters, such as the proxy for projected stellar momentum λ_R or the ratio between the ordered and random motion V/σ together with ellipticity, early-type galaxies are divided into fast-rotators and slow-rotators with different dominant motions of stars (Emsellem et al., 2004, 2007; Cappellari et al., 2007). van de Sande et al. (2017) further include high-order stellar kinematic moments for galaxy classification.

1.2 Galaxy observations

Galaxy classification schemes rely on comprehensive observations of galaxies: morphological classification requires galaxy images while kinematic classification requires galaxy kinematics obtained from galaxy spectra. I therefore introduce the major techniques for galaxy observations in this section, including photometry, spectroscopy and integral field spectroscopy for optical and near-infrared observations, and particularly the radio observations of neutral hydrogen.

1.2.1 Photometry and spectroscopy

Photometry is a technique which measures the flux of astronomical objects with photometers (e.g. CCD photometer and photoelectric photometer) installed on telescopes. The development of photometric surveys has provided images at multiple wavelengths for nearby (e.g. Abazajian et al., 2009; de Jong et al., 2015; Chambers et al., 2016) and even high-redshift galaxies (e.g. Grogin et al., 2011; Zou et al., 2017). Galaxy images are widely used not only for galaxy morphology classifications, but surface photometry and galaxy component decomposition as well.

Surface photometry is a useful tool to study extended objects as galaxies. It can obtain galaxy basic parameters such as the effective radius. By fitting ellipses of the isophotes, surface photometry can also obtain the variations of galaxy parameters (e.g. position angle and ellipticity) with radius. The shape of isophotes is analysed by measuring its deviation from an ellipse using the coefficient of the fourth order cosine term a_4 of the Taylor series (Bender et al., 1989), and are classified into boxy-like ($a_4 < 0$), discy-like ($a_4 > 0$) and nearly elliptical ($a_4 \sim 0$) isophotes accordingly, as shown in Figure 1.3. The shape of isophotes is one of the fundamental properties for elliptical galaxies, which is related to different formation processes of elliptical galaxies (e.g. Kormendy & Bender, 1996; Kormendy et al., 2009). Fitting the surface brightness of galaxies is a fundamental analysis for galaxy images. It is a relatively simple fitting for elliptical galaxies with one component, while it involves the technique of galaxy component decomposition for lenticular and spiral galaxies to decompose their structural components, mainly bulges and discs. The results of earlier 1-dimensional (e.g. Kormendy, 1977; Kent, 1985; Baggett et al., 1998) and later 2-dimensional component decomposition (e.g. de Jong, 1996; Simard et al., 2011; Méndez-Abreu et al., 2017), which provided large amounts of measurements for galaxy structural components and revealed a number of connections between galaxy properties, have notably promoted the understanding of galaxy formation and evolution.

Galaxy images show the light distributions of stars and gas, but they have a clear disadvantage in obtaining further information of galaxies, such as their kinematic motions and chemical compositions. Therefore, it is essential to measure galaxy spectra with the technique of spectroscopy.

The spectrum of a galaxy shows its energy distribution as a function of wavelength and

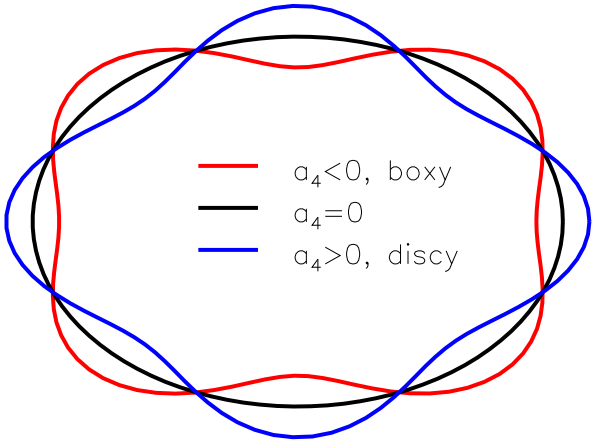

Figure 1.3: Sketch for boxy and discy isophotes. The black curve stands for an ellipse ($a_4 = 0$), the red curve stands for a boxy isophote ($a_4 < 0$) and the blue curve stands for a discy isophote ($a_4 > 0$).

provides the redshift and line-of-sight velocity dispersion according to the shift and width of emission and absorption lines, respectively. Single fibre-based spectroscopy generates a spectrum for each galaxy, and has been employed in galaxy redshift surveys (Huchra et al., 1983; Colless et al., 2001; Dawson et al., 2012; Huchra et al., 2012) for the study of galaxy clustering (e.g. Vogeley et al., 1992; Norberg et al., 2001; Crook et al., 2007; Alam et al., 2017) and luminosity functions (e.g. Marzke et al., 1994; Cole et al., 2001), which are important for the study of the large-scale structures of the universe and cosmological models. However, this fibre-based spectroscopy fails to provide spatially resolved kinematics within a galaxy for the study of galaxy dynamics. This problem is partly solved by long-slit spectroscopy which takes an aperture of a narrow long slit, and has been widely used to measure galaxy line-of-sight velocities along its major axis and then obtain its rotation curve for spiral galaxies (e.g. Rubin et al., 1978, 1980, 1985; Vogt et al., 1996; Spekkens et al., 2005). By arranging two long-slits along both the major and minor axes, long-slit spectroscopy also provides nearly 2-dimensional kinematics for elliptical galaxies (e.g. Schechter & Gunn, 1979; Couture & Hardy, 1988; Binney et al., 1990; Cinzano & van der Marel, 1994).

1.2.2 Integral field spectroscopy

Photometry and spectroscopy can provide spatial resolutions and spectral information, respectively. In order to combine the abilities of both photometry and spectroscopy, a powerful technique called integral field spectroscopy (IFS) was developed. IFS can provide spatially resolved spectral information of a galaxy with Integral Field Unit (IFU) instruments, which significantly enhances the capability of exploring galaxy dynamics. There are several major approaches of integral field spectrographs which have been applied in astronomical surveys for nearby galaxies: the lenslet approach, the fibre approach and the image slicer approach. I introduce these approaches and show their applications in the IFU surveys. I also include some technical details for the instruments which I will use in thesis.

In the lenslet approach, a lenslet array is placed in the slits plane before entering the spectrograph to result in a spectrum for each lenslet. This approach allows observations with high spatial resolution within a continuously sampled field of view, although it has relatively narrow wavelength coverage. It has been adopted by the Spectrographic Areal Unit for Research on Optical Nebulae (SAURON) integral-field unit on the William Herschel Telescope (Bacon et al., 2001) as the instrument in the SAURON survey (de Zeeuw et al., 2002) and the optical observations of the Atlas^{3D} Survey (Cappellari et al., 2011). It has a wavelength range of $4800-5380$ Å with a spectral resolution of 98 km/s (instrumental dispersion).

In the fibre approach, the light of astronomical sources is transported to the spectrograph with fibres to generate a spectrum for each fibre. This approach is used in the Calar Alto Legacy Integral Field Area survey (CALIFA; Sánchez et al., 2012) which includes a sample of about 600 nearby galaxies and the Sydney-Australian-Astronomical-Observatory Multi-object Integral field Spectrograph Galaxy survey (SAMI; Bryant et al., 2015) which observed a sample of about 3000 galaxies across a variety of galaxy environment. This approach is also adopted by the Mapping Nearby Galaxies at Apache Point Observatory survey (MaNGA; Bundy et al., 2014) which employs 17 IFUs, and each of IFU consists from 19 to 127 fibres arranged in a hexagonal bundle (Drory et al., 2015). The multi-object spectrograph covers a wavelength range of $3600-10000$ Å with a spectral resolution of 60 km/s (Smee et al., 2013). The MaNGA survey has a sample of about 10,000 nearby galaxies in the fourth-generation Sloan Digital Sky Survey (SDSS-IV; Blanton et al., 2017) on the 2.5 m Sloan Telescope (Gunn et al., 2006), which are selected depending on i-band absolute magnitude and have a spectroscopic

coverage from 1.5 to 2.5 effective radii (R_e) Wake et al. (2017). The disadvantage of the fibre approach that the field of view is not continuously sampled is overcome by dithering, which means to shift the pointing of the telescope slightly to cover the gaps between fibres. However, the spatial resolution is limited by the size of fibres.

In the image slicer approach, an image is segmented into slices and rearranged by an image slicer to obtain a spectrum for each slice. This approach allows a high spatial resolution, a wide wavelength coverage and a continuously sampled field of view, however, high costs limits the usage of this approach to a small number of instruments, such as the Multi Unit Spectroscopic Explorer (MUSE) on the European Southern Observatory's Very Large Telescope (Bacon et al., 2010).

1.2.3 Neutral hydrogen observations

Neutral hydrogen (H I) is atomic hydrogen which is widely distributed in galaxies. It emits radiation at the wavelength of 21.1 cm because of a change in the energy state of hydrogen atoms. As cold gas, H I is expected to be a good tracer for the circular orbital velocity of galaxies which provides strong constraints on the mass distribution of galaxies, and therefore used in this thesis.

The simplest way to obtain H I rotation curves is to measure H I line spectra for galaxies. The spatial resolution requirement to obtain rotation curves is hard to achieve by most of single-dish radio telescopes except for the radio telescopes with large diameters, therefore, there are only a few H I line spectral surveys conducted by single-dish radio telescopes, such as the H I Parkes All-Sky Survey (Koribalski, 2002) and the Arecibo Legacy Fast ALFA Survey (Giovanelli et al., 2005). Such difficulty is overcome by the advent of radio interferometry which significantly enhances the spatial resolutions of radio telescopes and therefore makes it possible to measure H I line spectra. For example, the Westerbork Synthesis Radio Telescope (WSRT) contributes a number of early H I line spectral measurements for rotation curves of spiral galaxies (e.g. Bosma, 1981; Warmels, 1988; Begeman, 1989).

The development of radio interferometry also allows the observations of 2-dimensional H I velocity fields for galaxies with radio telescopes. For example, there are the Westerbork HI Survey of Irregular and Spiral Galaxies (WHISP; van der Hulst et al., 2001) and the HI Nearby Galaxy Survey (THINGS; Walter et al., 2008) for late-type galaxies observed with the WSRT

and the Very Large Array (VLA), respectively. H I velocity fields are also obtained for early-type galaxies with these telescopes (e.g. Morganti et al., 2006; Weijmans et al., 2008; Oosterloo et al., 2010). These observations further increase the understanding of H I kinematics and the ability of constraining galaxy mass distributions.

1.3 Stellar populations in galaxies

Galaxy observations show that the major component of the luminous matter in galaxies are stars. Therefore, stellar properties, such as their mass distribution and chemical composition, are fundamental to the study of galaxy formation and evolution. The stellar mass distribution of a galaxy can be traced by its surface brightness with the consideration of the stellar mass-to-light ratio (M/L). M/L varies in different types of galaxies: elliptical galaxies usually have higher M/L than the disc galaxies (e.g Faber & Jackson, 1976; Schechter, 1980), and empirical scaling relations show a correlation between M/L and galaxy colours (e.g. Bell & de Jong, 2001; McGaugh & Schombert, 2014). Galaxy colours also give clues to the chemical compositions (age, metallicity) of a galaxy (e.g. Li et al., 2007; Tortora et al., 2010). Detailed research of stellar populations are essential for a better understanding of stars in galaxies.

The concept of stellar populations dates back to Oort (1926) and Baade (1944) who characterised stars in the Milky Way into two stellar populations, metal-rich young stars and metal-poor old stars. In a stellar viewpoint, a galaxy is composed of various single stellar populations (SSPs). Each SSP is a group of stars of the same age and metallicity, which almost forms simultaneously from the same origin and has similar kinematic characteristics. The initial mass function (IMF) which describes the mass distribution of the stars at birth is also a principal feature of an SSP. There are several IMFs proposed to describe various types of galaxies. For example, the Salpeter IMF (Salpeter, 1955) is a power-law IMF from the solar neighbourhood which agrees with the mass distribution well at the high-mass end, while the Kroupa IMF (Kroupa, 2001) and the Chabrier IMF (Chabrier, 2003) are measured for Milky Way-like galaxies. Bottom-heavy IMFs with higher fractions of low-mass stars (e.g. Cenarro et al., 2003; van Dokkum & Conroy, 2010) and top-heavy IMFs with higher fractions of massive stars (e.g. Dabringhausen et al., 2009; Bartko et al., 2010) are also proposed for massive elliptical galaxies and starburst galaxies, respectively. Figure 1.4 shows the number density profiles for these IMFs. However, it has been argued that there might not be a universal IMF for all galaxies. There is research suggesting that the IMF experienced a cosmic evolution (e.g. van Dokkum,

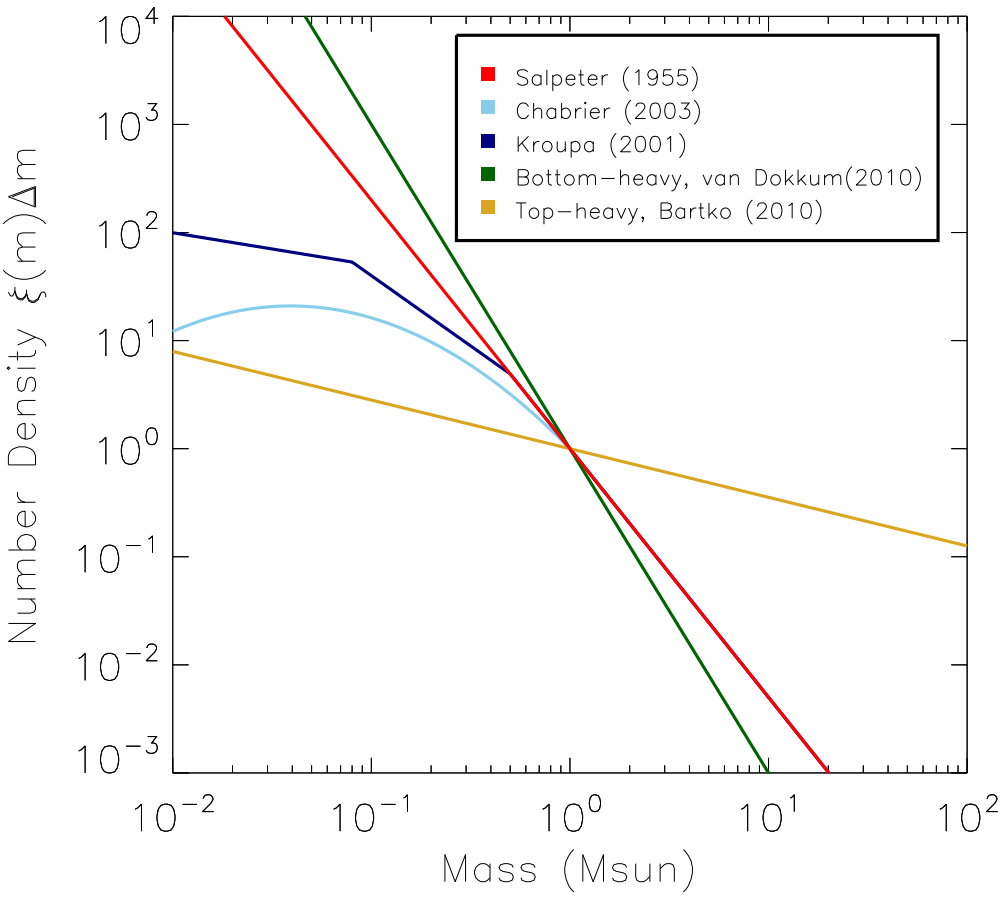

Figure 1.4: The number density profiles of IMFs as marked in the legends. The Chabrier and Kroupa IMFs have lower fractions of low-mass stars compared to the Salpeter IMF, while the IMF of van Dokkum & Conroy (2010) and Bartko et al. (2010) have a steeper and shallower power-law slope compared to the Salpeter IMF, respectively.

2008; Davé, 2008) and depends on galaxy properties such as star formation rate (SFR) (Gunawardhana et al., 2011) and metallicity (Martín-Navarro et al., 2015b). Besides, an IMF gradient has been found within a number of galaxies (e.g. Martín-Navarro et al., 2015a; Oldham & Auger, 2017; La Barbera et al., 2019), which further increases the complexity of this problem.

If the properties of each SSP is well known, the properties of a galaxy such as the stellar mass, age and metallicity can be obtained by decomposing the spectrum of the galaxy into a combination of spectra of SSPs, which is the idea of the stellar population synthesis (SPS) technique. In this technique, the star formation history (SFH), which is the SFR over time, is represented by the generation of stellar populations of all ages. There is usually a degeneracy between the SFH and the IMF, making it difficult to determine both of them without any assumptions.

The SPS which takes the evolution of SSPs into consideration is called the evolutionary stellar population synthesis (eSPS; e.g. Tinsley, 1972; Tinsley & Gunn, 1976; Renzini & Voli, 1981; Bruzual et al., 1983). The eSPS technique assumes an IMF and a SFH in advance and decomposes the spectrum of a galaxy into a combination of the evolutionary spectra of SSPs using stellar evolution models (e.g. Bruzual & Charlot, 2003; Maraston, 2005; Maraston & Strömbäck, 2011). Compared to the traditional SPS technique which fits the spectrum of the galaxy with the empirical spectra of SSPs, the eSPS technique is able to avoid the unphysical solutions caused by the degeneration of SSPs with different ages and metallicities.

The integrated spectral energy distribution (SED) fitting is a useful technique to obtain stellar populations for a galaxy. The principle of the SED fitting is similar to the SPS technique, but it fits the broadband photometry instead of spectra. Apart from the IMF and the SFH, the effect of the dust emission is also important in the SED fitting. Mobasher et al. (2015) present that there is no significant bias between the stellar masses from the SED fitting and the SPS with the same assumptions. The SED fitting and the SPS technique are powerful tools for obtaining the stellar mass of galaxies, which also provide important constraints on galaxy parameters such as stellar M/L and therefore improve our understanding of galaxy evolution.

1.4 Dark matter in galaxies

The concept of dark matter was first proposed by Zwicky (1933) which introduced a kind of unseen dark matter to explain the large velocities of several galaxies in the Coma cluster. Rogstad & Shostak (1972) confirmed that dark matter is essential to explain the extremely high M/L obtained from the neutral hydrogen (H I) rotation curve in the outskirts of 5 late-type spiral galaxies, and this conclusion was then supported by Bosma (1981). The existence of dark matter is also verified by a series of optical observations which studied the optical rotation curves of the edge-on spiral galaxies (e.g. Rubin et al., 1978, 1980, 1985). Most of the early evidence for the dark matter haloes in galaxies was obtained from late-type spiral galaxies. It was discovered later that early-type disc galaxies with declining rotation curves still require the existence of the dark matter haloes (e.g. Noordermeer et al., 2004, 2007). However, whether the dark matter halo assumption is essential to early-type galaxies was debated for a long time, until Bertola et al. (1993) observed flat rotation curves for the H I discs in elliptical galaxies and confirmed the necessity of dark matter haloes. Other research also obtained similar results (e.g. Morganti et al., 1997; Sadler et al., 2000). The existence of dark matter is also an important assumption of the standard cosmological model, Λ cold dark matter (ΛCDM) model (e.g. Blumenthal et al., 1984; Davis et al., 1985), and it is confirmed by the observations such as the Wilkinson Microwave Anisotropy Probe (WMAP; Spergel et al., 2003), which shows that matter contributes to 27% of the mass-energy density in total, and 85% of the matter is not visible, even though dark matter particles have not been directly detected yet.

The properties of dark matter haloes are not only crucial for investigating the nature of dark matter and testing cosmological models, but for galaxy formation and evolution as well. Galaxies form in dark matter haloes, and the accumulation of baryons reshapes the dark matter haloes. Therefore, studying the structure of dark matter haloes is a way to understand the co-evolution processes of dark matter and baryons in galaxies.

To describe the dark matter haloes in galaxies, different forms of dark matter profiles have been proposed. For example, Bahcall & Soneira (1980) and Kent (1984) used a pseudo-isothermal profile for dark matter haloes with a central core, which has the following form

$$\rho(r) = \frac{\rho_c}{1 + (r/r_c)^2}, \tag{1.2}$$

where ρ_c is the central density, and the r_c is the core radius. The mass density of the pseudo-isothermal sphere is proportion to r^{-2} in the outskirts of a galaxy. Navarro et al. (1996) presented the Navarro–Frenk–White (NFW) profile with a cusp instead of a core in the centre to fit dark matter haloes in simulations, which has a generalised form

$$\rho(r) = \frac{\rho_0}{(r/r_s)^{\gamma}(1+r/r_s)^{3-\gamma}}, \tag{1.3}$$

where r_s is the scale radius, ρ_s is the characteristic density, and γ is the inner slope of the density. $\gamma = 1$ stands for the original NFW profile, while it can take values within $[0,3]$. This profile becomes the Moore model (Moore et al., 1999) if $\gamma = 1.5$, and it becomes a core model if $\gamma = 0$. The Einasto profile (Einasto, 1965; Navarro et al., 2004), which has the same mathematical form as the Sérsic profile, is also used to describe the density profiles for dark matter haloes,

$$\rho(r) = \rho_{-2} \exp\left(-2n\left[(r/r_{-2})^{1/n} - 1\right]\right), \tag{1.4}$$

where n decides the shape of the profile, and ρ_{-2} is the density at r_{-2}, the radius at which the logarithmic slope equals -2.

One of the undetermined questions related to the properties of the dark matter haloes is the core or cusp problem, which concerns whether the central profile of dark matter haloes is cored or cusped. High-resolution cosmological N-body simulations show that the standard ΛCDM model predicts a central cusp for dark matter haloes. Earlier simulations found that the inner part of simulated dark matter haloes is well described by a power-law slope with $\gamma = 1$, where the density profile $\rho(r) \propto r^{-\gamma}$ (e.g. Dubinski & Carlberg, 1991; Navarro et al., 1996, 1997), and then a number of simulations generated dark matter haloes with steeper cusps (e.g. Moore et al., 1999; Ghigna et al., 2000; Klypin et al., 2001) and shallower cusps (Taylor & Navarro, 2001). There are also simulations which obtain dark matter haloes with central cusps, however, their slopes are turning flatter inwards at smaller radii instead of converging to a constant (e.g. Navarro et al., 2004; Stoehr, 2006; Stadel et al., 2009). However, the results obtained from observations are contradictory and seem to be correlated with galaxy masses. Many observations of dwarf galaxies (e.g. Moore, 1994; Simon et al., 2003; Battaglia et al., 2008; Walker & Penarrubia, 2011) and low surface brightness (LSB) galaxies (e.g. de Blok et al., 2001; de Naray et al., 2008) prefer shallow core-like inner slopes which might indicate warm dark matter particles although exceptions are also found (van den Bosch et al., 2000;

Swaters et al., 2003). There is a similar inconsistency for high-mass galaxies as well. A number of massive elliptical galaxies favour central cusps (e.g. Grillo, 2012; Sonnenfeld et al., 2015), while the core model is also preferred in some cases (e.g. Forestell & Gebhardt, 2010; Oldham & Auger, 2018). Since this undetermined core or cusp problem is important for the study of galaxy evolution, I will explore it by measuring dark matter inner slopes in this thesis.

1.5 Galaxy evolution

The previous sections about stellar population and dark matter provide a background to study the co-evolution of baryonic and dark matter in galaxies. In this section, I will introduce some important results about galaxy evolution, including galaxy morphological transformation and galaxy quenching.

The colour-magnitude or colour-mass diagrams obtained from galaxy surveys has revealed a bimodality of galaxy populations: the blue cloud with relatively low mass and blue colours and the red sequence with relatively high mass and red colours (e.g. Strateva et al., 2001; Baldry et al., 2004; Bell et al., 2004; Willmer et al., 2006; Brammer et al., 2009), as shown in Figure 1.5. Despite other factors such as galaxy environments (e.g. Bamford et al., 2009; Skibba et al., 2009) and the activity of active galactic nucleus (AGN; e.g. Salim et al., 2007; Schawinski et al., 2007), galaxy morphology is the main driver of this bimodality; the blue cloud is mainly composed of spiral galaxies and the red sequence has a large fraction of elliptical galaxies, although it has been confirmed that the fractions of blue lenticular and elliptical galaxies (Schawinski et al., 2009) and red spiral galaxies (Masters et al., 2010) in the Galaxy Zoo classification project are not negligible.

Morphological transformation is a fundamental issue of galaxy evolution, which is usually accompanied with the growth of galaxy bulges or spheroids, a type of spherical stellar halo. The major mechanisms of morphological transformation include mergers and disc instabilities. Since Toomre (1977) proposed that elliptical galaxies result from major mergers of spiral galaxies, this hypothesis has been supported by a number observational evidence (e.g. Toomre & Toomre, 1972; Schweizer, 1982; Shier & Fischer, 1998; van Dokkum, 2005). Although major mergers contributes dominantly to the formation and assembly of bulges and spheroids, the contribution of minor mergers is not negligible (e.g. Hopkins et al., 2010; López-Sanjuan et al., 2012; Rodriguez-Gomez et al., 2016). Disc instabilities of galaxies at high redshift is

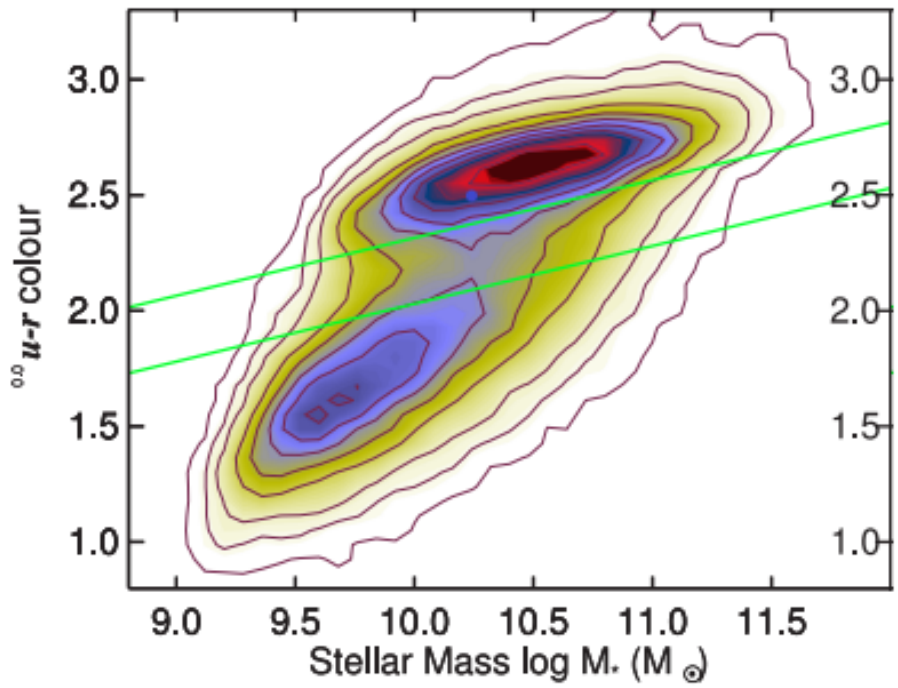

Figure 1.5: The $u-r$ colour-mass diagram taken from Schawinski et al. (2014). There is a clear bimodality on this diagram: galaxies in the blue cloud (lower left) are bluer (low $u-r$ value) with lower stellar mass, while galaxies in the red sequence (higher right) are redder with higher stellar mass. Galaxies between the two green lines on the diagram are the green valley galaxies.

another reason to form bulges and spheroids (e.g. Elmegreen & Elmegreen, 2005; Schreiber et al., 2006; Genzel et al., 2008; Dekel et al., 2009). In this scenario, the galaxy disc becomes unstable globally and break into clumps, then these clumps migrate to the galaxy centre and build up classical bulges. The instability of stellar discs is described with the Toomre's instability criterion (Toomre, 1964)

$$Q = \frac{\kappa \sigma_R}{3.36 G \Sigma}, \tag{1.5}$$

where κ is the epicyclic frequency at which radial oscillations happen, σ_R is the radial velocity dispersion and Σ is the surface density. For gas discs, the factor 3.36 should be replaced with π. The disc is axisymmetric stable only if $Q > 1$, or it will break into clumps. Additionally, bulge-like dense components which have more nearly exponential surface brightness (Andredakis & Sanders, 1994; Fisher & Drory, 2008) and higher rotations (Kormendy & Illingworth, 1982) compared to classical bulges, namely pseudo-bulges can build up through secular evolution majorly driven by bars (Kormendy & Kennicutt Jr, 2004; Sellwood, 2014), leading to galaxy morphological transformation.

There is another galaxy population sparsely distributed between the blue cloud and the red sequence in the colour-magnitude diagram, which is denoted as the green valley. It is regarded as the transition phase between the star-forming blue cloud and the quenched red sequence (e.g. Bell et al., 2004; Faber et al., 2007; Martin et al., 2007; Schawinski et al., 2014) and therefore holds important clues to understand the quenching of galaxy star formation.

Quenching can be caused by the deficient of gas in galaxies, in which galaxy environments play an important role (e.g. Kimm et al., 2009; Peng et al., 2012). There are several mechanisms to remove the gas reservoir of galaxies. The halt of gas accretion from the environment is the major mechanism for galaxy quenching, which leads to a gradually declining star formation (starvation or strangulation; e.g. Larson et al., 1980; Balogh et al., 2000; Peng et al., 2015). Alternatively, galaxies lose their gas because of the dense intergalactic medium which directly strips gas from galaxy discs during passing through (ram-pressure stripping; e.g. Gunn & Gott III, 1972; Abadi et al., 1999; McCarthy et al., 2008) or the gravitational tidal forces of galaxy clusters (tidal stripping; Mayer et al., 2006). Starbursts triggered by continual interactions with nearby galaxies (galaxy harassment; Moore et al., 1998) or galaxy mergers (e.g. Mihos & Hernquist, 1994a,b, 1996) can also exhaust the gas reservoir in galaxies and lead to quenching. For galaxies with a dark matter halo above a critical mass of $10^{12} M_\odot$, the star

formation can be shut down because the infalling gas is shock-heated to the viral temperature of the halo and kept hot because of other heating mechanisms such as AGN feedback (mass quenching; e.g. Cattaneo et al., 2006; Dekel & Birnboim, 2006).

Quenching can also happen without removing the gas reservoir. Martig et al. (2009) introduce a scenario called morphological quenching. In this scenario, the growth of bulges can stabilise the gas disc and therefore quench the star formation in galaxies, while this morphology transformation itself can be a result of mergers or disc instabilities.

1.6 This thesis

In this thesis, I present my work of mapping galaxies components by modelling stellar and gaseous kinematics in analytical and dynamical ways. I model a sample of galaxies from the MaNGA survey using a disc-dominated analytical model to obtain their dynamical mass and analyse the results. I also model a sample of early-type galaxies with H I observations using dynamical models mainly to obtain the properties of their dark matter haloes. This work involves multiple topics introduced in previous sections, such as galaxy classification, the IMFs and dark matter profiles of galaxies, and galaxy quenching process.

This thesis is structured as follows:

- Chapter 2 presents the application of an analytical model to MaNGA galaxies. I briefly introduce analytical models based on distribution functions (DFs) in Section 2.1, and then build an analytical model for stellar velocity and dispersion based on a thin-disc assumption (Section 2.2). I apply this model to a sample of MaNGA galaxies with regular stellar and gaseous rotation fields and kinematic position angle and inclination measurements (Section 2.3). The galaxies are classified into different kinematic types according to a series of criteria using parameters obtained from this model. I measure the dynamical mass and explain their difference with stellar mass for galaxies dominated by a thin disc. I study a number of galaxy properties and fit the result in a quenching scenario in Section 2.4.

- Chapter 3 includes an introduction to galaxy numerical dynamical models. I review the development of a number dynamical models, including DF-based models, the Jeans models, orbit-based and particle-based models (Section 3.1). I then introduce the method-

ology of Schwarzschild orbit-superposition technique in detail (Section 3.2), which I will use in the remaining chapters of this thesis. I show an example of applying the Schwarzschild technique in Section 3.3.

- Chapter 4 presents a dynamical model using combined stellar and cold gas kinematics. I first introduce previous applications of using combined tracers to model dark matter haloes (Section 4.1). I then describe this model in which the stellar kinematics is modelled with the Schwarzschild orbit-superposition technique and the cold gas is assumed to form a thin disc (ring) in the equatorial plane of the galaxy (Section 4.2). I apply this model to early-type galaxy NGC 2974 and compare it with a model using only stellar kinematics to show the significance of including the cold gas kinematics in (Section 4.3).

- Chapter 5 presents a generalisation of the dynamical model described in Chapter 4, which is able to model galaxies with misaligned stellar and cold gas disc. I first review previous studies of misaligned stellar and gas discs (Section 5.1). I then introduce the geometry of misaligned discs, describe the behaviour of the cold gas disc in the gravitational potential and deduce the uncertainty for modelling cold gas kinematics (Section 5.2). I apply this model to early-type galaxy NGC 3626 (Section 5.3), which has two-aperture stellar kinematics (i.e. high-resolution central stellar kinematics and extended stellar kinematics out to 3 $R_{\rm e}$) and a cold gas disc misaligned with the stellar disc and extended to over 10 $R_{\rm e}$. I show the results of this application and discuss the results (Section 5.4).

- Chapter 6 presents the Schwarzschild modelling of 10 early-type galaxies with two-aperture stellar kinematics, to obtain the dark matter properties for these galaxies. I first introduce the application (Section 6.1) and then discuss the result (Section 6.2), focusing on their dark matter properties and stellar orbit distributions.

- I summarise the conclusions of my thesis in Chapter 7, which highlights the major results of Chapters 2 and Chapters 4-6 (Sections 7.1-7.4). I then make a critical discussion about this thesis (Section 7.5). Lastly, I briefly introduce a future research plan based on this thesis (Section 7.6).

2

Galaxy classification based on an analytical model

In this chapter, I introduce an analytical galaxy model based on the asymmetric drift correction with a thin-disc assumption, its application to detect thin discs in galaxies and how to build a classification scheme accordingly (Yang et al., submitted). It is organised in the following way: I first review the theoretical work of analytical models. I then describe this analytical model and show its application to MaNGA galaxies, including the process of building a classification scheme according to this model. Finally, I explain the results which focus on the link between this classification scheme and galaxy evolution scenarios.

2.1 From collisionless Boltzmann equation to analytical models

Galaxies are collisionless systems. In a collisionless system, the probability of finding a particle at position $\mathbf{x}$ and velocity $\mathbf{v}$ in the phase space at time t can be described as the distribution

function (DF) $f(\mathbf{x}, \mathbf{v}, t)$, which satisfies

$$\int \mathrm{d}^3\mathbf{x}\mathrm{d}^3\mathbf{v}\, f(\mathbf{x}, \mathbf{v}, t) = 1. \tag{2.1}$$

The DF follows the collisionless Boltzmann equation,

$$\frac{\partial f}{\partial t} + \dot{\mathbf{q}}\frac{\partial f}{\partial \mathbf{q}} + \dot{\mathbf{p}}\frac{\partial f}{\partial \mathbf{p}} = 0, \tag{2.2}$$

where $(\mathbf{q}, \mathbf{p})$ is an arbitrary system of canonical coordinates of the phase space which becomes $(\mathbf{x}, \mathbf{v})$ for the Cartesian coordinates, and $(\dot{\mathbf{q}}, \dot{\mathbf{p}})$ denotes a time derivative.

The observables are related to the DF. Defining the probability per unit volume of finding a star at $\mathbf{x}$ is

$$\mu(\mathbf{x}) = \int \mathrm{d}^3\mathbf{v}\, f(\mathbf{x}, \mathbf{v}), \tag{2.3}$$

the mean velocity and velocity-dispersion tensor are then obtained by

$$\overline{\mathbf{v}}(\mathbf{x}) = \frac{1}{\mu(\mathbf{x})}\int \mathrm{d}^3\mathbf{v}\, \mathbf{v} f(\mathbf{x}, \mathbf{v}), \tag{2.4}$$

$$\begin{aligned}\sigma_{ij}^2(\mathbf{x}) &= \frac{1}{\mu(\mathbf{x})}\int \mathrm{d}^3\mathbf{v}\, (v_i - \overline{v}_i)(v_j - \overline{v}_j) f(\mathbf{x}, \mathbf{v}) \\ &= \overline{v_i v_j} - \overline{v}_i \overline{v}_j.\end{aligned} \tag{2.5}$$

By choosing a set of orthogonal axes, $\boldsymbol{\sigma}^2$ can be diagonal with $\sigma_{ij}^2 = \sigma_i^2 \delta_{ij}$. The velocity ellipsoid at $\mathbf{x}$ is hence defined as the ellipsoid which has the orthogonal axes as its principal axes and σ_i as its corresponding semi-axis.

The Jeans theorem (Jeans, 1915) demonstrates that any steady state solution of the collisionless Boltzmann equation corresponds with a function of the integrals of motion in the given potential and vice versa. Therefore, a number of analytical models are developed from the DF for particular systems. For an isotropic spherical system, the DF is determined by the energy E and can be deduced given a spherical distribution in a potential (Eddington's formula Eddington, 1916). For anisotropic spherical systems, the DF is determined by the energy E and total angular momentum L, and various models have been proposed to describe these systems with different anisotropies, such as the Osipkov-Merritt Models (Osipkov, 1979; Merritt, 1985) and a quasi-separable model defined by Gerhard (1991). Compared to spherical systems, axisymmetric models are more close to the reality of galaxies, which conserves the

energy E, the angular momentum along the symmetry axis L_z and a non-classical third integral I_3. Since I_3 usually has a complicated function form, it is practical to adopt the DF being a function of E and L_z for axisymmetric systems. Even so, fully analytical models are only built in a limited cases with specific form of DFs (e.g. Fricke, 1951; Toomre, 1982) including the Evans model (Evans, 1993, 1994; Evans & de Zeeuw, 1994) which constructed a set of power-law galaxies with the gravitational potential as a power of spheroidal radius. Other two-integral DFs are also found using different methods, such as the integral transform with strict requirement of density distributions (e.g. Lynden-Bell, 1962; Hunter, 1975; Dejonghe, 1986) or a contour integral with less restrictions (e.g. Hunter & Qian, 1993; Qian et al., 1995) which is an analogue for the axisymmetric case of Eddington's formula. However, numerical computation is often inevitable in searching for two-integral DFs (see also e.g. Dehnen & Gerhard, 1994; Dehnen, 1995; Kuijken, 1995).

Therefore, it is useful to develop methods which avoid using a particular form of DF. Jeans (1919) first applied the following Jeans equations in Cartesian coordinates to the motion of the stars,

$$\mu\frac{\partial\overline{v}_j}{\partial t}+\mu\overline{v}_i\frac{\partial\overline{v}_j}{\partial x_i}=-\mu\frac{\partial\Phi}{\partial x_j}-\frac{\mu\sigma_{ij}^2}{\partial x_i}, \tag{2.6}$$

where μ is the stellar density and Φ is the gravitational potential. In the cylindrical coordinates for an axisymmetric system in a steady state, the Jeans equation becomes (Jeans, 1922)

$$\begin{aligned}\frac{\mu(\overline{v_R^2}-\overline{v_\phi^2})}{R}+\frac{\partial(\mu\overline{v_R^2})}{\partial R}+\frac{\partial(\mu\overline{v_Rv_z})}{\partial z}+\mu\frac{\partial\Phi}{\partial R}=0,\\ \frac{\mu\overline{v_Rv_z}}{R}+\frac{\partial(\mu\overline{v_z^2})}{\partial z}+\frac{\partial(\mu\overline{v_Rv_z})}{\partial R}+\mu\frac{\partial\Phi}{\partial z}=0.\end{aligned} \tag{2.7}$$

In this case, the mean velocity $\overline{v}_\phi$ is different from the circular velocity V_c (Binney & Tremaine, 2008),

$$V_c^2=\overline{v}_\phi^2-\sigma_{R,\mathrm{d}}^2\left[\frac{\partial\ln\mu_\mathrm{d}}{\partial\ln R}+\frac{\partial\ln\sigma_{R,\mathrm{d}}^2}{\partial\ln R}+1-\frac{\sigma_{\phi,\mathrm{d}}^2}{\sigma_{R,\mathrm{d}}^2}+\frac{R}{\sigma_{R,\mathrm{d}}^2}\frac{\partial\overline{v_Rv_z}}{\partial z}\right]. \tag{2.8}$$

This difference is called the asymmetric drift of galaxies. Quantifying the asymmetric drift in galaxies offers us a starting point to analyse galaxy dynamics. The asymmetric drift correction has been proved practical to obtain circular velocity curves for lenticular galaxies (e.g. Neistein et al., 1999; Weijmans et al., 2008) and early-type spirals (e.g. Noordermeer et al., 2008; Williams et al., 2010). It also provides strong dynamical constraints to the model of

spiral galaxies (e.g. the Diskmass Survey: Bershady et al., 2010a; Westfall et al., 2011). The robustness of asymmetric drift correction within 1 R_e is also supported by the test performed by Leung et al. (2018) with a sample including galaxy types from lenticular to late-type spiral.

2.2 An analytical model of thin discs

In this section, I first introduce this analytical model, including the descriptions of the stellar velocity and dispersion profiles and the asymmetric drift correction of the stellar velocity based on a thin-disc assumption. I then introduce the strategy of valuing this model based on the result of asymmetric drift correction. Lastly, I introduce the method to obtain the dynamical mass densities for these thin discs.

2.2.1 Stellar model

Stellar velocity

I assume the galaxy is axisymmetric with an inclination i and use the cylindrical coordinate system (R, ϕ, z) to describe this galaxy. The stellar azimuthal velocity $\overline{v}_\phi$ has the following form as taken from the Evans model (Evans, 1993; Evans & de Zeeuw, 1994)

$$\overline{v}_\phi = \frac{A \cdot R}{(R_c^2 + R^2 + z^2/q_\phi^2)^{1/2+\delta/4}}, \tag{2.9}$$

where A is a constant, R_c is the core radius, δ stands for the logarithm slope of the rotation curve, and q_ϕ reflects the flattening of the equipotentials. Assuming the galaxy has a flat rotation curve, the logarithmic slope of the rotation curve $\delta = 0$ and A becomes the maximal rotation velocity v_{max}. The model is then simplified to

$$\overline{v}_\phi = \frac{v_{max} \cdot R}{\sqrt{R_c^2 + R^2 + z^2/q_\phi^2}}, \tag{2.10}$$

In the disc plane ($z = 0$), the stellar velocity reduces to

$$\overline{v}_\phi = \frac{v_{max} \cdot R}{\sqrt{R^2 + R_c^2}}, \tag{2.11}$$

and the line-of-sight (LOS) velocity is projected with

$$v_{\rm los} = \overline{v}_\phi \cos\phi \sin i. \tag{2.12}$$

Stellar dispersion

The velocity dispersion model is built with an anisotropic component $\sigma_{\rm d}$ and an isotropic component $\sigma_{\rm iso}$. The anisotropic dispersion component describes the rotation-dominated component in galaxies under a thin-disc assumption, whose radial component $\sigma_{R,\rm d}$ follows an exponential profile of $\sigma_{R,\rm d} = \sigma_{0,\rm d}\exp(-R/h_{\sigma,\rm d})$. Then the LOS velocity dispersion $\sigma_{\rm los,d}$ follows as:

$$v_{\rm los} = v_z \cos i + (v_R \sin\phi + v_\phi \cos\phi)\sin i, \tag{2.13}$$

$$\begin{aligned}\sigma^2_{\rm los,d} &\equiv \overline{v^2_{\rm los}} - \overline{v}^2_{\rm los} \\ &= \sigma^2_{z,\rm d}\cos i^2 + \sigma^2_{R,\rm d}\sin i^2 \sin\phi^2 + \sigma^2_{\phi,\rm d}\sin i^2\cos\phi^2 + \overline{v_R v_z}\sin 2i\sin\phi,\end{aligned} \tag{2.14}$$

with $\overline{v_R(v_\phi - \overline{v}_\phi)} = 0$ and $\overline{v_z(v_\phi - \overline{v}_\phi)} = 0$, which means the velocity ellipsoid is aligned with the azimuthal direction.

In the (R, z) plane, $\overline{v_R v_z} = 0$ if the velocity ellipsoid is aligned with the cylindrical coordinate system, while $\overline{v_R v_z} = (\sigma^2_{R,\rm d} - \sigma^2_{z,\rm d})(z/R)/[1-(z/R)^2]$ if the velocity ellipsoid is aligned with the spherical coordinate system. I follow the method of parameterising $\overline{v_R v_z}$ by Weijmans et al. (2008),

$$\overline{v_R v_z} = \kappa(\sigma^2_{R,\rm d} - \sigma^2_{z,\rm d})\frac{z/R}{1-(z/R)^2}, \tag{2.15}$$

where κ reflects the shape of the velocity ellipsoid, is between 0 and 1 indicating the velocity ellipsoid is aligned from the cylinder coordinate system to the spherical one.

In the disc plane, $\overline{v_R v_z} = 0$, then the light-of-sight velocity dispersion reduces to

$$\sigma^2_{\rm los,d} = \sigma^2_{R,\rm d}\left(\sin i^2\sin\phi^2 + \frac{\sigma^2_{z,\rm d}}{\sigma^2_{R,\rm d}}\cos i^2\right) + \frac{\sigma^2_{\phi,\rm d}}{\sigma^2_{R,\rm d}}\sin i^2\cos\phi^2. \tag{2.16}$$

$\sigma^2_{z,\rm d}/\sigma^2_{R,\rm d}$ and $\sigma^2_{\phi,\rm d}/\sigma^2_{R,\rm d}$ are deduced from the collisionless Boltzmann equation by Weijmans

et al. (2008) (see Appendix A of their paper),

$$\frac{\sigma^2_{z,\mathrm{d}}}{\sigma^2_{R,\mathrm{d}}} = \frac{\kappa z^2(1+\partial \ln \overline{v}_\phi/\partial \ln R)}{\kappa z^2(1+\partial \ln \overline{v}_\phi/\partial \ln R)-(R^2-z^2)\partial \ln \overline{v}_\phi/\partial \ln z}, \tag{2.17}$$

$$\frac{\sigma^2_{\phi,\mathrm{d}}}{\sigma^2_{R,\mathrm{d}}} \simeq \frac{1}{2}\left[1+\frac{\partial \ln \overline{v}_\phi}{\partial \ln R}+\kappa\frac{1-\sigma^2_{z,\mathrm{d}}/\sigma^2_{R,\mathrm{d}}}{1-(z/R)^2}\frac{\partial \ln \overline{v}_\phi}{\partial \ln z}\right]. \tag{2.18}$$

I then bring equation 2.10 in and obtain

$$\sigma^2_{z,\mathrm{d}} = \sigma^2_{R,\mathrm{d}}\left[1-\frac{R^2}{\kappa q_\phi^2(R^2+2R_\mathrm{c}^2)+R^2}\right], \tag{2.19}$$

$$\sigma^2_{\phi,\mathrm{d}} = \sigma^2_{R,\mathrm{d}}\left[1-\frac{R^2}{2(R^2+R_\mathrm{c}^2)}\right], \tag{2.20}$$

$$\sigma^2_{\mathrm{los,d}} = \sigma^2_{\mathrm{R,d}}\left[1-\frac{R^2\cos^2 i}{\kappa q_\phi^2(R^2+2R_\mathrm{c}^2)+R^2}-\frac{R^2\sin^2 i\cos^2\phi}{2(R^2+R_\mathrm{c}^2)}\right]. \tag{2.21}$$

κ and q_ϕ are both related to the flattening of the galaxy and they are correlated. I therefore deduce their relation in the Evans model. Considering $z << R$ in equation 2.15 and taking the partial derivative with respect to z,

$$\frac{\partial \overline{v_R v_z}}{\partial z} = \kappa\frac{(\sigma^2_{R,\mathrm{d}}-\sigma^2_{z,\mathrm{d}})}{R}. \tag{2.22}$$

According to equation 104 in Amendt & Cuddeford (1991),

$$\kappa = \left.\frac{R^2\Phi_{,Rzz}}{3\Phi_{,R}+R\Phi_{,RR}-4\Phi_{,zz}}\right|_{z=0}, \tag{2.23}$$

where $\Phi_{,R} = \partial\Phi/\partial R$, $\Phi_{,RR} = \partial^2\Phi/\partial R^2$ etc. Since I have assumed the stellar velocity $\overline{v}_\phi$ follows the form in equation 2.10 instead of circular velocity V_c, the gravitational potential Φ is not known directly, but I make the approximation to the following form

$$\Phi \simeq \frac{v_{\max}}{2}\ln(R_\mathrm{c}^2+R^2+z^2/q_\phi^2). \tag{2.24}$$

I then bring Φ into equation 2.23 and obtain that

$$\kappa \simeq \frac{R^2}{(2-q_\phi^2)R^2+2R_\mathrm{c}^2(1-q_\phi^2)}. \tag{2.25}$$

For a spherical gravitational potential with $q_\phi = 1$, $\kappa \simeq 1$, which means that the velocity ellipsoid is aligned with the spherical coordinate system. For a highly flattened gravitational potential with $q_\phi = 0$, $\kappa \simeq R^2/2(R_c^2 + R^2)$.

From equation 2.19 and 2.21, κ and q_ϕ appear in this model only through the form of κq_ϕ^2. I assume that the velocity ellipsoid is aligned with the spherical coordinate with $q_\phi = 1$ at galaxy centre considering the existence of a possible bulge, and at galaxy outskirts $0 < q_\phi < 1$. Therefore, I parameterise κq_ϕ^2 in the form of $\kappa q_\phi^2 = (1-t)\exp(-r/h_t) + t$ with $0 < t < 1$. Then

$$\kappa \simeq \frac{\kappa q_\phi^2 (2R_c^2 + R^2) + R^2}{2(R_c^2 + R^2)}. \tag{2.26}$$

The isotropic component is introduced to fit the velocity dispersion field, which might represent the non-rotational motions. I also assume it follows an exponential profile $\sigma_{\rm los,iso} = \sigma_{0,\rm iso}\exp(-R/h_{\sigma,\rm iso})$. Then LOS velocity dispersion becomes

$$\sigma_{\rm los}^2 = \sigma_{\rm los,d}^2 + \sigma_{\rm los,iso}^2 \tag{2.27}$$

The modelled velocity and velocity dispersion should be convolved with the PSF before comparing with observations. I follow the convolution procedure as outlined in Begeman (1989) for the case that the spatial pixel size of stellar observations is comparable to the PSF size.

2.2.2 Asymmetric drift correction

The asymmetric drift is the difference between the stellar velocity v_ϕ and the circular velocity V_c. In this model, I assume V_c is the velocity of Hα without asymmetric drift correction because gas is collisional. Since this model is based on a thin-disc assumption, I will obtain V_c through the asymmetric drift correction of stellar velocity v_ϕ correctly only for the galaxies dominated by a thin disc. Therefore, the asymmetric drift correction provides a kinematic way to identify thin discs in galaxies.

I bring equation 2.19, 2.20, 2.22 and 2.26 in equation 2.8 and also assume that the flux density of the disc follows an exponential profile with $\mu_{\rm d} \propto \sigma_{\rm R,d}^2$ (Binney & Tremaine, 2008),

then the asymmetric drift correction becomes

$$V_c^2 = \overline{v}_\phi^2 - \sigma_{R,\mathrm{d}}^2 \left(\frac{2\partial \ln \sigma_{R,\mathrm{d}}^2}{\partial \ln R} + \frac{R^2}{R^2 + R_\mathrm{c}^2} \right), \tag{2.28}$$

where all the parameters are obtained by fitting the velocity and velocity dispersion models (equation 2.12 and 2.27). Here I only adopt the velocity dispersion of the anisotropic component σ_d^2 for asymmetric drift correction, while the isotropic component σ_iso^2, which is introduced only for the fitting of velocity dispersion and might represent the non-rotation component with low tangential velocities, is not included in the thin-disc model and then ignored in the correction.

2.2.3 Dynamical mass density

The dynamical mass density is the total mass density obtained with a dynamical method. It can provide constraints on the amount of dark matter if the luminous mass density, such as stellar and gas mass densities are known beforehand. Therefore, I obtain the dynamical mass density of the thin discs identified with this model.

The dynamical mass density of an isothermal thin disc is derived by Binney & Tremaine (2008)

$$\Sigma_{\mathrm{dyn,d}} = \frac{\sigma_{z,\mathrm{d}}^2}{k\pi G h_z}, \tag{2.29}$$

which is a function of vertical velocity dispersion $\sigma_{z,\mathrm{d}}$, which is already resolved in the velocity dispersion model, and disc scale height h_z. I adopt $k = 1.5$ for exponential vertical mass distributions (Bershady et al., 2010b), and the only non-disc-dominated parameter is h_z.

To model the velocity dispersion profile of the galaxy, the galaxy should be nearly face-on. However, it is difficult to measure the disc scale height for nearly face-on galaxies. Therefore, I estimate the disc scale height from scaling relations. To obtain a robust disc scale height, I adopt two two independent scaling relations and take the weighted average for them. The first is the scale height versus the rotation velocity (van der Kruit & Freeman, 2011),

$$h_{z,1} = (0.45 \pm 0.05)(V_\mathrm{rot}/100\mathrm{km/s}) - (0.14 \pm 0.07)\mathrm{kpc}. \tag{2.30}$$

I take the maximal velocity v_max of the Evans model as the rotation velocity V_rot. The second

relation is the scale height versus the scale length (Kregel et al., 2002),

$$\log(h_\mu/h_{z,2}) = 0.367\log(h_\mu/\mathrm{kpc}) + 0.708 \pm 0.095, \tag{2.31}$$

where $h_\mu = 1/2h_{\sigma,\mathrm{d}}$ is obtained from the fitting of the velocity dispersion profile. I then take the weighted average value of $h_{z,1}$ and $h_{z,2}$ as the scale height h_z.

2.3 Application to MaNGA galaxies

In this section, I apply this analytical model to sample galaxies and set a set of standards to identify galaxies dominated by thin discs.

2.3.1 Data and sample

I employ the MaNGA (see Section 1.2.2) data released in SDSS data release 15 (DR15, Aguado et al., 2019) obtained from MaNGA output datacubes with the official software package, the MaNGA data analysis pipeline (DAP) (Westfall et al., 2019). DAP generates the stellar kinematics and gaseous kinematics simultaneously by penalised pixel-fitting (pPXF) (Cappellari & Emsellem, 2004) using the MILES stellar template library (Sanchez-Blazquez et al., 2006; Falcón-Barroso et al., 2011) and Gaussian emission line templates. DAP also provides the maps of several binning strategies, such as non-binning, radial binning, and the Voronoi binning (Cappellari & Copin, 2003) adaptive to S/N = 10. With consideration of galaxy 2-dimensional details and S/N, I adopt the Voronoi binned stellar and gaseous kinematics, including the LOS velocity and velocity dispersion maps of the stars and the LOS velocity map of Hα emission line.

The parent sample is selected from MaNGA DR15 with a classification in Galaxy Zoo 2 (Willett et al., 2013; Hart et al., 2016). The cross sample between DR15 and Galaxy Zoo 2 is 3841 galaxies. This analytical model requires galaxies to have the following features: i) regular morphologies; ii) nearly face-on to model the velocity and velocity dispersion fields together; iii) regular kinematic fields including aligned stellar and gaseous velocity field. Therefore, I set up these three standards to select proper sample galaxies:

1. Galaxies do not have odd features in their images according to Galazy Zoo 2 (t06_odd_a15_no_flag = 1.0)
2. The axis ratio of the Sérsic profile in NASA Sloan Atlas (NSA) catalogue (Blanton et al.,

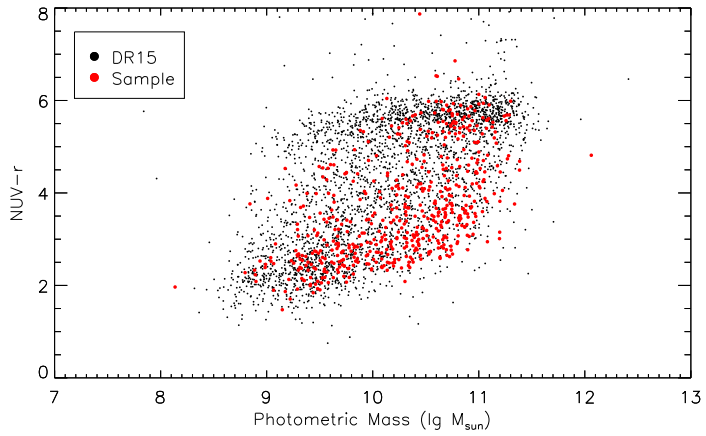

Figure 2.1: The colour-mass map of this sample (red dots) and the full DR15 sample (black dots).

2011) should be between 0.5 and 0.996.

3. The stellar and Hα velocity fields are aligned without other irregular kinematic features by visual check.

I selected 558 galaxies according to these standards, and show the colour-mass map of this sample and full DR15 sample in Figure 2.1. This sample is representative of the colour and mass distributions of the DR15 sample, containing not only red and blue galaxies, but also a number of green valley galaxies.

2.3.2 Position angle and inclination measurements

The application of this model strongly relies on accurate measurements of position angles (PA) and inclinations (i). Therefore, I measure the kinematic PA and axis ratio (Q), in which case $Q = \cos i$, from stellar velocity fields of the sample galaxies to avoid influences of the thickness for the measurements using images. The kinematic PA and Q are obtained with the package `KINEMETRY` (Krajnovic et al., 2006), which is a tool to analyse the maps of kinematic moments by generating the best-fitting ellipses and high-order moments through making harmonic expansions along every ellipse. I also employ the following strategy for robust measurements. For each galaxy, I reconstruct 100 velocity maps by adding Gaussian noise to LOS stellar velocity fields, with the standard deviation of the Gaussian noise being the uncertainty of stellar velocity. Then I measure the best-fitting PAs and Qs on ellipses at the same radii for all the velocity maps with `KINEMETRY` and get the distributions of PA and Q at different radius. Here I show a typical distribution of PAs and Qs of a galaxy 8135-12704 in Figure 2.2.

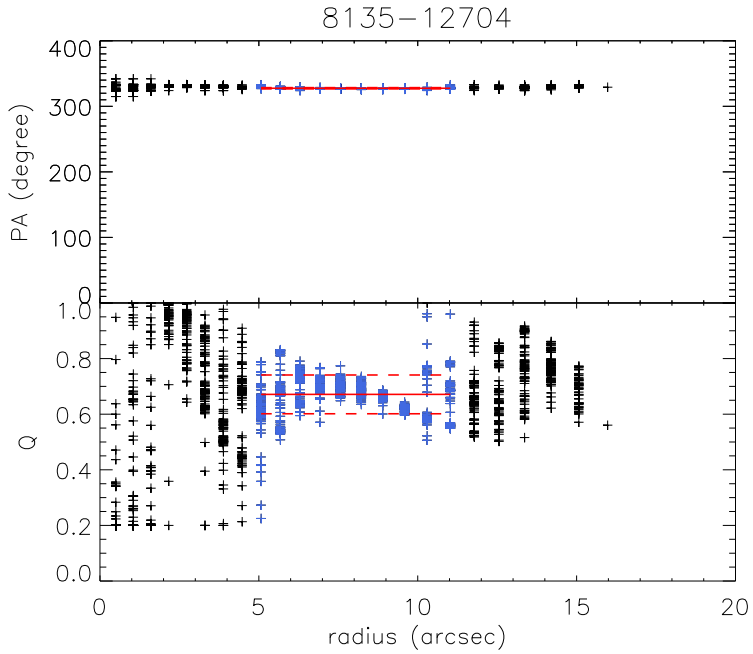

Figure 2.2: The distribution of PAs and Qs on each ellipse of an example galaxy 8135-12704. Blue plus signs stand for the values on the 'good' ellipses which are included in the average, and the black plus signs show the values on the remaining ellipses. The red solid and dashed lines show the PA and the Q of the galaxy and their 1-σ uncertainties. The fitting boundaries for Q are $[0.2, 1.0]$.

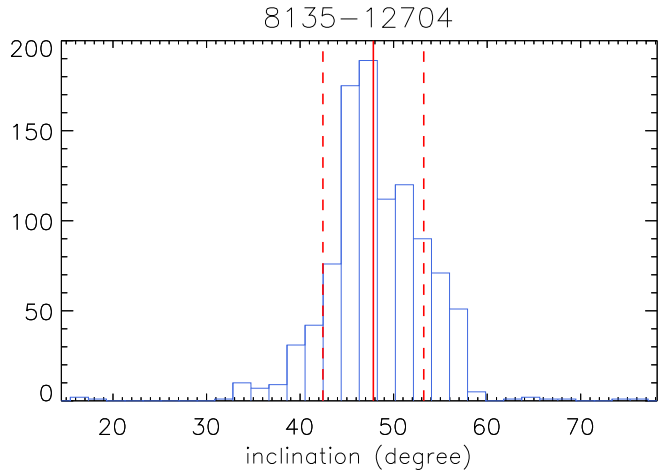

Figure 2.3: The distribution of the 'effective' inclinations of 8135-12704. The red solid and dashed lines shows the inclination and 1-σ uncertainties.

PAs are usually stable across the galaxy, however, that is not the same for Qs. Qs tend to have a wide distribution or hit fitting boundaries (set to $[0.2, 1.0]$) at the galaxy centre because of the existence of a bulge or a bar and limited data points on the ellipse, while at galaxy outskirts Qs are usually not well measured because of large bin sizes due to low S/N.

I therefore adopt the following steps to obtain a robust inclination for each galaxy. Firstly, I empirically exclude the radii at which the standard deviations of Qs are higher than 0.1 or over half of the measured Qs hit the fitting boundaries. Then I select a continuous 'good' radius range from the remaining radii for measurements, as marked in red lines in Figure 2.2.

For data points within the 'good' radius range, I kick out the outliers hitting the fitting boundaries, leaving the 'effective' data points marked in blue in Figure 2.2. Lastly, I take the average of these 'effective' data points to obtain the PA and the inclination of the galaxy. I note that Qs are converted to inclinations before measuring, for that I assume the inclinations follow a Gaussian distribution instead of Qs. The inclination distribution of galaxy 8135-12704 is shown in Figure 2.3. I also show the range of 'good' ellipses in its SDSS r-band image and velocity field for galaxy 8135-12704 in Figure 2.4, which indicates that the central region affected by a bulge or bar and the outskirts with a large bin size are excluded from the measurements of PA and Q.

I excluded the galaxies with an unrealistic standard deviation of the inclination (e.g. caused by an uniform inclination distribution) from the sample, because I cannot decide a best-fitting

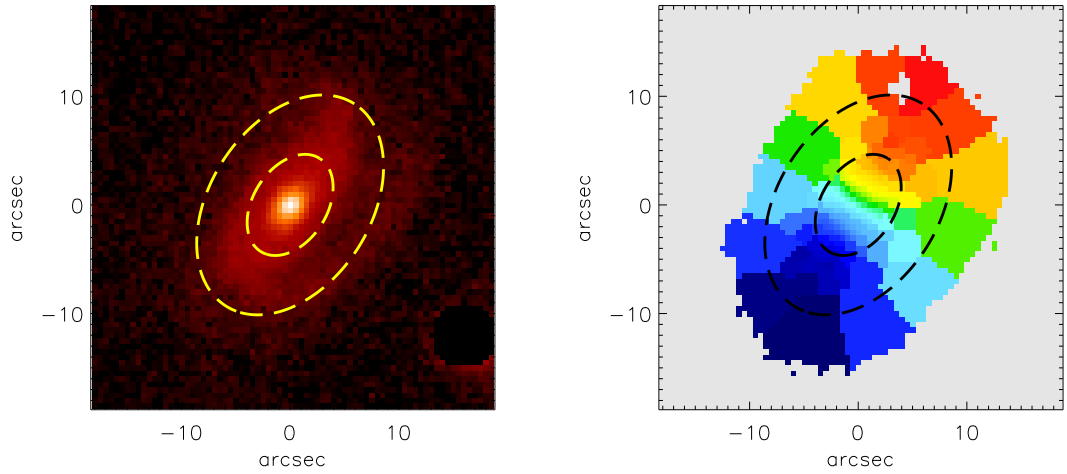

Figure 2.4: The 'good' range of 8135-12704 overlapped with its SDSS r-band image (left panel) and velocity field (right panel). The region between the dashed lines in each panel marks the radial range where we measure PA and Q.

inclination for them. I finally measure the best-fitting PA and inclination for 465 galaxies.

2.3.3 Examples of modelling MaNGA galaxies

I successfully modelled the stellar velocity and dispersion fields of 430 galaxies, and show their histograms of reduced-χ^2 in Figure 2.5. According to the distributions, I make a cutoff at reduced-$\chi^2_{\rm svel} = 4.0$ and reduced-$\chi^2_{\rm svd} = 4.0$ to exclude the galaxies which are poorly modelled and 404 galaxies remain. I show examples of fitting in Figure 2.6 and 2.7.

I then make the asymmetric drift correction for the stellar velocity according to equation 2.28 and obtain its LOS projection $v_{\rm corr}$. Then I compare $v_{\rm corr}$ with the observed LOS Hα velocity $v_{\rm gas}$ standing for the circular velocity and obtain a relative residual defined as $(v_{\rm gas} - v_{\rm corr})/v_{\rm gas}$. The corrected stellar velocity is consistent with Hα velocity for the majority of galaxies, while for part of galaxies, these two velocities have a significant difference, indicating the failure of the thin-disc assumption. Here I show an example for each case in Figure 2.8.

Finally, I obtain the dynamical mass density $\Sigma_{\rm dyn,d}$ and compare it with the stellar mass density in MaNGA DR15 FIREFLY value added catalog (VAC, Goddard et al., 2017). The stellar mass density is obtained with spectral fitting code FIREFLY using the high spectral resolution stellar population models (Maraston & Strömbäck, 2011) and a Kroupa IMF (Kroupa, 2001).

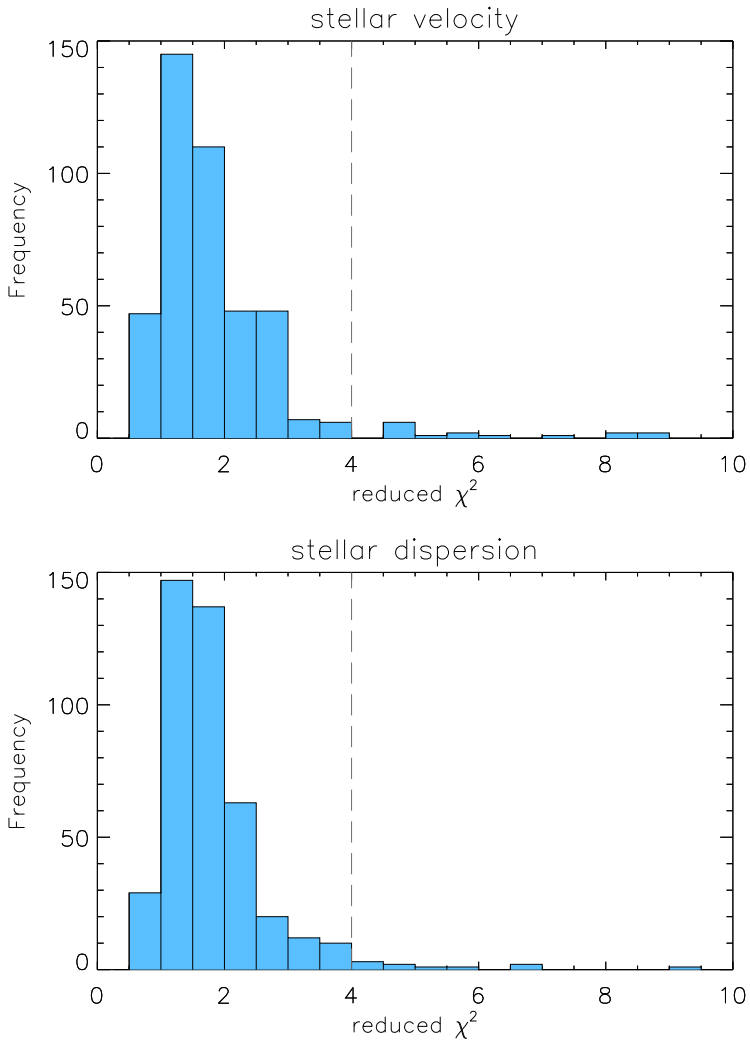

Figure 2.5: Reduced-χ^2 distribution of the stellar velocity (the upper panel) and the stellar velocity dispersion (the lower panel). The galaxies lie right to the dashed lines are regarded as poorly modelled.

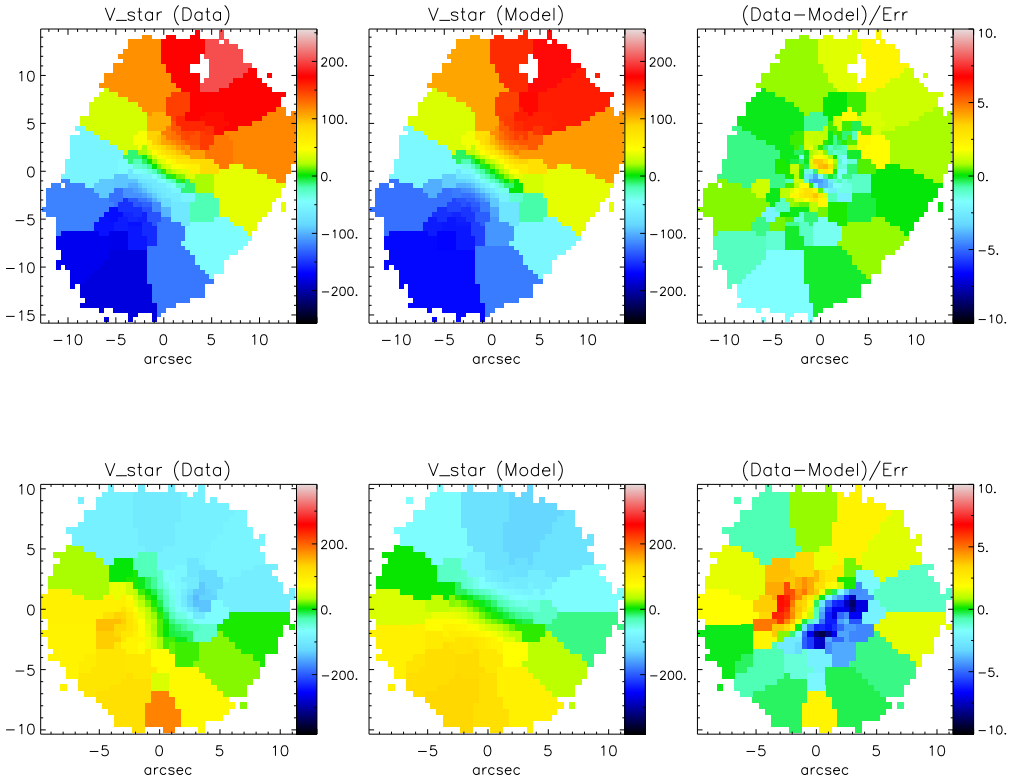

Figure 2.6: Stellar velocity fittings of 8135-12704 (above, reduced-$\chi^2_{\rm svel} \leqslant 4.0$) and 8311-6101 (bottom, reduced-$\chi^2_{\rm svel} > 4.0$). From left to right: data, model and residuals.

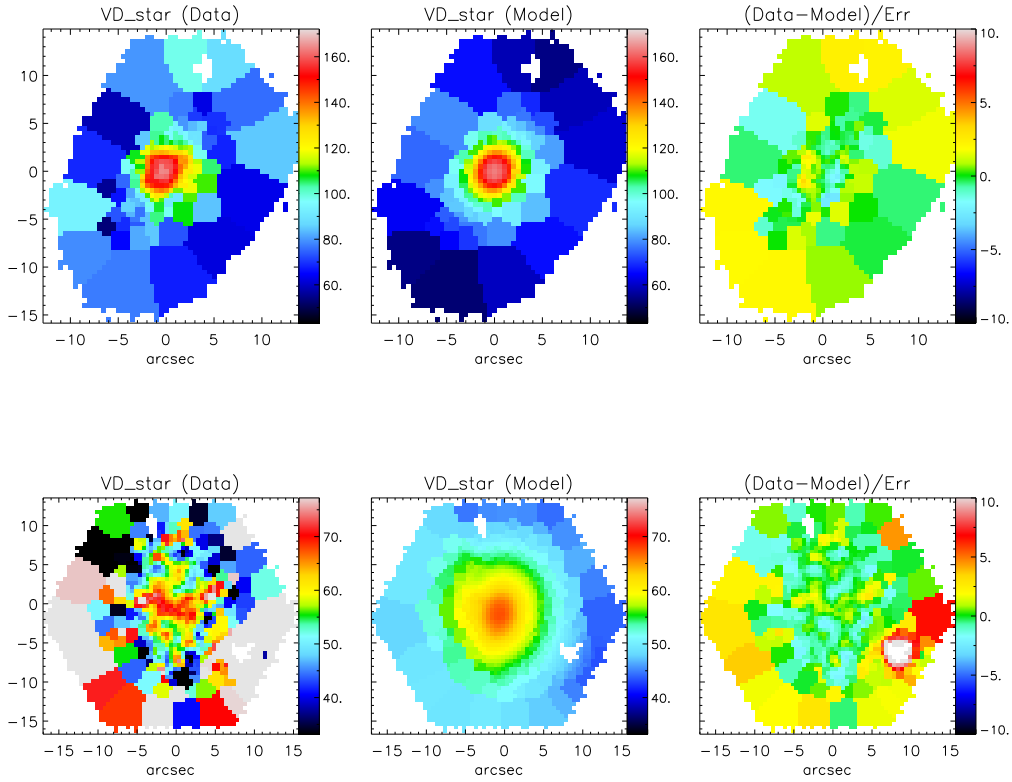

Figure 2.7: Stellar velocity dispersion fittings of 8135-12704 (above, reduced-$\chi^2_{\rm svd} \leqslant 4.0$) and 8139-12705 (bottom, reduced-$\chi^2_{\rm svd} > 4.0$). From left to right: data, model and residuals.

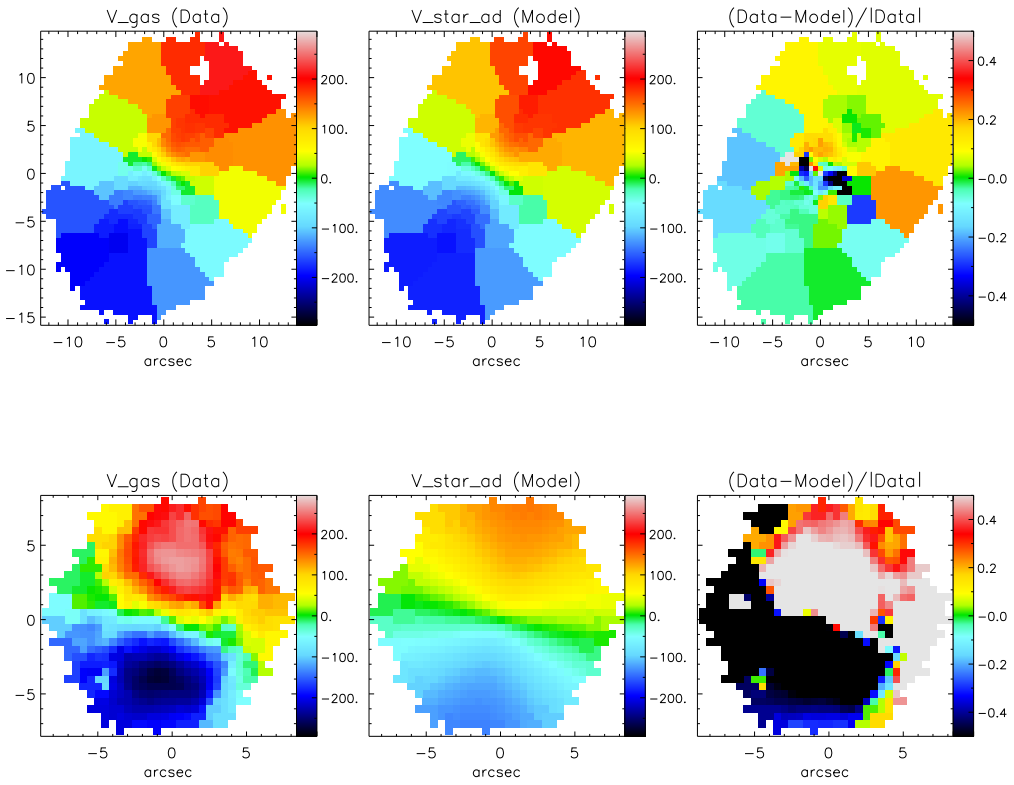

Figure 2.8: Comparison between Hα velocity and asymmetric drift corrected stellar velocity of galaxy 8135-12704 and 7957-3701. From left to right: Hα velocity, corrected stellar velocity and the relative difference. 8135-12701 represents the sample with matched corrected stellar velocity and Hα velocity, while 7495-3701 represents the sample with inconsistent velocities.

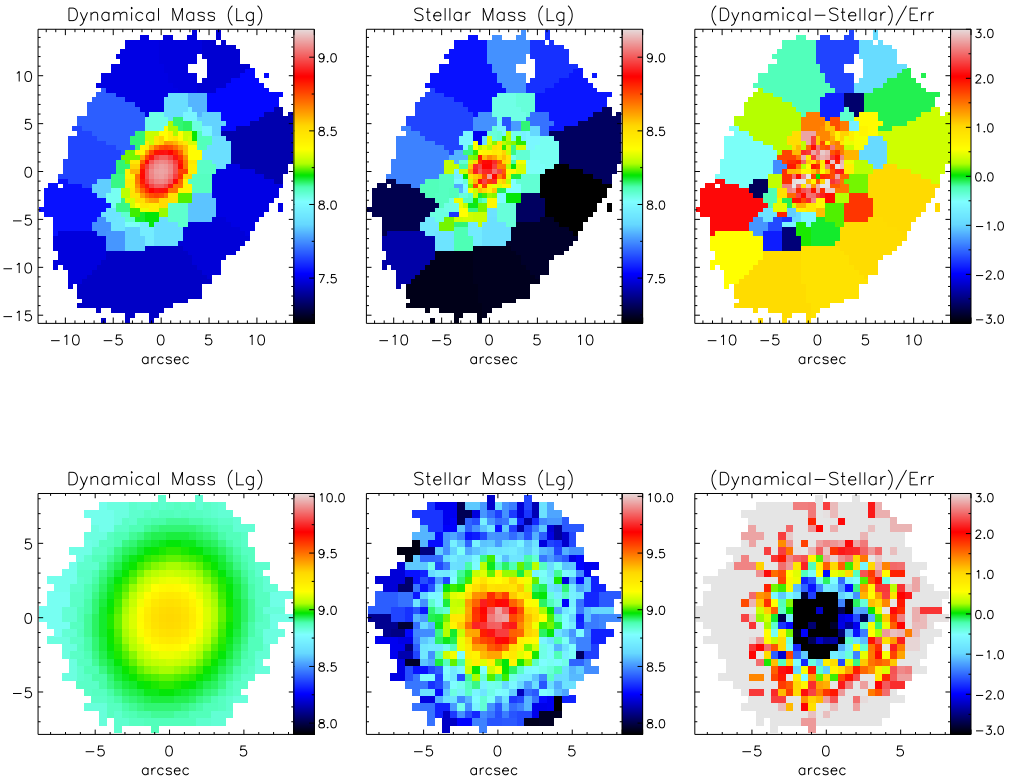

Figure 2.9: Comparison between dynamical and stellar mass densities of galaxy 8135-12704 and 7957-3701. From left to right: dynamical mass density, stellar mass density and the relative difference.

There are two examples in Figure 2.8, and here I show the mass densities of the same examples in Figure 2.9 as well. For galaxy 8135-12704, the dynamical mass density is in accordance with the stellar mass density at galaxy outskirts indicating a small fraction of non-stellar matter. At galaxy centre, the dynamical mass density is higher than stellar mass density with a different contour shape which suggest a small bulge. In contrast, the dynamical mass density of galaxy 7495-3701 is strongly deviated from the stellar mass density, indicating the disc assumption is failed in this galaxy.

Since the mass densities are not intuitive for further study, I also obtain the total dynamical and stellar mass within the MaNGA field of view $M_{\rm dyn}$ and M_* and the corresponding uncertainties for the sample galaxies.

2.3.4 Model validation and classification

This analytical model are built based on a thin-disc assumption, which is expressed in the following way.

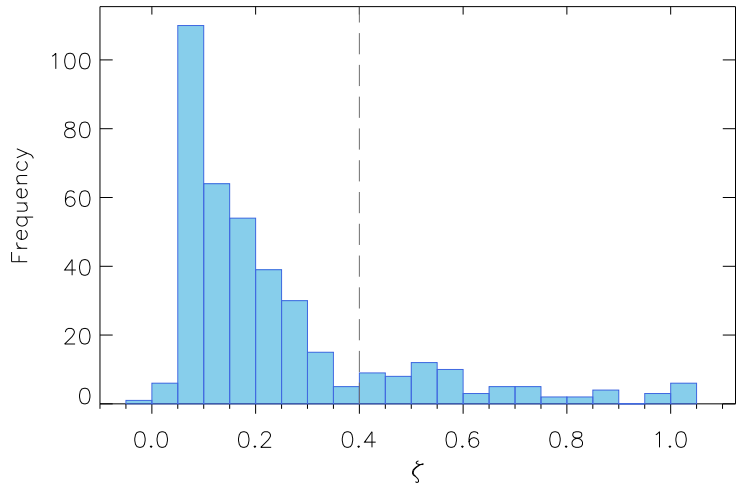

Figure 2.10: ζ-distribution of the sample. The galaxies right to the dashed line are regarded as disc-free galaxies.

1. For galaxies with a successful thin disc detection, the LOS stellar velocity corrected for asymmetric drift $v_{\rm corr}$ matches the Hα velocity $v_{\rm gas}$, and disc parameters are measured robustly.
2. For galaxies dominated by a thin disc, the influence of the isotropic component is negligible compared to the disc component in the stellar velocity dispersion model.

I parameterise each condition to measure its validation and then classify the sample into different types correspondingly.

To describe the consistency between $v_{\rm corr}$ and $v_{\rm gas}$, I introduce a parameter ζ defined as the median of the relative residual map,

$$\zeta = \text{median}(|(v_{\rm gas} - v_{\rm corr})/v_{\rm gas}|). \tag{2.32}$$

I avoid using a definition similar to reduced-χ^2 because of the strong non-circular motion and low S/N data in the Hα velocity fields. According to the ζ distribution in Figure 2.10, I make a cut-off at $\zeta = 0.4$. Galaxies with $\zeta > 0.4$ are regarded as no detection of thin discs.

The disc parameters are regarded to be measured robustly only if I obtain an acceptable relative uncertainty from the fitting of stellar velocity and dispersion fields. Since the uncertainty of disc parameters are passed to the uncertainty of the dynamical mass $M_{\rm dyn}$, I adopt a simple shortcut that if $M_{\rm dyn}$ of a galaxy has an relative uncertainty e($M_{\rm dyn}$) > 1dex , the disc

	definition	explanation
Disc-dominated	$\zeta \leqslant 0.4$ & $e(M_{dyn}) \leqslant 1$dex & $\eta \leqslant 1$	thin disc dominated
non-disc-dominated	$\zeta \leqslant 0.4$ & $e(M_{dyn}) \leqslant 1$dex & $\eta > 1$	thin disc detected, not dominated
disc-free	$\zeta > 0.4$ or $e(M_{dyn}) > 1$dex	no thin disc detection

Table 2.1: Definitions and explanations of this kinematic classification.

parameters of this galaxy are not measured robustly. It also means the detection of a thin disc (if there is a detection) is not reliable in this galaxy, so I classify it into the case of no disc detection as well.

I also introduce a parameter η to measure the influence of the isotropic component of the stellar velocity dispersion, defined as

$$\eta = \frac{\sigma_{0,\mathrm{iso}} \cdot h^2_{\sigma,\mathrm{iso}}}{\sigma_{0,\mathrm{d}} \cdot h^2_{\sigma,\mathrm{d}}}, \tag{2.33}$$

including the magnitude and influence area of both dispersion components. For galaxies with a thin disc, low η values indicate that the thin disc is dominating. I also make a cutoff empirically at $\eta = 1.0$.

With these parameters, I finally classify the sample into three kinematic types: disc-free, disc-dominated and non-disc-dominated galaxies. The definition and explanation of each kinematic types are shown in Table 2.1. I also show the colour-mass relation of the classifications in Figure 2.11, in which disc-dominated galaxies are bluer and disc-free galaxies are redder.

2.4 Results and discussions

By applying this analytic model to the sample, I have classified them into disc-dominated, non-disc-dominated and disc-free galaxies and obtained their dynamical mass. In this section, I will further explore other properties of the sample, such as stellar angular momentum, gas mass fraction and morphologies, to explain their mass composition and study their evolution scenario.

2.4.1 Stellar angular momentum

Stellar angular momentum reflects the kinematic motions of galaxies. The origin of stellar angular momentum are crucial for studying galaxy formation and evolution process. Emsellem

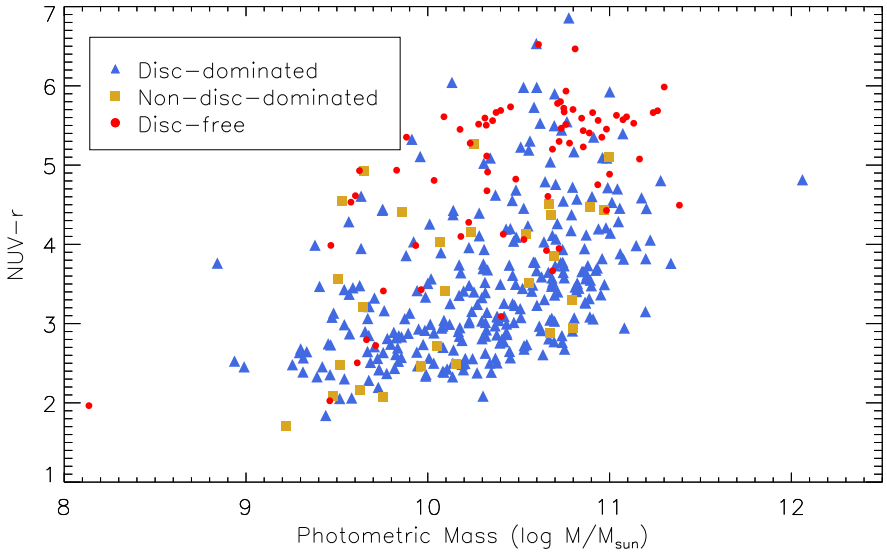

Figure 2.11: The colour-mass relation of the classifications. Blue triangles stand for disc-dominated galaxies, yellow squares stand for non-disc-dominated galaxies and red circles stand for disc-free galaxies.

et al. (2004) introduced a parameter λ_R defined as

$$\lambda_R \equiv \frac{\langle R|V|\rangle}{\left\langle R\sqrt{V^2+\sigma^2}\right\rangle}, \tag{2.34}$$

which is a proxy of projected stellar angular momentum by taking the luminosity-weighted average of 2-dimensional kinematic fields. Together with the observed ellipticity ϵ, the intrinsic morphology and dynamics of galaxies are then revealed. Emsellem et al. (2007) classify early-type galaxies into fast and slow rotators according to their λ_R values, while late-type galaxies are expected to be dominated by circular motions (e.g. Falcón-Barroso et al., 2019).

The final sample should contain late-type galaxies and fast-rotators because this model requires that galaxies have a regular velocity field. Furthermore, disc-dominated galaxies of this classification are dominated by circular motion while disc-free galaxies should have low fractions of circular motion. To examine this classification, I check the positions of the sample galaxies on the $\lambda_R - \epsilon$ diagram. I adopt the catalogue obtained from Graham et al. (2018), which contains the spin parameter λ_{R_e} introduced as a proxy for the stellar angular momentum within the half-light ellipse and ϵ and the ellipticity ϵ for MaNGA DR14 sample, which covers a sub-sample of 237 galaxies of the full sample. I plot the $\lambda_{R_e} - \epsilon$ diagram for this sub-sample in Figure 2.12. The $\lambda_{R_e} - \epsilon$ diagram shows a clear distinct in between disc-dominated galaxies

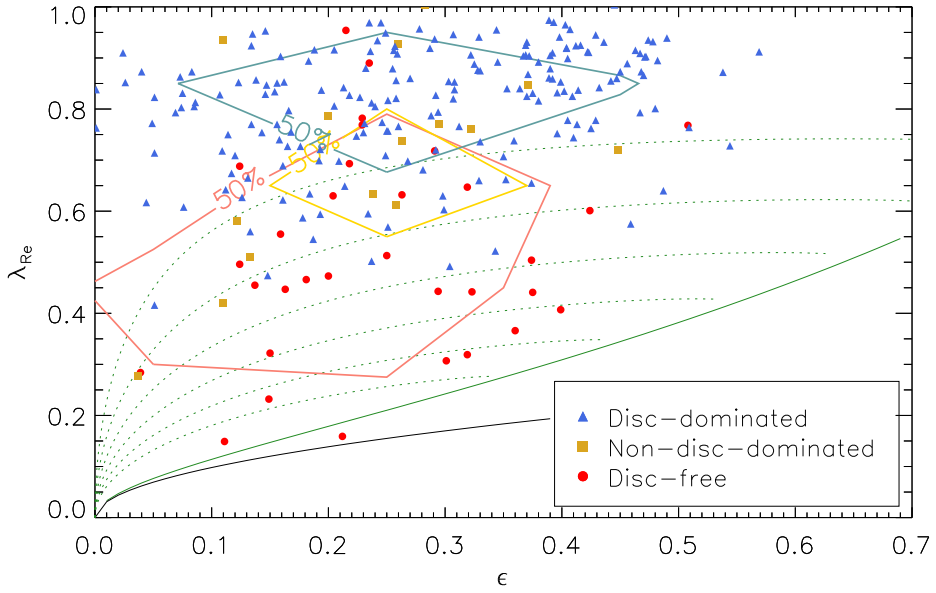

Figure 2.12: λ_{R_e} versus ellipticity ϵ for the sub-sample of 237 galaxies. Blue triangles stand for disc-dominated galaxies, yellow squares stand for non-disc-dominated galaxies and red circles stand for disc-free galaxies. The contours show half the maximum densities of the corresponding type. The black solid line $\lambda_{R_e} = 0.31\sqrt{\epsilon}$ distinguishes fast and slow rotators (Emsellem et al., 2011), and the green solid line corresponds with the theoretical curve that the anisotropy $\delta = 0.7\epsilon_{\rm intr}$, where $\epsilon_{\rm intr}$ is the intrinsic ellipticity (Cappellari et al., 2007). The green dotted lines show the location of galaxies with the intrinsic ellipticity $\epsilon_{\rm intr}$ is varied between $[0.35, 0.95]$ with a step of 0.1. The disc-dominated galaxies and disc-free galaxies are clearly distinct in the plot, and the non-disc-dominated galaxies lie in between.

and disc-free galaxies. 98% of disc-dominated galaxies have $\lambda_{R_e} > 0.5$, while 53% disc-free galaxies have $\lambda_{R_e} < 0.5$. The non-disc-dominated galaxies lie in between as an intermediate state. This result supports that this analytical model is capable of discerning thin discs in galaxies and the classification hence is based on galaxy intrinsic dynamics.

2.4.2 Mass property

The dynamical mass $M_{\rm dyn}$ is the total mass distributed in the disc, which provides crucial constraints on stellar mass M_* and dark matter. Therefore, I show the $M_{\rm dyn} - M_*$ correlations for the classification in Figure 2.13. There is a tight correlation between the dynamical and stellar mass for disc-dominated galaxies, while the correlation for non-disc-dominated galaxies has a larger scatter and several outliers. There is no clear correlation between the "dynamical" and stellar mass for disc-free galaxies: since I detect no thin discs in disc-free galaxies, the measurements of dynamical mass based on the thin-disc assumption are not physical.

The dynamical and stellar mass are close to the 1-to-1 line, but at the high-mass end the dynamical mass is slightly higher than the stellar mass. I first note that the dynamical mass density is obtained based on the thin-disc assumption without considering the dynamics of a possible bulge. This usually leads to an overestimation of the dynamical mass density in the bulge-dominated area at the galaxy centre as shown in the top-right panel in Figure 2.9. I therefore obtain a similar dynamical and stellar mass $M_{\rm dyn,nc}$ and $M_{*,\rm nc}$ by excluding the central area within a radius equals to $0.25R_{\rm hex}$ for each galaxy to reduce the influence of bulge, where $R_{\rm hex}$ is the radius of the MaNGA hexagon bundle. I also show the $M_{\rm dyn,nc} - M_{*,\rm nc}$ correlations for the classification in Figure 2.14. The $M_{\rm dyn,nc} - M_{*,\rm nc}$ correlation for disc-dominated galaxies show the same properties with the $M_{\rm dyn} - M_*$ correlation, indicating the effect of the bulge is negligible for explaining the mass difference at the high-mass for disc-dominated galaxies. Therefore, I explore other reasons to explain this mass difference.

The most probable explanation is that the dynamical mass is consistent with the total baryonic mass, which contains not only stellar mass but also the mass of other baryonic matter, such as gas and dust. Since disk-dominated galaxies are mostly spiral galaxies, the mass of the gas is not negligible. I obtain gas mass for disc-dominated galaxies within the MaNGA coverage obtained from the MaNGA DR15 PIPE3D VAC (Sánchez et al., 2016b,a), which contains the mass of H I and H_2 estimated from the dust attenuation as described in Barrera-Ballesteros et al. (2020). According to Martinsson et al. (2013), the atomic and molecular gas densities

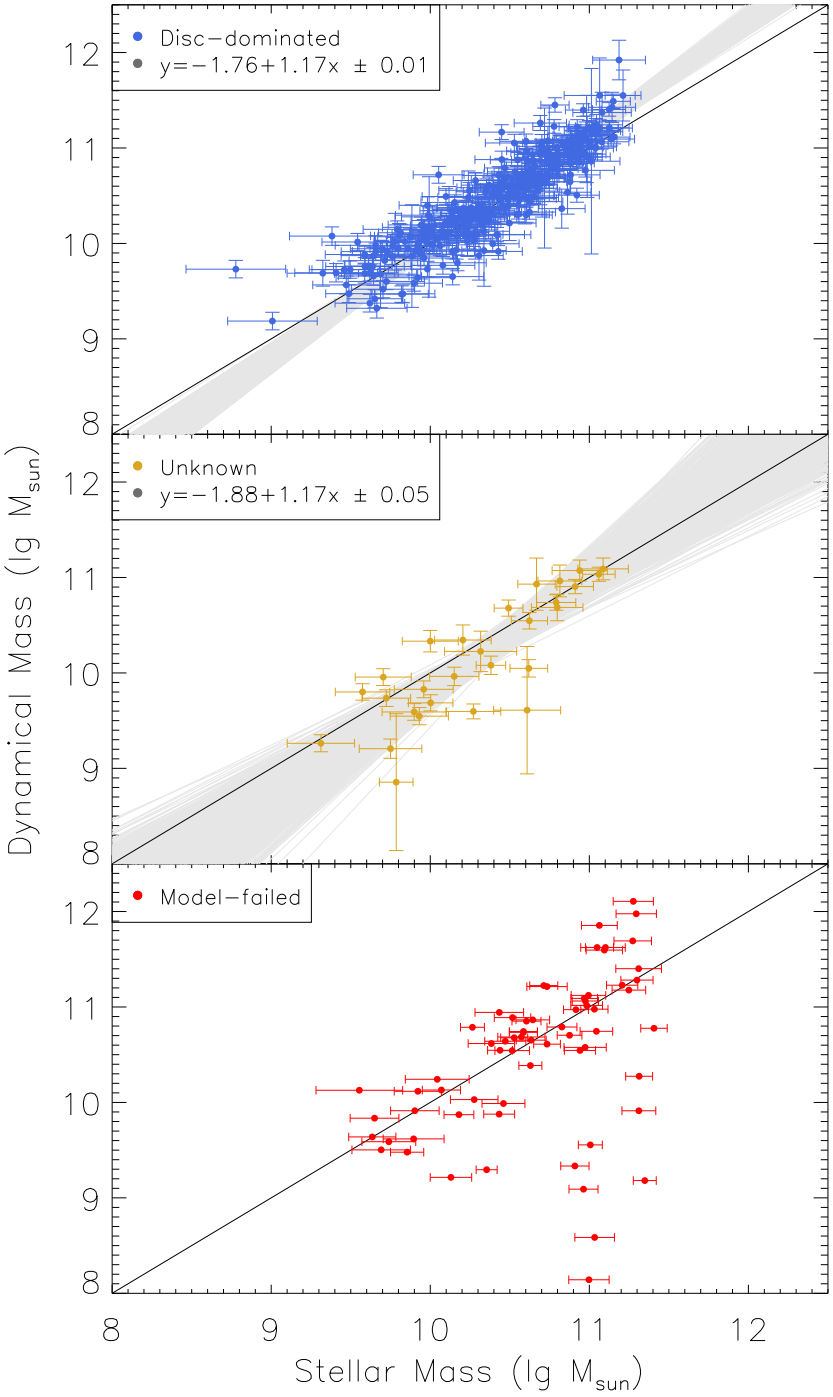

Figure 2.13: Dynamical mass versus stellar mass within the MaNGA field of view. From top to bottom: disc-dominated galaxies, non-disc-dominated galaxies and disc-free galaxies. The black solid line is the 1-to-1 line.

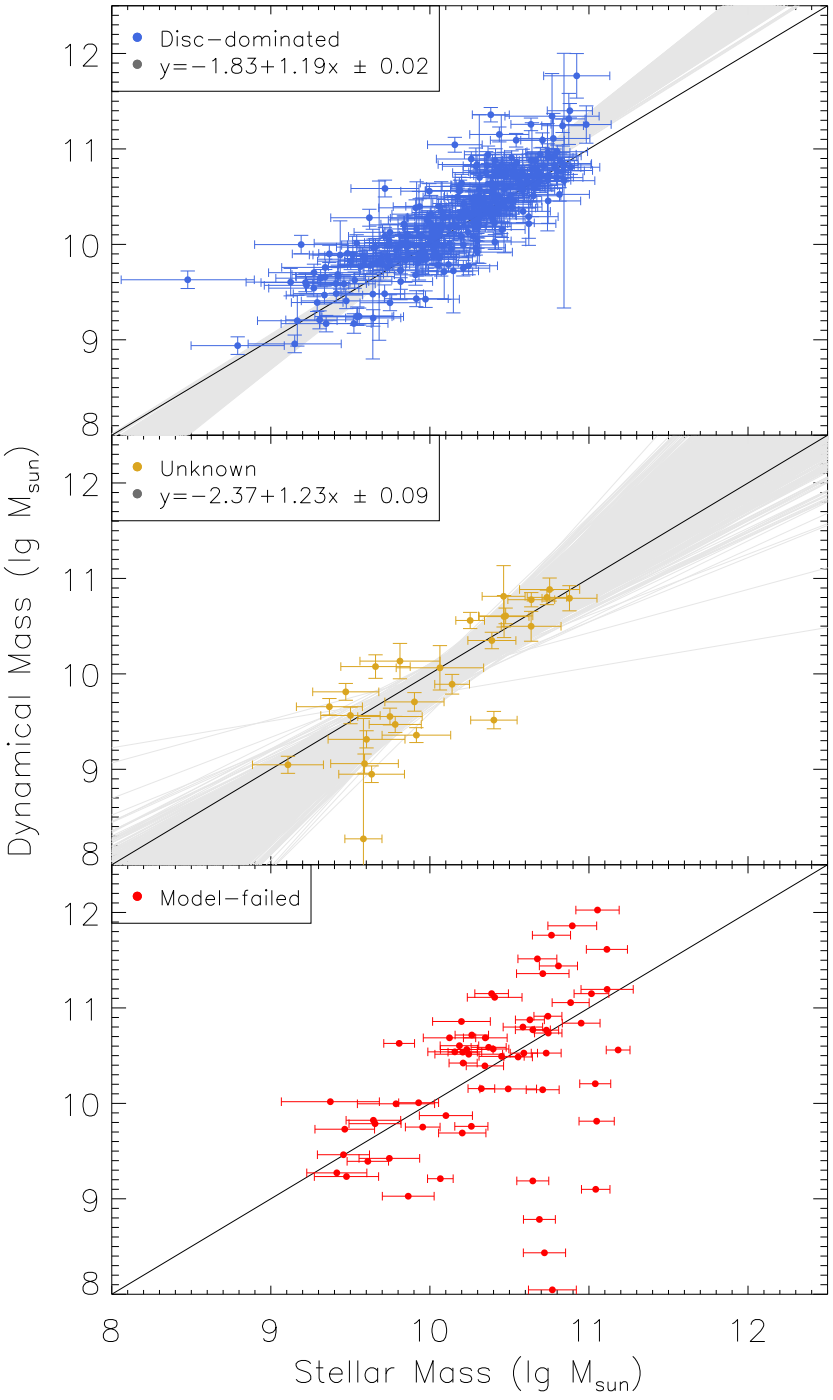

Figure 2.14: Dynamical mass versus stellar mass excluding the central area. The black solid line is the 1-to-1 line.

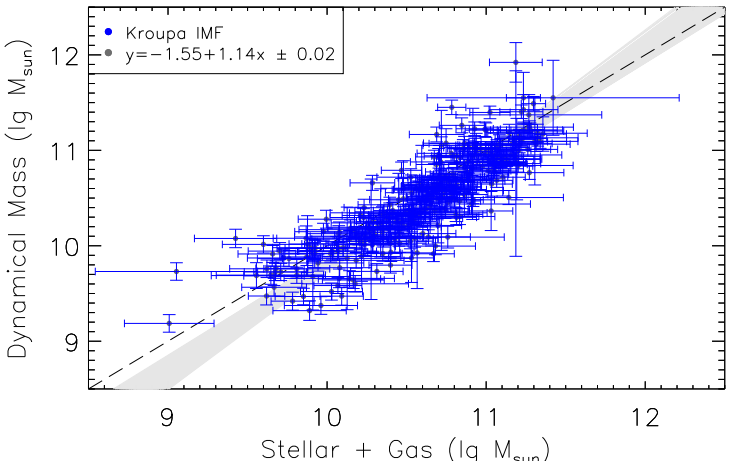

Figure 2.15: Dynamical mass versus baryonic mass within MaNGA coverage. The baryonic mass contains stellar mass (Kroupa IMF), atomic and molecular gas mass. The black dashed line is the 1-to-1 line.

can be obtained from the H I and H_2 densities by

$$\Sigma_{\rm atom} = 1.4\Sigma_{\rm HI}, \tag{2.35}$$

$$\Sigma_{\rm mol} = 1.4\Sigma_{\rm H_2}. \tag{2.36}$$

Therefore, I multiply a factor of 1.4 to the gas mass given in the PIPE3D VAC as the total gas mass within MaNGA coverage. I adopt the sum of stellar and gas mass as a proxy of total baryonic mass, and compare it with the dynamical mass in Figure 2.15. The correlation between dynamical and baryonic mass falls to the 1-to-1 line at the high-mass end, but at the low-mass end, the total baryonic mass exceeds the dynamical mass for some of the galaxies. The slope of the correlation between dynamical and total baryonic mass is still higher than 1. There are two possible reasons for that. First, the mass density for neutral hydrogen is overestimated for part of low-mass disc-dominated galaxies. Secondly, there is an IMF gradient and low-mass galaxies prefer an IMF producing lower stellar mass.

The stellar masses I adopt are measured with a constant Kroupa IMF, which is obtained from the Milky Way. However, massive early-type galaxies have an excess of low-mass stars compared to the prediction of the Kroupa IMF, resulting in a bottom-heavy IMF (van Dokkum & Conroy, 2010). A Salpeter-like IMF is also preferred by a number of early-type galaxies (e.g. Zhu et al., 2016). I therefore investigate the possibility that the IMF varies with stellar mass for disc-dominated galaxies by removing the gas mass from the dynamical mass and comparing

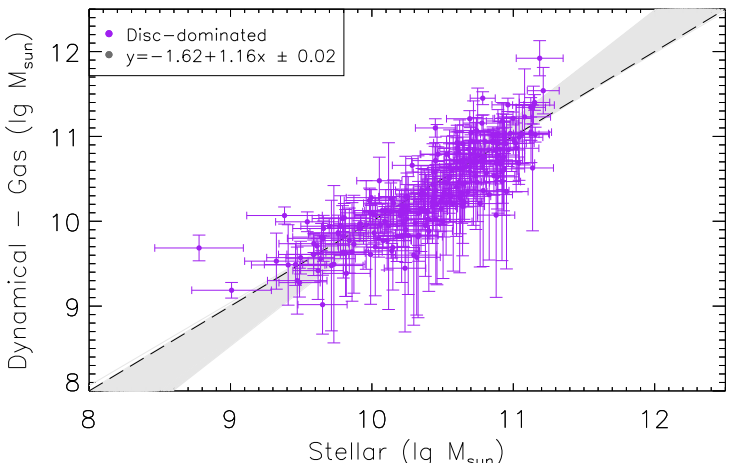

Figure 2.16: Stellar mass (Kroupa IMF) versus dynamical mass removing gas mass within MaNGA coverage. The black dashed line is the 1-to-1 line.

it with the stellar mass in Figure 2.16. The correlation almost falls on the 1-to-1 line, suggesting that if there is an IMF gradient across stellar mass for disc-dominated galaxies, it is a small gradient that low-mass galaxies prefer a lighter IMF producing less stellar mass than the Kroupa IMF while high-mass galaxies prefer a heavier one.

I note that there is a systematic error existence in the dynamical mass. The MaNGA MPL-7 data tend to overestimate the velocity dispersion systematically because of MaNGA DAP underestimate the line spread function. This over-estimation is mass dependent and ranges from 5% for the highest mass galaxies ($M_* > 10^{11} M_\odot$) to 40% for the lowest mass galaxies ($M_* < 10^{9.5} M_\odot$), which results in a sleeper slope in Figure 2.13 by about 2 percent, within $1-\sigma$ uncertainty due to sample variance and random errors, and also suggests a higher IMF gradient by increasing the slope Figure 2.16 by about 15 percent, at the marginal edge of $1-\sigma$ uncertainty.

These results about dynamical and baryonic mass also show that within the MaNGA coverage (typically $1.5R_e$), the dark matter content is negligible in galaxy discs.

2.4.3 Morphology

I have classified the sample into three kinematic types: disc-dominated, non-disc-dominated and disc-free galaxies. I am interested in the morphology distribution of each type. Therefore, I adopt two morphological catalogues, the Galaxy Zoo catalogue (Willett et al., 2013) which involves volunteers for visual classification, and the Deep Learning catalogue (Domínguez Sánchez

	Deep Learning	Galaxy Zoo
Spiral	TType > 0.0	t01_a01_d < 0.8 & t04_a08_d $\geqslant 0.5$
S0	TType $\leqslant 0.0$ & P_S0 > 0.5	t01_a01_d < 0.8 & t04_a08_d < 0.5
Elliptical	TType $\leqslant 0.0$ & P_S0 $\leqslant 0.5$	t01_a01_d $\geqslant 0.8$

Table 2.2: Morphology definition of two catalogues. The description for the Deep Learning catalogue: TType < 0 for early-type galaxies, TType > 0 for late-type galaxies, TType ~ 0 for S0s; P_S0 stands for the probability of being a S0 rather than a pure elliptical for galaxies with T-Type $\leqslant 0$. The description for the Galaxy Zoo catalogue: t01_smooth_or_features_a01_smooth_debiased is the debiased vote fraction of the question if the galaxy is smooth; t04_spiral_a08_spiral_debiased is the debiased vote fraction of the question if the galaxy has spiral arms.

et al., 2018) which trains Convolutional Neural Networks with a robust visual classification sample and then obtains the classification of a large dataset. I classify the sample into spirals, lenticulars (S0s) and ellipticals according to the schemes of these two catalogues, as shown in Table 2.2.

I then compare this kinematic classification with the Deep Learning catalogue in Table 2.3. The kinematic and morphological classification are correlated. Disc-dominated galaxies are mainly composed of spiral galaxies and a number of S0 galaxies, while disc-free galaxies are mostly elliptical and lenticular galaxies. non-disc-dominated galaxies have an even morphology distribution, which is not well explained yet. I also notice the unexpected disc-dominated ellipticals and disc-free spirals in Table 2.3. By checking their images and kinematic fields, I find the following reasons. Spirals have failed to be modelled because of their poor data qualities of Hα velocity or stellar velocity dispersion. Most of the disc-dominated ellipticals are actually S0s or spirals according to the Galaxy Zoo classification scheme, which is confirmed by the spiral arms or disc features found in their images in my visual check. They are wrongly classified as ellipticals because of the contamination of machine learning.

I also notice a clear dichotomy of S0 galaxies. I detect a dominating thin disc in the majority of S0 galaxies, while there are no thin discs detected in part of S0 galaxies. I therefore investigate various galaxy properties to explain this dichotomy. Finally, two major differences are found between disc-free S0s and disc-dominated S0s: the star formation rate and the molecular gas fraction. I find no clear differences in their distributions of stellar mass or other properties, including their environments in the Galaxy Environment for MaNGA DR15 VAC (Argudo-Fernández et al., 2015; Etherington & Thomas, 2015).

I adopt the integrated star formation rate (SFR) derived from the amount of stellar mass formed in the last 32 Myr provided by the PIPE3D VAC. The molecular gas fraction is defined

	Spiral	S0	Elliptical
Disc-dominated	244	40	10
non-disc-dominated	11	9	8
disc-free	10	23	38

Table 2.3: Morphology statistics (Deep Learning catalogue) for the kinematic classifications. The kinematic and photometric morphology are well correlated. There are disc-free spirals because of poor data quality and disc-dominated ellipticals because of machine learning contamination, which are classified as spirals and lenticulars according to the Galaxy Zoo classification scheme.

as the ratio between the molecular gas and stellar mass within MaNGA coverage obtained in Section 2.4.2. I show the corresponding distributions for disc-dominated S0s and disc-free S0s (disc-dominated spirals and disc-free ellipticals are also included for comparison) in Figure 2.17 and 2.18, respectively. In general, disc-dominated galaxies have the highest SFRs and the molecular gas fraction, while disc-free S0s and ellipticals have the lowest SFRs and molecular gas fractions. The disc-dominated S0s appear to be an intermediate class lying in between.

The descending SFRs between disc-dominated and disc-free S0s shows the quenching process of S0 galaxies. Since I have selected a sample with regular kinematics, this quenching is unlikely a result of violent processes (e.g. major mergers). The result that there is no clear difference between the environment of disc-dominated and disc-free S0s also suggests that there is no clear evidence that the quenching is caused by a process related to galaxy environments (e.g.ram-pressure stripping). Since the molecular gas takes a dominant role in the gas mass budget (Leroy et al., 2008, 2009), therefore, the depletion of gas in Figure 2.18 is majorly driven the depletion of molecular gas, which probably accounts for the quenching process in these S0 galaxies. This depletion of molecular gas is possibly a result of the gas consumption by star formation, AGN or stellar feedback (e.g. Fabian, 2012; Hopkins et al., 2014). This conclusion is consistent with the scenario proposed by Zhang et al. (2019) that massive quiescent disk galaxies are quenched because they have significantly reduced molecular gas content.

These results also suggest an in-situ evolution path of S0 galaxies. As the quenching process goes on, galaxy kinematic states change gradually. The kinematic similarity between disc-dominated S0s and spirals indicates that thin discs can remain stable in a period of time after the molecular gas fraction starts to decrease. As the molecular gas fraction further decreases, thin disc structures gradually dissolve in S0 galaxies, which leads to different kinematic types for S0s. Finally, as the molecular gas of disc-dominated S0s is used up (comparable to disc-free

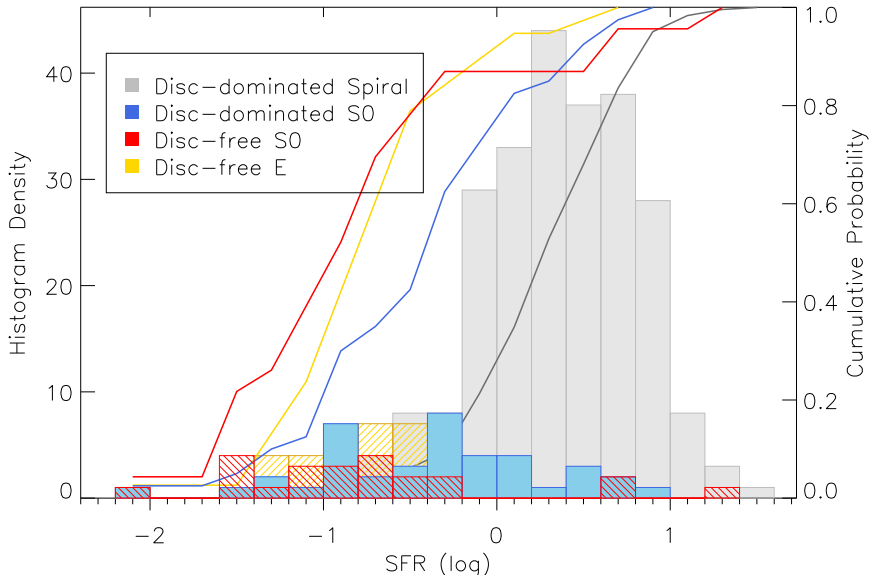

Figure 2.17: The histogram of the integrated SFR derived from stellar mass formed in the last 32 Myr for disc-dominated spirals, disc-dominated S0s, disc-free S0s and disc-free ellipticals. The solid lines stand for the corresponding cumulative distribution functions.

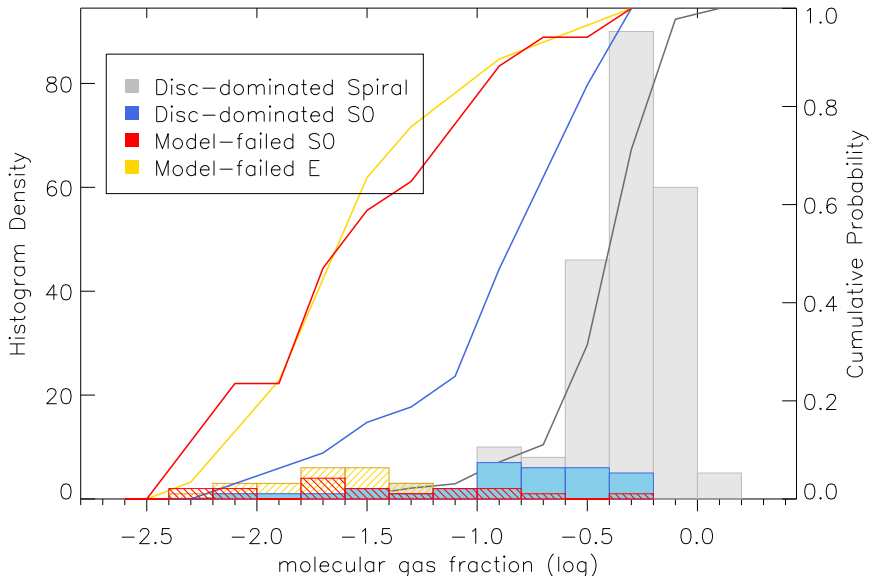

Figure 2.18: The histogram of the gas fractions for disc-dominated spirals, disc-dominated S0s, disc-free S0s and disc-free ellipticals. The solid lines stand for the corresponding cumulative distribution functions.

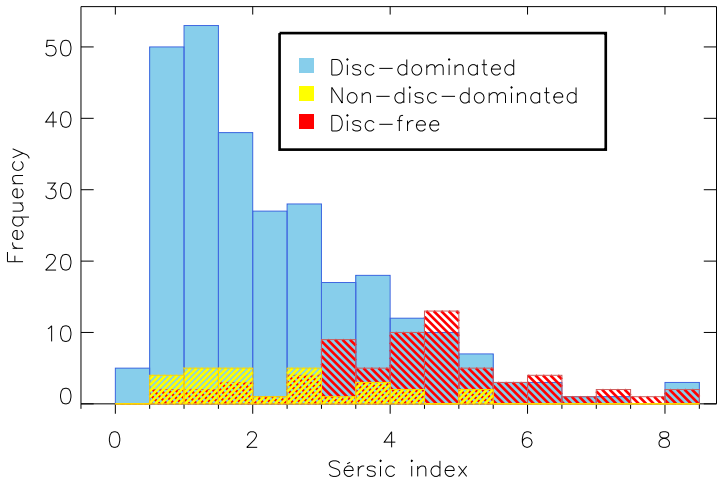

Figure 2.19: The Sérsic index distribution obtained from the 1-component fitting of PyMorph.

ellipticals), the quenching process finishes.

2.4.4 Structural parameters

Structural parameters (e.g. the Sérsic index and bulge-to-total ratio) hold clues to disclose galaxy morphology and components and are widely applied as criteria to distinguish the morphology of quantitative galaxies. I therefore investigate the distribution of two structural parameters for the kinematic classification, the Sérsic index of 1-component fitting and bulge-to-total ratio (B/T) of 2-component decomposition obtained from MaNGA DR15 PyMorph photometric catalogue (Fischer et al., 2018), which provides the result of a Sérsic fitting and a Sérsic + Exponential component decomposition to the 2-dimensional surface brightness profiles of the MaNGA sample with the PYMORPH algorithm (Vikram et al., 2010).

The distributions of the Sérsic index for the kinematic types are shown in Figure 2.19. Disc-dominated galaxies in general have lower Sérsic indices while disc-free galaxies have higher ones. As an intermediate state, non-disc-dominated galaxies have a similar distribution to disc-dominated galaxies These properties are consistent with the trend that Sérsic indices increase from disc galaxies to spherical galaxies. However, the overlap of disc-dominated galaxies and disc-free galaxies indicates that Sérsic indices are a reference instead of an accurate classification for galaxy morphologies.

The B/T distribution obtained from the 2-component decomposition is also shown in Figure 2.20. Similar to the Sérsic index, the distributions of B/T also follows the trend that B/T

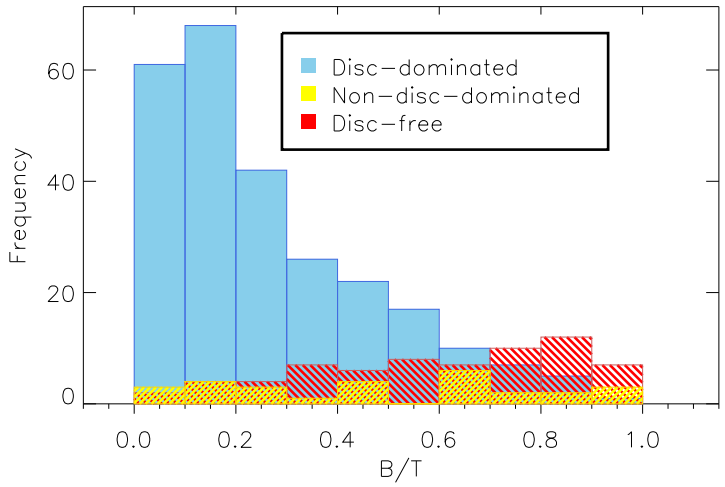

Figure 2.20: B/T distribution obtained from the two-component fitting of PyMorph.

increases from disc galaxies to spherical galaxies: the disc-dominated galaxies have lower B/T while disc-free galaxies are the opposite; the distribution of the non-disc-dominated galaxies are widely spread, different from both disc-dominated and disc-free galaxies.

There is a correlation between the Sérsic index distributions of disc-dominated and non-disc-dominated galaxies but not for the B/T distributions, which shows a clue to understand the formation of the non-disc-dominated galaxies. There are disc features in both types, leading to their similarity in their kinematics and their Sérsic index distribution, however, disc features play a dominant role for disc-dominated galaxies but not for non-disc-dominated galaxies, which causes different B/T distributions.

2.5 Summary

In this section, I built an analytical model to describe observed stellar velocity and velocity dispersion based on a thin-disc assumption. I then corrected the stellar velocity for asymmetric drift and compared it with the Hα velocity. By examining whether this model is successfully applied with introduced parameters, I can judge whether a thin disc is detected and whether it takes a dominant role in a galaxy, and obtain a kinematic classification scheme. The sample is finally classified into disc-dominated, non-disc-dominated and disc-free galaxies according to this classification scheme.

- The $\lambda_{R_e} - \epsilon$ diagram supports the kinematic classification. Disc-dominated galaxies have

different dynamic features from disc-free galaxies, while non-disc-dominated galaxies lie in between as an intermediate state.

- The difference between the dynamical and stellar mass for disc-dominated galaxies is explained by including the mass of atomic and molecular gas. These disc-dominated galaxies prefer a Kroupa-like IMF, while a slight IMF gradient is also acceptable. The dark matter is negligible in galaxy discs within $1.5R_e$.

- I found a clear dichotomy in the kinematic classifications for S0 galaxies. The majority of S0s are dominated by a thin disc, while I failed to detect a thin disc in some of the S0s. By comparing their SFRs and molecular gas fractions with disc-dominated spirals and disc-free ellipticals, I propose that an in-situ quenching process changes the kinematic state of galaxies, and the quenching starts because of the depletion of molecular gas.

This analytical model provides a simple method to identify thin discs in galaxies. Considering that surveys are producing large amounts of data nowadays, analytical models are valuable tools for modelling galaxies and then studying galaxy evolution because of their simplicity and efficiency.

3

Numerical dynamical modelling of galaxies

Most galaxies are usually regarded as stellar systems in dynamical equilibrium, therefore, they can be modelled based on the Jeans theorem (Jeans, 1915). Modelling such a stellar system in dynamical equilibrium is usually referred to as dynamical modelling, which is an important method to measure the most fundamental properties of galaxies: the mass distribution and orbital state of galaxies. Dynamical modelling can be implemented in analytic and numerical ways. Fully analytic models based on distribution functions (DFs) are developed for galaxy modelling, but the difficulty in searching for analytical DFs constrains the implementation of these models in a limited number of cases. In contrast, numerical dynamical models, which can recover the observational data and infer galaxy internal mass distribution, are more applicable for galaxy modelling and have been widely applied to observational data. Therefore, I introduce dynamical modelling of galaxies in this chapter.

3.1 Numerical dynamical models

Multiple numerical dynamical modelling techniques have been developed following different strategies. The first strategy is that a dynamical model is built self-consistently to infer the mass distribution of the stellar system, in which the density derived from DF is consistent with the density derived from the gravitational potential according to the Poisson equation. The second strategy is that a dynamical model focus on recovering the observational data to infer the mass distribution of the galaxy including the non-stellar mass such as a dark matter halo and a central black hole, regardless of the request of self-consistency. Here I briefly introduce several popular dynamical models, including DF-based models based on the first strategy, and the Jeans models, orbit-based and particle-based models based on the second strategy.

DF-based models

There is a long history of searching for DF for galaxies, however, analytic models built based on the DFs are still rare. Even if an analytic DF is found, it needs numerical methods to calculate the observables. Therefore, numerical dynamical models are developed based on various forms of DFs.

One strategy is to build dynamical models with a given form of DF, including DFs for a single component (e.g. bulges and discs) and multiple components as in real galaxies. For example, spherical models are built from two-integral DFs which conserve their energy E and total angular momentum L, to describe galaxy bulges (e.g. Jarvis & Freeman, 1985; Rowley, 1988; Shaw, 1993) and discs (Batsleer & Dejonghe, 1995). Axisymmetric models based on three-integral DFs, which conserve the energy E, the angular momentum along the symmetry axis L_z and a non-classical third integral I_3, are more realistic and have been successfully applied to early-type galaxies to obtain their black hole masses (e.g. Emsellem et al., 1999; Gebhardt et al., 2000; de Bruyne et al., 2001). Self-consistent models considering multiple components including bulges, discs and dark matter haloes are also developed (e.g. Kuijken & Dubinski, 1995; Widrow & Dubinski, 2005; Widrow et al., 2008) and applied to nearby disc galaxies with IFS observations (Taranu et al., 2017) to reproduce the surface brightness, rotation curves and velocity dispersion profiles of galaxies.

An alternative way of building DF-based models is to obtain non-parametric DFs from observations. Non-parametric DFs are the superposition of analytic DFs. The observables are

calculated for each DF component and the weights of DF components are then solved by comparing with observations. Theoretical models with different specific forms of DF components and methods of superposition are developed (e.g. Dejonghe, 1989; Merritt & Saha, 1993; Pichon & Thiébaut, 1998; Magorrian, 2014) to infer galaxy gravitational potential and mass distribution.

The major advantage of DF-based models is that galaxy kinematic states can be clearly known with the phase-space DFs. They are also continuous and therefore suitable for both continuous and discrete observational data. However, DF-based models require the galaxy gravitational potential to be integrable, which limits their implementation.

Jeans models

The Jeans models based on finding solutions of the Jeans equation (Jeans, 1922) to fit observed moments (line-of-sight velocity and velocity dispersion) of galaxies, and are widely applied for modelling galaxies. The Jeans models can either be built self-consistently to obtain the mass distribution of stellar systems, or be built non-self-consistently to infer the mass distribution of dark matter haloes as well. There are several types of Jeans models, according to their assumptions for the velocity anisotropy, which describes whether stars move tangentially or radially.

The spherical Jeans model, in which the mass distribution, velocity profile and velocity anisotropy are spherically symmetric, was first applied to elliptical galaxy M 87 by Binney & Mamon (1982), however, the spherical Jeans model suffers a mass-anisotropy degeneracy that the velocity dispersion, the velocity anisotropy and gravitational potential cannot be solved simultaneously without further assumptions to lift this degeneracy (e.g. Merrifield & Kent, 1990; Wilkinson et al., 2002; Walker & Penarrubia, 2011; Mamon et al., 2013).

For axisymmetric galaxies, several assumptions of galaxy anisotropy are introduced to simplify the case. One assumption is the semi-isotropic assumption, which has a circular velocity ellipsoid in the meridional plane and is popular for its simplicity. It was applied to galaxies by Satoh (1980) who modelled elliptical galaxy NGC 4697. This technique was then extended and applied to a larger sample of galaxies with long-slit stellar kinematics along major and minor axes (e.g. Binney et al., 1990; van der Marel et al., 1990; van der Marel, 1991; Cortés et al., 2008) and even galaxies with IFS observations (Cappellari et al., 2006) for the study

of rotation and mass-to-light ratios. Another popular assumption is the cylindrical assumption that the velocity ellipsoid in the meridional plane is aligned with the cylindrical coordinates. The implementation based on this assumption is called the anisotropic Jeans model, which is developed by Cappellari (2008). The package for this implementation of the Jeans Anisotropic MGE (`JAM`, see section 3.2.1 for the explanation of MGE) is frequently used for modelling galaxies observed with IFS surveys, such as the Atlas^{3D} (Cappellari et al., 2013b), CALIFA (Leung et al., 2018) and SDSS-IV MaNGA (Li et al., 2017) surveys, and also assessed by modelling simulated galaxies (Li et al., 2016).

The Jeans models has an advantage of requiring low computational resources, which makes it suitable for modelling the mass distribution of a large sample obtained from IFU surveys. Its ability to model discrete kinematic data, such as the velocities of planetary nebulae (PNe) and globular clusters (GCs), also expands its applicability. However, this technique usually requires a high symmetry of galaxies (spherical or axisymmetric) and therefore is not suitable for modelling triaxial galaxies.

Orbit-based models

Schwarzschild (1979) proposed an orbit-superposition technique which computes a large orbit library in a given potential and then solves the weights of orbits to reproduce the observations. This powerful technique to explore the mass distribution of galaxies is called the Schwarzschild orbit-superposition technique. There are a number of implementations of the Schwarzschild technique to the spherical (e.g. Richstone & Tremaine, 1984; Rix et al., 1997; Breddels et al., 2013) and axisymmetric geometry (e.g. Cretton et al., 1999; Gebhardt et al., 2000; Valluri et al., 2004). Although there have been theoretical studies for the triaxial geometry since the appearance of this technique (e.g. Schwarzschild, 1979, 1993; Merritt & Fridman, 1996; Siopis & Kandrup, 2000), this technique was not implemented to observational external galaxies until van den Bosch et al. (2008) proposed a triaxial code for modelling early-type galaxies which was then generalised to late-type galaxies by Zhu et al. (2018c). Vasiliev (2013) also proposed an implementation of this technique and developed it to model galaxies with bars or figure rotations (Vasiliev & Athanassoula, 2015; Vasiliev & Valluri, 2020).

The most significant advantage of the Schwarzschild technique is its ability of modelling triaxial galaxies and infer the total mass distribution, including a dark matter halo and a central black hole. This model is based on stellar orbits and therefore provides an advantage of

studying galaxy stellar dynamical structures with no requirement of a specific form of DF or self-consistency. However, this technique is applied to discrete data, such as PNe and GCs, only in limited cases (Chanamé et al., 2008; Magorrian, 2019) because it is difficult to evaluate the probability of discrete orbit-based models using discrete data. Compared to the DF-based and Jeans models, orbits-based models have higher demands for computing resources. I will introduce this method in more detail following the methodology of van den Bosch et al. (2008) and Zhu et al. (2018c) in Section 3.2, as I will make use of this method to develop new orbit-based models and model the mass distribution of early-type galaxies in Chapters 4, 5 and 6.

Particle-based models

Particle-based models are constructed for the realisation of N-body systems in dynamical equilibrium. Syer & Tremaine (1996) proposed a made-to-measure (M2M) algorithm which integrates a N-body system while adjusting the weights of particles slowly until the time-averaged density field converges and the observables predicted by the model match the observations. This algorithm was then developed to allow an evolving gravitational potential to form a self-consistent model (Bissantz et al., 2004) and implemented as the N-particle Made-to-measure AlGorithm mInimizing Chi squared (`NMAGIC`) code (de Lorenzi et al., 2007), which is applied to model nearby elliptical galaxies (e.g. de Lorenzi et al., 2008, 2009; Das et al., 2011; Morganti et al., 2013). Other implementations of M2M algorithms (e.g. Long & Mao, 2010; Hunt & Kawata, 2013) which can model disc galaxies have also been applied to observations (Long & Mao, 2012; Zhu et al., 2014). Iterative methods of constructing N-body models were also proposed for creating initial conditions for N-body simulations and modelling galaxies (Rodionov et al., 2009; Yurin & Springel, 2014) with applications for the latter purpose (e.g. Rodionov & Athanassoula, 2011; Saburova et al., 2018).

Particle-based models have similar properties with orbit-based models: it can model triaxial galaxies and infer their total mass distribution without requiring self-consistency or a specific form of DF; it has difficulty to model discrete kinematic data that they need to be binned to compute the likelihood of the model; it also requires high computational resources. However, orbit-based models have the advantage of decomposing dynamical components based on stellar orbit types, while it is not straightforward to obtain stellar orbit information in particle-based models.

3.2 Schwarzschild orbit-superposition technique

In this section, I introduce the Schwarzschild orbit-superposition technique in detail following the triaxial implementation described in van den Bosch et al. (2008) and Zhu et al. (2018c), which has been applied to galaxies with CALIFA and MaNGA observations (Zhu et al., 2018a; Jin et al., 2019). It includes the following steps: I first introduce how to regularise the stellar mass distribution from galaxy surface brightness using the Multiple Gaussian Expansion method to obtain galaxy gravitational potential; I then introduce the characteristics of stellar orbits and the strategy of orbit sampling to build orbit libraries. Lastly, I introduce the method of solving the weights for orbits in the orbit libraries.

3.2.1 Multiple Gaussian Expansion

The stellar mass distribution in galaxies are hardly directly described by an analytic function, therefore, it needs to be parameterised. The Multiple Gaussian Expansion (MGE) method was introduced for this purpose by Emsellem et al. (1994), which generalised the approach described by Monnet et al. (1992). This MGE method can provide analytical spatial luminosity density distribution for any assumed triaxial shape at a given line of view, which significantly simplifies the computation in numerical dynamical modelling. The fitting algorithm of MGE which I adopt in this work is described in Cappellari (2002).

The MGE method follows a principle that the surface brightness of a galaxy $S(R', \theta')$ can be written as a sum of Gaussian profiles,

$$S(R', \theta') = \sum_j S_j(x'_j, y'_j) = \sum_j \left(\frac{L_j}{2\pi\tilde{\sigma}_j^2 \tilde{q}_j} \exp\left[-\frac{1}{2\tilde{\sigma}_j^2} \left(x_j'^2 + \frac{y_j'^2}{\tilde{q}_j^2} \right) \right] \right), \tag{3.1}$$

with

$$\begin{aligned} x'_j &= R' \sin(\theta' - \psi'_j) \\ y'_j &= R' \cos(\theta' - \psi'_j) \end{aligned} \tag{3.2}$$

where (R', θ') are the polar coordinates on the sky plane, $S_j(x'_j, y'_j)$ is the surface brightness distribution of each Gaussian component with corresponding luminosity L_i, scale length σ'_i, axis ratio q'_i and position angle ψ'_j.

The observed scale length $\tilde{\sigma}_j$ and axis ratio $\tilde{q}_j$ are influenced by the point spread function (PSF). Assuming the PSF can be represented by a single normalised circular Gaussian with a scale length $\sigma_{\rm PSF}$, the intrinsic parameters of each Gaussian profile σ'_j and q'_j follows the relations below,

$$\begin{aligned} \tilde{\sigma}_j^2 &= \sigma_j'^2 + \sigma_{\rm PSF}^2 \\ \tilde{\sigma}_j^2 \tilde{q}_j^2 &= \sigma_j'^2 q_j'^2 + \sigma_{\rm PSF}^2 \end{aligned} \tag{3.3}$$

For each single Gaussian component $S(x', y')$ (the subscript j is omitted here), the intrinsic luminosity density can be written as (Cappellari, 2002),

$$\rho(x,y,z) = \frac{L}{(\sigma\sqrt{2\pi})^3 pq} \exp\left[-\frac{1}{2\sigma^2}\left(x^2 + \frac{y^2}{p^2} + \frac{z^2}{q^2}\right)\right], \tag{3.4}$$

where (x, y, z) are aligned with the principal axes of the Gaussian with the x-axis aligned with the long axis and z-axis aligned with the short axis, σ is the scale length, p and q are the intrinsic axis ratios with $0 \leq q \leq p \leq 1$. To describe the space orientation of the galaxy, a group of viewing angles (θ, ϕ, ψ) are introduced: (θ, ϕ) define the line-of-sight direction with respect to the principal axes, and ψ defines the rotation on the sky plane around the line-of-sight to align the major axis of the innermost Gaussian with the x'-axis ($\psi = 90°$ for an oblate asymmetric case). At given viewing angles (θ, ϕ, ψ), $(p, q, u \equiv \sigma'/\sigma)$ are decided according to the following equations:

$$\begin{aligned} 1 - q^2 &= \frac{\delta'[2\cos 2\psi' + \sin 2\psi'(\sec\theta\cot\phi - \cos\theta\tan\phi)]}{2\sin^2\theta[\delta'\cos\psi'(\cos\psi' + \cot\phi\sec\theta\sin\psi') - 1]}, \\ p^2 - q^2 &= \frac{\delta'[2\cos 2\psi' + \sin 2\psi'(\cos\theta\cot\phi - \sec\theta\tan\phi)]}{2\sin^2\theta[\delta'\cos\psi'(\cos\psi' + \cot\phi\sec\theta\sin\psi') - 1]}, \\ u^2 &= \frac{1}{q'}\sqrt{p^2\cos^2\theta + q^2\sin^2\theta(p^2\cos^2\phi + \sin^2\phi)}, \end{aligned} \tag{3.5}$$

where $\delta' = 1 - q'^2$. In an oblate axisymmetric geometry ($p = 1$), only one viewing angle θ is essential, representing the inclination. Then the above relations reduce to

$$q^2 = \frac{q'^2 - \cos^2\theta}{\sin^2\theta}. \tag{3.6}$$

This introduces a potential problem that there should be $\cos^2\theta < q'_j$ for all Gaussian components, which means the minimum inclination θ is decided by the minimum q'_j (Cappellari,

2002). Therefore, the fitting of MGE should be repeated until the minimum q'_j allows a reasonable range for the inclination.

The gravitational potential corresponding to the mass distribution in equation 3.4 is given in Emsellem et al. (1994) and also referred in van den Bosch et al. (2008). Here I only note that this gravitational potential is not analytic and has to be integrated numerically.

3.2.2 Stellar orbit library

The Schwarzschild technique is based on the superposition of stellar orbits to recover galaxy kinematic fields, therefore, it is important to build stellar orbit libraries containing orbits representative for all kinds of stellar orbits through a proper strategy of orbit sampling. To sample orbits efficiently, we need to understand the characteristics of stellar orbits.

The gravitational potential generated by Gaussian components are separable, i.e. $\Phi(x,y,z) = \Phi(x)\Phi(y)\Phi(z)$. All orbits in a separable potential are regular and conserve three analytical integrals of motion: E (energy), I_2 and I_3. The orbits can be characterised into four orbit families: three types of tube orbits (short axis tubes, outer and inner long axis tubes) and the box orbits, as shown in Figure 3.1. These orbit families cross well-defined regions in the (x,z) plane perpendicularly (Schwarzschild, 1993; van den Bosch et al., 2008), as shown in Figure 3.2. All tube orbits except thin orbits cross the (x,z) plane perpendicularly twice in two separate regions, while the box orbits also cross the (x,z) plane perpendicularly only once in another region. All these regions can be obtained analytically for a separable potential. These features are very important for orbit sampling.

A strategy for orbit sampling is built according to the properties of the orbit families (Schwarzschild, 1993; van den Bosch et al., 2008). Since orbits cross the (x,z) plane perpendicularly, their positions on the (x,z) plane are defined as their start points. These start points and their corresponding orbit energy E are the initial conditions of orbit sampling. The energy E is linked with a grid radius r_i such that E equals the potential at position $(x,y,z) = (r_i,0,0)$. r_i is sampled logarithmically with the minimum at least an order of magnitude smaller than the pixel size of the observations and the maximum includes over 99.9% of mass. For each energy E, the start points on the (x,z) plane is then sampled using a open linear polar grid (R,θ). It is only essential to sample between the thin orbit and the equipotential (the grey region in Figure 3.2), because all orbits cross this region perpendicularly only once. The initial velocity in

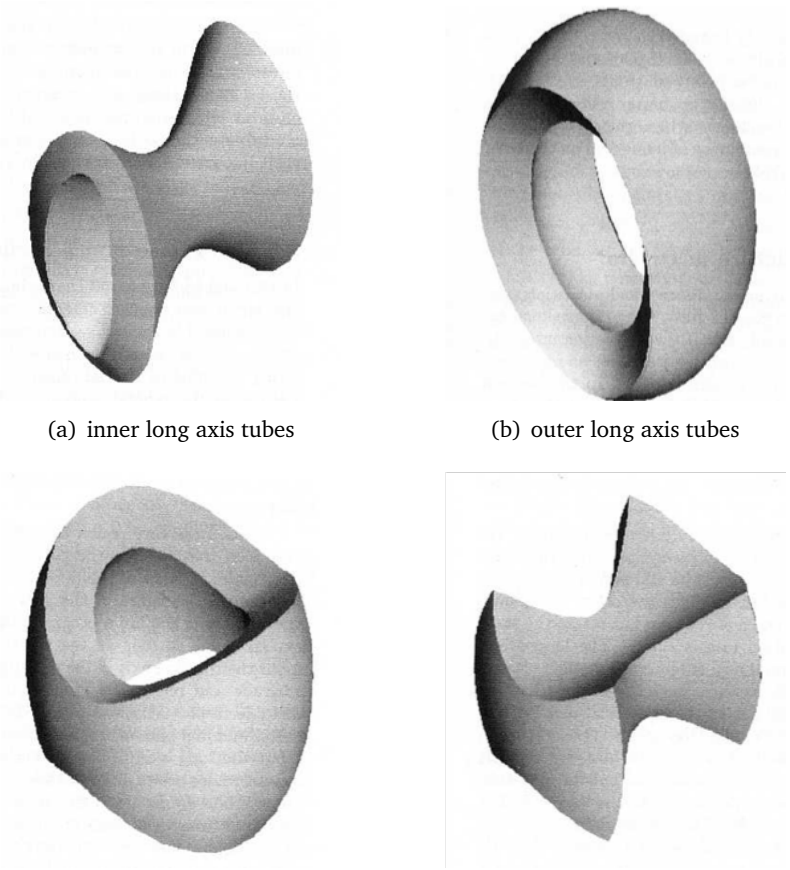

(a) inner long axis tubes

(b) outer long axis tubes

(c) short axis tubes

(d) box orbits

Figure 3.1: Orbit families in a non-rotating triaxial potential taken from Binney & Tremaine (2008). Short axis tubes rotate around the shortest axis of the galaxy potential. Inner and outer long axis tubes rotate around the longest axis. Box orbits can go through the centre, and the longest axis also emerges from the convex faces of box orbits.

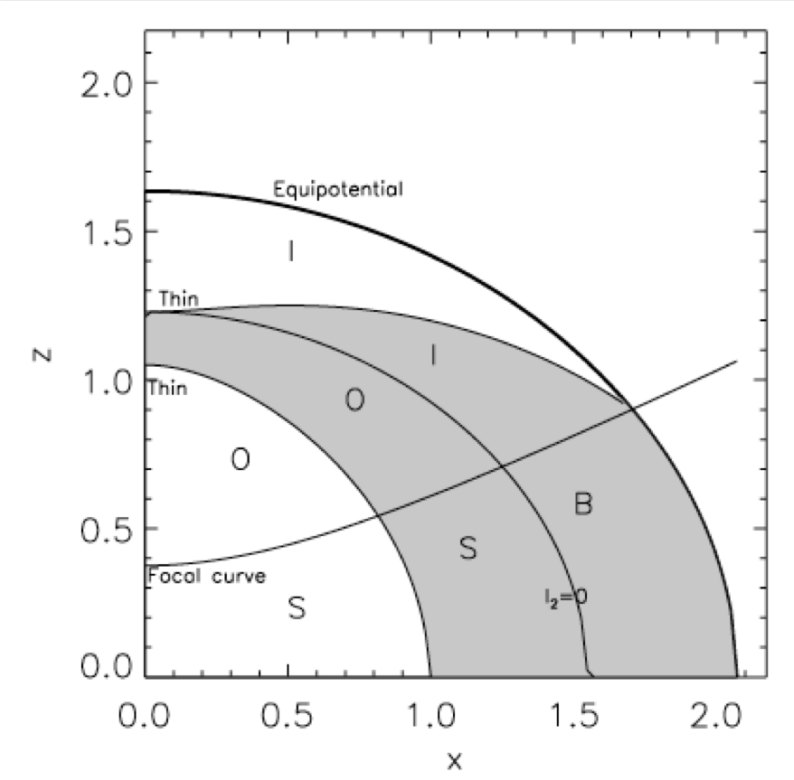

Figure 3.2: The (x,z) plane of a triaxial galaxy with a separable potential for the energy E high enough to generate all orbit families, taken from van den Bosch et al. (2008). 'B', 'S', 'I' and 'O' denote the box, short axis tube, inner and outer axis tubes respectively. The regions show where the corresponding orbit family crosses the (x,z) plane perpendicularly. Box orbits cross the (x,z) plane once in the grey region, while tube orbits cross twice, once in the white region and once in the grey region. In summary, all orbits cross the (x,z) plane within the grey region between two thin orbit curves once.

the y-direction is then decided by $v_{y,0}^2 = 2[V(x,0,z) - E]$ with $v_{x,0} = v_{z,0} = 0$. The directions of orbital motions decide whether the orbits are prograde or retrograde, however, it is more efficient to set up the orbits in one direction and then include the counter-rotating orbits when calculating orbit weights, because these two types of orbits have the same trajectories.

This orbit library (referred to as the ordinary library, to be distinguished from the additional box library mentioned below) sampling the start points on the (x,z) plane includes few box orbits at large radii. However, a number of box orbits are essential to recover the mass distribution of triaxial galaxies (Statler, 1987). Therefore, an additional box orbit library is introduced. Since the box orbits always touch the equipotential, this library is sampled on the equipotential surface using two spherical angles θ (inclination) and ϕ (azimuthal angle) for each energy E. This is called the stationary start space which results in box orbits or boxlets (resonant box orbits avoiding the centre) only (Schwarzschild, 1993). To keep the consistency between the ordinary and additional box libraries, E and θ in this box orbit library are sampled in the same way as the first library, and ϕ is also linearly sampled with the same number of grids as R in the first library.

With the start points, the orbits in the two orbit libraries are then integrated numerically. However, these single orbits correspond to δ-functions instead of smooth DF as expected in galaxies. The dithering method is then introduced to smooth the model. For each start point, n_d adjacent initial conditions are constructed along each dimension to form an orbit bundle of n_d^3 orbits. n_d needs to be an odd number to clearly define a central orbit in the orbit bundle. The observables for each orbit bundle are co-added.

3.2.3 Orbit weights

The observational data contains luminosity and kinematic data, which is reproduced simultaneously in a single Schwarzschild model by a superposition of all orbit bundles. The weights w_k of each orbit bundle k are obtained by solving the linear minimum χ^2 problem, which is

$$\chi^2 = \chi^2_{\rm lum} + \chi^2_{\rm kin}. \tag{3.7}$$

The luminosity data contains two parts: the surface brightness described by 2-dimensional MGE, and the corresponding deprojected 3-dimensional luminosity density, as described in Section 3.2.1. The surface brightness data are binned to the same apertures as the kinematic

data with a value S_l and an uncertainty ΔS_l for each aperture l. The luminosity density is binned with each bin n having a corresponding value ρ_n and an uncertainty $\Delta\rho_n$. Assuming each orbit bundle k contributes S_l^k to the surface brightness of the aperture l and ρ_n^k to the luminosity density of the bin n, the fitting needs to minimising

$$\begin{aligned}\chi^2_{\rm lum} &= \chi^2_S + \chi^2_\rho \\ &= \sum_l \left(\frac{S_l - \sum_k w_k S_l^k}{\Delta S_l} \right)^2 + \sum_n \left(\frac{\rho_n - \sum_k w_k \rho_n^k}{\Delta \rho_n} \right)^2 .\end{aligned} \tag{3.8}$$

Since the uncertainties ΔS_l and $\Delta\rho_n$ are usually not included in the MGE, they are set to $\Delta S_l = 0.01 S_l$ and $\Delta\rho_n = 0.02\rho_n$ empirically.

The observational line-of-sight velocity profiles (VPs) are usually described with a Gaussian-Hermite (GH) expansion (Gerhard, 1993; van der Marel et al., 1993; Rix et al., 1997)

$$GH(v;\gamma,V,\sigma,h_m) = \frac{\gamma}{2\pi\sigma} \exp\left[-\frac{1}{2} \left(\frac{v-V}{\sigma} \right)^2 \right] \sum_{m=0} h_m H_m \left(\frac{v-V}{\sigma} \right), \tag{3.9}$$

where γ is a velocity scale, and H_m are the Hermite polynomials and h_m are the GH moments, which are usually truncated at the fourth or second order for observational data. Figure 3.3 shows the effects of h_3 and h_4 to the VP on a Gaussian, which are related to the skewness and kurtosis of the VP.

For an observational aperture l, its VP f_l is usually expanded to $f_l = GH(v_l;\gamma_l,V_l,\sigma_l,h_{m,l})$ around its observational velocity and velocity dispersion (V_l,σ_l) with a fixed $h_{0,l} = 1$ and $h_{1,l} = h_{2,l} = 0$. Since γ_l is a scale parameter, it can be treated as 1.

This observational VP f_l is fitted by the superposition of VPs contributed by orbit bundles, with each orbit bundle k contributing a modelled VP of f_l^k, which is also expanded around the same (V_l,σ_l) by GH expansion $f_l^k = GH(v_l^k;\gamma_l^k,V_l,\sigma_l,h_{m,l}^k)$. Then the fitting of observational VP f_l becomes the fitting of observational GH moments $h_{m,l}$.

There is a degeneracy of γ_l^k and $h_{0,l}^k$ in the GH expansion of modelled VPs. In practice of modelling early-type galaxies, γ_l^k is fixed with $\gamma_l^k = 1$ and $h_{0,l}^k$ is allowed to vary. The fitting of $h_{0,l}$ have to be skipped, because $\chi^2_{h_0} = \sum_l \left(\frac{S_l h_{0,l} - \sum_k w_k S_l^k h_{0,l}^k}{S_l \Delta h_{0,l}} \right)$ and $\chi^2_S = \sum_l \left(\frac{S_l - \sum_k w_k S_l^k}{\Delta S_l} \right)^2$ cannot be minimised simultaneously, while the latter should be guaranteed anyway as a normalisation. Therefore, the fitting of observational GH moments $h_{m,l}$ becomes fitting ($h_{1,l} =$

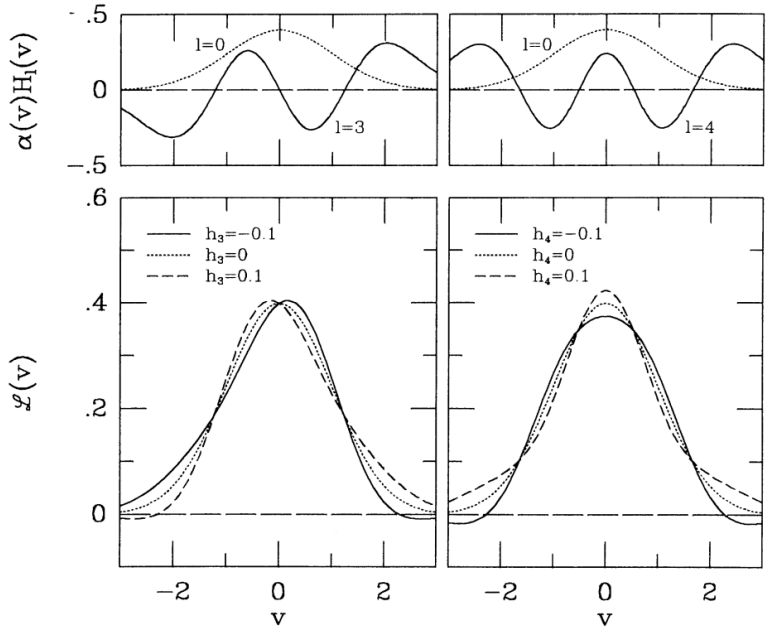

Figure 3.3: The effect of h_3 and h_4 on the VP of a Gaussian (credit: van der Marel et al., 1993). The top panels show $\alpha(v)H_3(v)$ and $\alpha(v)H_4(v)$ where $\alpha(v)$ is a standard Gaussian profile. The lower panels show $\alpha(v)[1+h_3H_3(v)]$ and $\alpha(v)[1+h_4H_4(v)]$.

$0, h_{2,l}=0, h_{3,l}, h_{4,l}$) with the corresponding errors ($\Delta V_l/\sqrt{2}\sigma_l, \Delta\sigma_l/\sqrt{2}\sigma_l, \Delta h_{3,l}, \Delta h_{4,l}$) with $h^k_{m,l}$ which are expanded from the VPs contributed by orbit bundles (van der Marel et al., 1993; Magorrian & Binney, 1994) . Then $\chi^2_{\rm kin}$ becomes

$$\chi^2_{\rm kin} = \sum_l \sum_{m=1} \left(\frac{S_l h_{m,l} - \sum_k w_k S^k_l h^k_{m,l}}{S_l \Delta h_{m,l}} \right)^2 \tag{3.10}$$

The Schwarzschild technique builds a number of single models from parameter space, with different combinations of free parameters such as inclination, stellar mass-to-light ratio and dark matter halo parameters. Orbit libraries are then generated for each single model and orbit bundle weights w_k are then solved by fitting to the data. Once the orbit bundle weights w_k of a single model are solved, the χ^2 for this model is fixed. Finally, the best-fitting model is selected by finding the model with the minimum χ^2 among all the models.

In practice, the luminosity data are well fitted anyway and the residual of fitting luminosity data $\chi^2_{\rm lum}$ varies little between different single models compared to the residual of fitting stellar kinematics $\chi^2_{\rm kin}$. Therefore, $\chi^2_{\rm lum}$ is usually negligible and $\chi^2 = \chi^2_{\rm kin}$ is adopted.

3.2.4 Examples of applying the Schwarzschild technique

Here I show two examples of the application of the Schwarzschild technique which are taken from Zhu et al. (2018c) in Figure 3.4. The upper panels show the images of early-type galaxy NGC 6278 and late-type galaxy NGC 4210, and the lower panels show the orbit distribution of the corresponding best-fitting model for each galaxy. The orbit distribution is displayed on the phase space of the circularity λ_z versus the intrinsic radius r (mentioned as r_i in Section 3.2.2), where λ_z is defined as the ratio of circular motion and total motion $\lambda_z = \overline{L_z}/(r\overline{V_c})$. The orbits are characterised with their λ_z in the following way: $|\lambda_z| = 1$ indicates a circular orbit, and orbits with high $|\lambda_z|$ ($|\lambda_z| > 0.8$ in this work) are dynamically cold; $|\lambda_z| = 0$ indicates a box or radial orbit, and orbits with low $|\lambda_z|$ ($|\lambda_z| \leq 0.1$ in this work) are dynamically hot. Orbits with $0.1 < |\lambda_z| \leq 0.8$ are dynamically warm. The orbit distributions explain galaxy morphologies: early-type galaxy NGC 6278 has a dominant hot component contributing to the dominant bulge, and a minor warm component contributing to the thick disc. Late-type galaxy NGC 4210 has a dominant thin disc which is mainly contributed by the dominant cold component. However, the dynamical components are not one-to-one correspondent to the morphological structures: the spiral arms cannot be reproduced by the Schwarzschild technique, the bar in NGC 4210 is mimicked but not fully recovered by a counter-rotating component ($\lambda_z < 0$) in the centre, and it is hard to find a structure corresponding to the warm component in the image of NGC 4210.

Applying the Schwarzschild technique to 300 galaxies in the CALIFA survey, Zhu et al. (2018b) further show that there are more stars on the warm orbits (defined in their work as $0.25 \leq |\lambda_z| \leq 0.8$) than cold or hot orbits across various morphological types and a stellar mass range of $10^{8.7} - 10^{11.9} M_\odot$, which allows a direct comparison with the orbit fractions in simulations and therefore provides a constraint on the simulations of galaxy formation in a cosmological context.

3.3 Summary

In this chapter, I first introduced the concept of dynamical modelling and the development of several popular dynamical modelling techniques. Although DF-based models are self-consistent with clear physical meaning, they can only model a stellar system without considering other content such as the dark matter and central black hole, therefore, its application is limited.

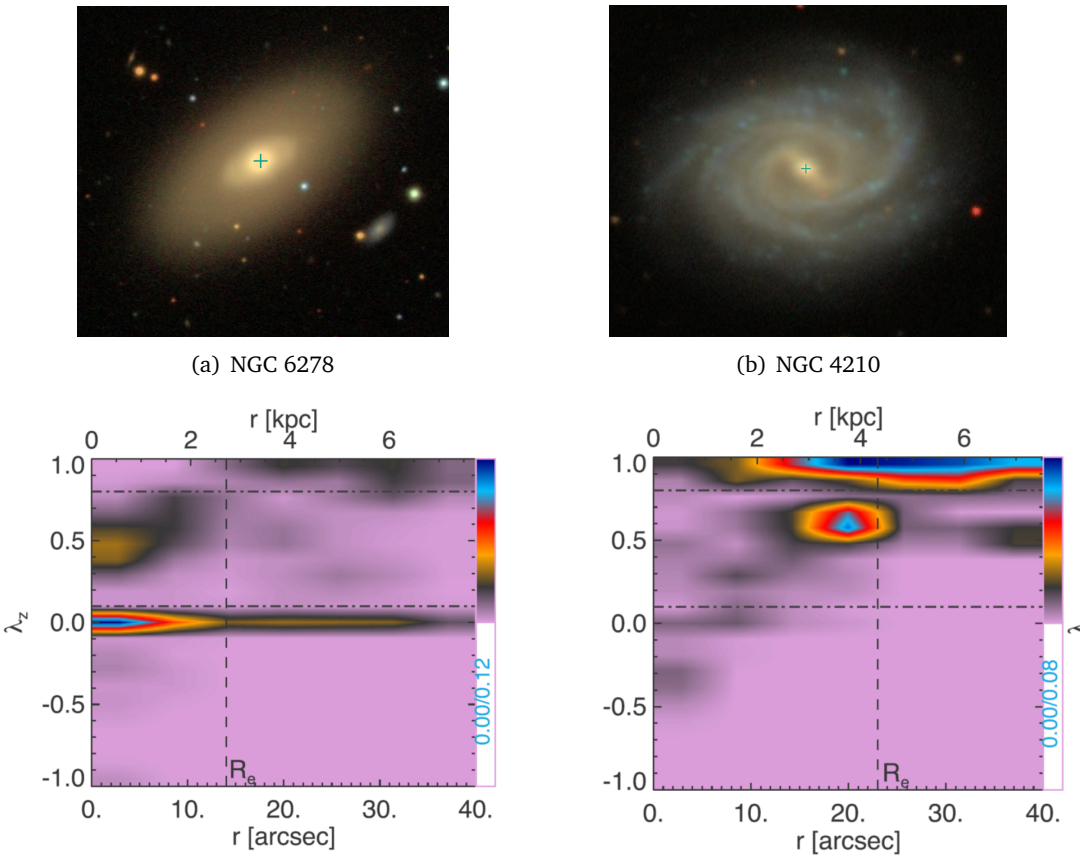

(a) NGC 6278

(b) NGC 4210

(c) Circularity of NGC 6278

(d) Circularity of NGC 4210

Figure 3.4: The images and circularity map of NGC 6278 and NGC 4210 (credit: Zhu et al., 2018c). NGC 6278 is an early-type galaxy and has a large fraction of box orbits with low $|\lambda_z|$. NGC 4210 is a late-type galaxy and mainly composed of short axis tubes with high $|\lambda_z|$.

Among the other techniques which are able to recover the mass distribution of real galaxies, the Jeans models are simple but can only be applied to galaxies with high symmetry, while orbit-based and particle-based models are able to model triaxial galaxies with high demands to computational resources. Therefore, orbit-based models are superior in studying stellar dynamical structures of galaxies. I then described the formalism of the Schwarzschild orbit-superposition technique in detail following the triaxial implementation of van den Bosch et al. (2008) and Zhu et al. (2018c), which is widely applied to model galaxies observed with IFU surveys.

In the next chapter, I will introduce a new orbit-based technique to model combined stellar and cold gas kinematics, in which I adopt the Schwarzschild technique to model stellar kinematics.

4

Orbit-based models with combined stellar and cold gas kinematics

In this chapter, I introduce an orbit-based model involving combined stellar and cold gas kinematics (Yang et al., 2020). I first demonstrate the formalism of this technique. I then show its application to early-type galaxy NGC 2974 to obtain its dark matter properties. By comparing this to the result of dynamical modelling without including the cold gas, I will show the capability of this technique in mapping the dark matter profile in galaxies.

4.1 Dynamical models with combined tracers - an overview

Mapping the mass distribution of galaxies with dynamical models relies on spatially resolved stellar kinematics provided by IFS. For example, Cappellari et al. (2013b) modelled the Atlas^{3D} sample of 260 early-type galaxies with the JAM modelling method; Taranu et al. (2017) built a self-consistent dynamical model to reproduce the properties of SAMI galaxies; Zhu et al. (2018a) adopted the Schwarzschild technique to decompose the orbital components of 250

CALIFA galaxies across Hubble sequence; and MaNGA galaxies were also modelled with these techniques (e.g. Li et al., 2017; Jin et al., 2019).

The studies above are measured with stellar kinematics, however, the coverage of galaxies obtained with stellar kinematics is usually limited, as the surface brightness of galaxies decreases fast at the outer regions of galaxies, which makes them too faint to observe with IFS. The typical coverage of stellar kinematics is $1-2\ R_{\rm e}$. Even though recent surveys have increased the coverage of their sample, it is still difficult to make a significant difference. Only 50% of CALIFA galaxies and 40% of SAMI galaxies have coverage extended to 2 $R_{\rm e}$ (Walcher et al., 2014; Bryant et al., 2015), and 80% of the MaNGA Secondary sample ($\sim$ 3300 galaxies) are covered to 2.5 $R_{\rm e}$ (Bundy et al., 2014). The limited coverage of stellar kinematics makes it difficult to constrain the properties of the dark matter halo in galaxies with dynamical models. The dark matter fraction in galaxy centre of early-type galaxies varies with measurements, but in general it takes no dominant role. Tortora et al. (2009) reported a typical dark matter fraction of 30% within 1 $R_{\rm e}$ for 339 early-type galaxies. Cappellari et al. (2013b) found a median dark matter fraction of 13% within 1 $R_{\rm e}$ for 260 Atlas$^{\rm 3D}$ early-type galaxies. Jin et al. (2019) also measured the dark matter fraction within 1 $R_{\rm e}$ for 149 early-type galaxies in MaNGA and summarised that the low-mass early-type galaxies have an average dark matter fraction of 20% while this value is 40% for high-mass early-type galaxies. Other measurements (e.g. Gerhard et al., 2001; Thomas et al., 2011) obtained similar results using a smaller sample size, and the measurement of individual early-type galaxies (e.g. Weijmans et al., 2008; Das et al., 2011; Zhu et al., 2016) also support this conclusion.

In contrast, dark matter usually dominates the gravitational potential in the outer regions in galaxies. For example, Alabi et al. (2017) found that the dark matter fractions are higher than 60% within 5 $R_{\rm e}$ in most of their sample which contains 32 nearby early-type galaxies. The results of individual galaxies also show that dark matter fraction increases several times from galaxy centre to outskirts (e.g. Weijmans et al., 2008; Das et al., 2011; Zhu et al., 2016). Therefore, seeking for datasets extended to galaxy outskirts is essential to overcome the coverage limitation of stellar kinematics and obtain the properties of dark matter halos for galaxies.

It is possible to obtain more extended stellar kinematics. For example, Boardman et al. (2017) present the stellar kinematics of early-type galaxies outside 3 $R_{\rm e}$ obtained with Mitchell IFS. Long-slit spectroscopy can also provide stellar kinematics even extended to 5 $R_{\rm e}$ (Napoli-

tano et al., 2011). However, the extended stellar kinematics obtained with IFS usually have low spatial resolutions and large bin size because of low S/N, while the stellar kinematics obtained with long-slit spectroscopy are not suitable for dynamical modelling alone for it cannot provide 2-dimensional information of the galaxy. With these disadvantages of adopting extended stellar kinematics for dynamical models alone, a combination of central (within $\sim 1\ R_e$) and extended (to $\sim 4\ R_e$) stellar kinematics is proposed and proved to be successful in a number of cases, for both extended IFS (e.g. Boardman et al., 2016) and long-slit spectroscopy (e.g Forestell & Gebhardt, 2010; Cappellari et al., 2015). Unfortunately, the difficulty of observing faint galaxy outskirts outside $3\ R_e$ still limits the sample size of extended stellar kinematics and the application of this combination. Therefore, combing stellar kinematics with other tracers extending out to over $5\ R_e$ in galaxies, including discrete and continuous tracers, are of great importance.

The discrete tracers used for dynamical models are mainly planetary nebulae (PNe) and globular clusters (GCs). PNe kinematics were first used alone to detect the existence of the dark matter halo for the early-type galaxy NGC 5128 (Hui & Ford, 1993), and then used to measure dark matter distribution of early-type galaxies in more cases (e.g. Tremblay et al., 1995; Napolitano et al., 2007). Recently, PNe kinematics are also used together with long-slit stellar kinematics in dynamical models (e.g. Napolitano et al., 2009, 2011). PNe kinematics in these researches are extended to $4-7\ R_e$, which shows a significant advantage in tracing dark matter profiles.

GCs are good tracers for early-type galaxies because of their ubiquity and adequate luminosity for spectroscopic observation to a far distance (Norris et al., 2012), and they also contain the information of stellar populations. The GC system of M87 is a well-studied case. It was first modelled using a sample of 278 GCs by Côté et al. (2001) in a global (for the entire sample) and a separate (for the metal-rich and metal poor sample) way. Zhu et al. (2014) then modelled M87 together with stellar kinematics using a sample of 922 GCs extended to $25\ R_e$. For other early-type galaxies, GCs kinematics exceeding $5\ R_e$ also contributes to constrain their dark matter content with dynamical models (Norris et al., 2012; Alabi et al., 2017).

Unlike discrete tracers such as PNe and GCs, cold gas is a continuous tracer following the intrinsic shape of the gravitational potential. There is a long history of ascertaining the dark matter content of late-type galaxies with cold gas (typically neutral hydrogen H I), by

modelling rotation curves obtained from integrated line profiles and velocity fields (e.g. Rubin et al., 1978; Bosma, 1981; van Albada et al., 1985). However, the existence of H I in early-type galaxies was underestimated, until a series of observations discovered that H I gas are also present in early-type galaxies, although typically with lower surface brightness than in late-type galaxies (e.g. Morganti et al., 1997; Oosterloo et al., 2007). The detection rate of H I depends on galaxy environments. Serra et al. (2012) detected H I in about 40% of early-type galaxies outside the Virgo cluster in their sample and about 10% in the Virgo cluster. Moreover, H I exists in the form of regularly rotating disc or ring in half of the early-types galaxies with H I detection (Morganti et al., 2006; Oosterloo et al., 2007, 2010), which makes it a suitable tracer for the gravitational potential.

Combining stellar kinematics and discrete tracers can provide further insights, and has been applied in a number of dynamical models, including a series of Jeans models and M2M methods, and provided crucial measurements of the dark matter profile in early-type galaxies. There are a number of applications of Jeans models and I highlight the following studies. Napolitano et al. (2009) constructed Jeans models with PN kinematics and extended long-slit stellar kinematics for an elliptical galaxy NGC 4494 and a similar method was also applied to another elliptical galaxy NGC 4374 (Napolitano et al., 2011). (Napolitano et al., 2014) applied the Jeans models to central long-slit stellar kinematics and GCs kinematics for a giant elliptical galaxy NGC 5846, and Zhu et al. (2016) modelled the same galaxy using a more comprehensive dataset, including stellar kinematics obtained with SAURON IFS, GCs and PNe kinematics. Bellstedt et al. (2018) applied the JAM modelling method to a large sample of 21 fast-rotating early-type galaxies with a combination of the Atlas^{3D} IFS stellar kinematics and GCs kinematics. For the M2M method, de Lorenzi et al. (2008) first modelled long-slit stellar kinematics and PNe kinematics with χ^2-made-to-measure (χ^2M2M) particle code `NMAGIC` for early-type galaxy NGC 4697. This method was then applied to more early-type galaxies to obtain their dark matter halo properties (e.g. de Lorenzi et al., 2009; Das et al., 2011), and Morganti et al. (2013) also included the stellar slitlet data in this model. These combinations have provided various measurements of dark matter properties, especially dark matter inner slopes which are related to the core or cusp problem. However, a combination of stellar kinematics and discrete tracers still lacks application based on the Schwarzschild technique. As an orbit-based model, the Schwarzschild technique faces the same difficulty of computing likelihood for discrete datasets.

Cold gas kinematics can easily sidestep this likelihood computation problem for discrete dynamical models (e.g. M2M and the Schwarzschild technique). Furthermore, if cold gas forms a regular thin disc in the galaxy, its simple kinematic properties with low velocity dispersion (< 10km/s) make a rotation model applicable, instead of complicated dynamical models. Therefore, cold gas kinematics can be used as an additional tracer of the gravitational potential and total mass distribution for galaxies, regardless of the modelling method of stellar kinematics or other tracers. An example is that adopting the molecular gas as a gravitational potential tracer while modelling the stellar kinematics with the JAM modelling method (Tsukui, 2019), and similar applications are promising for other dynamical models.

I therefore developed a combination of stellar kinematics modelled by the Schwarzschild technique, and cold gas kinematics as a tracer of the gravitational potential at large radii. The trial of modelling stellar kinematics with Schwarzschild technique while using an independent tracer for the gravitational potential for early-type galaxies was already done by Cretton et al. (2000), although they adopted the long-slit stellar velocity and the ionised gas kinematics within 1 R_e. In this chapter, I first demonstrate this technique. I then apply this technique to early-type galaxy NGC 2974, which is one of the well-studied early-type galaxies with cold gas: it is a lenticular galaxy with an extended regular H I ring (Kim et al., 1988; Weijmans et al., 2008), and its stellar kinematics was modelled by the axisymmetric Schwarzschild technique (Krajnović et al., 2005).

4.2 Methods

In this section, I describe my orbit-based model with combined stellar and cold gas kinematics. Stellar kinematics are modelled with an orbit-superposition Schwarzschild model, while cold gas kinematics are modelled as an ideal thin ring aligned with the stellar disc. First, I introduce the method of defining a gravitational potential based on a choice of parameters (e.g., stellar mass, dark matter profile). I then describe how I build a stellar orbit library and construct a cold gas ring separately from this potential. Finally, I introduce the combined weights of stellar and cold gas kinematics to select the best-fitting model.

4.2.1 Gravitational potential

The gravitational potential of a galaxy consists of contributions from the following components: stellar mass, gas mass, dark matter mass and the mass of a central supermassive black

hole. The mass distribution of these components should be parameterised to compute their gravitational potential. Therefore, I adopt a technique to obtain the parameterised mass distribution.

Stellar mass

The stellar mass distribution of a galaxy can be obtained from IFS observations, however, IFS datasets have limited field of view which is not suitable for computing the gravitational potential. Therefore, I obtain the stellar mass distribution $M(x', y')$ of a galaxy using its surface brightness $S(x', y')$ and stellar mass-to-light ratio $\Upsilon(x', y')$, which have the following relation,

$$M(x', y') \equiv S(x', y') \cdot \Upsilon(x', y'). \tag{4.1}$$

The surface brightness profile can be expanded to a series of Gaussian profiles using the 2-dimensional MGE method described in Section 3.2.1,

$$S(x', y') = \sum_i S_i(x', y'), \tag{4.2}$$

where $S_i(x', y')$ is the surface brightness distribution of each Gaussian component.

To approximate the stellar mass distribution also with an MGE model, based on the surface brightness, I introduce a group of free parameters $\tilde{\Upsilon}_j$,

$$M(x', y') = \sum_j \left[S_j(x', y') \cdot \tilde{\Upsilon}_j \right]. \tag{4.3}$$

Here $M(x', y')$ is the stellar mass distribution, and each $\tilde{\Upsilon}_j$ is a proxy for the mass-to-light ratio of the corresponding Gaussian component, albeit with no attached physical meaning. Then the mass-to-light ratio Υ is defined as,

$$\Upsilon(x', y') \equiv \frac{M(x', y')}{S(x', y')} = \frac{\sum_j \left[S_j(x', y') \cdot \tilde{\Upsilon}_j \right]}{\sum_j S_j(x', y')}. \tag{4.4}$$

which is a function of a group of unknown parameters $\tilde{\Upsilon}_j$ and the MGE parameters of the surface brightness.

If $\Upsilon(x', y') = \Upsilon_0$ is a constant in the galaxy, all the $\tilde{\Upsilon}_j$ have the same value of Υ_0. However, $\Upsilon(x', y')$ usually is not a constant. Therefore, I decide $\tilde{\Upsilon}_j$ by fitting the mass-to-light ratio Υ.

The stellar mass and consequently Υ are affected by the initial mass function (IMF): for example, a Chabrier IMF (Chabrier, 2003) produces almost 40% less stellar mass than a Salpeter IMF (Salpeter, 1955) with the same observables (Santini et al., 2012). Here I introduce a IMF factor α to indicate the stellar mass variation caused by the choice of IMF as a free parameter in the Schwarzschild modelling. Thus, the stellar mass distribution used in the Schwarzschild modelling becomes,

$$M_{\rm mod}(x', y') = \alpha \cdot M(x', y') = \alpha \cdot \sum_j \left[S_j(x', y') \cdot \tilde{\Upsilon}_j \right]. \tag{4.5}$$

Dark matter mass

To study the dark matter profile of galaxies, especially to establish the presence of a core or cusp, I adopt a spherical generalized NFW (gNFW) dark matter halo (Navarro et al., 1996; Zhao, 1996) with a density profile of

$$\rho_r = \frac{\rho_{\rm s}}{(r/r_{\rm s})^{\gamma}[1 + (r/r_{\rm s})^{\eta}]^{(3-\gamma)/\eta}}. \tag{4.6}$$

This halo model has four free parameters: $\rho_{\rm s}$ is the scale density, $r_{\rm s}$ is the scale radius, γ is the inner slope, while η controls the turning point. The outer slope of this profile becomes -3 for $r \gg r_s$. When $\gamma = 1$ and $\eta = 1$, the gNFW halo profile reduces to the NFW profile. For $\gamma = 0$, the halo model has a core in its centre.

To avoid calculating the gravitational potential of the gNFW profile analytically, I expand the halo density profile to an MGE as well. As the halo is spherical, I employ the 1-dimensional MGE expansion of Cappellari (2002).

Black hole

The central black hole of a galaxy is regarded as a point source with the following gravitational potential form,

$$\Phi_{\rm c,BH} = -\frac{GM_{\rm BH}}{\sqrt{r^2 + r_{\rm soft}^2}}. \tag{4.7}$$

Here $r_{\rm soft}$ is the softening length of the black hole, which is introduced to avoid the computing problems caused by a singular point. It is set to $r_{\rm soft} = 10^{-3}$ pc empirically.

Gas mass

The gas mass distribution can also be parameterised by the 2-dimensional MGE method. Generally, for the early-type galaxies in which H I forms a thin disc, the gas mass is negligible compared to the dark matter halo mass in galaxy outskirts and therefore not included in the model.

4.2.2 Stellar orbit sampling

The stellar orbit structure of Schwarzschild models is already introduced in Section 3.2.2. Here I only describe how I sample the stellar orbits in this model.

I sample the initial conditions of the orbits with their energy E and their starting point on the (x, z) plane according to van den Bosch et al. (2008). Each E is linked with a grid radius r_i such that E equals the potential at position $(x, y, z) = (r_i, 0, 0)$, and r_i is sampled logarithmically. For each energy, I then sample the starting point (x, z) from a linear open polar grid (R, θ) in between the location of the thin orbits and the equipotential of this energy. The number of sample points across three dimensions $n_E \times n_\theta \times n_R = 21 \times 10 \times 7$. I introduce 3 ditherings in every dimension (E, θ and R) and create an orbit bundle of $3 \times 3 \times 3$ dithering orbits for each orbit in the libraries to smooth the model, and this results in 39,690 orbits in total. More details of the orbits sampling can be found in van den Bosch et al. (2008).

This orbit library includes mostly short and long axis tubes and hardly contains box orbits in the inner region. In practice however, early-type galaxies are not perfectly axisymmetric and should contain a number of box orbits. To generate enough box orbits for a triaxial shape, I also add an additional box orbit library dropped from the equipotential surface following the method in Zhu et al. (2018c), using energy E and two spherical angles θ (inclination) and ϕ (azimuthal angle). Energy E and inclination θ are sampled in the same way as the first library, while ϕ is linearly sampled. The number of sample points $n_E \times n_\theta \times n_\phi$ for this library also equals $21 \times 10 \times 7$. I also smooth the model by introducing 3 ditherings in E, θ and ϕ for each orbit and create 39,690 orbits in the box orbit library.

4.2.3 Model of cold gas kinematics

I assume that the H I gas forms an axisymmetric thin disc aligned with the stellar disc in the equatorial plane of the galaxy. The H I gas moves on circular orbits on the disc plane with a

velocity of

$$V_{\rm c} = \sqrt{r \frac{\partial \Phi}{\partial r}\bigg|_{z=0}}, \tag{4.8}$$

where Φ is the total gravitational potential, including stars, dark matter halo and black hole. As shown, the H I velocity allows us to constrain the total gravitational potential although it provides no constraints on the stellar orbit distribution.

In this model, the H I gas is assumed to be dynamically cold, and its velocity dispersion is hence neglected. Since the typical H I velocity dispersion in discs is less than 10 km/s on the same order of typical H I velocity errors, this is a reasonable assumption.

The model light-of-sight velocity is given by

$$v_{\rm mod} = V_{\rm c} \sin\theta \cos\phi, \tag{4.9}$$

where ϕ is the azimuthal angle from the major axis and θ is the inclination. To compare the model and observational velocity directly, I then convolve the model velocity to take the beam smearing into account. I adopt a homogeneous H I mass distribution, therefore, I can directly convolve the model velocity map with the beam.

4.2.4 Combining kinematics weights

This method requires fitting two different data sets: the stellar kinematics (including the zero moment or surface brightness, as described by the MGE model), and the cold gas kinematics. The total χ^2 for each model built from the model parameters therefore contains two terms:

$$\chi^2 = \chi^2_{\rm star} + \chi^2_{\rm gas}. \tag{4.10}$$

The best-fitting models are determined by selecting the models with the minimum χ^2.

The stellar surface brightness and kinematics are reproduced simultaneously in a single Schwarzschild model by a superposition of all orbit bundles. Each orbit bundle k has a weight w_k. The weights of these orbit bundles are solved by minimising $\chi^2_{\rm star}$ as:

$$\chi^2_{\rm star} = \chi^2_{\rm s,lum} + \chi^2_{\rm s,kin}. \tag{4.11}$$

In practise I only take residuals of stellar kinematics $\chi^2_{\rm s,kin}$ into consideration, because the

residual of the surface brightness distribution fitting $\chi^2_{\rm lum}$ is negligible compared to the other terms as described in Section 3.2.3. Once the orbit bundle weights of a model are solved, the $\chi^2_{\rm s,kin}$ for this model is fixed.

The model confidence level for *all* Schwarzschild models is enlarged by the fluctuation of $\chi^2_{\rm s,kin}$, which has a standard deviation of $\sim \sqrt{2N_{\rm s,kin}}$. I therefore set $\Delta\chi^2_{\rm star} = \sqrt{2N_{\rm s,kin}}$ as the $1-\sigma$ confidence level. A more detailed description of this method for calculating $\chi^2_{\rm star}$ can be found in van den Bosch et al. (2008); van den Bosch & van de Ven (2009); Zhu et al. (2018c).

The residual of cold gas kinematics for each model $\chi^2_{\rm gas}$ equals

$$\chi^2_{\rm gas} = \sum \left(\frac{v_{\rm mod} - v_{\rm los}}{\epsilon_{\rm los}} \right)^2, \tag{4.12}$$

with $\epsilon_{\rm los}$ the error in observed velocity.

In practice, the $1-\sigma$ confidence level for fitting the cold gas kinematics is larger than $\sqrt{2N_{\rm g,kin}}$. I perturb the H I velocity by adding random Gaussian noise to the kinematic data with the standard deviations of the Gaussian noise being the $1-\sigma$ uncertainties of H I velocity, and measure the standard deviation $\Delta\chi^2_{\rm gas}$ of $\chi^2_{\rm gas}$ fluctuation as the $1-\sigma$ confidence level for fitting the cold gas kinematics.

Combining the confidence intervals for stellar and cold gas data, the $1-\sigma$ confidence level for *all* models is

$$\Delta\chi^2_{\rm tot} = \Delta\chi^2_{\rm star} + \Delta\chi^2_{\rm gas}. \tag{4.13}$$

4.3 Application to NGC 2974

In this section, I introduce the application of the model with combined tracers to early-type galaxy NGC 2974 to obtain its properties. I particularly focus on its dark matter inner slope γ, which decides whether this galaxy has a core or cusp for its dark matter halo. I first introduce the data sets I need to model this galaxy, including its surface brightness, stellar and cold gas kinematics. I then show the results of this application and compare the results obtained with the Schwarzschild models with stellar kinematics only.

Parameter	Value
Hubble type	S0[a]
Distance	20.89 Mpc
Distance scale	101.3 pc/arcsec
Position Angle	41°
Effective radius (R_e)	24 arcsec
K-band magnitude (M_K)	-23.62 mag
Effective stellar velocity dispersion (σ_e)	226 km/s

Table 4.1: Basic Properties of NGC 2974. [a] NGC 2974 was first classified as an E4 galaxy, and then Cinzano & van der Marel (1994) found it to be a lenticular (S0) galaxy. All other values were taken from Weijmans et al. (2008), except M_K (Cappellari et al., 2011) and σ_e (Cappellari et al., 2013b).

4.3.1 Data

To construct the dynamical models of NGC 2974, I make use of a variety of datasets, including surface brightness, stellar kinematics and H I velocity, which I describe below. I first list the basic properties of NGC 2974 in Table 4.1 and show an image of this galaxy on the left panel of Figure 4.3.

Stellar kinematics

The stellar kinematics of NGC 2974 (velocity, velocity dispersion and Gaussian-Hermite moments h_3, h_4) were first presented by Emsellem et al. (2004) as part of the SAURON survey (de Zeeuw et al., 2002), and then re-reduced as part of the Atlas^{3D} Survey (Cappellari et al., 2011). The spectra of NGC 2974 were Voronoi binned (Cappellari & Copin, 2003) to a S/N of 40 and fitted using the penalised pixel fitting method pPXF(Cappellari & Emsellem, 2004). In this work, I use the kinematic maps as published by Atlas^{3D}, as shown Figure 4.1. The stellar kinematics show that NGC 2974 rotates regularly and the h_3 field is anti-correlated with its velocity field. There is a single peak in the centre of the velocity dispersion field, while there is a dip in the centre of the h_4 field.

Cold gas kinematics and mass

I use the H I kinematics (velocity) of NGC 2974 presented by Weijmans et al. (2008). The H I observations were obtained by the Very Large Array (VLA) in C-configuation. The data were reduced and calibrated using the `MIRIAD` software package (Sault et al., 1995), resulting in a data cube with spectral resolution 20 km/s and a spatial beam of 19.9×17.0 arcsec^2. The H I velocity map of NGC 2974 is shown in Figure 4.2: note that the stellar and cold gas discs are

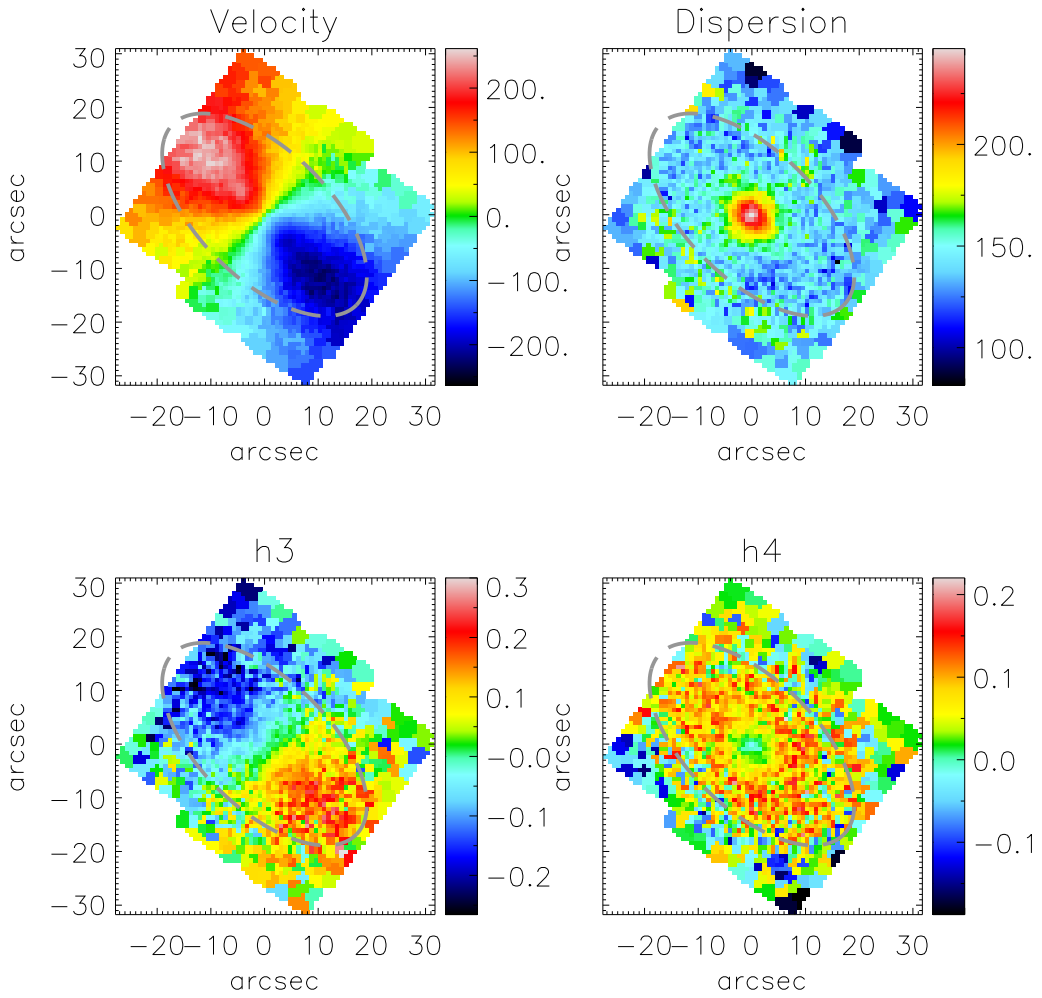

Figure 4.1: The stellar kinematic maps of NGC 2974 observed with SAURON, including velocity (km/s), velocity dispersion (km/s), the third and fourth orders of Gauss-Hermite moments. The maps are orientated so that north is up and east is to the left-hand side. The 1-R_e ellipse is plotted in dashed grey line. The data show that NGC 2974 rotates regularly and the h_3 field is anti-correlated with its velocity field. There is a single peak in the centre of the velocity dispersion field, while there is a dip in the centre of the h_4 field.

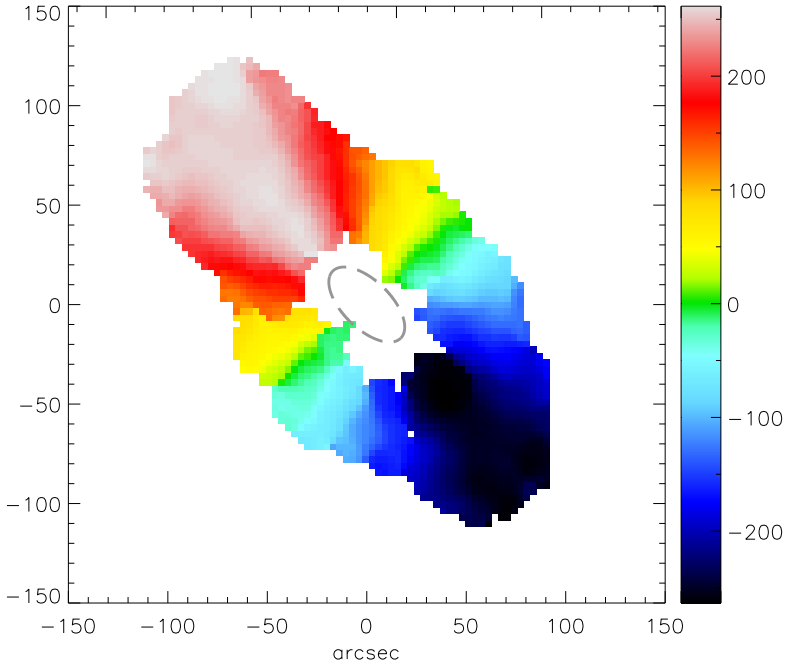

Figure 4.2: The H I velocity map (km/s) of NGC 2974 observed with the VLA. The map is orientated so that north is up and east is to the left. The H I ring is aligned with the stellar disc (see Figure 4.1). The 1-R_e ellipse is plotted in dashed grey line.

kinetically aligned.

The H I intensity is also included in the H I observations, from which I can calculate the H I mass distribution and parameterise it with the MGE method. However, as the total H I mass of NGC 2974 is three orders smaller than the stellar mass (Weijmans et al., 2008), its contribution to the gravitational potential is negligible compared to the dark matter halo. Therefore I do not include the H I mass in the dynamical model.

Surface brightness and mass-to-light ratio

To trace the stellar mass, I choose compatible surface brightness and mass-to-light ratio dataset. The surface brightness of NGC 2974 is the r-band imaging taken from the Panoramic Survey Telescope and Rapid Response System (Pan-STARRS), as shown in Figure 4.3(a). The mass-to-light ratio $\Upsilon(x', y')$ is the SDSS r-band mass-to-light ratio distribution (Poci et al., 2017, Υ-maps available on Atlas3D website). These datasets are compatible because the Pan-STARRS r-band filter is comparable to the r-band filter of the Sloan Digital Sky Survey (SDSS) (Gunn

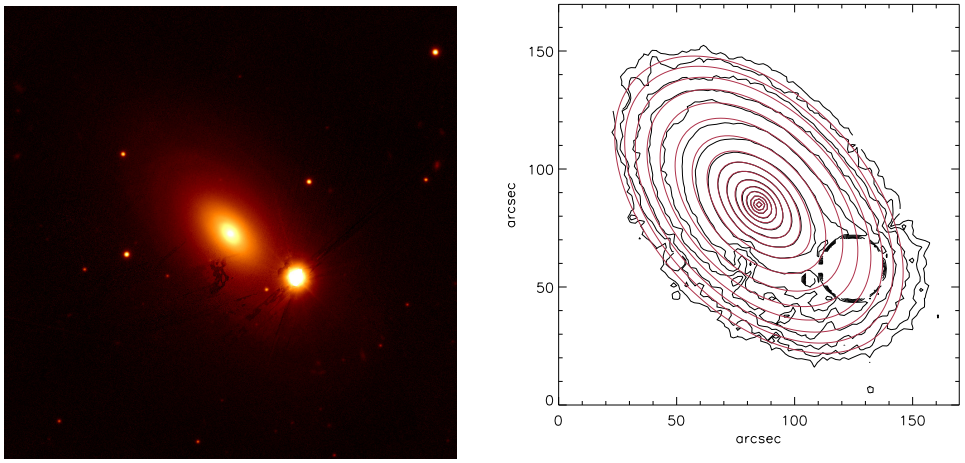

(a) r-band image (b) contour map

Figure 4.3: The r-band image of NGC 2974 from Pan-STARRS; (b) The surface brightness contours of NGC 2974 (black) and its Multi Gaussian Expansion (MGE) model (red). There is also a foreground star in the image, which is masked in the MGE model.

et al., 2006; Doi et al., 2010), avoiding additional calibration for surface brightness.

The Pan-STARRS images are stacked from short exposure images, to reach a limiting magnitude of 23.2 in r-band. In NGC 2974, this correspond to a radius of 3.5 R_e, which is beyond the extent of the stellar kinematic data sets. More descriptions of Pan-STARRS can be found on the Pan-STARRS website and in the Pan-STARRS papers (e.g. Chambers et al., 2016).

I apply the MGE technique to the r-band Pan-STARRS image of NGC 2974. The resulting MGE model contains 7 Gaussians as shown in Table 4.2. The contour map of the MGE fitting results is shown in Figure 4.3(b). The 1-dimensional residuals (shown in Figure 4.4) are within 2% in the inner region and about 10% in the outskirts of the galaxy.

I then adopt the r-band mass-to-light ratio distribution in Poci et al. (2017) as $\Upsilon(x', y')$ to fit the free parameters $\tilde{\Upsilon}_j$ based on the MGE result. The resulting 1-dimensional fit of $\Upsilon(x', y')$ is shown in Figure 4.5, and the corresponding MGE central mass density $M_j = L_j \cdot \tilde{\Upsilon}_j$ is shown in Table 4.2.

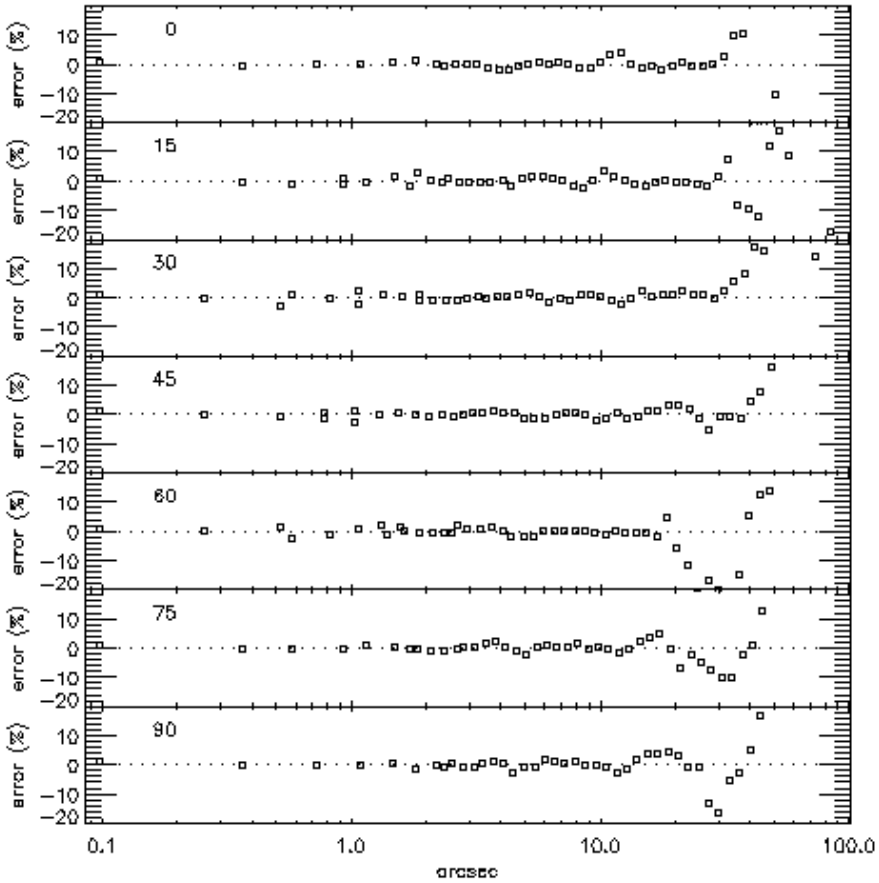

Figure 4.4: 1-dimensional residuals of MGE. From top to bottom are the fittings along the directions varying from the major to the minor axis of the galaxy with a step of 15°.

j	$L_j(\mathrm{L}_\odot/\mathrm{pc}^2)$	σ (arcsec)	q_j	$M_j(\mathrm{M}_\odot/\mathrm{pc}^2)$
1	4276.01	0.54153	0.83144	16208.47
2	7782.37	0.88097	0.82501	26366.23
3	2853.55	1.44526	0.94271	13148.71
4	3171.34	3.81993	0.67267	11329.50
5	220.000	6.64704	0.99990	1966.17
6	970.160	10.7437	0.55375	2890.09
7	252.150	28.4453	0.61238	778.71

Table 4.2: MGE Parameters of the surface brightness and stellar mass distribution of NGC 2974. From left to right: index, central luminosity intensity, width (standard deviation), axis ratio, central mass density of each Gaussian. The values of central mass density M_j are already rescaled to the stellar mass-to-light ratio according to the Chabrier IMF.

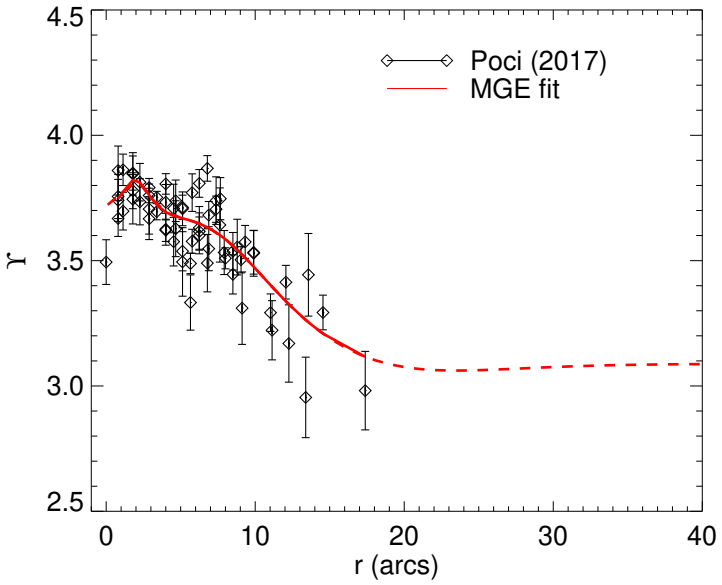

Figure 4.5: The r-band mass-to-light ratio of NGC 2974. The diamonds are data from Poci et al. (2017) but rescaled to the Chabrier IMF; the solid line is the best fitting Υ; the dashed line is a constant extension of Υ because of the limited radial coverage in Poci et al. (2017).

To be noticed, the mass-to-light ratio in Poci et al. (2017) is obtained with a constant Salpeter IMF. Here I still assume NGC 2974 has a constant IMF, the choice of which is indicated by a constant IMF factor α, but I rescale the values of M_j such that the Chabrier IMF corresponds to $\alpha = 1$ and the Salpeter IMF corresponds to $\alpha = 1.7$ (Speagle et al., 2014) for the convenience of calculation in this method.

I also notice that there is a dip in the r-band mass-to-light ratio at the galaxy centre ($r = 0$) in Figure 4.5, which is caused by a single data point. However, it is unusual to claim there is a significant change of mass-to-light ratio in the galaxy centre based on a single data point. Furthermore, there is an AGN (Maia et al., 2003) in the centre of NGC 2974, which could possibly affect the measurement of the mass-to-light ratio of this central data point and cause this dip. I therefore neglect this single data point in the fitting of $\Upsilon(x', y')$. The influence of including this dip in the fitting of $\Upsilon(x', y')$ is discussed in Section 4.3.4.

4.3.2 Model setting

Here I introduce my strategy to set the model parameters, including the IMF factor α, the viewing angles, the parameters for the dark matter profile and the black hole mass.

The IMF factor α is a free parameter, varies from 1.0 to 2.0 in steps of 0.1, to represent the

total mass produced by different IMFs, from the Chabrier IMF ($\alpha = 1$) to the bottom-heavy IMF ($\alpha \sim 2$).

I deproject the 2-dimensional mass distribution to 3-dimensional mass density following Cappellari (2002); van den Bosch et al. (2008), and introduce the intermediate and minor axis ratio p_i and q_i. Since NGC 2974 is nearly axisymmetric with $p_i \sim 1$, I adopt only one viewing angle, the inclination θ as a valid parameter in the model, with minor triaxiality still allowed. As Weijmans et al. (2008) have already shown that the H I ring has an inclination of $60 \pm 2°$, I fix the inclination θ to 60°.

There are four free parameters in the gNFW dark matter halo model. After running test models, I found that the turning point of the dark matter profile η was not well constrained even with cold gas kinematics. Therefore, I fix η to 2 in the model. For the other parameters of the dark matter profile, the central density ρ_s and the scale radius r_s are sampled on a logarithmic grid, $\log[\rho_s/(\mathrm{M}_\odot f \cdot \mathrm{pc}^{-3})] \in [-5, 1]$ and $\log(r_s/\mathrm{pc}) \in [3, 5]$. The inner slope of the dark matter profile, $\gamma \in [0, 1]$ is in a linear grid with a step of 0.1, and has a minimum step of 0.05 around the best-fitting model.

Based on the $M_{\mathrm{BH}}-\sigma$ relation (e.g. Tremaine et al., 2002), a black hole mass for NGC 2974 is expected to be $M_{\mathrm{BH}} = 2.5 \times 10^8 \mathrm{M}_\odot$ (see also Krajnović et al., 2005), which gives a radius of influence of just 0.2 arcsec. As this is below the spatial resolution of the SAURON spectrograph (0.8 arcsec), I at first neglected the contribution of the black hole to the gravitational potential. However, after running a few testing models, I found that the observed velocity dispersions of the central regions could not be reconstructed in the models without the inclusion of the black hole or with a black hole mass setting smaller than $10^6 \mathrm{M}_\odot$. Therefore, I include the black hole mass as a free parameter sampled on a logarithmic grid, with $\log(M_{\mathrm{BH}}/\mathrm{M}_\odot)$ sampled on the interval $[6, 10]$ in steps of 0.25.

In summary, I have 5 free parameters in the model: these are the IMF factor α, the three parameters of the dark matter halo profile (ρ_s,r_s,γ) and the black hole mass M_{BH}.

4.3.3 Results

I introduce the result of application of this modelling technique to NGC 2974. In total I generated dynamical models of NGC 2974 from 4,259 groups of parameters, and these models are selected in two different ways: by including both the cold gas kinematics and stellar kinemat-

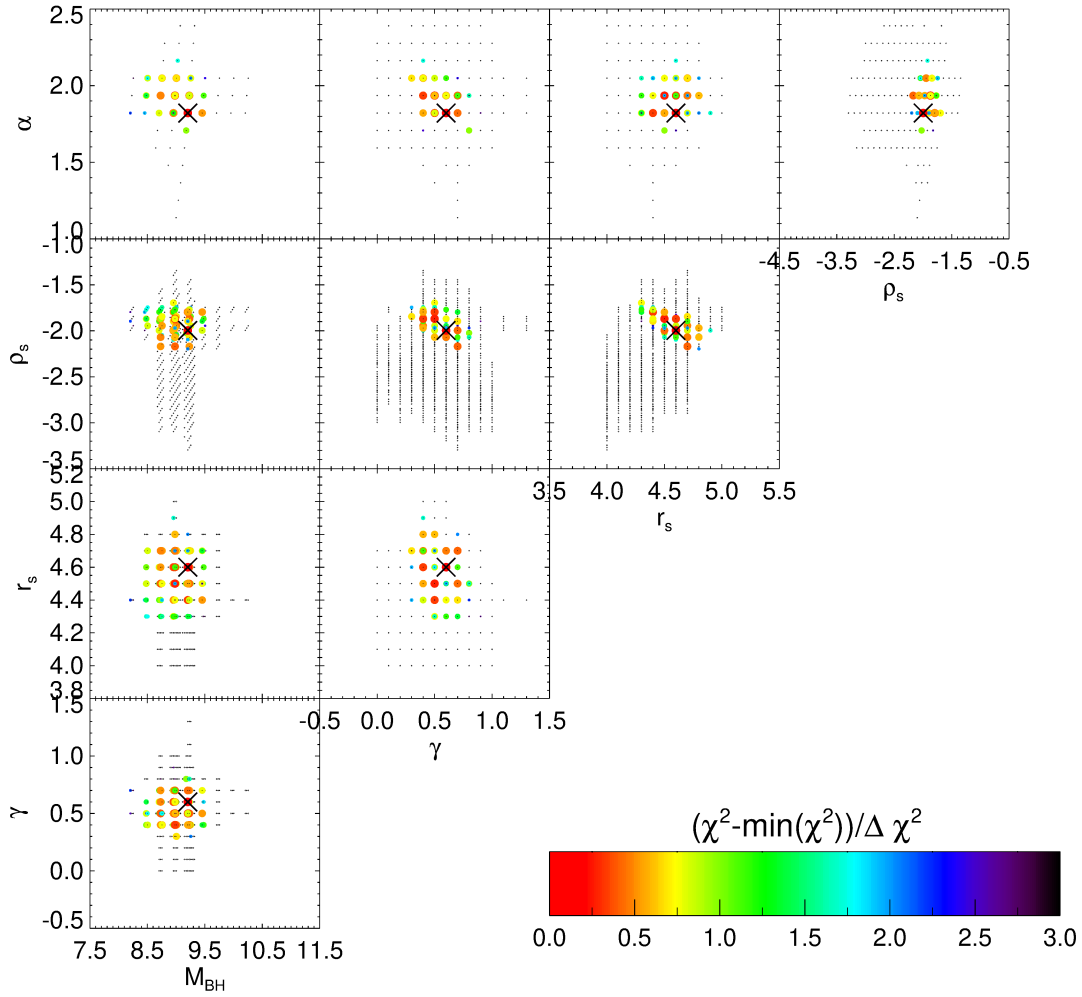

Figure 4.6: The grids of parameter space with cold gas kinematics. The best-fitting model is marked with a cross sign. The coloured dots represent models within $3-\sigma$ confidence level, and larger and redder dots stand for models with smaller $\chi^2_{\rm tot}$. The small black dots are the remaining models.

ics, and by fitting the stellar kinematics only.

Parameter grids

The free parameters of this modelling technique form a 5-dimensional parameter space. Here I plot the parameter grids which are the 2-dimensional projections of this parameter space in Figure 4.6 and 4.7. The dots represent all the models I have run, and the coloured dots are the models within $3-\sigma$ confidence level, where $1-\sigma$ confidence levels are defined as $\chi^2_{\rm tot} - \min(\chi^2_{\rm tot}) < \Delta\chi^2_{\rm tot}$, and $\chi^2_{\rm star} - \min(\chi^2_{\rm star}) < \Delta\chi^2_{\rm star}$ for the cases with and without cold gas kinematics, respectively. Here $\Delta\chi^2_{\rm tot} = \Delta\chi^2_{\rm star} + \Delta\chi^2_{\rm gas}$ where $\Delta\chi^2_{\rm star} = \sqrt{2N_{\rm s,kin}} = 118$ and

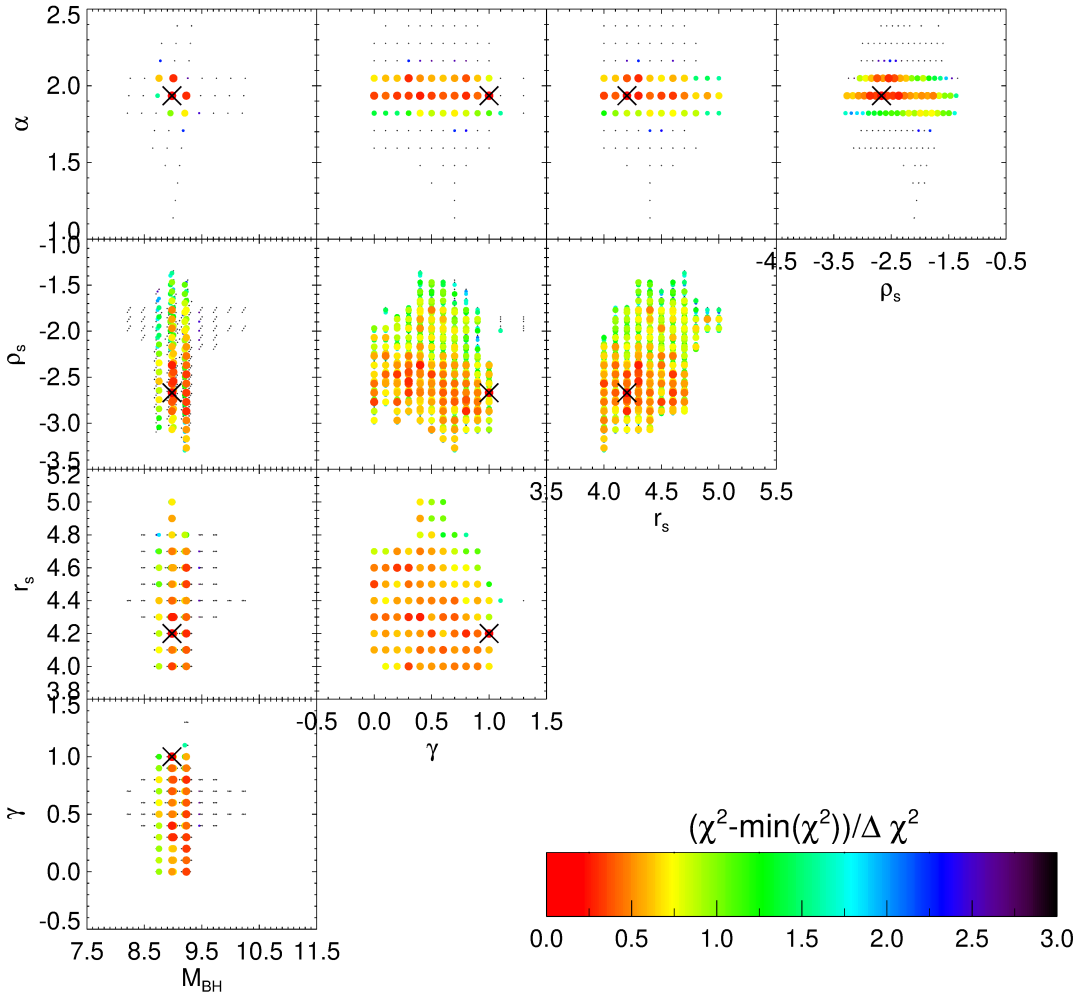

Figure 4.7: The grids of parameter space without cold gas kinematics. The best-fitting model is marked with a cross sign. The coloured dots represent models within $3-\sigma$ confidence level, and larger and redder dots stand for models with smaller $\chi^2_{\rm star}$. The small black dots are the remaining models.

	α	$\rho_s(10^{-3}M_\odot/pc^3)$	r_s(kpc)	γ	$M_{BH}(10^9M_\odot)$
star + gas	$1.8^{+0.2}_{-0.1}$	$10.1^{+10.0}_{-3.3}$	40^{+23}_{-20}	$0.6^{+0.2}_{-0.3}$	$1.6^{+1.2}_{-1.3}$
star only	$1.9^{+0.1}_{-0.1}$	$2.1^{+31.8}_{-1.6}$	16^{+84}_{-6}	$1.0^{+0.0}_{-1.0}$	$1.0^{+0.7}_{-0.4}$

Table 4.3: The best-fitting parameters for two cases: with and without cold gas kinematics. The uncertainties are the lower and upper limits of all models within $1-\sigma$ confidence level. Here ρ_s and M_{BH} are already multiplied by α to obtain their actual values.

$\Delta\chi^2_{gas} = 310$ obtained by perturbing the gas kinematics.

It is obvious that cold gas kinematics significantly lessen the models within $3-\sigma$ confidence level. Using stellar kinematics only, 1110 of 4259 models are within the $1-\sigma$ confidence interval, and I have not looped over the parameter space to generate all the models within $3-\sigma$ confidence interval. While including the cold gas kinematics in the model, only 48 models fall within the $1-\sigma$ confidence interval.

The parameters of the models are also more tightly constrained with smaller uncertainties by cold gas kinematics, especially the parameters related to the dark matter profile ρ_s, r_s and γ. This clearly demonstrates the importance of including the cold gas kinematics as a constraint to the gravitational potential.

Best-fitting model

I show the best-fitting parameters for the modelling in Table 4.3. The best-fitting parameters are the values of the best-fitting model identified as having the smallest χ^2, and the uncertainties quoted as the lower and upper limits of all models within the $1-\sigma$ confidence level. I list both the best-fitting parameters for the models with and without cold gas kinematics. The parameters of the dark matter profile are better constrained by including the cold gas measurements.

α is around 1.8, and it produces a total stellar mass 6% more than the total mass produced by the Salpeter IMF in Poci et al. (2017). I would like to emphasise that although the total mass produced by the actual IMF is similar to the that produced by the Salpeter IMF, the shape of this actual IMF cannot be inferred from the value of α within this modelling technique. The stellar Υ in r-band is $5.4M_\odot/L_\odot$ in the outskirts and rises up to $6.8M_\odot/L_\odot$ in the centre. Cappellari et al. (2013a) measure a stellar Υ in r-band of $8.9M_\odot/L_\odot$ with the assumption of a NFW halo, which is significantly heavier than my measurements. However, when they assume

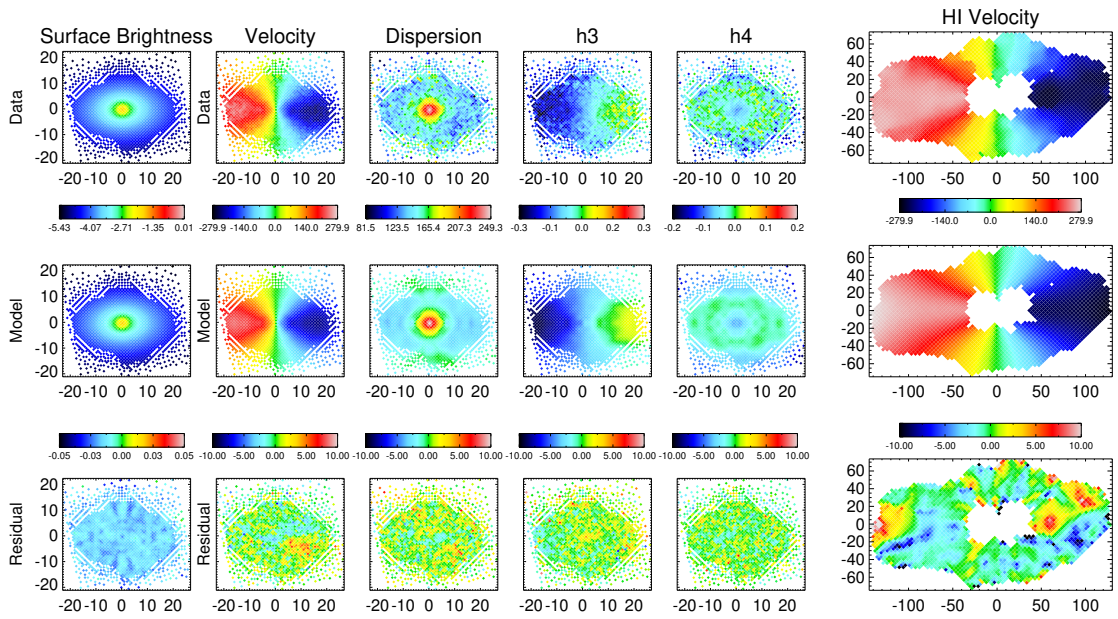

Figure 4.8: The data (top), model (middle) and relative residual (bottom; defined as (model-data)/error) of the surface brightness, stellar velocity, velocity dispersion, the third and fourth orders of Gauss-Hermite moments and cold gas velocity of NGC 2974 from left to right for the case of including cold gas kinematics.

a Salpeter IMF, their Υ within 1 R_e is $6.1 M_\odot/L_\odot$, consistent with my measurements.

Krajnović et al. (2005) included a central black hole in their Schwarzschild model of NGC 2974 with a fixed mass as predicted by the $M_{BH} - \sigma$ relation ($2.5 \times 10^8 M_\odot$)(e.g. Tremaine et al., 2002). My best-fit models return a black hole mass of $1.6^{+1.2}_{-1.3} \times 10^9 M_\odot$. However, this result might be biased due to the spatial resolution of the data, the existence of an AGN, as well as the not well understood behaviour of Υ in the very central parts of the galaxy. Besides, whether a higher sampling of orbits will change the best-fitting value of the black hole mass is not tested yet. Therefore, I do not make any claims about the true mass of the supermassive black hole in NGC 2974 from these models.

The corresponding best-fitting surface brightness and kinematics maps for the model with and without cold gas kinematics are shown in Figure 4.8 and 4.9. The residual plots of stellar moments do not show strong sub-structures for both cases. However, there is a strong difference between the residual maps of H I velocity. Using stellar kinematics within $1-2\,R_e$ alone may cause a strong deviation of the gravitational potential outside $4\,R_e$.

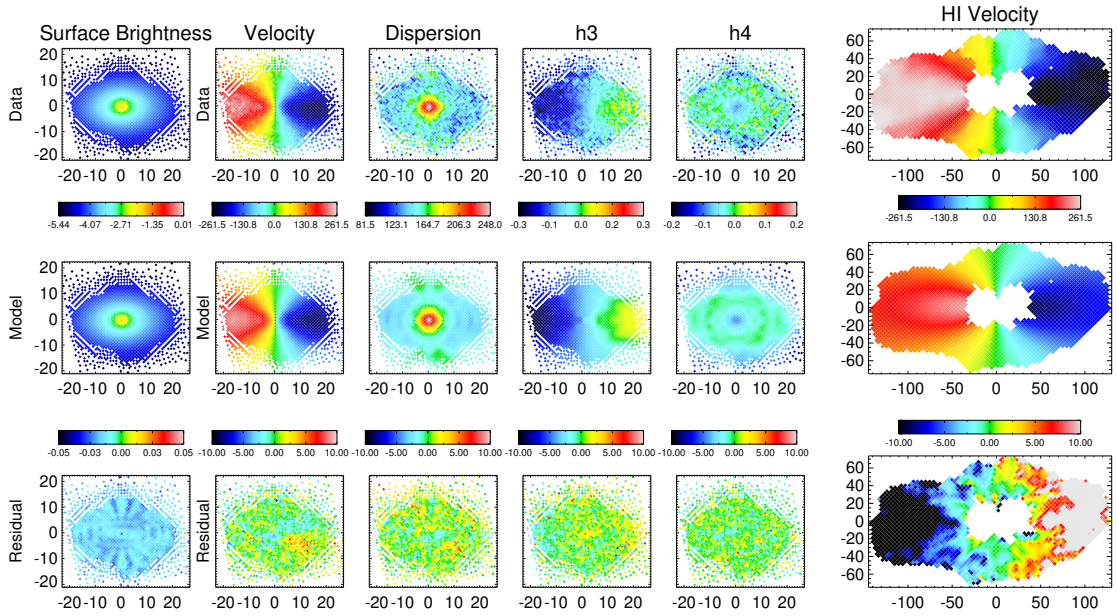

Figure 4.9: The data (top), model (middle) and relative residual (bottom; defined as (model-data)/error) of the surface brightness, stellar velocity, velocity dispersion, the third and fourth orders of Gauss-Hermite moments and cold gas velocity of NGC 2974 from left to right for the case of including stellar kinematics alone.

Enclosed mass profile

The enclosed mass profiles of NGC 2974, which describe the enclosed masses within a certain radius, are shown in Figure 4.10, both for the cases with and without cold gas kinematics. The black, red and green solid lines stand for the enclosed total, stellar and dark matter mass, respectively. The corresponding dashed lines show the lower and upper limits for the models within $1-\sigma$ confidence level. The stellar mass profile changes little between the two plots, as it dominates the inner region within 2 R_e and is mainly constrained by the stellar kinematic data. The dark matter fraction is 7% within 1 R_e, consistent with the measurement in Cappellari et al. (2013a) and smaller than the measurements of Weijmans et al. (2008) and Poci et al. (2017). The dark matter fraction is 66% within 5 R_e with an uncertainty of 10% for the case with cold gas kinematics, which is significantly better constrained with the cold gas covering the region outside 4 R_e, where the dark matter begins to be dominating. The dark matter fraction within 5 R_e is hardly constrained with stellar kinematics alone. This again emphasises the importance of including extended tracers for dark matter measurements.

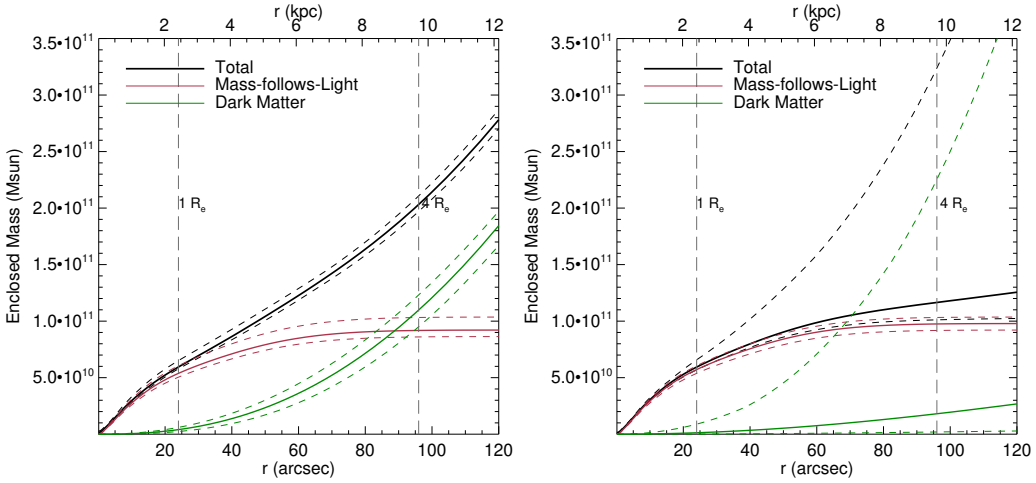

(a) cold gas included

(b) cold gas excluded

Figure 4.10: The enclosed mass profile of NGC 2974: (a) modelling with cold gas kinematics, (b) modelling without cold gas. The black, red and green solid lines stand for the total, stellar and dark matter mass, respectively. The corresponding dashed lines are their $1-\sigma$ uncertainties. The dark matter fraction is measured with much smaller uncertainty for the model that includes the cold gas kinematics. The red dashed line representing the lower uncertainty overlaps with the red solid line in the right-hand panel.

Dark matter profile

I show the dark matter density profiles for the models within $1-\sigma$ confidence level for both cases with and without the cold gas kinematics in Figure 4.11. In each plot, the orange line shows the dark matter profile for the best-fitting model and the grey lines show the dark matter profiles for the other models within $1-\sigma$ confidence level. It is apparent that the dark matter profile is constrained much better by including the cold gas kinematics.

Figure 4.11 again highlights the significance of the cold gas kinematics. Including the cold gas kinematics in the model significantly reduces the uncertainties of γ and shows that NGC 2974 prefers a shallow cuspy dark matter profile. As shown in the right panel of this figure, with the stellar kinematics only the $1-\sigma$ uncertainties include the full parameter range for γ, indicating γ cannot be constrained without the cold gas kinematics.

Two parameters are commonly utilised to describe the dark matter halo: the virial mass M_{200}, which is defined as the enclosed mass within the virial radius r_{200}, where the average density within r_{200} is 200 times the critical density ($\rho_{\rm crit} = 1.37 \times 10^{-7} {\rm M}_{\odot}/{\rm pc}^3$, adopting a Hubble constant $H_0 = 70$km/s/Mpc); and the concentration c, which is defined as the ratio

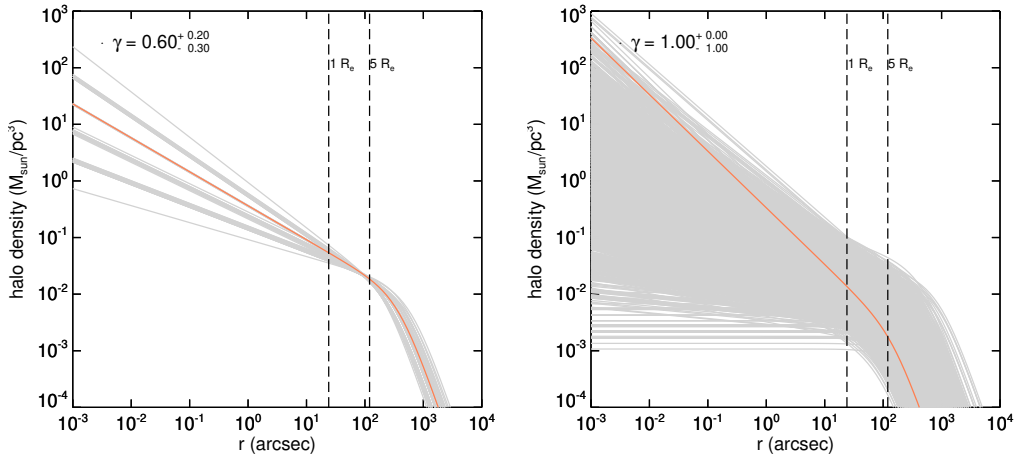

(a) cold gas included (b) cold gas excluded

Figure 4.11: The dark matter profiles of all models within $1-\sigma$ uncertainties: (a) modelling with cold gas kinematics, (b) modelling without cold gas. Each grey line represents the dark matter profile of a model, and the orange line is the profile of the best-fitting model. I also list the inner slope γ of the best-fitting model and its uncertainty. The dark matter halo inner slope is much better constrained by including the cold gas kinematics.

of the viral radius r_{200} and the scale radius r_s. These parameters are listed in Table 4.4 for the best-fitting models, which shows again that the dark matter profile is better constrained by including the cold gas kinematics in the modelling. However, I would like to emphasise the following facts. The turning point of the dark matter halo η is fixed to 2 and the outer slope of the dark matter halo is -3, which are not covered even with cold gas kinematics as shown in Figure 4.11, therefore, the measurements of M_{200} and c are strongly model-dependant.

Stellar orbit distribution

The stellar orbit distribution offers information on the galaxy components and morphology, based on their model kinematics. I characterise the stellar orbits with their circularity, defined as the ratio of circular motion and total motion as:

$$\lambda_z = \overline{L_z}/(r\overline{V_c}), \tag{4.14}$$

where $\overline{L_z} = \overline{xv_y - yv_x}$, $r = \overline{\sqrt{x^2+y^2+z^2}}$ and $\overline{V_c} = \overline{\sqrt{v_x^2+v_y^2+v_z^2+2v_xv_y+2v_xv_z+2v_yv_z}}$, taken the average for each orbit. Based on this parameter, I classify the orbits in the model into three dynamical components: hot ($|\lambda_z| \leq 0.25$), warm ($0.25 < \lambda_z < 0.8$), and cold ($\lambda_z \geq 0.8$). The circularity map (Figure 4.12) shows that three major dynamical components

	r_{200}(kpc)	$M_{200}(10^{13}\mathrm{M}_{\odot})$	c
star + gas	560^{+340}_{-200}	$2.0^{+6.3}_{-1.5}$	14^{+4}_{-2}
star only	130^{+1430}_{-80}	$0.022^{+43.125}_{-0.021}$	8^{+14}_{-4}

Table 4.4: The dark matter halo parameters (virial mass M_{200}, virial radius r_{200} and concentration c) deduced from the best-fitting models for the two fitting cases: with and without cold gas kinematics. The uncertainties are the lower and upper limits of all models within $1-\sigma$ confidence level.

are distinguished in this dynamical modelling of NGC 2974: an extended hot component related to a prominent bulge, a central warm component possibly representing a thick disc, and an extended cold component linked to a thin disc. This is consistent with NGC 2974 being a lenticular galaxy. The cold gas kinematics lead to little differences in the stellar orbit distribution in the best-fitting model, because the stellar orbit distribution is mainly decided by the stellar kinematics.

Krajnović et al. (2005) modelled NGC 2974 with an axisymmetric orbit-superposition model, which generated a strong counter-rotating component, while in this model, a strong hot component is produced and there is hardly any counter-rotating component. The reason for this difference is that box orbits are forbidden in an axisymmetric model, and the corresponding kinematic features are mimicked by a combination of rotating and counter-rotating orbits. I allow a triaxial shape and also sample enough box orbits by adding an additional box library, therefore, my modelling technique can recover the hot component in this galaxy.

Galaxy anisotropy reveals the intrinsic motions of early-type galaxies. Therefore, I also measure two parameters of galaxy anisotropy. The first parameter is the vertical-orthogonal parameter δ, which is defined as,

$$\delta = 1 - \frac{\sigma_z^2}{\sigma_x^2} \equiv 1 - \frac{\sigma_z^2}{(\sigma_R^2 + \sigma_\phi^2)/2}. \tag{4.15}$$

The second is the tangential-radial parameter β_r, which is defined as,

$$\beta_r = 1 - \frac{\sigma_t^2}{\sigma_r^2} \equiv \frac{(\sigma_\phi^2 + \sigma_\theta^2)/2}{\sigma_r^2}. \tag{4.16}$$

I plot their 1-dimensional distributions in Figure 4.13. The figure clearly reveals that the galaxy anisotropy is not constant, but varies with radius. β_r is in general below 0, indicating that NGC 2974 has tangential anisotropy. Cappellari et al. (2007) measured the global anisotropy with

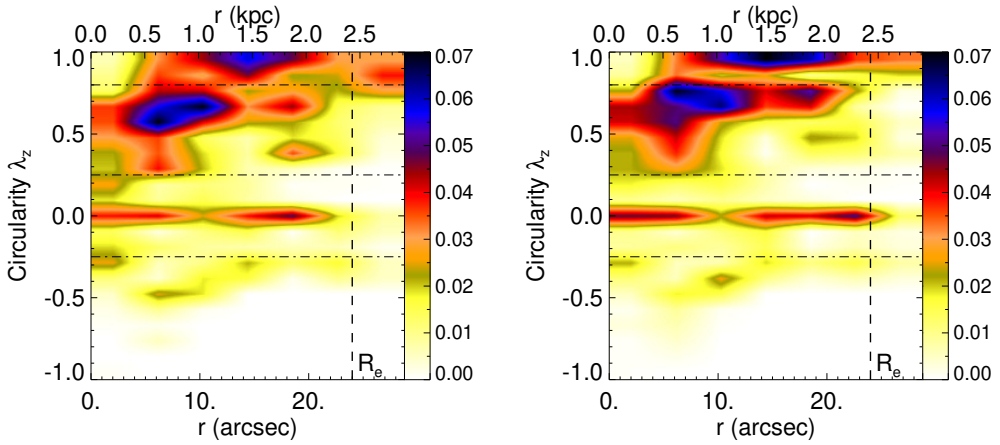

(a) cold gas included

(b) cold gas excluded

Figure 4.12: The stellar orbit distribution on the phase-space of λ_z vs. r of the best-fitting model to NGC 2974: (a) modelling with cold gas kinematics, (b) modelling without cold gas. The colour bar indicates the probability density of orbits. There are a hot central component, an extended warm central component, and an extended cold component in both cases.

similar definition for NGC 2974 with $\delta = 0.24$ and $\beta_r = -0.20$, which are consistent with my results.

4.3.4 Discussion

Dark matter inner slope

In this work I constrain the inner slope γ of the gNFW dark matter profile of NGC 2974, which decides whether the dark matter halo of this galaxy has a core or cusp. Here I review the wide range of values quoted in literature for γ in early-type galaxies for a comparison. Most measurements prefer the cusp model, such as an NFW-like or steeper inner slope. For example, Wasserman et al. (2018) modelled the massive elliptical galaxy NGC 1407 and found an NFW-like inner slope $\gamma = 1.0^{+0.2}_{-0.4}$, consistent with the average inner slope $\gamma = 0.80^{+0.18}_{-0.22}$ of 81 strong lenses early-type galaxies as obtained by Sonnenfeld et al. (2015) using a constant mass-to-light ratio. Grillo (2012) showed that the average logarithmic slope of 39 strongly lensed early-type galaxies is $\gamma = 2.0 \pm 0.2$ or $\gamma = 1.7 \pm 0.5$ with a Chabrier or Salpeter-like IMF and a constant mass-to-light ratio as well, respectively. Mitzkus et al. (2016) also found $\gamma = 1.4 \pm 0.3$ in a gNFW dark matter profile for lenticular galaxy NGC 5102 with stellar kinematics. Oldham & Auger (2018) obtained similar results using strong lensing, showing that the majority of massive early-type galaxies have an average $\gamma = 2.01^{+0.19}_{-0.22}$. However, a core-like dark matter

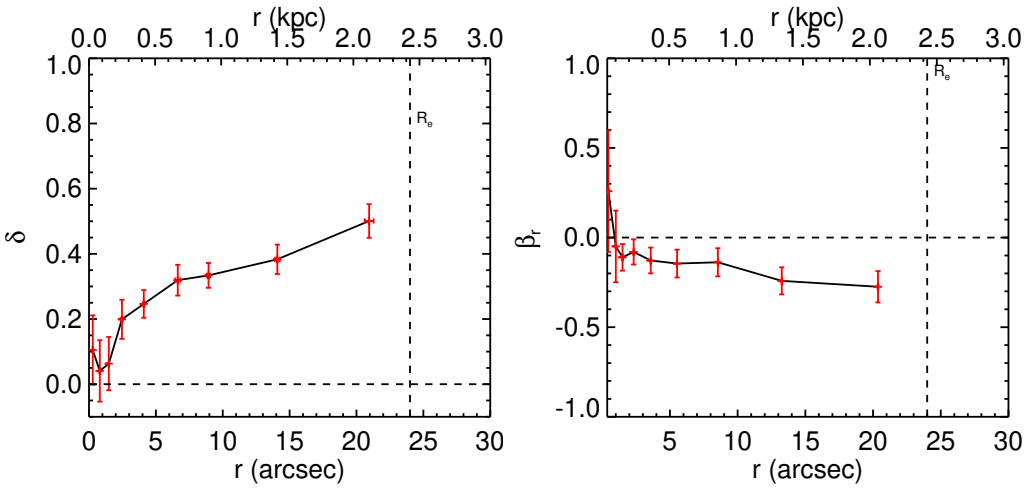

(a) vertical-orthogonal parameter (b) tangential-radial parameter

Figure 4.13: 1-dimensional anisotropy distributions. The vertical-orthogonal anisotropy $\delta = 1 - \sigma_z^2/\sigma_x^2$, and the tangential-radial anisotropy $\beta_r = 1 - \sigma_t^2/\sigma_r^2$.

profile is not ruled out for early-type galaxies: Forestell & Gebhardt (2010) found a power-law slope of 0.1 in their best-fit dark halo model and rule out the NFW profile at 99% confidence level for NGC 821 using the Schwarzschild model assuming a constant mass-to-light ratio. Zhu et al. (2016) made JAM models with stellar kinematics combined with GCs and PNe assuming a constant mass-to-light ratio and found that a core model is preferred for massive elliptical NGC 5846, although a cusp model would still be acceptable. A small number of early-type galaxies in Oldham & Auger (2018) are also consistent with cored models (average $\gamma = 0.10^{+0.33}_{-0.10}$). I obtain a shallow cuspy dark matter profile for NGC 2974, with an inner slope of $\gamma = 0.6^{+0.2}_{-0.3}$, which is not frequently reported in early-type galaxies. However, my result is still consistent with Wasserman et al. (2018) and Sonnenfeld et al. (2015) on $1-\sigma$ confidence level.

I emphasise that the measurements of dark matter inner slopes are carried out in various techniques with different assumptions. It is concerning that a number of measurements failed to consider a spatially varying stellar mass-to-light ratio (e.g. Sonnenfeld et al., 2015; Grillo, 2012; Forestell & Gebhardt, 2010; Zhu et al., 2016), which is degenerate with the dark matter inner slope, while some of the measurements have no extended tracers to constrain the measurements of dark matter profiles (e.g. Mitzkus et al., 2016; Oldham & Auger, 2018). Therefore, more measurements with detailed assumptions and extended datasets are still needed to understand the behaviour of the dark matter in early-type galaxies.

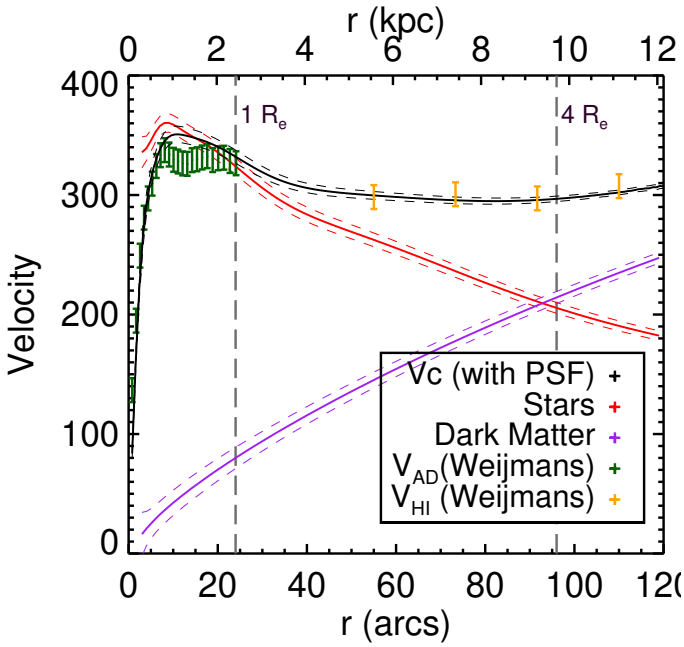

Figure 4.14: The circular velocity of NGC 2974. The black solid line is the rotation curve calculated from the gravitational potential and convolved with the SAURON PSF; the red and purple solid lines are the stellar and dark matter contributions without the PSF convolution; the corresponding dashed lines are their $1-\sigma$ uncertainties. The error-bars are from Weijmans et al. (2008): the green error-bars are the stellar velocity after asymmetric drift correction and the orange error-bars are the H I velocity. The difference at 1 kpc is because Weijmans et al. (2008) adopt an analytical model based on asymmetric drift correction.

Asymmetric drift correction

Weijmans et al. (2008) corrected observed stellar velocities of NGC 2974 for asymmetric drift, to obtain the circular velocity representative of the gravitational potential of the galaxy. I compare the rotation curve extracted from my best-fitting model for the case with cold gas kinematics with their rotation curve in Figure 4.14. The black solid and dashed lines are the rotation curve and corresponding uncertainties generated from the gravitational potential of my models with cold gas kinematics within the $1-\sigma$ confidence level. The rotation curve of Weijmans et al. (2008) has two parts: the orange dots show the H I velocity data extracted from the H I data which I also used for my models; the green dots are the stellar velocities corrected for asymmetric drift. My model is therefore consistent with the earlier work by Weijmans et al. (2008), confirming the effectiveness of obtaining rotation curves with asymmetric drift correction.

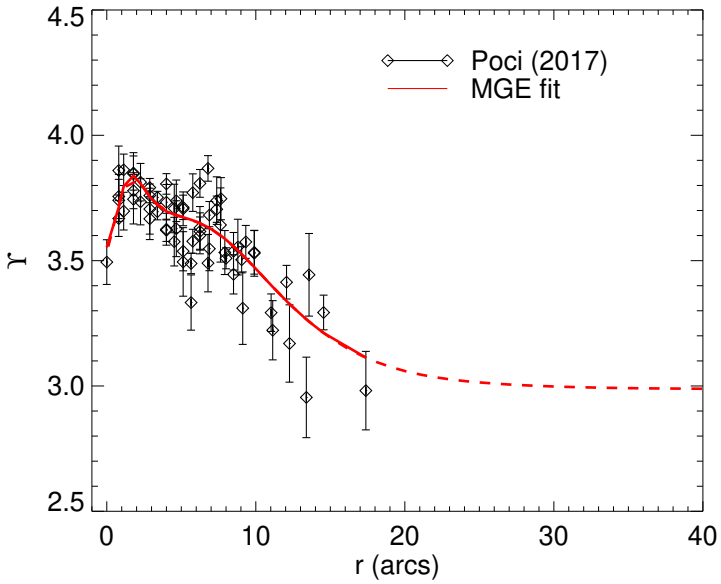

Figure 4.15: The r-band mass-to-light ratio of NGC 2974 including the central data point.

Influence of the central dip in mass-to-light ratio

There is a dip in the galaxy centre in the r-band mass-to-light ratio as I mentioned in 4.15 and I excluded the single data point in the fitting. Here I will discuss the influence of including this data point to the results, especially the dark matter inner slope γ.

I show the fitting of including the central single data point in Figure 4.15. This results in a group of different stellar mass MGE parameters M_j (see Table 4.5), especially for the first two MGEs. I construct 1,609 models based on this MGE model, with the exact same procedures as for the other models. The parameter space around the best-fitting models are looped, however, the $1-\sigma$ confidence intervals might not be accurate because of a possible missing of models. I show the comparisons of the best-fitting parameters in Table 4.6.

In general, including the single data point in the mass-to-light ratio fitting does not significantly change the best-fitting parameters. However, fitting this dip *does* change the dark matter profile, including the dark matter inner slope γ, instead of changing the mass of central black hole only. Surprisingly, the change caused by this single data point in the galaxy centre has an influence on the dark matter profile other than the mass of the central supermassive black hole, which demonstrates the degeneracy between the stellar mass distribution and the dark matter profile might be strong in dynamical modelling. To obtain reliable measurements

j	$M_j(\mathrm{M}_\odot/\mathrm{pc}^2)$ (with dip)	$M_j(\mathrm{M}_\odot/\mathrm{pc}^2)$ (no dip)
1	10624.64	16208.47
2	29155.03	26366.23
3	12573.17	13148.71
4	11440.99	11329.50
5	1851.09	1966.17
6	2975.66	2890.09
7	753.48	778.71

Table 4.5: The comparison of stellar mass MGE Parameters of NGC 2974 for the case for including and excluding the central data point.

of the dark matter inner slope, the behaviour of stellar mass distribution (e.g. the mass-to-light ratio and IMF gradient) should be fully considered and treated with caution.

4.4 Summary

In this chapter, I introduced a newly developed orbit-based method with combined stellar and cold gas kinematics and applied it to early-type galaxy NGC 2974. The main results are as follows.

1. This modelling shows a preference for a shallow cuspy dark matter halo profile, with the inner slope of the halo $\gamma = 0.6^{+0.2}_{-0.3}$ in a gNFW profile. The dark matter halo has a total mass of $M_{200} = 2.0^{+6.3}_{-1.5} \times 10^{13}\mathrm{M}_\odot$ and a concentration of $c = 10.8^{+3.2}_{-1.5}$. I also find that the stellar mass is slightly heavier than the mass produced if assuming a Salpeter IMF, with a corresponding stellar Υ in r-band decreasing from $6.8\mathrm{M}_\odot/\mathrm{L}_\odot$ in the centre to $5.4\mathrm{M}_\odot/\mathrm{L}_\odot$ in the outskirts.

2. The comparison between the results of the modelling with and without cold gas kinematics clearly shows that extended tracers are essential to constrain the dark matter profile in galaxies. Including the cold gas kinematics does an excellent job on obtaining the inner slope γ of the dark halo profile and constraining the dark matter fraction. The cold gas kinematics excluded more than 95% of models within the $1-\sigma$ confidence level of the Schwarzschild modelling with stellar kinematics only and reduced the relative uncertainty of the dark matter fraction to 10% within 5 R_e.

3. I characterise the stellar orbits of NGC 2974 into three principal components: an extended hot component, a central warm component, and an extended cold component,

	α	$\rho_s(10^{-3}M_\odot/pc^3)$	r_s(kpc)	γ	$M_{BH}(10^9M_\odot)$
with dip	$1.8^{+0.1}_{-0.1}$	$5.1^{+7.6}_{-0.3}$	79^{+0}_{-54}	$0.70^{+0.05}_{-0.20}$	$1.6^{+0.1}_{-1.1}$
no dip	$1.8^{+0.2}_{-0.1}$	$10.1^{+10.0}_{-3.3}$	40^{+23}_{-20}	$0.6^{+0.2}_{-0.3}$	$1.6^{+1.2}_{-1.3}$

Table 4.6: The best-fitting parameters for two cases: including and excluding the central data point. The uncertainties are the lower and upper limits of all models within $1-\sigma$ confidence level. Here ρ_s and M_{BH} are already multiplied by α to obtain their actual values.

corresponding to a prominent bulge, a central thick disc or a core, and a thin disc, respectively. As the cold gas kinematics are outside the field-of-view of the stellar kinematic data, the introduction of cold gas kinematics does not alter the orbit distribution significantly.

This orbit-based method with combined tracers has been proved successful. However, this method can only be applied to galaxies with aligned stellar and gaseous discs, which limits its application. Therefore, I will further develop this technique for galaxies with misaligned stellar and gaseous discs in the next chapter.

5

Generalised orbit-based models to misaligned stellar and cold gas discs

In Chapter 4, I described an orbit-based method with combined stellar and cold gas kinematics and applied this method to early-type galaxy NGC 2974 to study its mass distribution, assuming that the cold gas (H I) disc is a thin disc sitting in the equatorial plane of the galaxy. This assumption describes the case of NGC 2974, however, the stellar and gas discs are not always aligned in galaxies. Therefore, I will introduce the case that the stellar and gaseous discs are misaligned in galaxies as a further study, and then generalise this method to model galaxies with misaligned stellar and cold gas discs in this chapter. I will also apply this method to early-type galaxy NGC 3626 with misaligned two-aperture stellar kinematics and cold gas kinematics, to explore the prospect of this new modelling method for a wider application to galaxies.

5.1 Misalignment between stars and gas in galaxies

Galaxies with kinematically misaligned stars and gas are commonly observed in the universe. Early observations found over 20% misaligned stars and ionised gas in lenticular galaxies (Bertola et al., 1992; Kuijken et al., 1996). Despite of a small sample size, Kannappan & Fabricant (2001) found the fraction of such misalignment depends on galaxy morphology: they detected misalignment in early-type galaxies but not in spiral galaxies. The development of IFU surveys provides a much larger sample for this problem, and confirms the earlier conclusion. In the SAMI Galaxy Survey, 11% of galaxies on average have misaligned stars and ionised gas, but the result has strong morphology dependence: the fraction is 45% for early-type galaxies and 5% for late-type galaxies (Bryant et al., 2019). Duckworth et al. (2020) found a similar morphology dependence for about 2600 galaxies in the MaNGA Survey: 28% of elliptical galaxies, 10% of lenticular galaxies and 5% of spiral galaxies are misaligned. Barrera-Ballesteros et al. (2015) reported a higher fraction of misalignment between stars and ionised gas in interacting galaxies than non-interacting galaxies in the CALIFA survey. Apart from the ionised gas, misalignments between stars and molecular gas (Young, 2002; Young et al., 2008; Crocker et al., 2011) or atomic gas (Morganti et al., 2006) were also found in a small sample size of early type galaxies. Davis et al. (2011) further found that all the detected gas content in galaxies, including ionised, molecular and atomic gas, are always aligned with each other, even though the ionised gas of 36% of fast-rotating galaxies are misaligned with stars in the Atlas^{3D} Survey.

This common existence of misaligned stars and gas provides an additional sample for the application of dynamical modelling with combined stellar and gaseous kinematics, however, whether misaligned gas can be modelled depends on the dynamical process of its formation. The misalignment between stars and gas is regarded as evidence supporting the external origin of gas, such as galaxy mergers (Balcells & Quinn, 1990; Hernquist & Barnes, 1991; Barnes & Hernquist, 1996) and gas accretion from haloes (Roškar et al., 2010). Galaxy mergers are violent processes, and the misaligned gas formed in mergers can hardly be in dynamic equilibrium. On the contrary, simulations have shown that the accreted gas discs can remain misaligned with stars consistently for a time scale longer than 2 Gyr in early-type galaxies (Starkenburg et al., 2019; van de Voort et al., 2015). It is reasonable to assume that a misaligned gas disc with a regular shape is in a dynamical equilibrium and therefore can be modelled either analytically or numerically. Therefore, I expanded the orbit-based model in

Chapter 4 for galaxies with misaligned stellar and gaseous disc. This will enlarge the galaxy sample with combined stellar and extended gaseous kinematics, and further benefit the study of dark matter properties.

5.2 Generalisation to misaligned discs

In this section, I describe the generalised orbit-based model for misaligned stellar and gaseous discs, which contains two parts: I first discuss the geometry of a misaligned stellar and cold gas discs and then the behaviour of the cold gas disc inclined from the equatorial plane of the gravitational potential. I then introduce a method to predict the $1-\sigma$ confidence level for the cold gas kinematics theoretically, which replaces the perturbation method described in Chapter 4.

5.2.1 Deprojection of misaligned discs

In this section, I will show the method to deproject the misaligned discs in 3-dimensional space. Here I assume the cold gas disc to be circular, because cold gas usually moves in circular orbits. The stellar disc is also assumed to be circular, described by a nearly axisymmetric model.

First, I deproject misaligned discs to 3-dimensional space. Assuming the PA and inclination of the stellar disc are (PA_1, i_1) and those of the gas disc are (PA_2, i_2), each disc has two possible positions in 3-dimensional space: rotating clockwise or counter-clockwise around its major axis, as shown in Figure 5.1. Considering the symmetry, the relative position between the stellar and gas discs have two cases: both discs rotate in the same direction (clockwise or counter-clockwise), or they rotate in different directions (one clockwise and the other counter-clockwise), as shown in Figure 5.2. The angle θ between the symmetry axes of the stellar and gas discs is given by the following equation

$$\begin{aligned}\cos\theta &= \cos i_1 \cos i_2 \pm \sin i_1 \sin i_2 \cos(PA_1 - PA_2) \\ &= q_1 q_2 \pm \sqrt{1-q_1^2}\sqrt{1-q_2^2}\cos(PA_1 - PA_2)\end{aligned} \tag{5.1}$$

where $q_{1,2} = \cos i_{1,2}$ is the kinematic axis ratio which can be measured with the method described in Chapter 2, and the sign of $\pm$ decides the case: the $+$ sign stands for the same direction and the $-$ sign stands for the opposite direction.

Here I note that the galaxies with so-called 'aligned' stellar and gas discs are only aligned in

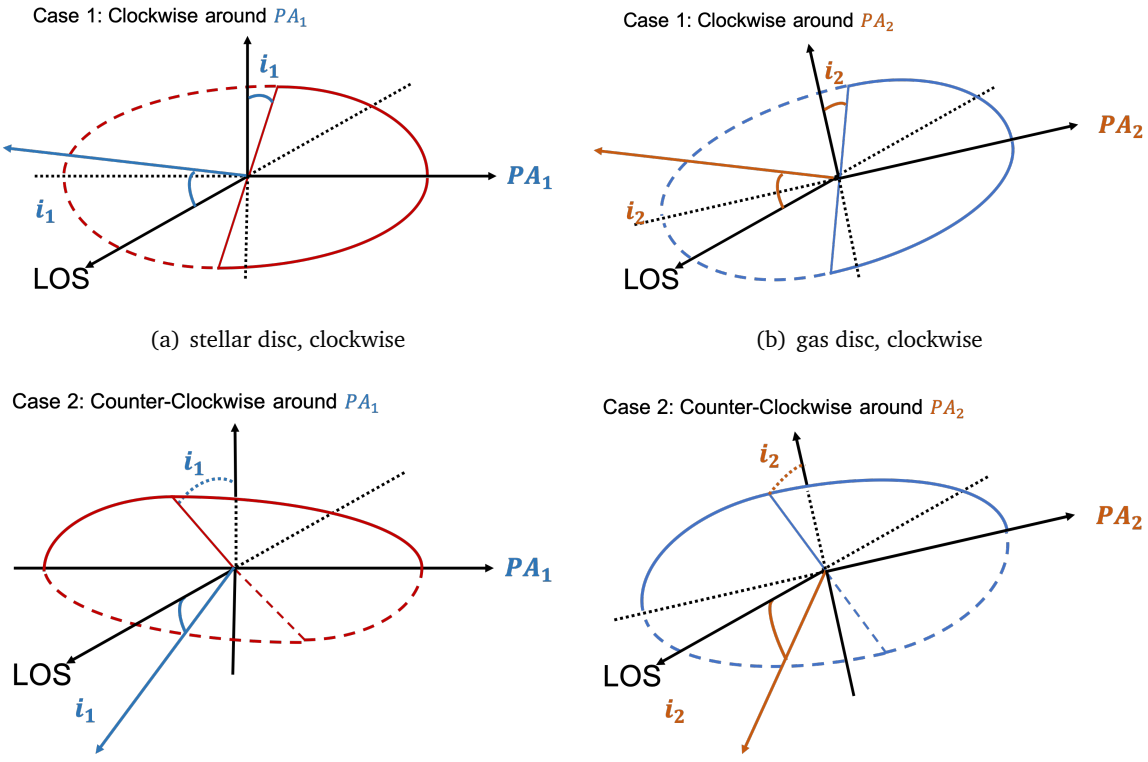

(a) stellar disc, clockwise

(b) gas disc, clockwise

(c) stellar disc, counter-clockwise

(d) gas disc, counter-clockwise

Figure 5.1: Deprojections of stellar (red) and gas (blue) discs. The line-of-sight (LOS) axis stands for the LOS direction and the PA axis stands for the major axis of each disc. Each disc has two possible projection: rotating clockwise or counter-clockwise around the PA axis from the sky plane.

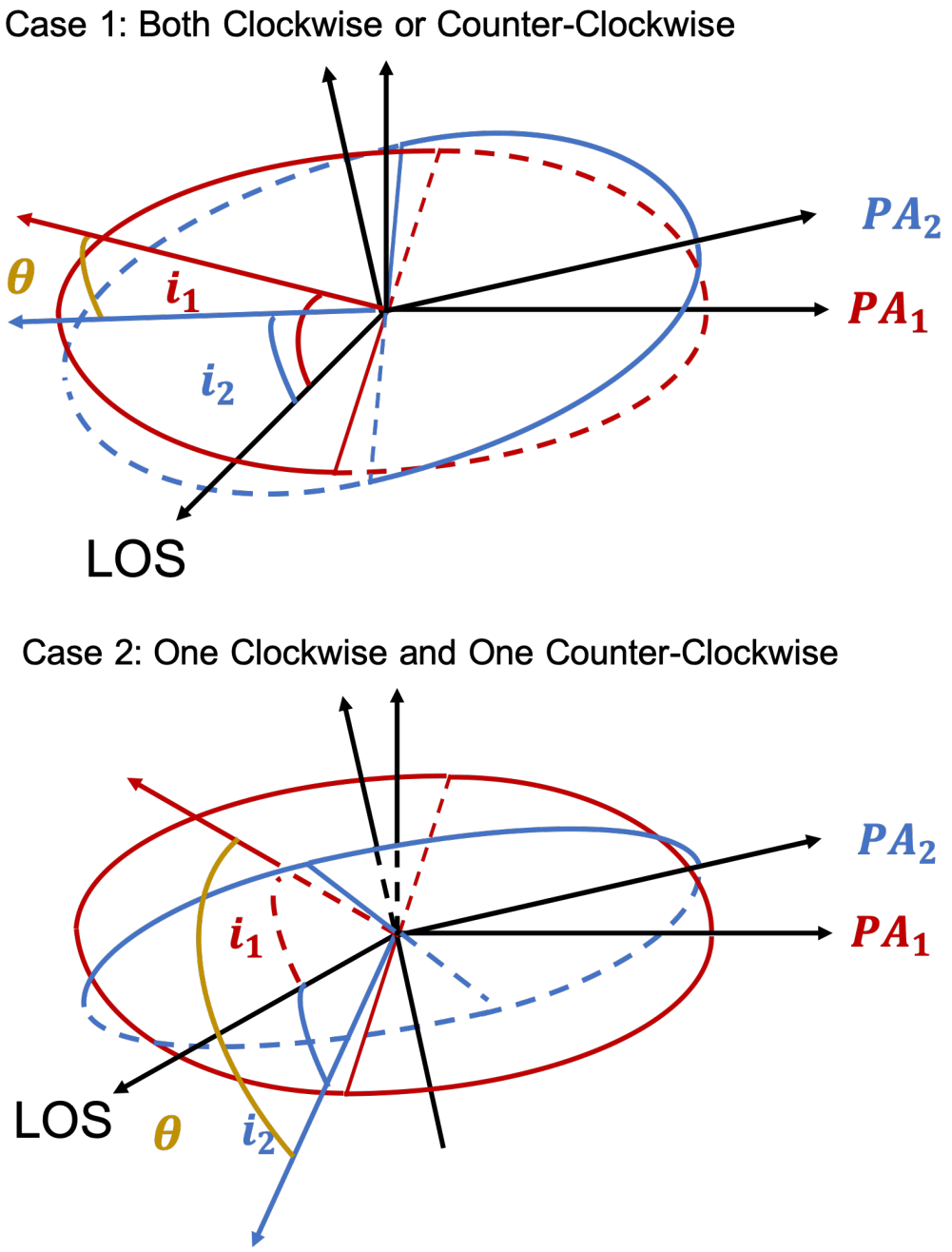

Figure 5.2: Relative positions between stellar (red) and gas (blue) discs. The LOS axis stands for the LOS direction and the PA axis stands for the major axis of each disc. The relative positions between two discs have two cases considering the symmetry: both rotating clockwise/counter-clockwise around the PA axis of each disc, or one rotating clockwise and the other rotating counter-clockwise around the PA axis of each disc.

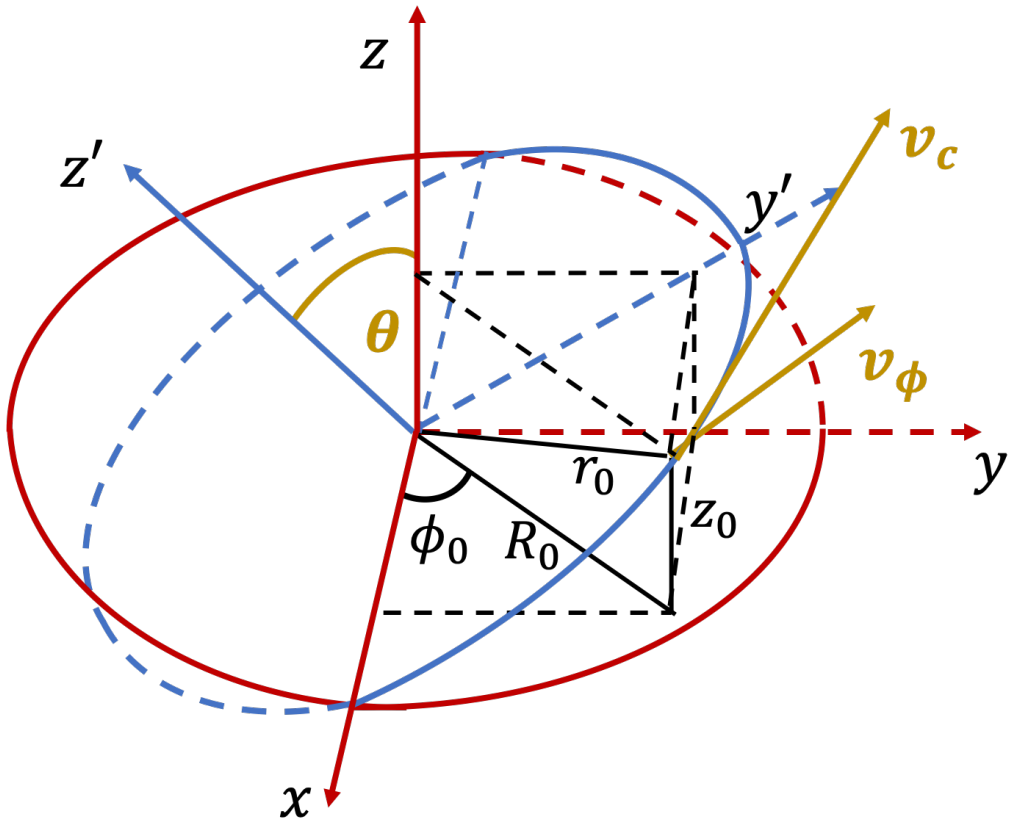

Figure 5.3: The behaviour of the gas disc misaligned with the stellar disc. The stellar disc is marked in red and the gas disc is in blue. The stellar disc sits in the xy-plane, and the gas disc rotates an angle θ around the x-axis.

the 2-dimensional projection. Even if the stellar and gas discs have the same PA and inclination, the possibility of case 2 where two discs rotate in different directions exists, which means they are still misaligned in 3-dimensional space. However, case 2 is usually neglected for so-called 'aligned' discs because the possibility that two misaligned discs happen to be projected with the same PA and inclination is negligible.

5.2.2 Gas disc behaviour in gravitational potential

I now discuss the behaviour of the gas disc which is misaligned with the stellar disc, as shown in Figure 5.3. The stellar disc is marked in red and the gas disc is marked in blue. The stellar disc sits in the xy-plane with its rotation axis aligned with the z-axis, and the gas disc rotates at angle θ around the x-axis. A particle in the gas disc at radius r_0 only has a circular motion v_c around the z'-axis. Assuming that this particle has coordinates of (R_0, z_0, ϕ_0) in the stellar

cylindrical coordinates, its projection along the ϕ-direction is

$$v_\phi = \frac{r_0 \cos\theta}{R_0} v_c, \tag{5.2}$$

I assume that there is a dynamical equilibrium along the R-direction as

$$v_\phi = \sqrt{-\mathrm{AccR}_{R_0} \cdot R_0}, \tag{5.3}$$

where AccR_{R_0} is the gravitational acceleration along the R-direction at R_0, which can be computed with the `MgeFit` package (Cappellari, 2002).

The modelled light-of-sight velocity of the gas is given by

$$v_{\mathrm{mod}} = v_c \sin i_2 \cos\phi', \tag{5.4}$$

where ϕ' is the azimuthal angle from the major axis of the gas disc. The modelled velocity is then convolved with the beam of the observation for a direct comparison with the observational velocity.

5.2.3 Uncertainty of cold gas kinematics

In Section 4.2.4, I adopted the residual of cold gas kinematics as

$$\chi^2_{\mathrm{gas}} = \sum_i \left(\frac{v_{\mathrm{mod},i} - v_{\mathrm{los},i}}{\epsilon_{\mathrm{los},i}} \right)^2, \tag{5.5}$$

where v_{mod} is the modelled gas velocity, v_{los} is the observational gas velocity and ϵ_{los} is the corresponding error. The $1-\sigma$ uncertainty of χ^2_{gas} was obtained with the perturbation method numerically, which adds random Gaussian noise to the kinematic data with the standard deviations of the Gaussian noise being the $1-\sigma$ uncertainties of H I velocity, and then measures the standard deviation $\Delta\chi^2_{\mathrm{gas}}$ of the χ^2_{gas}. Here I deduce a theoretical prediction for $\Delta\chi^2_{\mathrm{gas}}$.

Adding random Gaussian noise to the kinematic data is actually introducing a random

variable x_i to each data point i for $\chi^2_{\rm gas,p}$,

$$\begin{aligned}\chi^2_{\rm gas,p} &= \sum_i \left(\frac{v_{{\rm mod},i} - (v_{{\rm los},i} + x_i \cdot \epsilon_{{\rm los},i})}{\epsilon_{{\rm los},i}} \right)^2 \\ &= \chi^2_{\rm gas} + \sum_i \frac{2x_i \cdot (v_{{\rm mod},i} - v_{{\rm los},i})}{\epsilon_{{\rm los},i}} + \sum_i x_i^2\end{aligned} \tag{5.6}$$

where every x_i follows the standard normal distribution. Although the x_i^2 term does not follow a Gaussian distribution, in practice it is much smaller than the other term and therefore negligible. Then $\chi^2_{\rm gas,p}$ becomes

$$\chi^2_{\rm gas,p} \simeq \chi^2_{\rm gas} + \sum_i \frac{2x_i \cdot (v_{{\rm mod},i} - v_{{\rm los},i})}{\epsilon_{{\rm los},i}}, \tag{5.7}$$

which has a mean of $\chi^2_{\rm gas}$ and a standard deviation of

$$\Delta\chi^2_{\rm gas} = 2\sqrt{\chi^2_{\rm gas}}, \tag{5.8}$$

which is adopted as the $1-\sigma$ uncertainty of $\chi^2_{\rm gas}$. For NGC 2974, $\chi^2_{\rm gas} = 24086$ with a theoretical corresponding $\Delta\chi^2_{\rm gas} = 2\sqrt{\chi^2_{\rm gas}} = 310$, which is consistent with the $1-\sigma$ uncertainty obtained with the perturbation method in Section 4.3.3.

5.3 Application to early-type galaxy NGC 3626

Boardman et al. (2017) selected 12 early-type galaxies from the Atlas^{3D} survey with stellar kinematics within 1 $R_{\rm e}$ and presented their observations out to 3 $R_{\rm e}$ by the Mitchell integral field spectrograph (IFS; Hill et al., 2008) on the Harlan J. Smith telescope. The presence of extended H I discs had been detected in these galaxies by the observations of the Westerbork Synthesis Radio Telescope (WSRT; Serra et al., 2012), and only 5 out of 12 galaxies have settled H I discs. Among these 5 galaxies, NGC 3626 has a regular H I disc which is clearly misaligned with the stellar one. I therefore choose NGC 3626 as a test case for this misaligned method, because the combination of its extended Mitchell stellar kinematics and very extended H I velocity provides a valuable opportunity to explore the ability of this method to constrain dark matter profiles. I list the basic information of NGC 3626 in Table 5.1 and show an image in Figure 5.4.

Parameter	Value
Effective radius (R_e)	25.7 arcsec
K-band magnitude (M_K)	-23.30 mag
Distance	19.5 Mpc
Stellar mass ($\log M_*/M_\odot$)	10.71
Effective stellar velocity dispersion (σ_e)	131 km/s

Table 5.1: Basic properties of NGC 3626. The values are taken from (Cappellari et al., 2011), except M_* Boardman et al. (2017) and σ_e (Cappellari et al., 2013b).

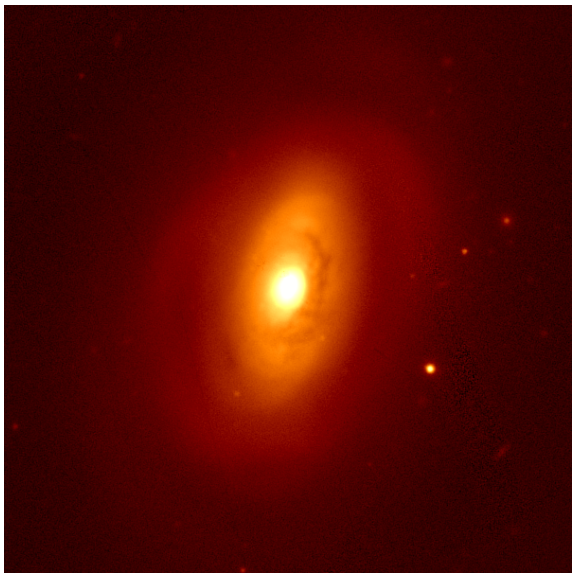

Figure 5.4: The r-band image of NGC 3626 from Pan-STARRS (Chambers et al., 2016). NGC 3626 is a lenticular galaxy with disc structures. We can also see dust in the centre of this galaxy.

5.3.1 Two-aperture stellar kinematics

The stellar kinematics of NGC 3626 has two datasets, an Atlas^{3D} observation and a Mitchell observation. The instrument of the Atlas^{3D} survey is the SAURON integral field spectrograph, which has a field-of-view of 33×41 arcsec^2 sampled with 0.94 arcsec^2 lenslets and a instrumental velocity dispersion of 105 km/s (Emsellem et al., 2004; Cappellari et al., 2011). The Mitchell IFS has a large field-of-view of 1.68×1.68 arcmin, a large fibre size of 2.08 arcsec and a maximum instrumental velocity dispersion of 42 km/s (Boardman et al., 2017). I show the stellar velocity fields of NGC 3626 in the left panel of Figure 5.5.

Two-aperture stellar kinematics were modelled with the Schwarzschild technique in Copin et al. (2004) for the central black hole in NGC 3377. Boardman et al. (2016) also modelled NGC 3998 with the SAURON and Mitchell stellar kinematics. To include two-aperture stellar kinematics, I adopt two independent stellar apertures in the process of solving the orbital weights for each dataset and minimise the residual of stellar kinematics

$$\chi^2_{\rm s,kin} = \chi^2_{\rm s,kin,1} + \chi^2_{\rm s,kin,2}, \tag{5.9}$$

where $\chi^2_{\rm s,kin,i}$ stands for the residual of the i-th dataset.

There is a problem that there are overlaps between the Atlas^{3D} and Mitchell stellar kinematics. To deal with this problem, I follow the strategy of Boardman et al. (2016) to mask the low-resolution Mitchell stellar kinematics in the central overlapped area. I adopt this strategy for the following reasons: including both stellar kinematics in the dynamical modelling will increase the weights of the central data, and therefore makes it difficult to fit the stellar kinematics at the outskirts; the Atlas^{3D} stellar kinematics have higher spatial resolution than the Mitchell ones, providing more detailed structures in the galaxy centre.

5.3.2 Cold gas kinematics

The H I kinematics (velocity) of NGC 3626 was obtained by the WSRT. The data were reduced and calibrated using the `MIRIAD` software package (Sault et al., 1995), resulting in a data cube with spectral resolution 16 km/s and a spatial beam of 41.2×11.8 arcsec^2. The other technical details of this observation were identical to those presented in Serra et al. (2012), except that the observing time was 9 times longer.

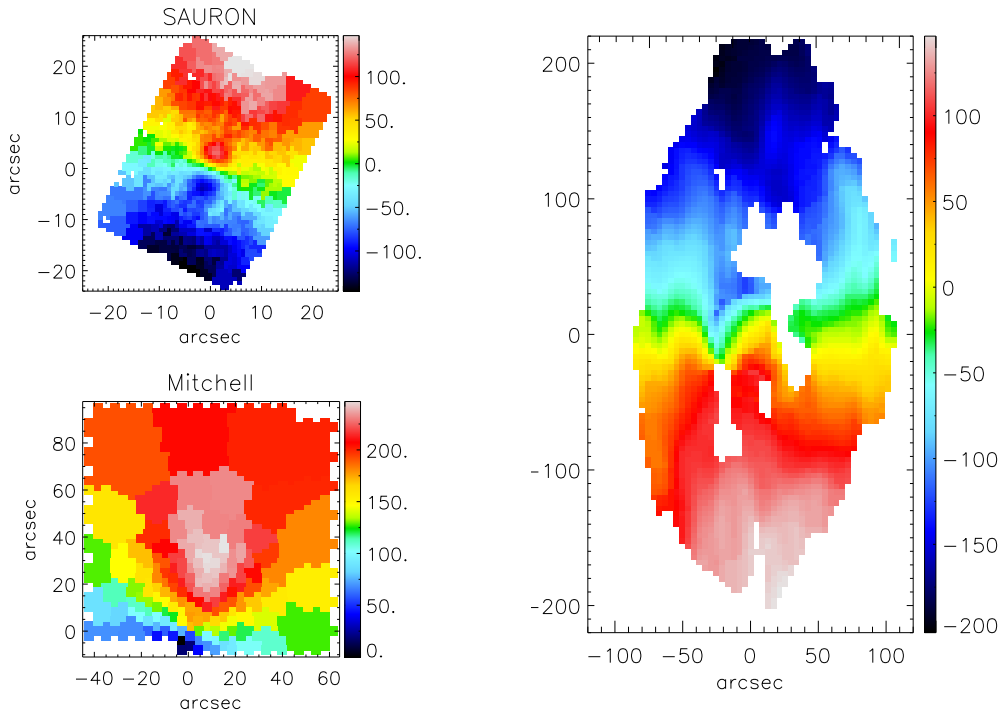

Figure 5.5: The stellar and H I velocity fields of NGC 3626. Upper left: the SAURON stellar velocity; Lower left: the Mitchell stellar velocity; Right: the WSRT H I velocity. The Mitchell instrument only covers one half of the galaxy to reach galaxy outskirts within the limited field-of-view. The H I and stellar discs are misaligned.

The H I velocity field of NGC 3626 is shown in the right panel of Figure 5.5, in which there is a clear misalignment between the H I and stellar discs. I note that I make a cutoff at 10 R_e of the H I observation to exclude the blobs around the H I disc and the noisy data at the outskirts. Using the method to measure PA and inclination described in Chapter 2, Section 2.3.2, I measure the H I disc of NGC 3626 has $PA_2 = 180.5°$ and a kinematic axis ratio $q_2 = 0.625$, while the stellar disc has $PA_1 = 340.5°$.

5.3.3 Mass distribution

The mass budget contains three components for each galaxy: the stellar mass, a dark matter halo and a central black hole. Here I introduce the process of parameterising the mass distribution using the method described in Chapter 4, Section 4.2.1.

In Chapter 4, I introduced the method to obtain stellar mass distribution with the Mult-Gaussian Expansion (MGE), which first obtains the MGE parameters (central luminosity intensity L_j, width σ, axis ratio q_j for each Gaussian) from galaxy surface brightness profiles,

Galaxy	j	$L_j(\mathrm{L}_\odot/\mathrm{pc}^2)$	σ (arcsec)	q_j	$M_j(\mathrm{M}_\odot/\mathrm{pc}^2)$
NGC 3626	1	16953.60	0.54231	0.99990	31284.82
	2	7062.40	1.60892	0.47412	15850.34
	3	4455.16	2.24908	0.87134	4.46
	4	2113.40	3.74169	0.65303	3994.76
	5	425.85	15.17164	0.46503	992.46
	6	164.81	31.60752	0.64170	534.15

Table 5.2: MGE Parameters of the surface brightness and stellar mass distribution of NGC 3626. From left to right: index, central luminosity intensity, width (standard deviation), axis ratio and central mass density of each Gaussian.

and then fits the mass-to-light ratio distribution $\Upsilon(x', y')$ to obtain the central mass density M_j for each Gaussian. The initial mass function (IMF) factor α is also introduced to indicate the IMF of the galaxy.

Here I again adopt the compatible r-band images taken from the Pan-STARRS as the surface brightness profile for Multi-Gaussian Expansion. The mass-to-light ratio distribution $\Upsilon(x', y')$ contains two parts: the first part is the SDSS r-band mass-to-light ratio distribution derived from the SAURON observations taken from Poci et al. (2017); the second part is the V-band mass-to-light ratio derived from the Mitchell observations taken from Boardman et al. (2017), which is then rescaled to match the SDSS r-band mass-to-light ratio. I show the MGE for the surface brightness and the corresponding central mass density in Table 5.2. The MGE fitting of the surface brightness and the 1-dimensional fitting of $\Upsilon(x', y')$ are shown in Figure 5.6. The stellar mass-to-light ratio is obtained with assuming a constant Salpeter IMF across the galaxy. I still assume the IMF is constant, introducing the IMF factor α to indicate the IMF choice. I note that the values of M_j is not rescaled as I did in Chapter 4. Therefore, $\alpha = 1$ indicates the Salpeter IMF.

I include a generalised-NFW dark matter halo for each galaxy, which is described with its central mass density ρ_s, scale radius r_s, inner slope γ and turning point η. The density distribution of the dark matter black hole is described with the MGE method to generate its gravitational potential. A central black hole is also included as a point source.

5.3.4 Orbit sampling and model settings

Following the method described in Chapter 4, Section 4.2.2, I sample the initial conditions of the orbits with energy E and their starting points on the (x, z) plane using the (θ, R) co-

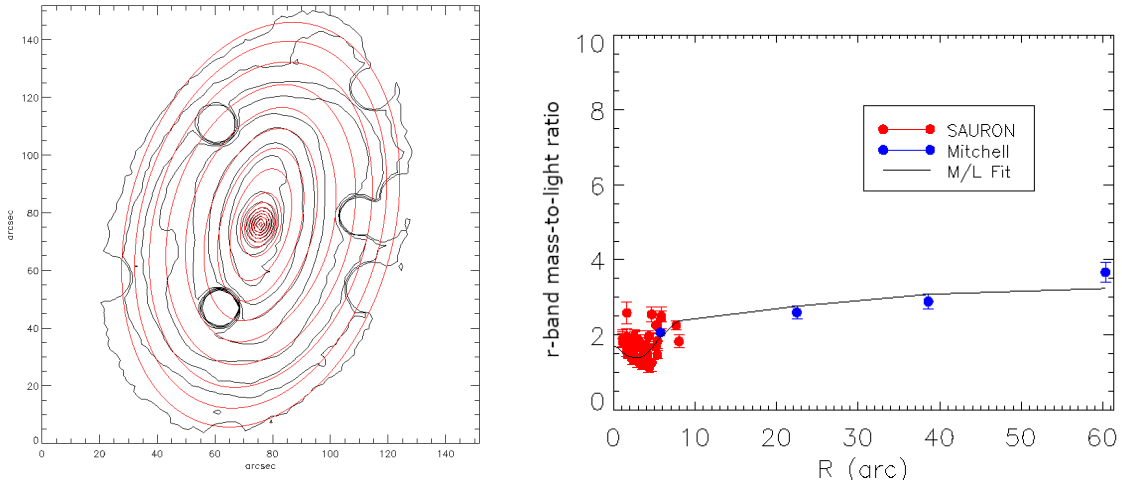

(a) Contour map

(b) r-band mass-to-light ratio Υ_r

Figure 5.6: Left: The surface brightness contours (black) and its MGE model (red) of NGC 3626. Foreground stars are masked in the image. Right: The r-band mass-to-light ratio of NGC 3626. The red dots are data from Poci et al. (2017) and the blue dots are data from Boardman et al. (2017). The solid line is the best fitting Υ_r.

ordinates with $n_E \times n_\theta \times n_R = 32 \times 10 \times 7$. I also sample the initial conditions for the box orbit library using energy E and two spherical angles θ (inclination) and ϕ (azimuthal angle) with $n_E \times n_\theta \times n_\phi = 32 \times 10 \times 7$. The sampling n_E for NGC 3626 is higher than that of NGC 2974, because its stellar kinematics are extended to over 3 R_e and therefore require more high energy orbits. For each orbit, 3 ditherings are introduced in every dimension to create an orbit bundle, resulting total orbits of 60,480 for each orbit library.

Here I summarise the free parameters in the model. The first is the IMF factor $\alpha \in [0.5, 1.5]$ with a step of 0.1, where $\alpha = 1$ indicates the Salpter IMF. There are three free parameters for the dark matter halo profile: the central density ρ_s and the scale radius r_s are sampled logarithmically in the same way as described in Chapter 4, Section 4.3.2; the inner slope $\gamma \in [0, 2]$ is in a linear grid with a step of 0.1 and the parameter η which controls the turning point is fixed to 2. The mass of a central black hole M_{BH} is also a free parameter sampled on a logarithmic grid with $M_{BH} \in [6, 10]$ in a step of 0.1. There is one free parameter regarding the projection of discs: the inclination of the stellar disc i_1, while the inclination of the gas disc i_2 and the PAs for both discs are already determined in Section 5.3.2.

Galaxy	$i_1(^\circ)$	α	$\rho_s(10^{-3}M_\odot/pc^3)$	r_s(kpc)	γ	$M_{BH}(10^7M_\odot)$
NGC 3626	72^{+0}_{-7}	$1.4^{+0.2}_{-0.3}$	$8.8^{+7.5}_{-4.4}$	$5.6^{+1.4}_{-3.4}$	$2.0^{+0.0}_{-0.0}$	$3.5^{+12.4}_{-3.4}$

Table 5.3: The best-fitting parameters for NGC3626. The uncertainties are defined the lower and upper limits of all models within $1-\sigma$ confidence level. Here ρ_s and M_{BH} are already multiplied by α to obtain their actual values.

5.4 Results

In this section, I introduce the results of fitting NGC 3626 and then evaluate the model according to the results. I show the best-fitting models, the enclosed mass profile, dark matter profile and stellar orbit distribution.

5.4.1 Best-fitting model

The best-fitting parameters are shown in Table 5.3, which are defined as the values of the best-fitting model identified as having the smallest $\chi^2 = \chi^2_{s,kin} + \chi^2_{gas}$. The uncertainties are defined as the lower and upper limits of all models within $1-\sigma$ confidence level. The fitting shows that the stellar and H I discs of NGC 3626 rotate in the same direction, and the angle between the rotating axes of the stellar and H I discs $\theta = 120.3^\circ$.

The best-fitting model of stellar kinematics is shown in Figure 5.7, and that of the H I velocity field is shown in Figure 5.8. The central stellar kinematics (within 1 R_e) covered by the SAURON observations are well-fitted, however, the model failed to recover the stellar velocity and velocity dispersion at the galaxy outskirts ($1-3\,R_e$) covered by the Mitchell observations. The recovery of H I velocity field shows a similar property: there is a strong inconsistency between the observational and modelled H I velocity within 3 R_e. This inconsistency of modelling Mitchell kinematics and H I velocity field indicates that the gravitational potential of NGC 3626 is not modelled well. I will discuss the reason for this inconsistency by investigating the mass distribution. I also note that there seems to be a little misalignment between the observational and modelled H I velocity field, which might be a result of an inaccurate PA or a twist of the H I disc. Since the gravitational potential is not well modelled, it is difficult to determine the reason for this misalignment.

Given the inconsistency between the observed and modelled stellar and H I kinematics, I note that the best-fitting values and its $1-\sigma$ uncertainty might not be robust at this stage. Since the gravitational potential is not fully recovered yet, the parameters related to the dark

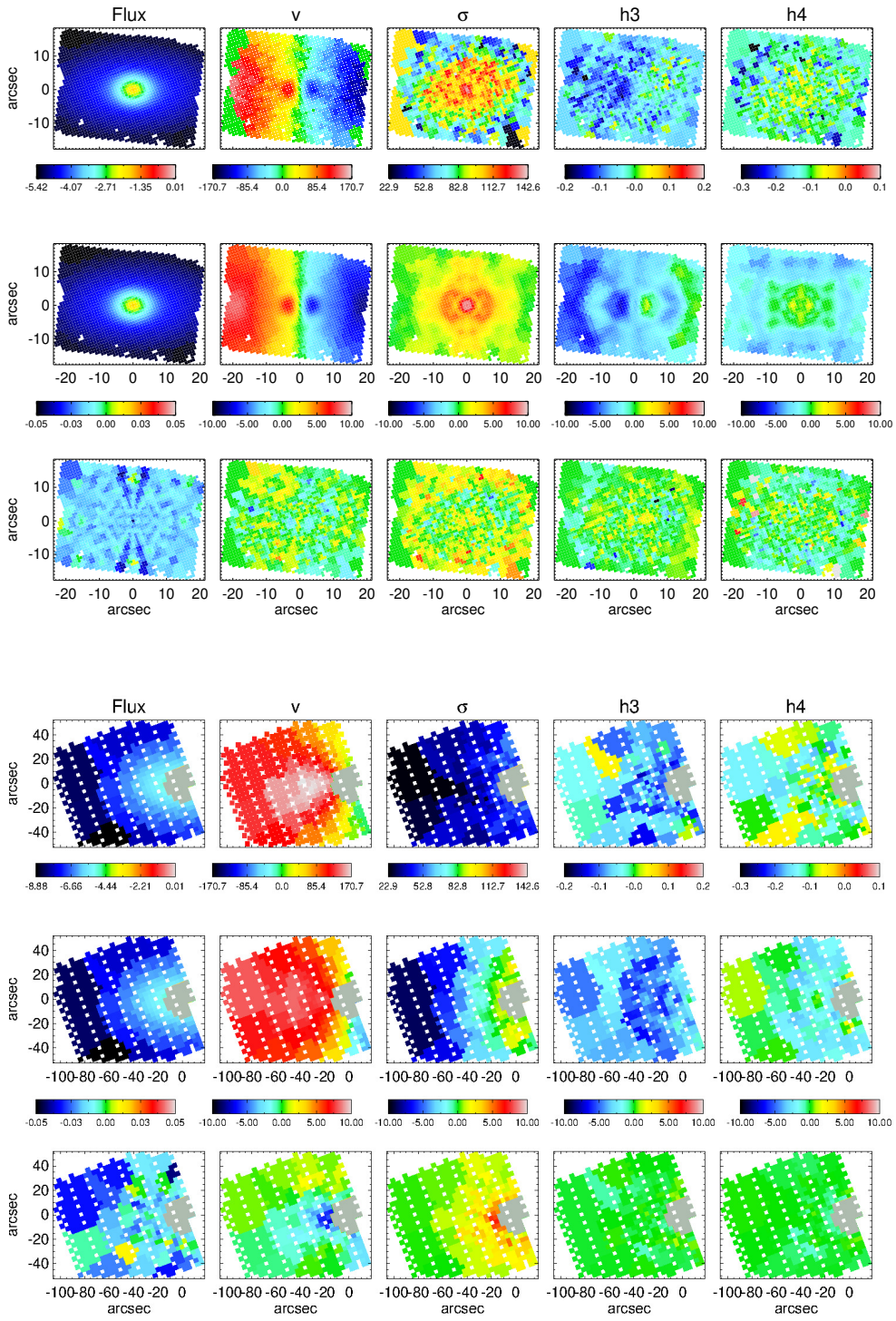

Figure 5.7: Stellar kinematics of NGC 3626. The upper panel is the SAURON data and the lower panel is the Mitchell data. For each panel, there are the data (top), model (middle) and relative residual (bottom; defined as (model-data)/error) of the surface brightness, stellar velocity, velocity dispersion, the third and fourth orders of Gauss-Hermite moments from left to right. The grey regions in the Mitchell data show the masked region in the galaxy centre. The SAURON kinematics are well fitted, while there are features which are not fully fitted in the velocity and velocity dispersion of the Mitchell data.

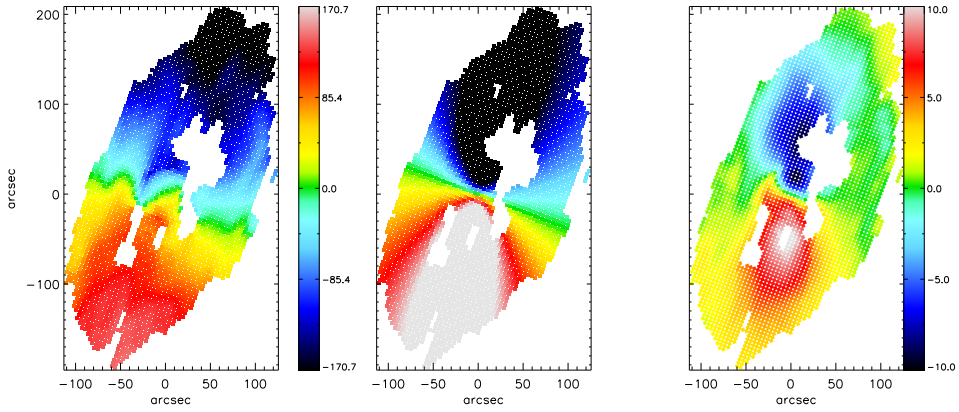

Figure 5.8: H I velocity of NGC 3626. From the to right: data, model and residual (defined as (model-data)/error). The residual map shows that the H I velocity is not perfectly fitted.

matter profile are not reliable. The following parameters related to the mass distribution and stellar kinematics within 1 R_e should be reliable: NGC 3626 has an inclination of 72° and an IMF producing 1.4 times more stellar mass than the Salpeter IMF. Considering that the influence radius of the central black hole with a mass of $3.5 \times 10^7 M_\odot$ is lower than the spatial resolution of the SAURON spectrograph as stated in Chapter 4, Section 4.3.3, the black hole mass might not be an accurate measurement.

5.4.2 Mass distribution

I plot the enclosed mass profile of NGC 3626 in Figure 5.9. It shows that its stellar mass distribution within 3 R_e covered by the Mitchell observations, while the dark matter takes a dominant role outside 10 R_e. The dark matter fraction is 35% within 3 R_e and rises up to over 50% at 10 R_e. I note that the dark matter fraction here might not be robust, for the total gravitational potential is not perfectly constrained.

The dark matter profiles of all models within $1-\sigma$ uncertainties are shown in Figure 5.10, which reveals the reason that the total gravitational potential is not well constrained. There are several settings of the fitting parameters responsible for the inconsistency between the observational and modelled velocity: the dark matter inner slope γ hits the upper limits of the fitting; the parameter η which controls the turning point is fixed to 2; the outer slope of the dark matter halo is -3, which is determined by the form of gNFW halo. Since the H I observation is very extended, the turning point is located within the range of the data.

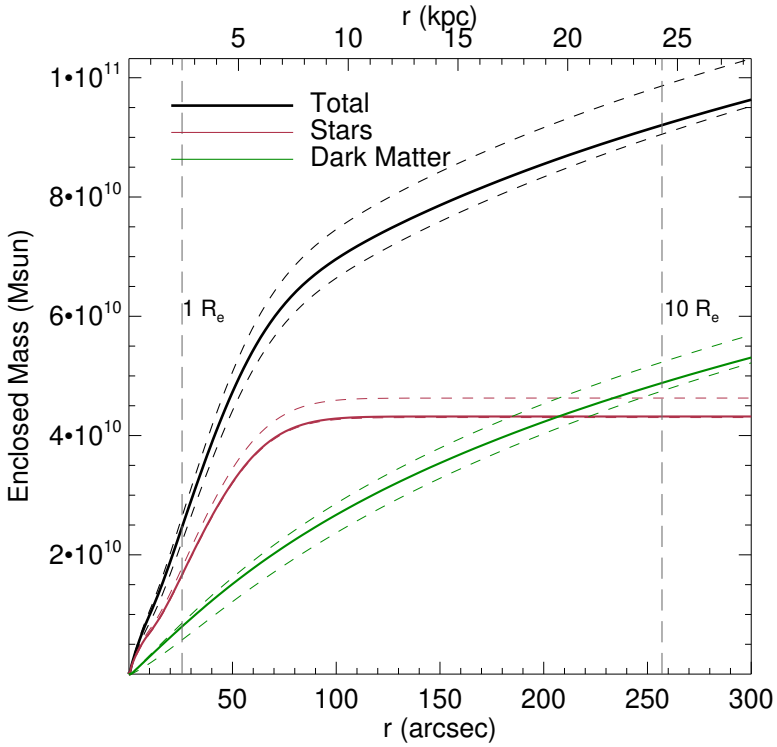

Figure 5.9: The enclosed mass profile of NGC 3626. The black, red and green solid lines stand for the total, stellar and dark matter mass, respectively. The corresponding dashed lines are their $1-\sigma$ uncertainties.

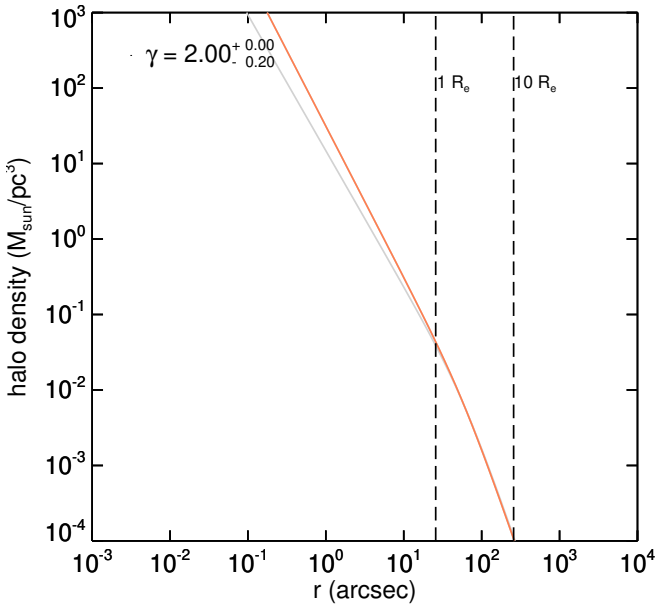

Figure 5.10: The dark matter profiles of all models within $1-\sigma$ uncertainties of NGC 3626. The orange line represents the dark matter profile of the best-fitting model, and the grey line represents the profile of the other model within $1-\sigma$ uncertainties. The left dashed line marks the position of 1 R_e and the right dashed line marks 10 R_e. I also list the inner slope γ of the best-fitting model and its uncertainty.

However, these settings prevent the model adjusting the dark matter distribution appropriately. Therefore, the dark matter distribution is not well described by the model, which affects the modelled gravitational potential and velocity fields.

The solution to this problem is to increase the freedom of the dark matter distribution in the way of freeing the turning point controlling parameter η and introducing the dark matter outer slope as a free parameter in the gNFW dark matter halo. If the gravitational potential cannot be recovered with a gNFW dark matter halo, I will have to adopt a different form of dark matter halo, such as the Einasto profile (Merritt et al., 2006).

5.4.3 Stellar orbit distributions

I plot the circularity (λ_z, see definition in Chapter 4, Section 4.3.3) map of NGC 3626 in Figure 5.11, which shows NGC 3626 has a central bulge composed of hot and warm orbits and an extended disc composed of cold and warm orbits. However, I note that the hot component might be far more extended than 1 R_e, because the stellar velocity dispersion of the Mitchell observation in the galaxy outskirts ($1-3$ R_e) is not fitted well as shown in Figure 5.7.

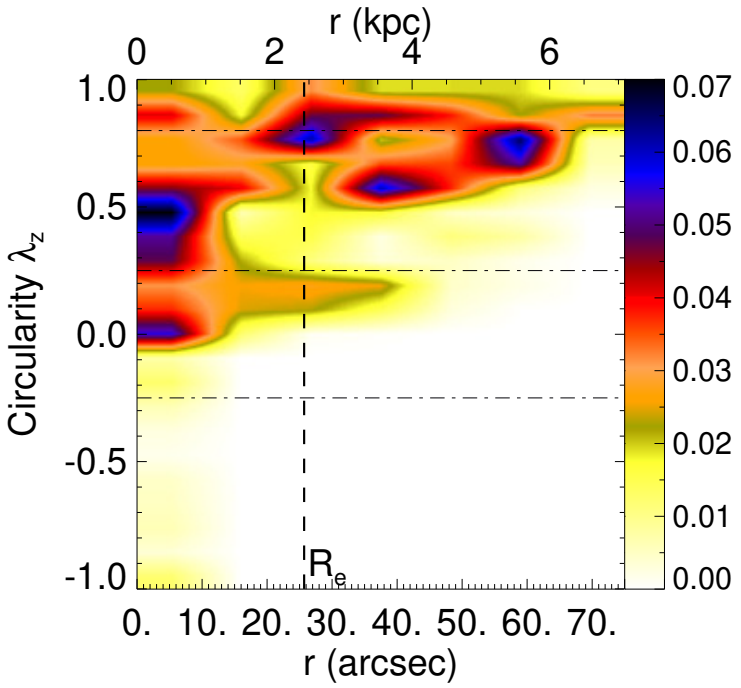

Figure 5.11: The stellar orbit distribution on the phase-space of λ_z vs radius of the best-fitting model to NGC 3626. The colour bar indicates the probability density of orbits. In the central region within 10 arcsec, there are mainly hot and warm stellar orbits, while outside 10 arcsec, there are cold and warm orbits.

5.5 Summary

In this chapter, I generalise the orbit-based model to galaxies with misaligned stellar and gaseous discs. I then apply this method to NGC 3626, an early-type galaxy with central SAURON stellar kinematics (1 R_e), extended Mitchell stellar kinematics (3 R_e) and a very extended H I velocity field (10 R_e), as a first exploration of this new orbit-based modelling approach.

With these extended data, this method shows an exciting prospect of constraining dark matter halo profiles. The current results show an inconsistency between the modelled and observational kinematics in the outskirt of this galaxy, because the halo model adopted in this chapter did not provide enough degrees of freedom to adjust the shape of dark matter profiles. This problem can be solved by freeing the fixed parameter of this gNFW dark matter profile, or adopting halo models. This method will be able to constrain the overall shape of dark matter haloes or even distinguish different halo models, which will significantly benefit the measurements of dark matter halo profiles, and therefore improve our understanding of the nature of dark matter.

6

Dark matter fractions of early-type galaxies

In previous chapters, I showed that including extended cold gas discs in orbit-based models can significantly improve their ability to constrain dark matter halo profiles by showing their applications to NGC 2974 and NGC 3626. However, extended cold gas discs are not available for all galaxies, which leads me to turn to galaxies with extended stellar kinematics for a larger sample. Exploring the mass distribution of a larger sample will allow me to study galaxy stellar orbits and dark matter profiles across a wider mass range, and therefore investigate the formation of galaxy components and the co-evolution of baryonic and dark matter. In this chapter, I model a larger sample of galaxies, which have SAURON stellar kinematics within 1 R_e and Mitchell stellar kinematics extended to 3 R_e, with the Schwarzschild orbit-superposition technique. Together with NGC 2974 and NGC 3626 modelled in previous chapters, I will build a larger sample to study the stellar orbit components and dark matter distributions.

There are 12 nearby early-type galaxies with both the SAURON and Mitchell stellar kinematics presented in Boardman et al. (2017). Here I list the basic information of these galaxies in Table 6.1. Since the combined SAURON and Mitchell stellar kinematics of NGC 3626 and

	R_e (arcsec)	M_K (mag)	Distance (Mpc)	$\log M_*/M_\odot$
NGC 680	14.5	-24.17	37.5	11.09
NGC 1023	47.9	-24.01	11.1	11.02
NGC 2685	25.7	-22.78	16.7	10.48
NGC 2764	12.3	-23.19	39.6	10.66
NGC 3522	10.2	-21.67	25.5	9.99
NGC 4203	29.5	-23.44	14.7	10.77
NGC 5582	27.5	-23.28	27.7	10.70
NGC 5631	20.9	-23.70	27.0	10.89
NGC 6798	16.9	-23.52	37.5	10.80
UGC 03960	17.4	-21.89	33.2	10.09
NGC 3626*	25.7	-23.30	19.5	10.71
NGC 3998*	20.0	-23.33	13.7	10.73

Table 6.1: Basic properties of the sample galaxies, including the effective radius R_e, K-band magnitude M_K, distance taken from (Cappellari et al., 2011) and stellar mass M_* taken from Boardman et al. (2017). * NGC 3626 and NGC 3998 will not be modelled in this chapter, but will be included in the analysis.

NGC 3998 were modelled with the Schwarzschild technique in Chapter 5 and Boardman et al. (2016), respectively, I will refer to those results in my analysis instead of modelling these galaxies repeatedly in this chapter.

6.1 Methods

In this section, I introduce the application of the Schwarzschild technique to the sample, including the mass budget and the model setting.

6.1.1 Mass distribution

The mass budget is modelled with the same method as described in Chapter 4, which includes the stellar mass parameterised with MGE, a generalised-NFW dark matter halo and a central supermassive black hole.

I adopt the r-band images taken from Pan-STARRS (Chambers et al., 2016) as the surface brightness profile to trace the stellar mass distribution for each galaxy. I apply MGE to the r-band image of each galaxy and show the contour maps and the resulting MGE models in Appendix A of this chapter. Here I particularly note that to fit the central twist of NGC 680, I introduce a twist angle ψ_j to the MGE fit, which allows the major axis of each Gaussian deviating ψ_j from the PA of the galaxy. For the other galaxies in the sample, the major axes of all the Gaussians for each galaxy are aligned.

I then fit the r-band mass-to-light ratio distribution $\Upsilon(x', y')$ to obtain the central mass density M_j for MGE of the stellar mass distribution. The r-band mass-to-light ratio distributions are composed of the SDSS r-band mass-to-light ratio distributions taken from Poci et al. (2017) and V-band mass-to-light ratio taken from Boardman et al. (2017), which is then rescaled to match the SDSS r-band mass-to-light ratio. The mass density M_j and the 1-dimensional fittings to $\Upsilon(x', y')$ for all galaxies can also be found in Appendix A.

The stellar mass-to-light ratio are obtained assuming a constant Salpeter IMF. The IMF is assumed to be constant in the model, and the IMF factor α is introduced such that $\alpha = 1$ indicates the Salpeter IMF. I adopt the generalised-NFW dark matter halo as described in Chapter 4, which is parameterised with its scale density ρ_s, scale radius r_s, inner slope γ and turning point controller η fixed to 2. A central black hole is also included as a point source.

6.1.2 Orbit sampling and model settings

The initial conditions of the orbit library are again sampled with energy E and their starting points on the (x, z) plane using the (θ, R) coordinates, and the initial conditions of the additional box orbit library are sampled with their energy E and two spherical angles θ (inclination) and ϕ (azimuthal angle). As the stellar kinematics are extended to more than 3 R_e, I adopt a different sampling of the energy E to balance between the number of orbits and computing speed. For all sample galaxies except NGC 1023 and NGC 2685, $n_E \times n_\theta \times n_R = n_E \times n_\theta \times n_\phi = 25 \times 10 \times 7$ with 3 ditherings in every dimension, resulting in 47,250 orbits in each orbit library. For NGC 1023 and NGC 2685, the settings above are not enough to reproduce their galaxy orbits, therefore, I set $n_E \times n_\theta \times n_R = n_E \times n_\theta \times n_\phi = 32 \times 10 \times 7$ also with 3 ditherings in every dimension, resulting in 60,480 orbits in each orbit library.

The free parameters in the model are summarised as following: The inclination θ of each galaxy has a step of 1°. The IMF factor α varies within $[0.5, 1.5]$ with a step of 0.1, where $\alpha = 1$ indicates the Salpter IMF. The dark matter halo has three free parameters, in which the central density ρ_s and the scale radius r_s are sampled logarithmically, and the inner slope $\gamma \in [0, 2]$ is sampled in a linear grid with a step of 0.1. The black hole mass M_{BH} is sampled on a logarithmic grid with $M_{BH} \in [6, 10]$ in steps of 0.1.

Galaxy	$\theta(^\circ)$	α	$\rho_s(10^{-3}M_\odot/pc^3)$	r_s(kpc)	γ	$M_{BH}(10^7M_\odot)$
NGC 680	69^{+0}_{-15}	$0.8^{+0.0}_{-0.2}$	8^{+24}_{-6}	10^{+30}_{-7}	$1.0^{+0.6}_{-1.0}$	8^{+0}_{-2}
NGC 1023	65^{+3}_{-0}	$0.6^{+0.1}_{-0.0}$	12^{+0}_{-6}	20^{+12}_{-0}	$1.0^{+0.2}_{-0.0}$	19^{+3}_{-0}
NGC 2685	85^{+0}_{-1}	$0.8^{+0.3}_{-0.1}$	12^{+3}_{-5}	10^{+1}_{-4}	$1.2^{+0.0}_{-0.1}$	$1.6^{+0.9}_{-1.2}$
NGC 2764	80^{+3}_{-2}	$1.3^{+0.3}_{-0.7}$	13^{+17}_{-7}	10^{+10}_{-4}	$1.2^{+0.4}_{-0.6}$	$1.6^{+4.3}_{-0.6}$
NGC 3522	82^{+3}_{-1}	$0.7^{+0.1}_{-0.1}$	8^{+8}_{-6}	8^{+12}_{-3}	$1.2^{+0.2}_{-0.6}$	$1.4^{+1.4}_{-0.9}$
NGC 4203	55^{+3}_{-2}	$0.6^{+0.0}_{-0.0}$	$6.0^{+9.1}_{-5.5}$	$1.6^{+14.3}_{-0.6}$	$1.0^{+0.6}_{-0.4}$	5^{+14}_{-2}
NGC 5582	65^{+4}_{-2}	$0.9^{+0.1}_{-0.0}$	9^{+5}_{-0}	10^{+0}_{-0}	$1.2^{+0.0}_{-0.4}$	$1.8^{+69.6}_{-1.5}$
NGC 5631	40^{+8}_{-2}	$0.8^{+0.2}_{-0.0}$	20^{+16}_{-16}	13^{+37}_{-6}	$1.0^{+0.4}_{-0.6}$	10^{+4}_{-4}
NGC 6798	65^{+7}_{-3}	$1.1^{+0.5}_{-0.6}$	11^{+71}_{-9}	2^{+60}_{-0}	$1.4^{+0.6}_{-1.4}$	$4.4^{+77.6}_{-3.9}$
UGC 03960	80^{+5}_{-3}	$1.5^{+0.1}_{-0.5}$	24^{+8}_{-21}	4^{+16}_{-1}	$1.0^{+0.6}_{-0.8}$	$1.2^{+7.6}_{-0.9}$

Table 6.2: The best-fitting parameters for all galaxies. The uncertainties are the lower and upper limits of all models within $1-\sigma$ confidence level. Here ρ_s and M_{BH} are already multiplied by α to obtain their actual values.

6.2 Results

Following the method described in Chapter 5, Section 5.3.1, I model the sample galaxies which have two-aperture stellar kinematics (the SAURON and Mitchell stellar kinematics) with the Schwarzschild technique. The orbital weights of each model are solved by minimising the residual of stellar kinematics, and the best-fitting model is defined as the model with the minimum residual within all models. In this section, I show the results of this modelling, which contain three parts: the best-fitting models, the mass distributions and the stellar orbit distributions.

6.2.1 Best-fitting models

The best-fitting values for the free parameters in the model of all sample galaxies are listed in Table 6.2. There are two parameters regarding the mass distribution of galaxies which are particularly interesting: the IMF factor α and the dark matter inner slope γ.

The IMF factor α varies between 0.6 and 1.5, which produces a wide total mass range. The IMF factors of NGC 680, NGC 1023, NGC 3522 and NGC 4203 show a preference for the Kroupa IMF; while NGC 2685, NGC 5582 and NGC 5631 are close to the Salpeter IMF, and UGC 03960 prefers a heavier IMF than the Salpter one. The IMF factors of NGC 2764 and

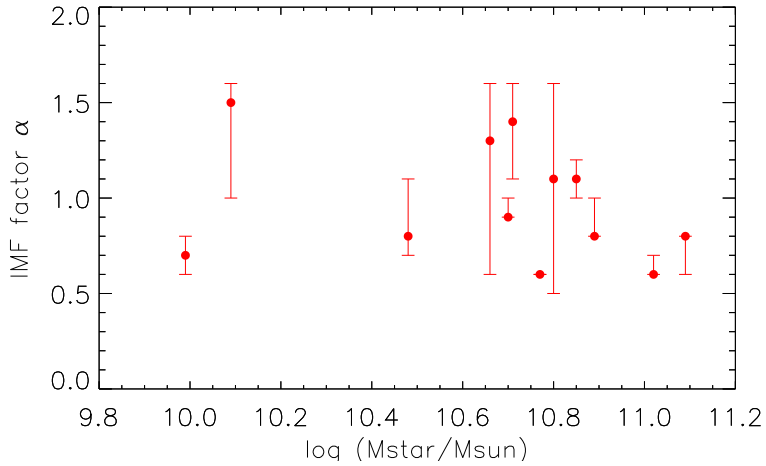

Figure 6.1: IMF factor α versus stellar mass for all sample galaxies. The length of lower/higher error bar equals 0 means that the best-fitting value equals the lower/higher limit of $1-\sigma$ uncertainties.

NGC 6798 are not well constrained. I show a plot of the IMF factor α versus stellar mass in Figure 6.1, in which I find no clear correlation between the IMF factor and stellar mass. The average of the IMF factors is consistent with previous results that early-type galaxies have a Salpeter-like IMF, but my result is inconsistent with the trend that there is a positive correlation between the IMF factor and stellar mass (e.g. Cappellari et al., 2012; Sonnenfeld et al., 2015).

For the dark matter inner slope γ, a central cusp is supported by all the sample galaxies with an average of $\gamma = 1.1$. However, the core model ($\gamma \sim 0$) is favoured by NGC 680, NGC 6798 and UGC 03960. Although the cusp model is preferred by all sample galaxies, the core model is not yet fully ruled out for NGC 2764, NGC 3522 and NGC 5631. The plot of the dark matter inner slope γ versus stellar mass is shown in Figure 6.2, and there is no clear correlation between the dark matter inner slope γ and stellar mass. The average stellar mass of this sample is lower than previous measurements for early-type galaxies (Sonnenfeld et al., 2012, 2015; Newman et al., 2013, 2015; Oldham & Auger, 2016, 2018; Wasserman et al., 2018), therefore, this work fills in the gap at this mass range ($10^{10}-10^{11}M_{\odot}$) for the study of dark matter inner slopes in early-type galaxies.

The best-fitting stellar kinematics of all sample galaxies are shown in the Appendix B, in which I discuss more details of the fittings. In general, the SAURON stellar kinematics within 1 R_e are well-fitted with almost no structures in the residual maps, while the Mitchell stellar kinematics are fitted relatively worse with some structures left in the residual maps, mainly because of low signal-to-noise ratio (S/N) and large bin sizes in the galaxy outskirts.

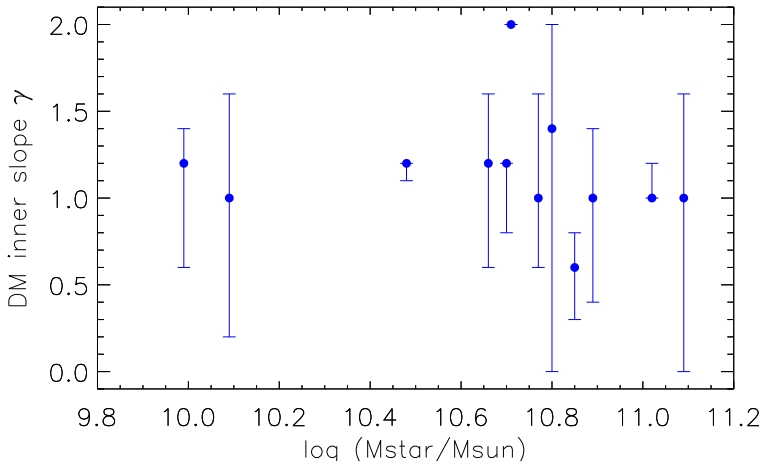

Figure 6.2: Dark matter inner slope γ versus stellar mass for all sample galaxies. The length of lower/higher error bar equals 0 means that the best-fitting value equals the lower/higher limit of $1-\sigma$ uncertainties.

6.2.2 Enclosed mass and dark matter profiles

Studying the dark matter content in early-type galaxies is important for understanding the co-evolution of early-type galaxies and their host dark matter haloes. Therefore, the dark matter profiles of early-type galaxies are my main focus in this chapter.

I plot the enclosed mass profiles for all the sample galaxies in Figure 6.3. As I expected, the stellar content dominates the enclosed mass profiles in the galaxy centre and the dark matter fraction within 1 R_e is commonly very low. The stellar mass content almost stops increasing at 4 R_e and dark matter dominates the growth of the enclosed mass profile. These results again indicate the importance of including extended tracers to study the dark matter in galaxies.

The dark matter profiles for all the sample galaxies are shown in Figure 6.4. This figure shows that the slopes of the dark matter profiles begin to vary within 3 R_e for some galaxies (NGC 2764, NGC 4203, NGC 5582 and NGC 6798 and UGC 03960), suggesting that the turning point η might be constrained with these two-aperture stellar kinematics. The dark matter slopes change to -3 at 10 R_e for all galaxies, which confirms the conclusion of Chapter 5 that the orbit-based models with very extended cold gas kinematics will be able to constrain the overall shape of dark matter haloes (including the outer slope) or even distinguish different halo models.

These results point out one direction of next steps. There are four galaxies which have very extended H I kinematics (NGC 2685, NGC 4203, NGC 5582 and NGC 6798), and I will

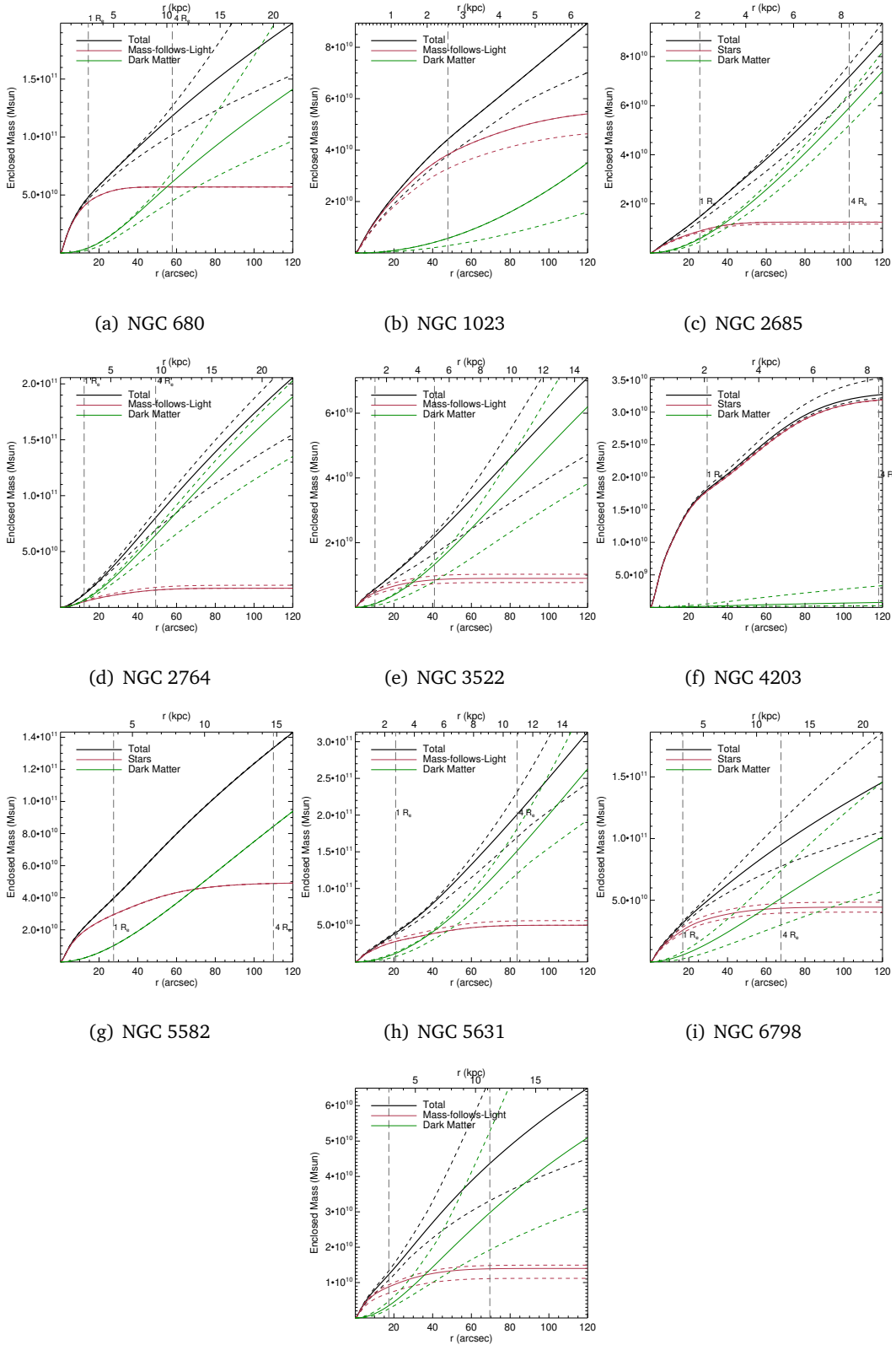

(a) NGC 680 (b) NGC 1023 (c) NGC 2685

(d) NGC 2764 (e) NGC 3522 (f) NGC 4203

(g) NGC 5582 (h) NGC 5631 (i) NGC 6798

(j) UGC 03960

Figure 6.3: The enclosed mass profile. The black, red and green solid lines stand for the total, stellar and dark matter mass, respectively. The corresponding dashed lines are their $1-\sigma$ uncertainties. The vertical dashed lines mark the radii of 1 R_e and 4 R_e.

remodel them with orbit-based models with a halo model which the overall halo shape can be adjusted. For the other galaxies with two-aperture stellar kinematics only, I will try to free the turning point η to see if this parameter can be constrained.

I show the dark matter fractions within 1 R_e ($f_{DM}(R_e)$) and 3 R_e ($f_{DM}(3R_e)$) of all sample galaxies in Table 6.3, including NGC 2974 and NGC 3626 modelled in Chapters 4 and 5, and NGC 3998 modelled in Boardman et al. (2016). I also include the dark matter fraction within 1 R_e measured with the JAM method taken from Cappellari et al. (2013a) for comparison. For most of the galaxies, the dark matter fractions are between 10%-30% within 1 R_e and rise up to 40%-70% at 3 R_e, showing again the importance of measuring dark matter with extended stellar kinematics My measurements of $f_{DM}(R_e)$ are consistent with (NGC 680, NGC 3522, NGC 4203, NGC 6798) or slightly different from (NGC 1023, NGC 2685, NGC 5582, NGC 5631, UGC 03960) the measurements of Cappellari et al. (2013a). Since Cappellari et al. (2013a) adopted an NFW halo model and a constant mass-to-light ratio to model stellar kinematics within 1 R_e, these slight inconsistencies are within my expectation. However, there is a significant inconsistency between my measurement and the measurement of Cappellari et al. (2013a) for NGC 2764, where I obtain $f_{DM}(R_e) = 0.56$ while Cappellari et al. (2013a) found no dark matter. This significant inconsistency is partly caused by the different assumptions and less extended data adopted by Cappellari et al. (2013a), however, the imperfect fitting of NGC 2764 might also cause an inaccurate measurement of dark matter fraction, which I will discuss in Appendix B.

I show the dark matter fractions versus stellar mass for all sample galaxies (including NGC 2974, NGC 3626 and NGC 3998.) in Figure 6.5. I also include the fitting curve for the dark matter fractions within 1 R_e of the Atlas^{3D} sample with NFW halo models presented in Cappellari et al. (2013b), which shows a trend that galaxies at the low-mass and high-mass ends have higher dark matter fractions than galaxies with intermediate mass ($\sim 10^{10.6} M_\odot$). My measurements of the dark matter fractions show no trends with stellar mass within both radii. Although this sample has a narrower mass range than the Atlas^{3D} sample, $f_{DM}(R_e)$ in the intermediate mass range ($\sim 10^{10.6} M_\odot$) are too far away from the fitting curve of the Atlas^{3D} sample to establish such a trend. This result is not surprising because their fitting curve was obtained with a NFW halo model, and it reminds us to be cautious to make any conclusions about galaxy evolution with such kind of trends.

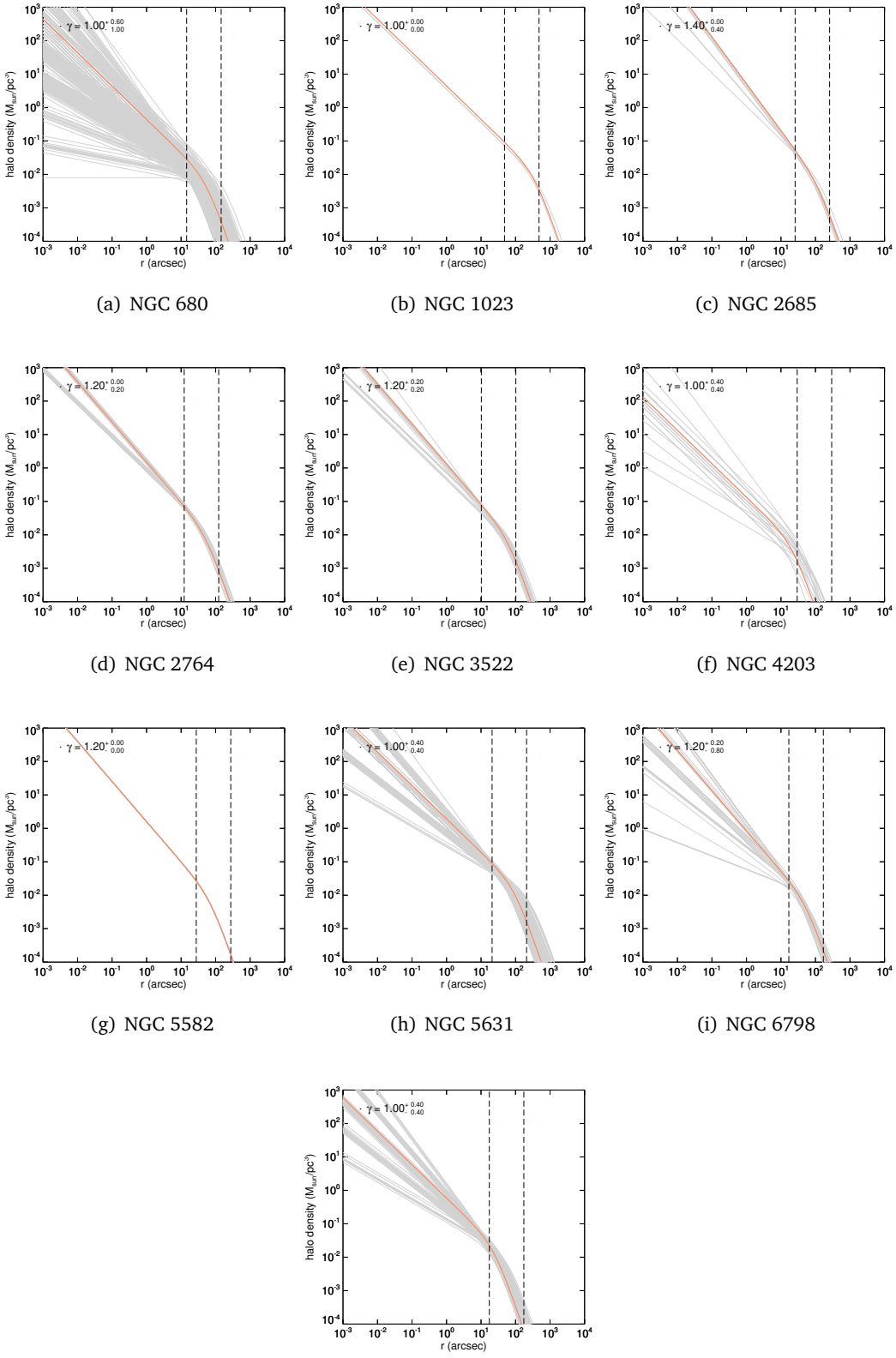

(a) NGC 680 (b) NGC 1023 (c) NGC 2685

(d) NGC 2764 (e) NGC 3522 (f) NGC 4203

(g) NGC 5582 (h) NGC 5631 (i) NGC 6798

(j) UGC 03960

Figure 6.4: The dark matter profiles of all models within $1-\sigma$ uncertainties. Each grey line represents the dark matter profile of a model, and the orange line is the profile of the best-fitting model. The vertical dashed lines mark the radii of 1 R_e and 10 R_e, and the position in the middle of the two vertical lines is about 3 R_e for each plot.

Galaxy	$f_{\rm DM}(R_{\rm e})$	$f_{\rm DM}(3R_{\rm e})$	$f'_{\rm DM}(R_{\rm e})$
NGC 680	0.09	0.40	0.08
NGC 1023	0.13	0.64	0.00
NGC 2685	0.39	0.72	0.18
NGC 2764	0.56	0.76	0.00
NGC 3522	0.20	0.51	0.24
NGC 4203	0.01	0.02	0.00
NGC 5582	0.26	0.56	0.37
NGC 5631	0.29	0.66	0.10
NGC 6798	0.18	0.45	0.16
UGC 03960	0.28	0.60	0.04
NGC 2974*	0.07	0.40	0.07
NGC 3626*	0.32	0.35	0.23
NGC 3998*	0.07	0.28	0.15

Table 6.3: The dark matter fractions of all sample galaxies. From left to right: $f_{\rm DM}(R_{\rm e})$ is the dark matter fraction within 1 $R_{\rm e}$, $f_{\rm DM}(3R_{\rm e})$ is the dark matter fraction within 3 $R_{\rm e}$ and $f'_{\rm DM}(R_{\rm e})$ is the dark matter fraction within 1 $R_{\rm e}$ $f'_{\rm DM}(R_{\rm e})$ taken from Cappellari et al. (2013a) for comparison. * The data for NGC 2974 and NGC 3626 are taken from Chapters 4 and 5, and the data for NGC 3998 are taken from Boardman et al. (2016).

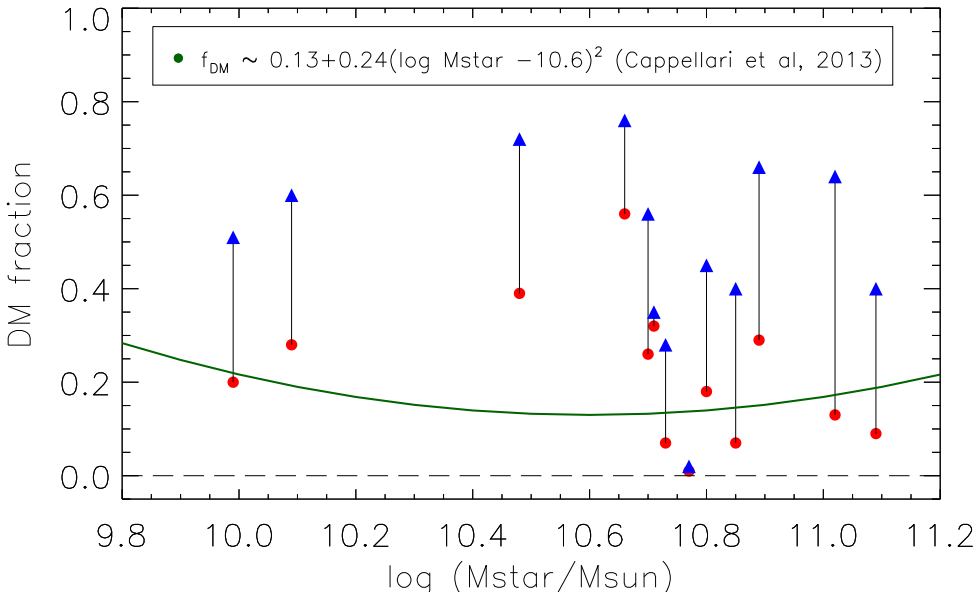

Figure 6.5: Dark matter fractions versus stellar mass for all sample galaxies including NGC 2974, NGC 3626 and NGC 3998. The red dots stand for the dark matter fractions within 1 $R_{\rm e}$ and the blue triangles stand for the dark matter fractions within 3 $R_{\rm e}$. The green line is a parabolic fit for the dark matter fractions within 1 $R_{\rm e}$ of the Atlas$^{\rm 3D}$ sample presented in Cappellari et al. (2013b).

6.2.3 Stellar orbit distributions

The stellar orbit distributions of galaxies exhibit the orbit components of galaxies, and therefore are important to the study of galaxy dynamical components. Following the method described in Chapter 4, Section 4.3.3, I characterise the stellar orbits with their circularity λ_z, as shown in Figure 6.6. Emsellem et al. (2011) classified these galaxies into fast and slow rotators according to their spin parameter λ_{R_e} and ellipticity ϵ_e (see more details in Chapter 2, Section 2.4.1), and I also include their classifications and λ_{R_e} values in the subtitle for each galaxy in Figure 6.6. In general, the stellar orbit distributions are consistent with this classification that fast rotators have large fractions of cold and warm orbits while slow rotators are dominated by hot orbits as I expected. The only exception is NGC 1023, which is dominated by a hot component but classified as a fast rotator. This is due to the fitting problem of NGC 1023, which leads to an underestimation of cold orbits for this galaxy (there is a minor cold component in NGC 1023), and I will discuss this fitting problem in detail in Appendix B. There is another interesting question that NGC 5631 and UGC 03960 are classified as fast rotators with $\lambda_{R_e/2}$ but slow rotators with λ_{R_e} in Emsellem et al. (2011). This inconsistency is easy to explain with the stellar orbit distributions that NGC 5631 and UGC 03960 have more warm orbits within $R_e/2$ while they mainly have hot orbits with $\lambda_z = 0$ outside $R_e/2$.

There are several typical orbital structures shown in the stellar orbit distribution, and here I discuss them in detail.

- Central hot component with $\lambda_z = 0$. This hot component dominates NGC 1023 and NGC 3522 within 0.5 R_e. It also appears in NGC 2685 within 1 R_e alongside with a disc component. This component is merely composed of box or radial orbits, which suggests such hot components might form in a common origin, such as mergers.

- Central hot/counter-rotating component with double λ_z peaks ($\lambda_z \sim 0$ and $\lambda_z \sim 0.25$). This component is composed of box and short-axis tube orbits. NGC 6798 and UGC 03960 have such components within 1 R_e. Although there is a disc component in UGC 03960, their similar central hot/counter-rotating components suggest that these galaxies might experience a similar formation process in the past.

- Central hot/warm component with extended λ_z distribution (peaking at $\lambda_z \sim 0$ and $\lambda_z \sim 0.5$). This component covers the inner region of NGC 680, NGC 4203, NGC 5582

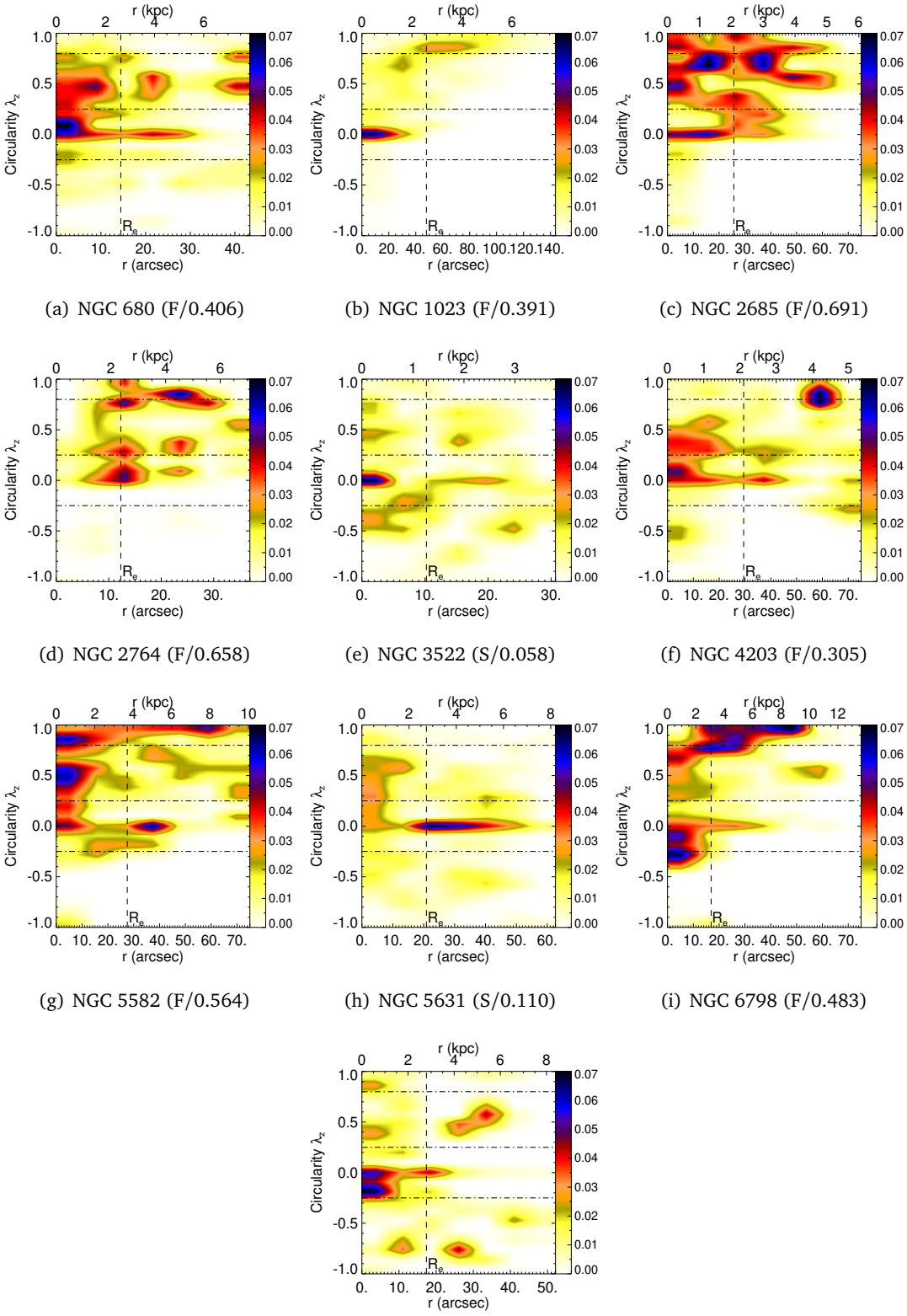

(a) NGC 680 (F/0.406) (b) NGC 1023 (F/0.391) (c) NGC 2685 (F/0.691)

(d) NGC 2764 (F/0.658) (e) NGC 3522 (S/0.058) (f) NGC 4203 (F/0.305)

(g) NGC 5582 (F/0.564) (h) NGC 5631 (S/0.110) (i) NGC 6798 (F/0.483)

(j) UGC 03960 (S/0.119)

Figure 6.6: The stellar orbit distribution on the phase-space of λ_z versus radius of the best-fitting model for all sample galaxies. The colour bar indicates the probability density of orbits. The letters 'F' and 'S' are denoted as the fast rotators and slow rotators classified by Emsellem et al. (2011), followed by their λ_{R_e} values used for this classification.

and NGC 5631. This component is also composed of box and short-axis tube orbits, and might form in more complicated formation processes.

- Cold component with $\lambda_z \sim 1.0$. The cold component appears in NGC 2685, NGC 2764, NGC 4203, NGC 5582 and NGC 6798, indicating these galaxies are lenticular galaxies. Among these galaxies, NGC 4203 is particularly interesting because it shows a clear narrow thin ring feature instead of an extended thin disc.

Although I found some characteristic orbital features within this sample, it is difficult to link them with particular formation processes. There are two methods to further explore this question: modelling simulated galaxies for which the formation history is already known, or including galaxy population information into dynamical models (e.g. age and metallicity; Zhu et al., 2020).

I classify the orbits in the model into four dynamical components: hot ($|\lambda_z| \leq 0.25$), warm ($0.25 < \lambda_z < 0.8$), cold ($\lambda_z \geq 0.8$) and counter-rotating ($\lambda_z < -0.25$), and I show the fractions of each component for all sample galaxies together with the λ_{R_e} values taken from Emsellem et al. (2011) in Table 6.4. I found a relation between the λ_{R_e} and the fractions of dynamical components with the linear regression analysis, as shown in Figure 6.7. The regression function shows that λ_{R_e} can usually reflect whether a galaxy has strong rotation motions or radial motions: $f_{\rm cold}$ has a strong positive correlation with λ_{R_e}, $f_{\rm warm}$ has a weak correlation and $f_{\rm hot}$ correlates little with λ_{R_e}. However, λ_{R_e} will not be a good indicator in the case of strong counter rotations, because $f_{\rm counter}$ cancels the contribution of $f_{\rm cold}$ and $f_{\rm warm}$, making it difficult to distinguish counter-rotating galaxies from slow rotators with λ_{R_e} only.

6.3 Summary

In this chapter, I applied the Schwarzschild orbit-superposition method with two-aperture stellar kinematics to a sample of early-type galaxies, which have high spatial resolution SAURON stellar kinematics within 1 R_e and extended Mitchell stellar kinematics out to 3 R_e.

The stellar kinematics of some galaxies are well fitted, although the Mitchell stellar kinematics of other galaxies are not well recovered mainly because of low S/N and large bin size in the outskirts. The best-fitting results show a wide range of IMF factors and a universal preference for a cusp dark matter halo, although a core model is not ruled out for several galaxies.

Galaxy	$f_{\rm hot}$	$f_{\rm warm}$	$f_{\rm cold}$	$f_{\rm counter}$	$\lambda_{R_{\rm e}}$
NGC0680	0.396	0.438	0.062	0.104	0.406
NGC1023	0.390	0.451	0.108	0.051	0.391
NGC2685	0.266	0.487	0.181	0.067	0.691
NGC2764	0.349	0.456	0.125	0.070	0.658
NGC3522	0.388	0.260	0.060	0.291	0.058
NGC4203	0.364	0.436	0.061	0.139	0.305
NGC5582	0.289	0.424	0.203	0.084	0.564
NGC5631	0.309	0.382	0.059	0.250	0.110
NGC6798	0.346	0.375	0.090	0.189	0.483
UGC03960	0.434	0.236	0.087	0.244	0.119
NGC3626*	0.255	0.534	0.163	0.048	0.660
NGC2974*	0.219	0.457	0.212	0.112	0.663

Table 6.4: The fractions of four dynamical components for all sample galaxies: hot ($|\lambda_z| \leq 0.25$), warm ($0.25 < \lambda_z < 0.8$), cold ($\lambda_z \geq 0.8$) and counter-rotating ($\lambda_z < -0.25$). The $\lambda_{R_{\rm e}}$ values taken from Emsellem et al. (2011) are also included. * NGC 3626 was modelled with two-aperture stellar kinematics with misaligned H I disc, and NGC 2974 was modelled the central stellar kinematics with aligned H I disc.

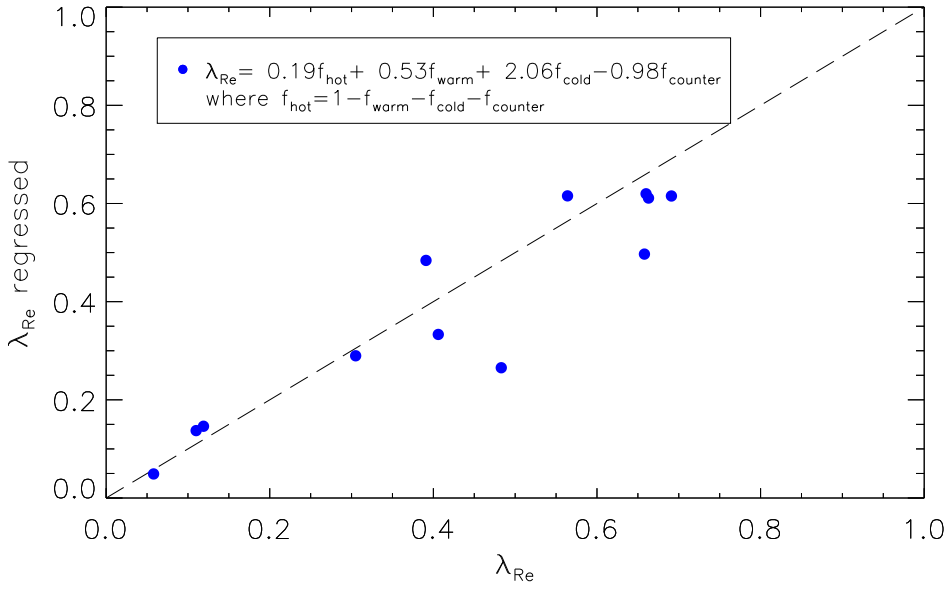

Figure 6.7: The regression of $\lambda_{R_{\rm e}}$ with $f_{\rm warm}$, $f_{\rm cold}$ and $f_{\rm counter}$, and the black dashed line is the 1-to-1 line. Since $f_{\rm hot} = 1 - f_{\rm warm} - f_{\rm cold} - f_{\rm counter}$ is not an independent variable, it is not included in the regression but used to replace the constant in the regression function.

I found that both the IMF factor and dark matter inner slope have no clear correlation with stellar mass. The dark matter profiles show the importance of including extended stellar kinematics to model dark matter haloes, and support the conclusion of Chapter 5 that the shape of dark matter haloes could be better determined with cold gas kinematics extended to 10 R_e. The dark matter fraction within 1 R_e is usually between 10%-30%, and it rises up to 40%-70% at 3 R_e. I found no clear trends between the dark matter fraction and stellar mass, which is inconsistent with the result of Cappellari et al. (2013b), because they adopted an NFW halo model with central stellar kinematics within 1 R_e.

I found that there are some characteristic features in the stellar orbital distributions, which suggests they originate from different formation processes. However, it is difficult to link them to any specific mechanism without stellar population distributions or merger histories. I also obtained the fractions of different stellar orbit components for all sample galaxies, and studied their relations with the spin parameter λ_{R_e}. The result shows that λ_{R_e} is in general a good indicator of fast and slow rotators, but not very suitable for distinguish fast-rotating galaxies with strong counter-rotating components.

Appendix A: Mass models

In this section, I show the mass models of all sample galaxies. NGC 680 is fitted with the twist MGE method which allows the major axis of each Gaussian deviating ψ_j from the PA of the galaxy, while other galaxies are fitted without the twist. Figure 6.8 contains the contour maps for the MGE fitting of the surface brightness profile and the 1-dimensional fittings to the r-band mass-to-light ratio distribution $\Upsilon(x', y')$ for all galaxies. Table 6.5 shows the MGE parameters of the surface brightness and stellar mass distribution, including central luminosity intensity L_j, width σ_j (standard deviation), axis ratio q_j, central mass density M_j and relative position angle of each Gaussian only for NGC 680 ψ_j.

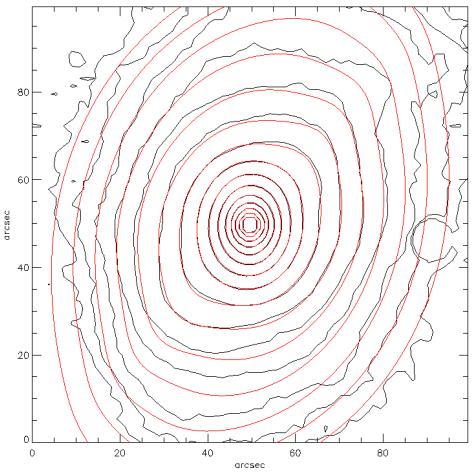

(a) Contour map of NGC 680

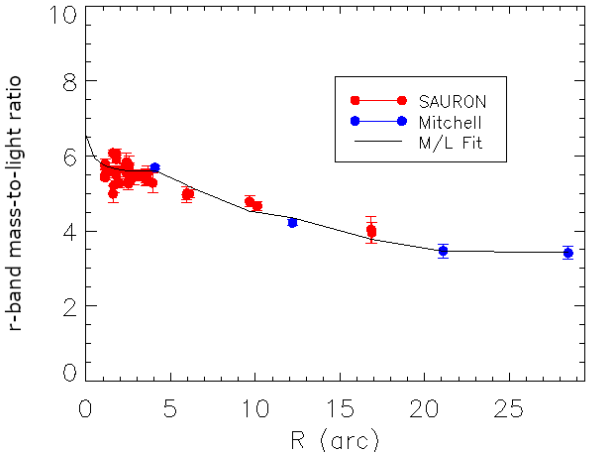

(b) Υ_r of NGC 680

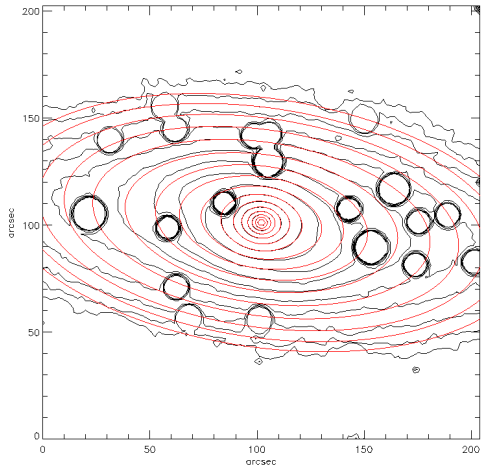

(c) Contour map of NGC 1023

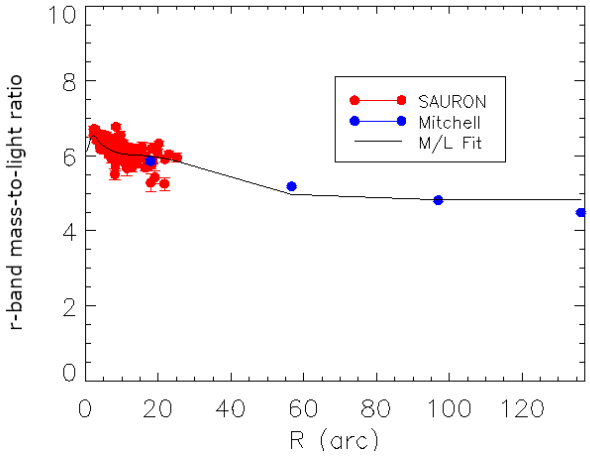

(d) Υ_r of NGC 1023

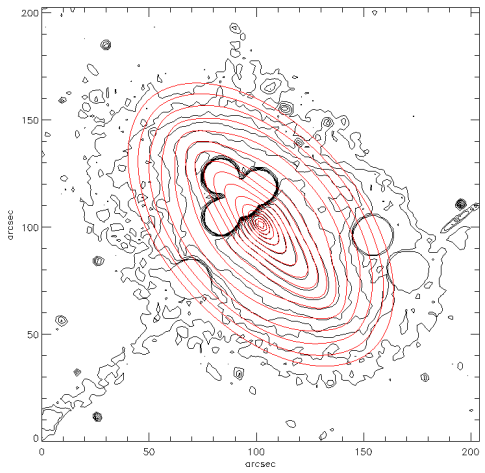

(e) Contour map of NGC 2685

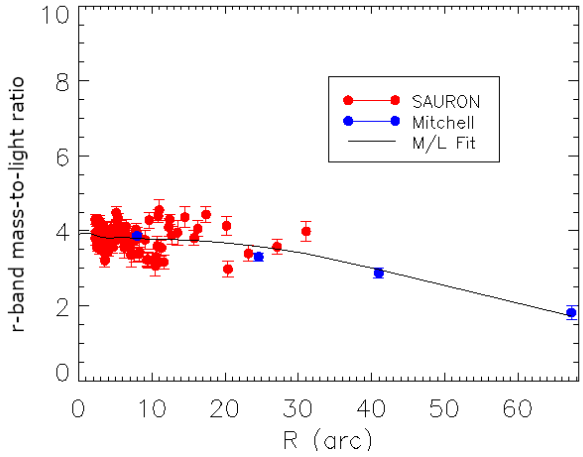

(f) Υ_r of NGC 2685

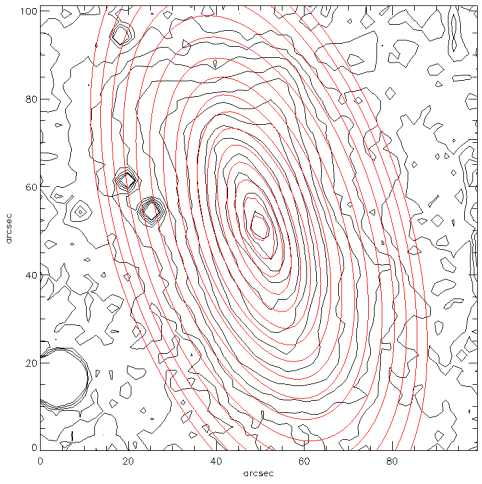

(g) Contour map of NGC 2764

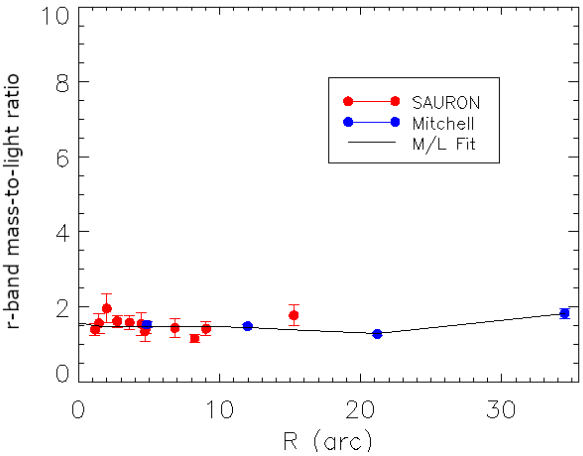

(h) Υ_r of NGC 2764

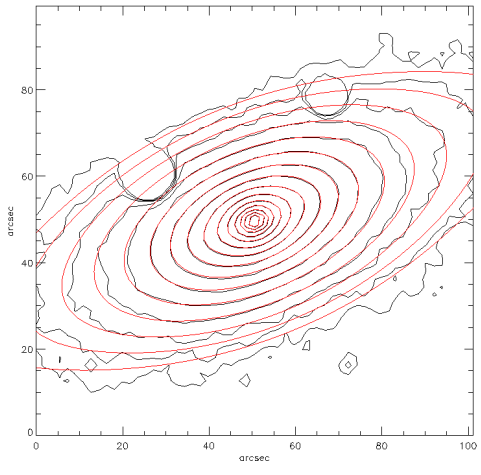

(i) Contour map of NGC 3522

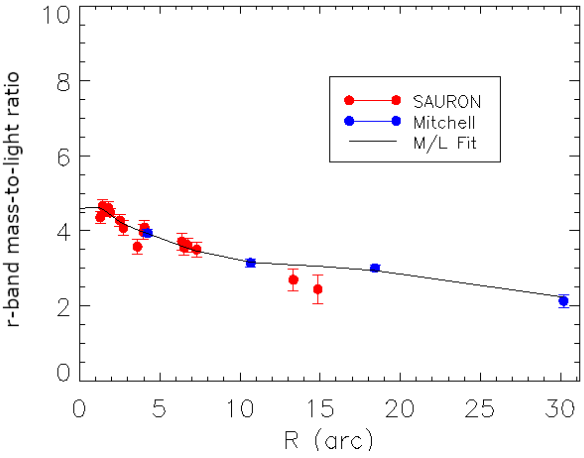

(j) Υ_r of NGC 3522

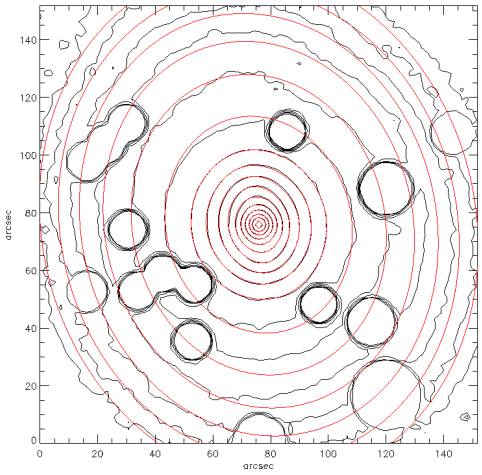

(k) Contour map of NGC 4203

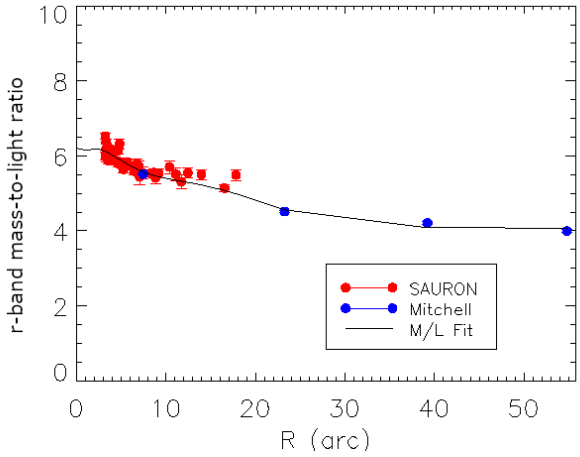

(l) Υ_r of NGC 4203

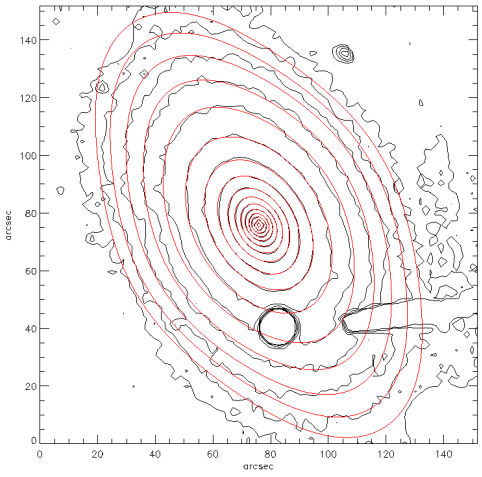

(m) Contour map of NGC 5582

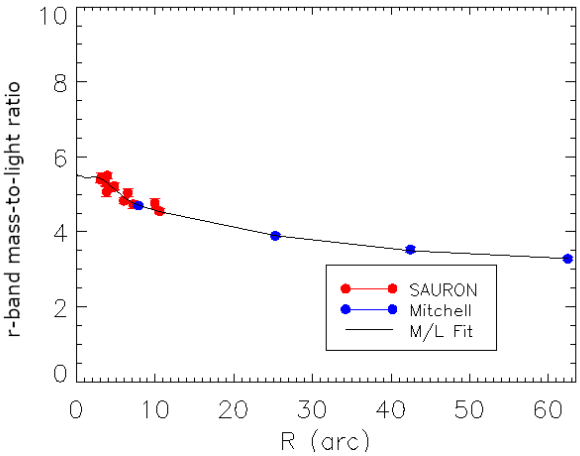

(n) Υ_r of NGC 5582

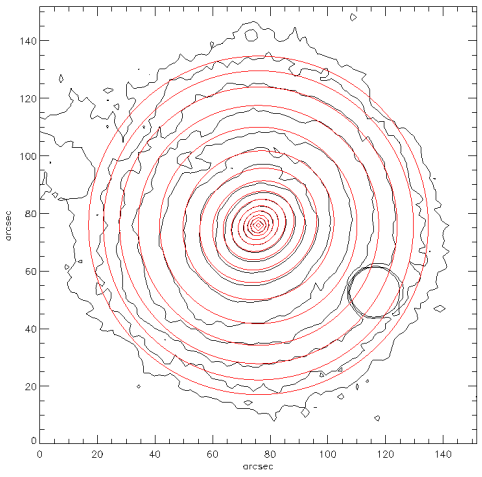

(o) Contour map of NGC 5631

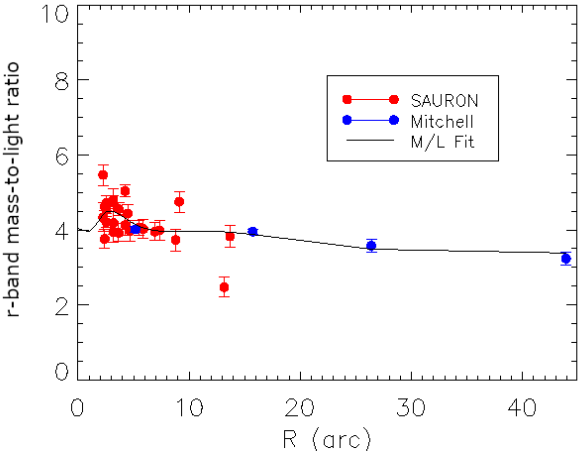

(p) Υ_r of NGC 5631

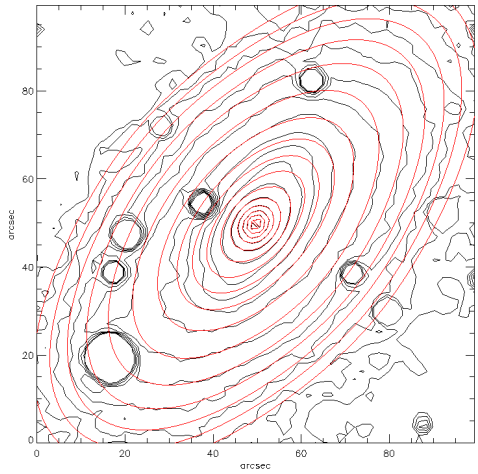

(q) Contour map of NGC 6798

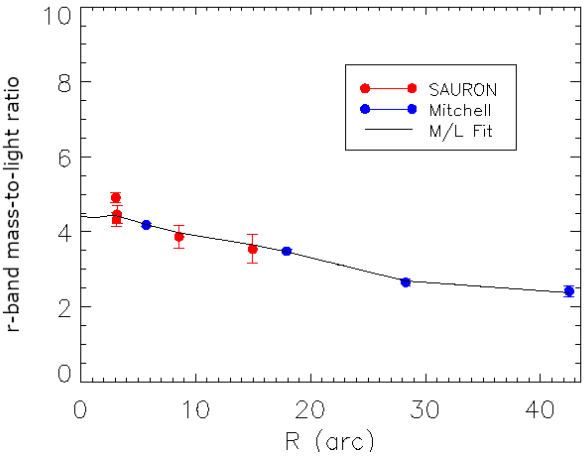

(r) Υ_r of NGC 6798

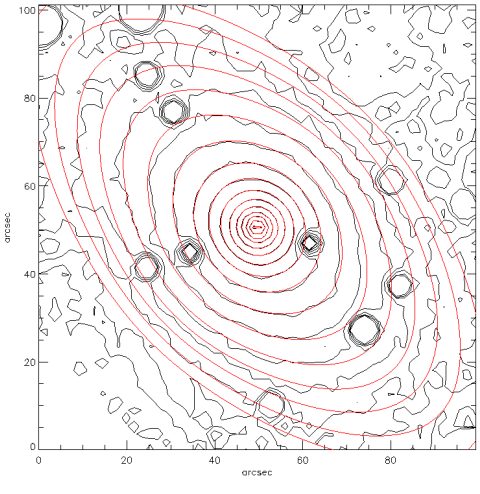

(s) Contour map of UGC 03960

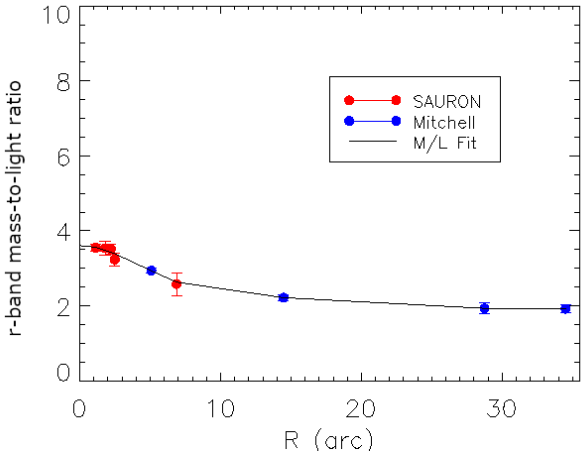

(t) Υ_r of UGC 03960

Figure 6.8: Left: The surface brightness contours (black) and its MGE model (red). Foreground stars are masked in the image. Right: The r-band mass-to-light ratio. The red dots are data from Poci et al. (2017) and the blue dots are data from Boardman et al. (2017); the solid line is the best fitting Υ.

Galaxy	j	$L_j(\mathrm{L}_\odot/\mathrm{pc}^2)$	σ_j (arcsec)	q_j	$M_j(\mathrm{M}_\odot/\mathrm{pc}^2)$	$\psi_j(^\circ)$
	1	1156.58	0.25800	0.78540	17603.04	-30.00
	2	6126.21	0.59817	0.89077	37755.57	-30.00
	3	1412.26	1.09693	0.61895	1.41	7.82
NGC 680	4	3779.23	1.20486	0.91512	32301.89	-24.36
	5	1547.05	2.04657	0.99990	1605.07	-0.01
	6	978.39	2.80364	0.69142	11469.52	-0.89
	7	735.31	5.33008	0.78026	1960.83	-6.05
	8	75.11	8.41520	0.56310	1755.87	30.00
	9	106.88	11.00219	0.99990	566.59	-0.75
	10	82.02	13.27689	0.54616	0.08	-30.00
	11	23.77	26.12805	0.78434	0.02	30.00
	12	50.12	31.77651	0.56890	243.38	-25.49
	1	16306.87	0.75647	0.78560	87673.39	
	2	10815.33	1.60448	0.86584	75676.20	
	3	5234.06	3.53124	0.83321	34464.11	
NGC 1023	4	2134.50	7.48736	0.80103	12727.27	
	5	835.37	19.89070	0.58097	5512.77	
	6	309.76	50.43351	0.46734	1495.29	
	1	3352.88	0.62174	0.74221	12562.72	
	2	4205.54	1.59578	0.49139	18334.12	
	3	424.58	2.42846	0.99990	0.42	
NGC 2685	4	1687.04	3.33709	0.43096	7270.42	
	5	212.92	6.47909	0.99990	0.21	
	6	1054.43	6.56803	0.36612	4695.01	
	7	488.86	19.04572	0.27513	2126.71	
	8	106.75	31.26491	0.58728	158.83	

Galaxy	j	$L_j(\mathrm{L}_\odot/\mathrm{pc}^2)$	σ_j (arcsec)	q_j	$M_j(\mathrm{M}_\odot/\mathrm{pc}^2)$	$\psi_j(^\circ)$
NGC 2764	1	443.95	0.47110	0.89710	773.32	
	2	675.20	1.13043	0.96622	1057.72	
	3	365.31	5.49309	0.38997	434.70	
	4	168.43	9.85028	0.27302	603.21	
	5	224.41	13.18530	0.43023	15.26	
	6	39.05	24.37662	0.49756	104.19	
NGC 3522	1	4248.58	0.46580	0.99866	18457.75	
	2	2675.56	1.02574	0.62610	14095.84	
	3	1351.80	1.79349	0.73379	5771.59	
	4	502.43	3.64760	0.76576	2483.96	
	5	90.96	5.54363	0.32530	199.02	
	6	202.74	9.25535	0.55984	675.62	
	7	51.21	19.04030	0.54919	193.86	
	8	11.86	35.45227	0.36580	0.01	
	9	2.54	91.58851	0.16573	0.00	
NGC 4203	1	6942.93	0.48545	0.96083	44590.58	
	2	7702.94	1.02305	0.93006	45509.91	
	3	3503.09	2.03714	0.94590	23083.96	
	4	2596.83	3.26032	0.99990	16569.52	
	5	757.37	7.86818	0.64494	4299.56	
	6	575.68	10.33409	0.93968	3214.23	
	7	143.33	38.41405	0.83391	584.09	
NGC 5582	1	6143.40	0.52906	0.78262	34768.39	
	2	3583.28	1.16920	0.75049	18493.49	
	3	1948.79	2.47521	0.74193	11914.86	
	4	783.66	5.03676	0.70009	3918.37	
	5	244.37	10.54088	0.66338	1135.10	
	6	33.40	22.16161	0.99990	171.90	
	7	57.98	37.57404	0.50788	185.86	

Galaxy	j	$L_j(\mathrm{L}_\odot/\mathrm{pc}^2)$	σ_j (arcsec)	q_j	$M_j(\mathrm{M}_\odot/\mathrm{pc}^2)$	$\psi_j(^\circ)$
NGC 5631	1	4248.58	0.46580	0.99866	18457.75	
	2	2675.56	1.02574	0.62610	14095.84	
	3	1351.80	1.79349	0.73379	5771.59	
	4	502.43	3.64760	0.76576	2483.96	
	5	90.96	5.54363	0.32530	199.02	
	6	202.74	9.25535	0.55984	675.62	
NGC 6798	1	2353.80	0.50865	0.94883	10711.71	
	2	1600.75	1.27743	0.67308	6262.45	
	3	1345.39	1.75292	0.80425	6410.54	
	4	577.19	3.49335	0.76825	2723.09	
	5	303.30	9.70910	0.52051	1284.22	
	6	10.03	14.24625	0.99990	71.29	
	7	65.89	26.44594	0.49854	154.24	
UGC 03960	1	1418.94	0.45277	0.99220	5113.24	
	2	1106.13	0.89960	0.90465	4100.06	
	3	604.77	1.70147	0.90085	2169.88	
	4	267.54	2.99375	0.99990	1063.41	
	5	125.87	5.99112	0.87847	312.22	
	6	21.18	11.48793	0.99990	65.03	
	7	28.61	22.91414	0.60697	50.28	
	8	1.77	75.84200	0.23047	4.72	

Table 6.5: MGE parameters of the surface brightness and stellar mass distribution for the sample galaxies. From left to right: index, central luminosity intensity, width (standard deviation), axis ratio, central mass density and relative position angle of each Gaussian only for NGC 680 to accurately describe the twist.

Appendix B: fitting two-aperture stellar kinematics

In this section, I first introduce more details of the fitting of two-aperture stellar kinematics, and then show the best-fitting stellar kinematics for all sample galaxies.

There is a mask problem of fitting two-aperture stellar kinematics. As I discussed in Chapter

5, Section 5.3.1, the central low-resolution Mitchell kinematics should be masked to avoid inconsistency between the SAURON and Mitchell data or increasing the weights of the central region. However, only three galaxies (NGC 4203, NGC 5582, NGC 6798) were masked in this way in this sample. The other galaxies (except NGC 1023) were not masked for the following reason: this mask strategy left only a few data points in the galaxy outskirts because of the low S/N and large bin size of the Mitchell stellar kinematics for these galaxies (NGC 680, NGC 2685, NGC 2764, NGC 3522, NGC 5631, UGC 03960), which causes the Mitchell stellar kinematics to be almost neglected in the fittings. NGC 1023 was not masked because it was initially forgotten in the mask list, however, this happens to provide an example for the inconsistency between the SAURON and Mitchell observational data.

The Mitchell kinematics of NGC 2685 (also NGC 3626 in Chapter 5) only cover one half of the galaxy in its field-of-view. These galaxies were observed in this way to cover the outskirts within a limited field-of-view, which hardly affects the Schwarzschild modelling. The only potential problem is that the weights of galaxy outskirts are decreased because of fewer data points.

Both problems above could be solved in the same way: manually increasing the weights (decreasing the error) of the Mitchell stellar kinematics by a constant factor. This constant should be carefully determined to fit the outskirts of Mitchell stellar kinematics and avoid over-fitting. I have not developed a proper strategy to decide this constant yet, but this will be the next step for this project.

The best-fitting stellar kinematics of all sample galaxies are shown in Figure 6.9-6.18. In each figure, the upper panel is the SAURON data and the lower panel is the Mitchell data. The rows from top to bottom are the data, model and relative residual defined as (model-data)/error) for each panel. The columns from left to right are the surface brightness, stellar velocity, velocity dispersion, the third and fourth orders of Gauss-Hermite moments.

A good fitting is decided visually with the following criteria. Firstly, there are no clear structures in the residual maps. Secondly, the modelled and observed stellar kinematics look similar. According to this standard, I summarise the fitting results for all sample galaxies as follows.

- NGC 4203, NGC 5582 and NGC 6798: well-fitted galaxies with no clear structures in the residual maps of both SAURON and Mitchell stellar kinematics. These are the galaxies

with high S/N in the outskirts and are therefore properly masked, which indicates they are described well with the current dark matter halo models.

- NGC 1023 (forgotten to be masked): The SAURON stellar kinematics are fitted well, while there are clear structures left in the central regions of the Mitchell stellar kinematics, which reflects clearly the inconsistency between two datasets. This galaxy will be well fitted by including the mask. In Section 6.2.3, I mentioned that NGC 1023 is dominated by a hot component but classified as a fast rotator, and the reason for that is clearly shown in the Mitchell residual maps. The velocity residual map indicates that the rotation (cold component) is underestimated and the velocity dispersion residual map indicates the random motion (hot component) is overestimated.

- NGC 680, NGC 2685, UGC 03960: The SAURON stellar kinematics are fitted well with no clear structures, while the residual maps of the Mitchell stellar kinematics have clear structures. These galaxies need to be centrally masked, and the weights of the Mitchell stellar kinematics need to be adjusted.

- NGC 2764, NGC 3522, NGC 5631: There are no clear structures in the SAURON residual maps, however, the modelled velocity dispersion have strong features which do not appear in the observed data, which I point out in the caption of their figures. The residual maps of the Mitchell stellar kinematics have clear structures. These galaxies also need to be masked, and the weights of the Mitchell stellar kinematics need to be adjusted. The orbit samplings for these galaxies might need to be increased to see whether the fitting of the SAURON velocity dispersion can be improved.

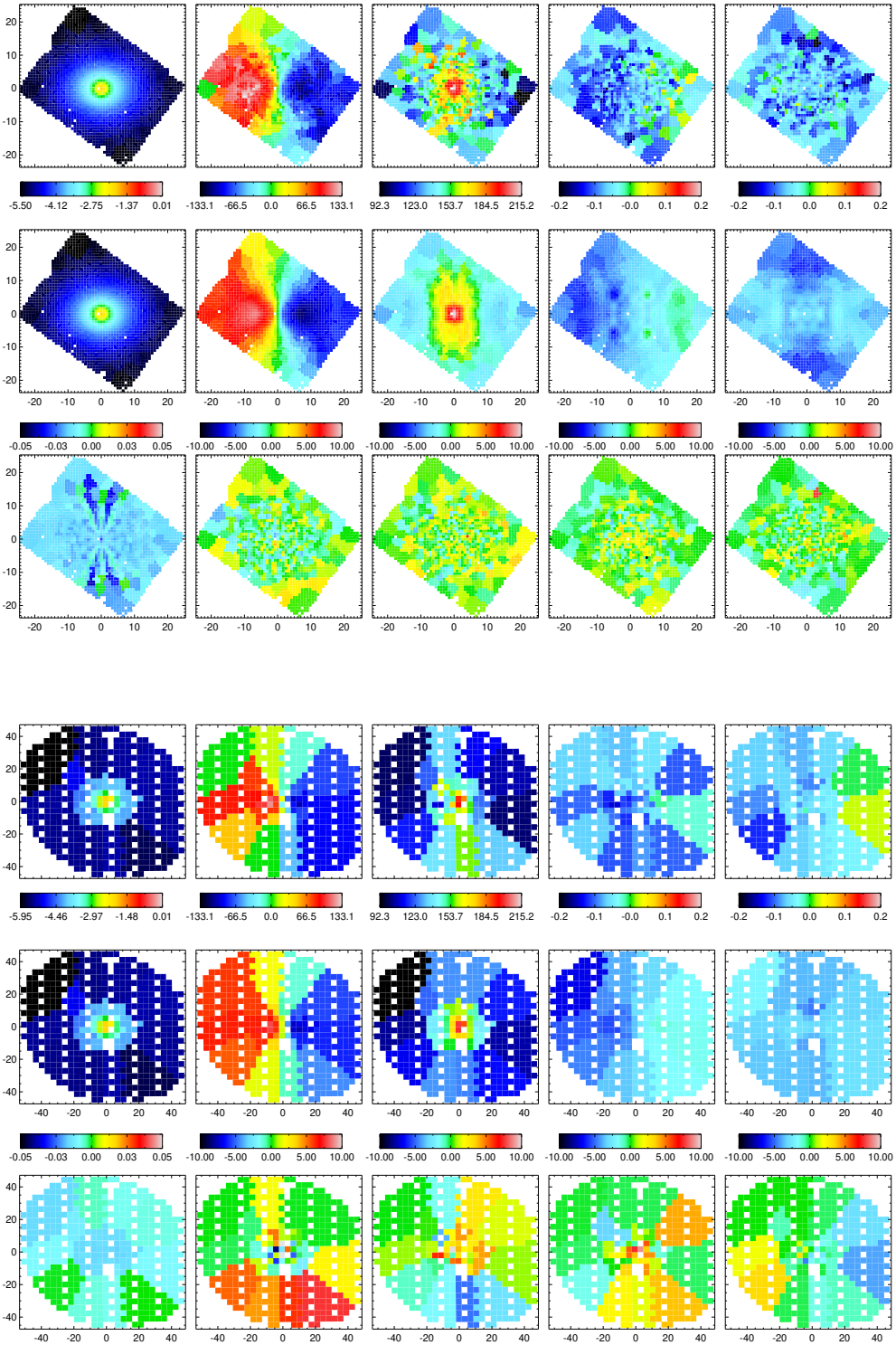

Figure 6.9: Stellar kinematics of NGC 680. The SAURON stellar kinematics are fitted well with no clear structures, while the residual maps of the Mitchell stellar kinematics have clear structures.

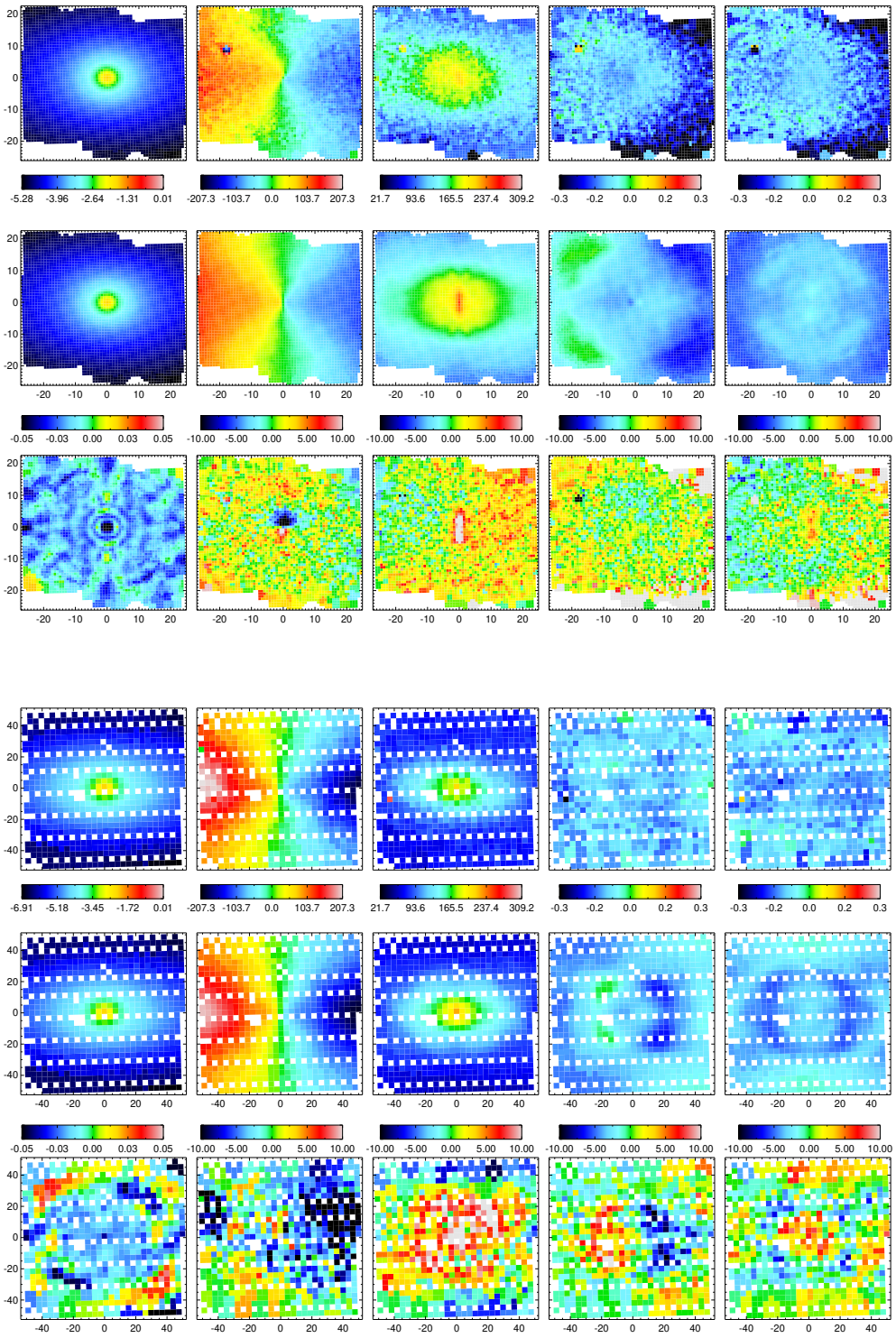

Figure 6.10: Stellar kinematics of NGC 1023. The central region of SAURON velocity was not well fitted because of an asymmetry in the data. The Mitchell stellar kinematics show that the model underestimate the circular motions (velocity) and overestimated the random motion (velocity dispersion).

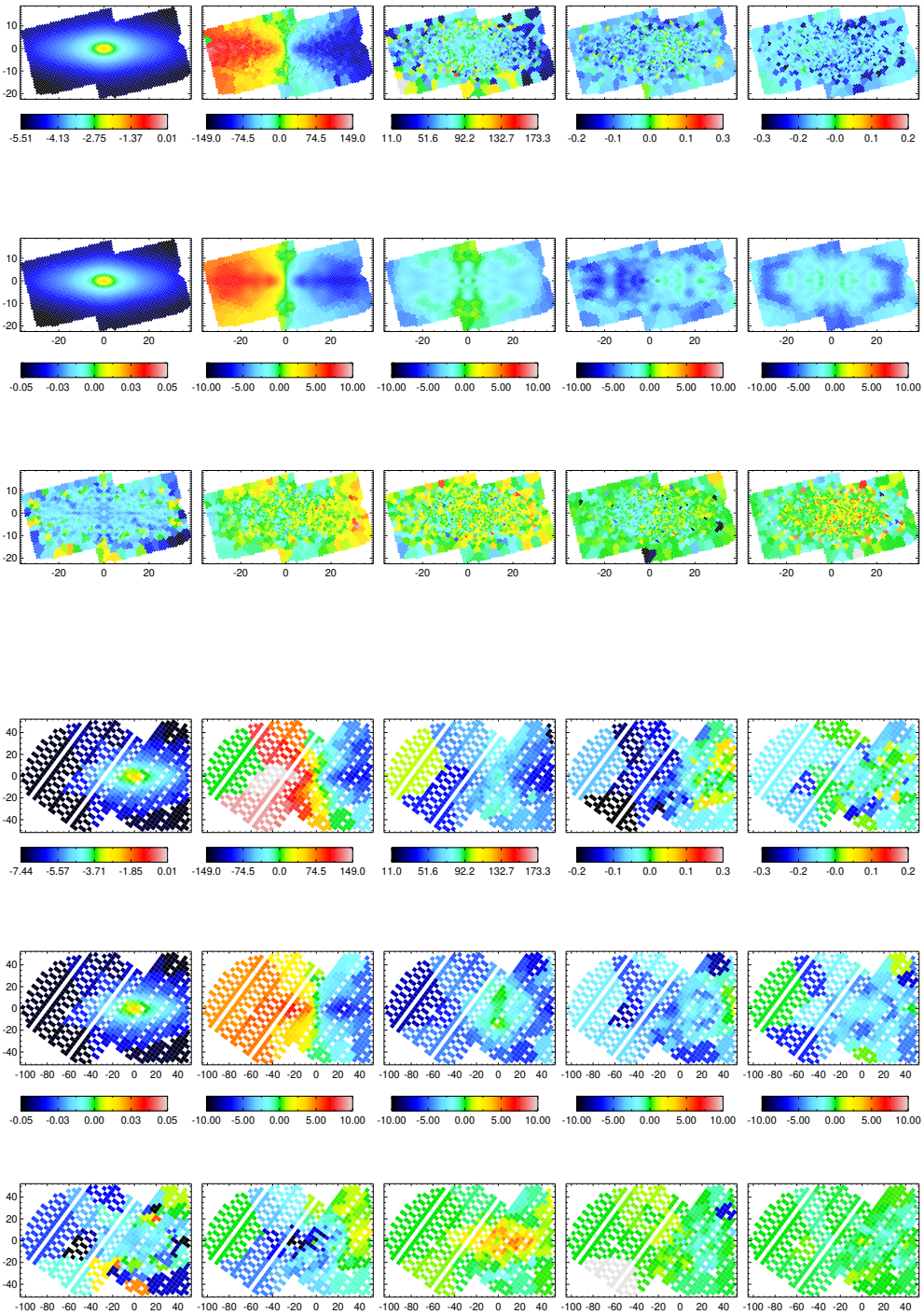

Figure 6.11: Stellar kinematics of NGC 2685. The velocity dispersion, h_3 and h_4 of both SAURON and Mitchell data are fitted well, except that the central region of Mitchell velocity dispersion needs to be masked. The Mitchell velocity is not fitted well, and the outskirts of SAURON velocity is slightly fitted unwell.

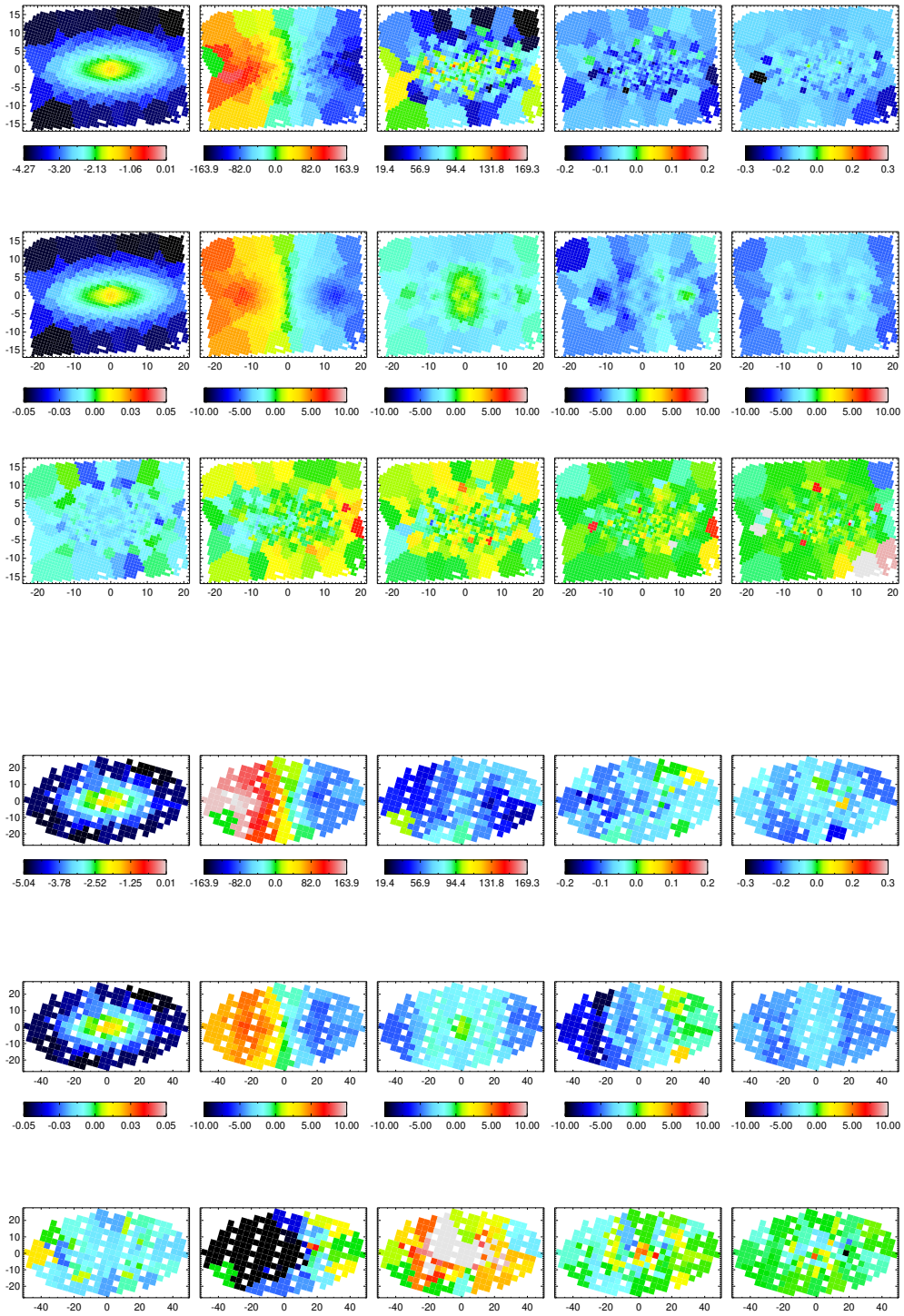

Figure 6.12: Stellar kinematics of NGC 2764. The modelled SAURON velocity dispersion has a central vertical structure, which is not clearly seen in the observed data. However, there are no clear structures in the corresponding residual map. In Section 6.2.2, I mentioned that NGC 2764 has a high dark matter fraction within 1 R_e ($f_{DM}(R_e) = 0.56$), which might be a result of this fitting problem in the SAURON stellar kinematics.

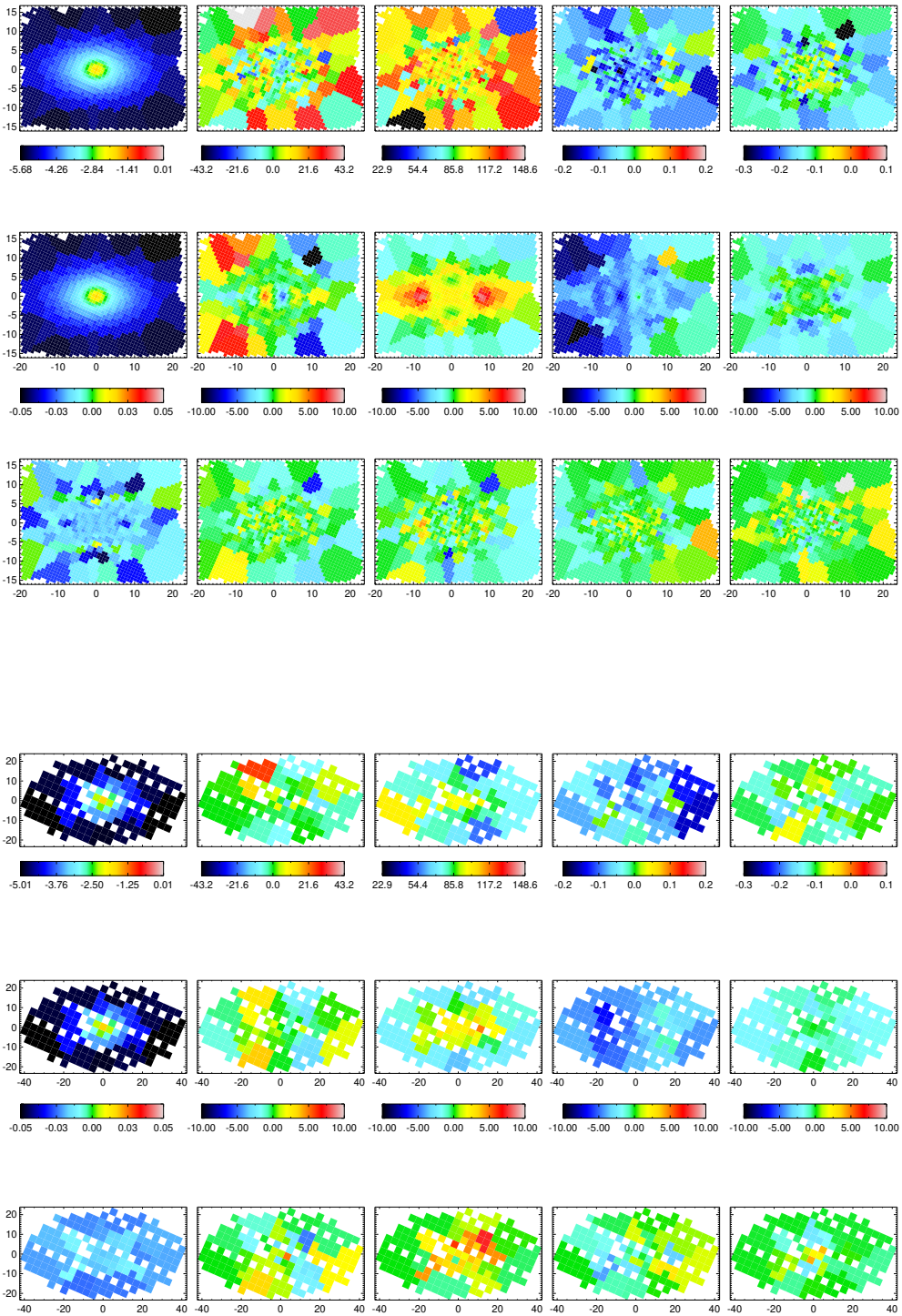

Figure 6.13: Stellar kinematics of NGC 3522. There is a two-sigma structure in the modelled SAURON velocity dispersion map, and an asymmetry in the modelled SAURON h_3 map, which cannot be seen in the observed data. However, there are no clear structures in the corresponding residual maps.

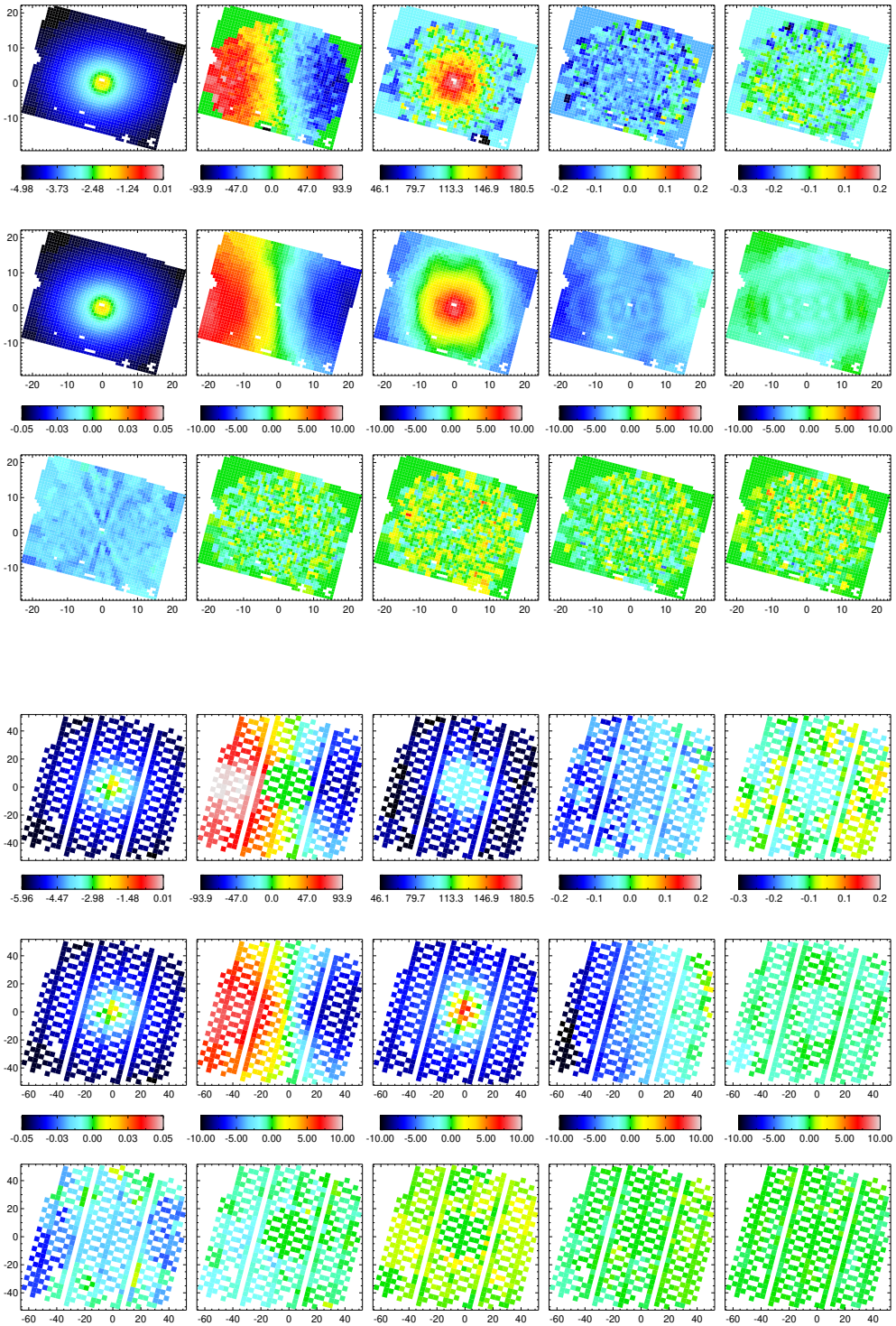

Figure 6.14: Stellar kinematics of NGC 4203. This galaxy is well fitted with no clear structures in the residual maps of both datasets.

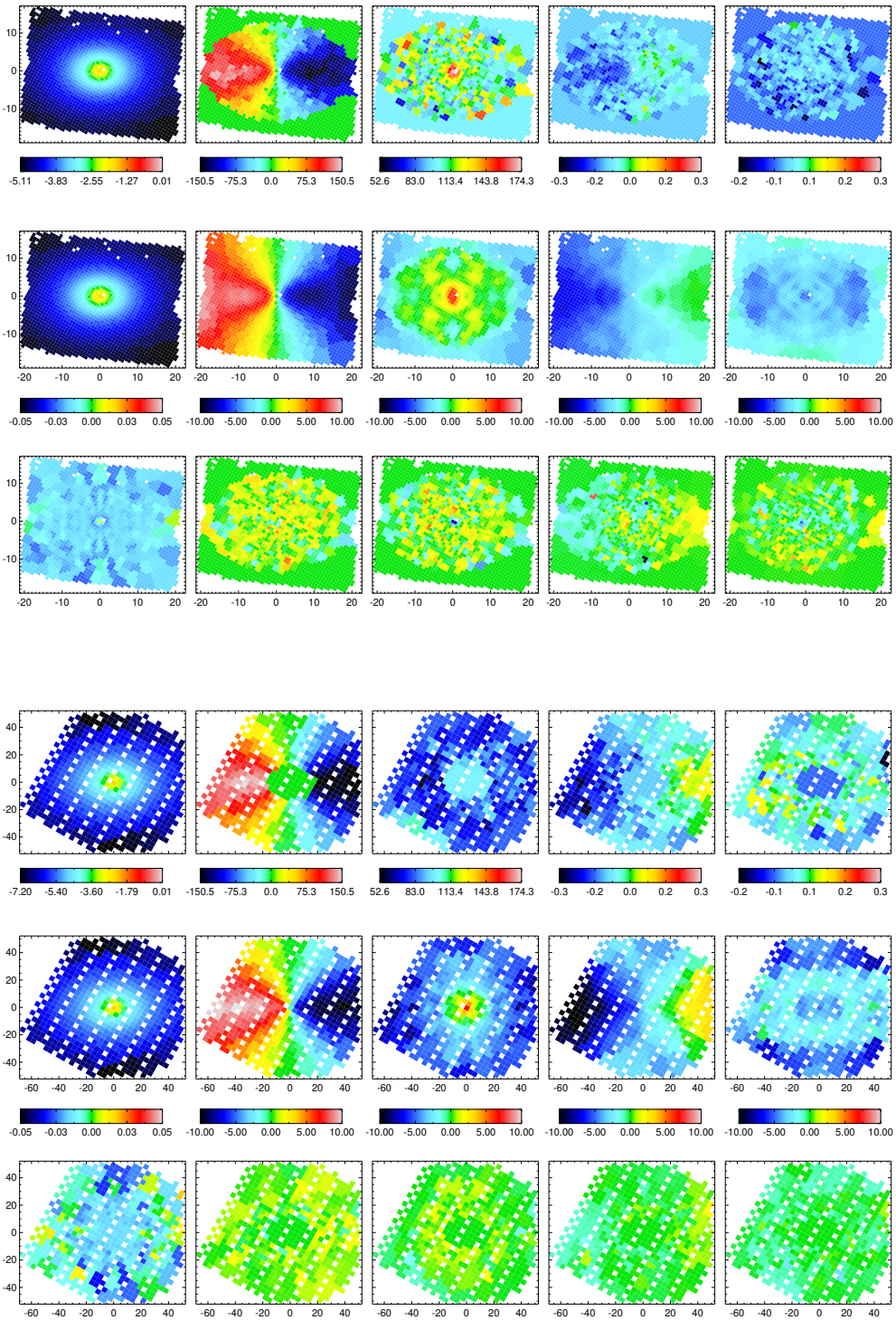

Figure 6.15: Stellar kinematics of NGC 5582. This galaxy is well fitted with no clear structures in the residual maps of both datasets.

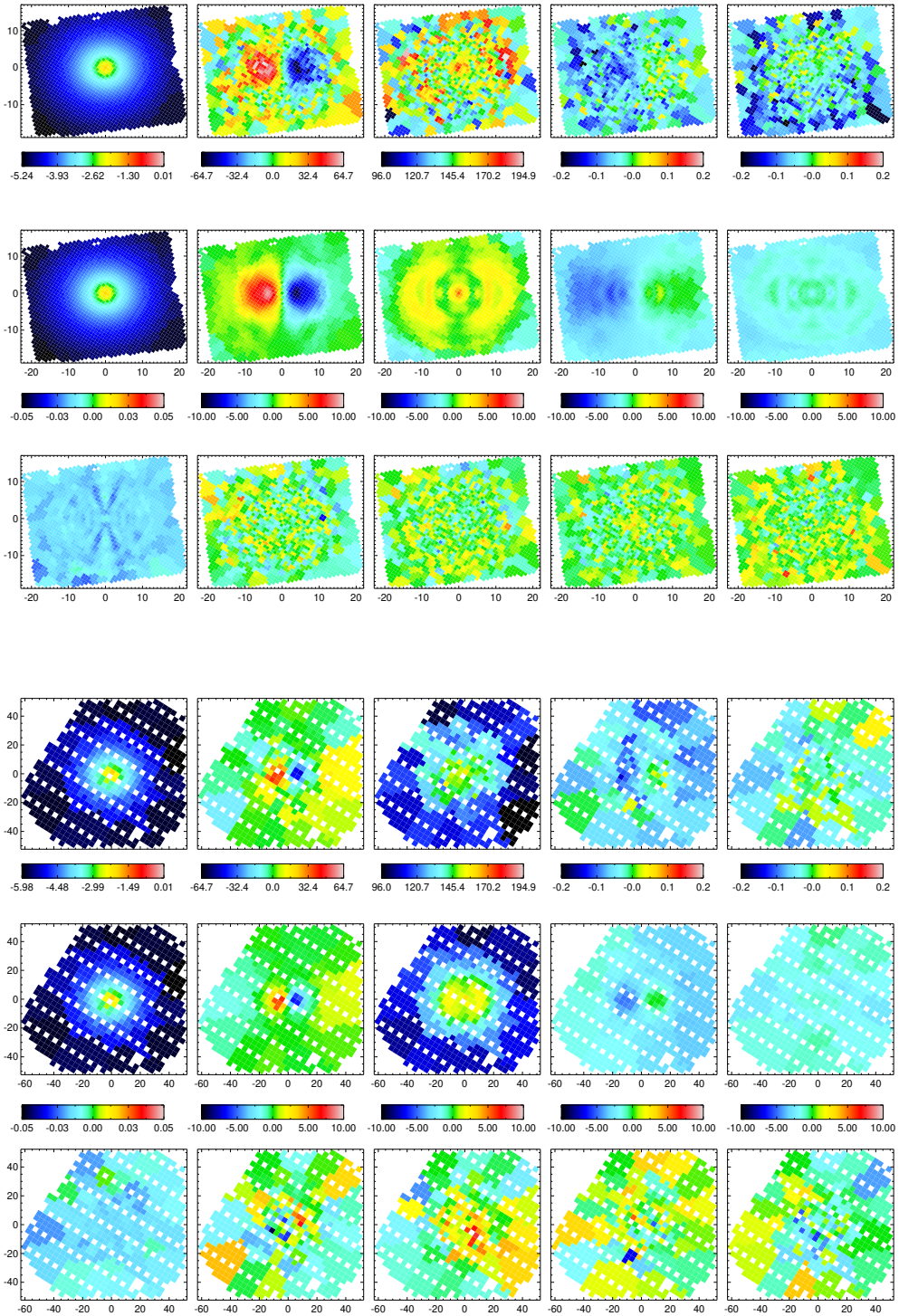

Figure 6.16: Stellar kinematics of NGC 5631. There is a clear structure in the modelled SAURON velocity dispersion but not in the observed one. The corresponding residual map shows no structures.

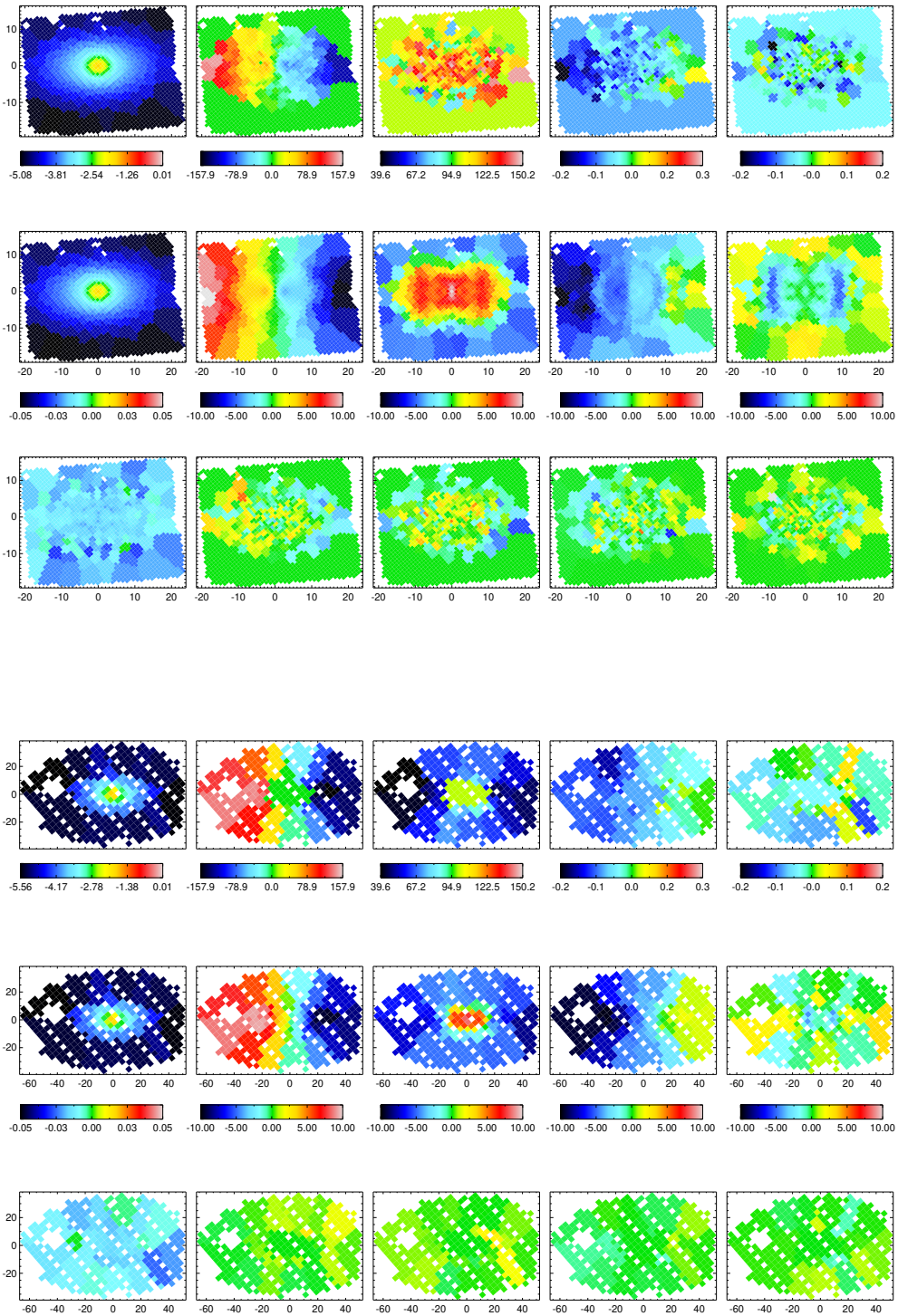

Figure 6.17: Stellar kinematics of NGC 6798. This galaxy is well fitted with no clear structures in the residual maps of both datasets.

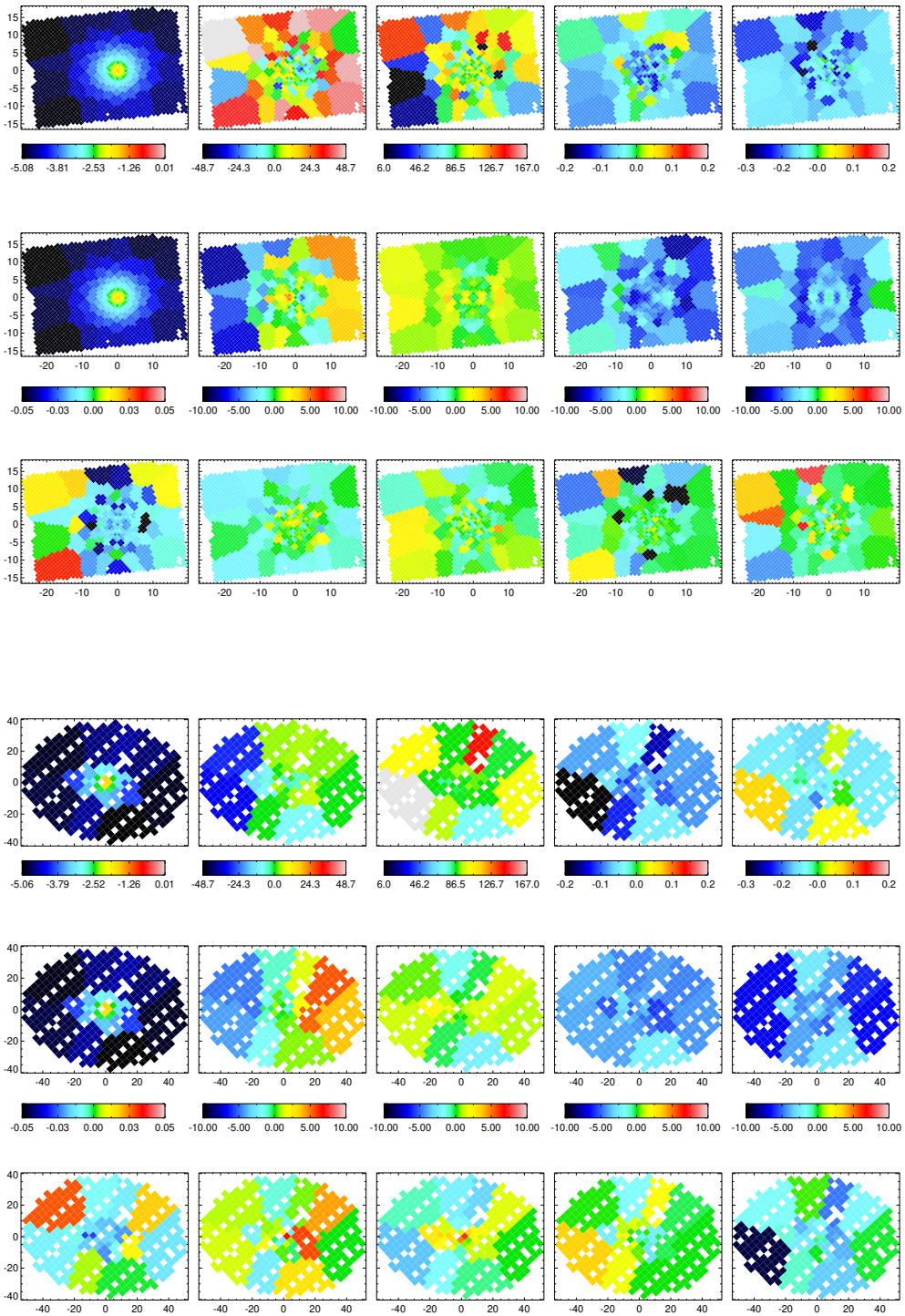

Figure 6.18: Stellar kinematics of UGC 03960. The SAURON stellar kinematics are fitted well, but the model hardly reproduce the structures in the Mitchell stellar kinematics, possibly because of the low S/N of Mitchell data for this galaxy.

7

Summary and future work

The picture of galaxy formation and evolution is not fully clear yet, and there are many important processes in galaxy evolution remain to be ambiguous, such as the process of galaxy quenching and the co-evolution of baryonic and dark matter in galaxies. Galaxy mass distribution, as one of the most fundamental properties of galaxies, is a key to the study of these processes.

One important way to explore galaxy mass distribution is to make use of galaxy kinematics, including stellar and gaseous kinematics in analytical and numerical dynamic models. In recent decades, the appearance of various IFU surveys, such as the SAURON (de Zeeuw et al., 2002), Atlas^{3D} (Cappellari et al., 2011), CALIFA (Sánchez et al., 2012), SAMI (Bryant et al., 2015) and MaNGA (Bundy et al., 2014), provides spatially resolved galaxy kinematics for galaxies across the Hubble sequence. These IFU surveys also provide abundant data to build dynamical models for mapping galaxy mass distributions and therefore enhances the understanding the formation and evolution of galaxy structures.

In this thesis, I make use of stellar and gaseous kinematics to map galaxy components with dynamical models. I constructed an analytical model for a sample mainly composed of late-type galaxies from the MaNGA survey to study their mass distribution of thin discs. I also constructed dynamical models for early-type galaxies and focused on constraining their dark matter profiles. With these models, I explored several unsolved problems related to galaxy evolution, including galaxy quenching process and the core or cusp problem of dark matter. I summarise the main results in the following sections.

7.1 An analytical model to identify thin discs in galaxies

I started mapping galaxy distributions to explore galaxy morphology transformation and quenching process with analytical models using central stellar and gaseous kinematics within 1 R_e, whose major advantage is its simplicity. In Chapter 2, I presented an analytical model for disc galaxies using a thin-disc assumption. This model adopts a stellar velocity profile taken from the Evans model (Evans, 1993; Evans & de Zeeuw, 1994) and a two-component stellar velocity dispersion profile which includes a disc component and an isotropic non-disc component. I also assumed the corrected stellar velocity for asymmetric drift should match the Hα velocity which represents the circular velocity of the galaxy. I applied this model to a sample of MaNGA galaxies with regular rotating velocity fields and robust kinematic PA and inclination measurements. By parameterising the validation of each assumption, I finally classified a full sample of 393 galaxies into three kinematic types: disc-dominated galaxies which are dominated by a thin disc, non-disc-dominated galaxies with a detected, non-dominating thin disc and disc-free galaxies without a thin disc detection.

I plotted the $\lambda_{R_e} - \epsilon$ diagram (Figure 2.12) for a sub-sample of 237 galaxies which has the measurements of the spin parameter λ_{R_e} as a proxy for stellar angular momentum within R_e, and ellipticity ϵ. There is a clear dichotomy for the disc-dominated and disc-free galaxies in this diagram, which indicates this analytical model is successful in detecting thin discs in galaxies and classifying galaxies based on their intrinsic dynamics: almost all the disc-dominated galaxies occupy an upper position with $\lambda_{R_e} > 0.5$; about one half of the disc-free galaxies have $\lambda_{R_e} < 0.5$. The non-disc-dominated galaxies lie between disc-dominated and disc-free galaxies as an intermediate state.

Following Binney & Tremaine (2008), I obtained the dynamical mass density and the total

dynamical mass within MaNGA coverage for disc-dominated galaxies. I compared the dynamical mass with the stellar mass (Goddard et al., 2017) obtained with the Kroupa IMF (Kroupa, 2001), and showed that the difference between these two masses can be explained by including the mass of atomic and molecular gas, and a slight IMF gradient across galaxy masses is also acceptable. This result shows that the fraction of dark matter is negligible in galaxy centre (typically $1.5R_e$) for disc-dominated galaxies.

I finally studied the morphologies of all three kinematic types using the Deep Learning catalogue (Domínguez Sánchez et al., 2018). As expected, disc-dominated galaxies are composed of spiral galaxies and a small fraction of S0 galaxies, and disc-free galaxies are mainly elliptical and S0 galaxies. I noticed a dichotomy of the kinematic types of S0 galaxies, therefore, I studied a number of properties and found that the star formation rate and the molecular gas fraction is the major difference between disc-dominated and disc-free S0s. With references to disc-dominated spirals and disc-free ellipticals, I further explained this dichotomy with a quenching scenario that the clear depletion of molecular gas accounts for the quenching process in these S0 galaxies, which is consistent with the conclusion of Zhang et al. (2019). I also proposed that the quenching of S0 galaxies leads to an in-situ evolution of the kinematic state in galaxies, which will finally dissolve the disc-structures.

7.2 Orbit-based models with combined stellar and cold gas kinematics

Although the analytical model was successfully applied to MaNGA disc galaxies, its disadvantages (e.g. the model is descriptive and difficult to include a bulge) make me switch to numerical dynamical models to map galaxy mass distribution with high accuracy. I also found that it was difficult to measure dark matter fractions with central kinematics within 1 R_e, and therefore realised the importance of including extended tracers to constrain dark matter profiles. In Chapter 4, I developed orbit-based models which include combined stellar and cold gas kinematics to map the mass distribution of galaxies. In this method, the stellar kinematics are modelled with the Schwarzschild orbit-superposition technique (Schwarzschild, 1979) following the triaxial implementation described in van den Bosch et al. (2008) and Zhu et al. (2018c) as I previously described in Chapter 3. The cold gas (H I) is assumed to be an axisymmetric thin disc (ring) which sits in the equatorial plane of the galaxy aligned with the

stellar disc, and moves on circular orbits with a circular velocity which directly reflects the gravitational potential of the galaxy, with a negligible velocity dispersion. The surface brightness distribution is modelled with the MGE method (Emsellem et al., 1994; Cappellari, 2002). I also adopted a radially variable mass-to-light ratio profile to fit the stellar mass distribution obtained from the IFU observation and introduced a parameter to represent the variation of the stellar mass scale due to the choice of IMF. The dark matter halo follows a gNFW profile with four parameters including the scale density, the scale radius, the inner and outer slopes. The mass of a central supermassive black hole is also considered.

I applied this method to early-type galaxy NGC 2974, which has stellar kinematics obtained from the SAURON survey (de Zeeuw et al., 2002) and H I observation presented in Weijmans et al. (2008). I adopted the r-band image taken from the Pan-STARRS Survey (Chambers et al., 2016) and a compatible mass-to-light ratio mass distribution presented in (Poci et al., 2017, Υ-maps available on Atlas3D website). I adopted 5 free parameters in this methods (the IMF factor, three parameters of the dark matter halo profile with a fixed outer slope and the black hole mass) and finally generated 4,259 dynamical models for NGC 2974.

The main results are as following: NGC 2974 prefers an IMF which generate a total stellar mass close to the Salpeter IMF (Salpeter, 1955). It also prefers a shallow cuspy dark matter halo profile with the inner slope of $0.6^{+0.2}_{-0.3}$. The dark matter fraction is 7% within $1R_{\rm e}$, which is consistent with previous research Cappellari et al. (2013a), and rises to 66% at $5R_{\rm e}$. Including the cold gas kinematics significantly improves the ability of constraining the dark matter profile: there are more than 1000 models within the $1-\sigma$ confidence level of the Schwarzschild modelling with stellar kinematics only, only less than 5% of these models are remained within the $1-\sigma$ confidence level of this method using combined stellar and cold gas kinematics. The inner slope of the dark matter profile and the dark matter fraction are also much better constrained, which the former cannot be constrained without the cold gas kinematics and the relative uncertainty of the latter are is significantly reduced to 10% within $5R_{\rm e}$. These results show that extended cold gas kinematics are crucial to understand dark matter halo profiles.

7.3 Generalised orbit-based models to misaligned stellar and cold gas discs

The orbit-based models described in Chapter 4 are only applicable to galaxies with aligned stellar and gaseous discs, however, the stellar and gas discs are not always aligned in galaxies. I therefore generalised the orbit-based model to galaxies with misaligned stellar and cold gas discs for a wider application in Chapter 5. I first introduced the geometry of stellar and gas discs. There are two cases for the deprojection of stellar and gas discs in 3-dimensional space considering the direction of inclination: both discs rotate in the same direction, and two discs rotate in different directions. I then discussed the behaviour of the gas disc in the gravitational potential. I adopted a Cartesian coordinate system that the stellar disc sit in the xy-plane with its rotation axis aligned with the z-axis. I assumed gas moves circularly within the gas disc, and it reaches a local dynamical equilibrium along the R-direction in the stellar cylindrical coordinates. Therefore, the circular velocity of the gas is decided in a given gravitational potential, which can be obtained with the MGE method. I also made a theoretical deduction for the uncertainty of modelling the cold gas kinematics, whose prediction is consistent with the result obtained with the perturbation method in Chapter 4.

I applied this generalised model to early-type galaxy NGC 3626, which has two-aperture stellar kinematics, consisting of the central SAURON observation within 1 R_e and the extended Mitchell observation out to 3 R_e. It also possesses a very extended H I disc out to 10 R_e misaligned with the stellar disc observed with the Westerbork Synthesis Radio Telescope. I adopted the same mass model technique as that in Chapter 4. There are 6 free parameters, including 5 parameters inherited from Chapter 4 (the IMF factor, three parameters of the dark matter halo profile with a fixed outer slope and the black hole mass) and the inclination of the stellar disc, while the inclination of the gas disc and the PA of both discs are decided with the method described in Chapter 2, Section 2.3.2. I increased the total number of orbits to recover the more spatially extended stellar kinematics.

The results are preliminary and promising: the SAURON stellar kinematics are well recovered, while between the modelled and observational Mitchell kinematics and H I velocity field. Considering that the SAURON stellar kinematics are well fitted, the following measurements regarding the central mass distribution are robust: NGC 3626 has an inclination of 72° and an IMF producing a total mass 1.4 times more stellar mass than the Salpeter IMF. The incon-

sistent fitting in the galaxy outskirts is caused by not providing enough degrees of freedom to adjust the shape of the dark matter halo: the turning point and outer slope are fixed, or the gNFW halo model is not suitable for this galaxy. This problem can be solved by freeing the fixed parameter of this gNFW dark matter profile, or adopting other halo models, such as the Einasto profile. Although the measurements regarding the dark matter halo are not robust with the current model setting, further exploration is now possible thanks to extended stellar and H I coverage. This will provide an opportunity to determine the overall shape of dark matter profiles in galaxies and even distinguish different dark matter halo models, and therefore improve our understanding of the nature of dark matter.

7.4 Dark matter fractions of early-type galaxies

I modelled two early-type galaxies NGC 2974 and NGC 3626 which have extended cold gas kinematics, however, extended cold gas discs are not available for all galaxies. I therefore modelled 10 other early-type galaxies with two-aperture SAURON and Mitchell stellar kinematics with the Schwarzschild orbit-superposition technique in Chapter 6. With the SAURON stellar kinematics within 1 R_e and Mitchell stellar kinematics extended to 3 R_e, I explored the dark matter profiles and stellar orbit distributions of galaxies in a wider mass range, and therefore investigated the formation of galaxy components and the co-evolution of baryonic and dark matter. The mass model in this chapter was built in the same way as described in Chapter 5, and I also included the same 6 free parameters (the inclination, the IMF factor, three parameters of the dark matter halo profile with a fixed outer slope and the black hole mass) in the model.

The results show that the current model setting is able to recover the stellar kinematics for some galaxies, although the Mitchell stellar kinematics of other galaxies are not well fitted mainly because of low S/N and large bin size in the outskirts. The best-fitting results show a wide range of IMF factor and a universal preference of a cusp dark matter halo, although a core model is not ruled out for several galaxies. There are no clear correlations with stellar mass for both the IMF factor and dark matter inner slope.

The dark matter profiles show the importance of including extended stellar kinematics to model the dark matter halo, and also support the conclusion of Chapter 5 that the shape of the dark matter halo will be better determined with cold gas kinematics extended to 10 R_e.

The dark matter fraction within 1 R_e is usually between 10%-30%, and it rises up to 40%-70% at 3 R_e. I found no clear trends between the dark matter fraction and stellar mass, which is inconsistent with the result of Cappellari et al. (2013b), because they adopted an NFW halo model with central stellar kinematics within 1 R_e. The dark matter profiles show again the importance of including extended stellar kinematics to model dark matter haloes, and support the conclusion of Chapter 5 that the shape of dark matter haloes could be better determined with cold gas kinematics extended to 10 R_e.

I found several typical orbital structures in stellar orbit distributions, which suggests they formed in different processes. I also obtained the fractions of different stellar orbit components and studied their relations with the spin parameter λ_{R_e}. The result shows that λ_{R_e} is in general a good indicator to distinguish fast and slow rotators, but it might have difficulty to identify fast-rotating galaxies with strong counter-rotating components.

7.5 Discussion

In this section, I would like to share some thoughts about modelling stellar and gaseous kinematics with analytical and dynamical models in this thesis.

The development of computing sources makes it possible to model a large sample of galaxies obtained from galaxy surveys (e.g. Zhu et al., 2018a; Li et al., 2017). However, analytical models still have their unique advantages other than simplicity. Analytical models have a higher tolerance of poor data quality than dynamical models. Analytical models can describe galaxies approximately with relatively low resolution or S/N data at a lower cost to reach statistical conclusions, while it is difficult or not worthy for dynamical models. This property makes analytical models useful in dealing with large amounts of galaxy survey data.

The nature of dark matter haloes is not determined yet, and one important reason is the contradictive measurements of the slopes of the dark matter halo at galaxy central, which is called the cusp or core problem. I would like to emphasise here that the current measurements in literature have adopted various assumptions, some of which might not describe the baryonic matter well and therefore affect the measurements of dark matter properties. For example, some measurements of the dark matter inner slope do not consider the gradient of mass-to-light ratio, which leads to systematic bias of the results. The IMF gradient within a galaxy has not yet been considered in the measurements of the dark matter profile even in this thesis,

although such a gradient has been discovered in massive early-type galaxies (La Barbera et al., 2019).

The importance of including extended kinematic data in constraining dark matter profiles has been clearly shown in this thesis. Very extended H I velocity fields out to 10 R_e can not only provide accurate measurements for dark matter fractions and dark matter inner slopes, but also constrain the overall shape of dark matter haloes and even distinguish different halo models. Since the detection rate of H I in field early-type galaxies is about 40% (Serra et al., 2012), and H I exists in the form of regularly rotating discs or rings in half of the early-types galaxies with H I detection (Morganti et al., 2006; Oosterloo et al., 2007, 2010), the application of extended H I discs in dynamical modelling is promising. For galaxies without H I discs, stellar kinematics extended to 3 R_e can also improve the measurements of dark matter, which points out a direction to increase the galaxy coverage for future IFU surveys.

The deprojection of misaligned discs is also an important issue for the study of misaligned galaxies. The misalignment between stellar and gaseous discs is usually measured with the difference between their position angles ΔPA, however, this observable might not be a good indicator of the misalignment in 3-dimensional space. Instead of ΔPA, the misalignment is better described by the angle between the rotating axis of two discs. This angle is not only related to ΔPA, but also affected by the inclinations of two discs with two possibilities as I described in Chapter 5. This deprojection problem makes it imprudent to tell whether the misalignment is large or small just by ΔPA, therefore should be paid more attention to when seeking for the connection between the misalignment of galaxy discs and other galaxy properties.

7.6 Future work

I have investigated galaxies of various morphology using stellar and gaseous kinematics in this thesis, and have shown that the combination of stellar and gaseous kinematics in dynamical modelling is powerful in exploring galaxy evolution by mapping galaxy mass distributions. This thesis has discussed several topics, including the link between galaxy kinematics and quenching, the cusp / core problem of dark matter haloes, and possible links between dark and baryonic matter. However, further work is still needed to establish more decisive conclusions.

I have proposed that the deficiency of molecular gas causes galaxy quenching in-situ and finally changes the kinematic state of galaxies by analysing the disc structures in lenticular

galaxies. However, the sample size of lenticular galaxies is limited. Besides, the analytical model adopted cannot include a bulge or quantify the strength of the disc structures. Therefore, this scenario needs further evidences to support or disprove it. I would like to keep working on this scenario with a large sample of lenticular galaxies, which had better be modelled with dynamical models for a detailed study of their structures to reveal their link with molecular gas, star formation rate or other galaxy properties.

I also would like to expand my work by applying the orbit-based models developed in these thesis to a large sample of observed nearby galaxies to continue the research of galaxy mass distributions and galaxy dynamics. This method has shown its advantage in breaking the degeneracies between different properties, such as the IMF, the inner slope of dark matter haloes and the mass of the central black hole, therefore, a further study is promising. Recent IFU surveys and upcoming H I surveys (e.g. WEAVE-APERTIF; Hess et al., 2020) will significantly increase the number of galaxies with combined stellar and cold gas kinematics. Besides, gaseous kinematics within $1R_e$ (e.g. Hα and molecular gas) with high spatial resolution can also play the role of H I kinematics in this methods, for high spatial resolution gaseous kinematics can also constrain the galaxy gravitational potential and break the degeneracies at galaxy centre by providing accurate black hole and stellar masses (Tsukui, 2019).

As I have mentioned, although multiple dynamical modelling techniques have provided plenty of measurements of galaxy properties such as the inner slopes of dark matter haloes and dark matter fractions, the conflicting results make the conclusion indecisive because of various assumptions adopted in literature. Therefore, I also plan to carry out a systematic evaluation of dynamical models to enhance the understanding of these methods and interpret previous results correctly. This evaluation needs simulated galaxies with properties known beforehand, which can be provided by cosmology simulations (e.g. Schaye et al., 2015; Nelson et al., 2019). By making mock observations of different resolutions, I will be able to apply multiple dynamical models to simulated galaxies covering various galaxies morphologies, dark matter haloes and stellar properties, e.g. stellar ages, metallicities and mass-to-light ratios.

Finally, I would like to further develop the dynamical modelling technique. Although IFU observations provide spatially resolved spectra for galaxies, the stellar and dynamical mass distributions are obtained with the stellar population synthesis techniques and dynamical modelling techniques, respectively, which makes it difficult to reveal the spatial distribution of

a particular single stellar population (SSP). From an orbit-superposition view of point, an SSP with similar origin probably stays on similar orbits during evolution, therefore, a chemo-dynamical model which combines the orbit-superposition technique and stellar population synthesis techniques can finally disclosure the intrinsic connections between SSPs and galaxy orbits, and significantly broaden our knowledge of galaxy formation and evolution process.

Bibliography

Abadi, M. G., Moore, B., & Bower, R. G. 1999, Monthly Notices of the Royal Astronomical Society, 308, 947

Abazajian, K. N. et al. 2009, The Astrophysical Journal Supplement Series, 182, 543

Aguado, D. S. et al. 2019, The Astrophysical Journal Supplement Series, 240, 23

Alabi, A. B. et al. 2017, Monthly Notices of the Royal Astronomical Society, 468, 3949

Alam, S. et al. 2017, Monthly Notices of the Royal Astronomical Society, 470, 2617

Amendt, P., & Cuddeford, P. 1991, The Astrophysical Journal, 368, 79

Andredakis, Y., & Sanders, R. 1994, Monthly Notices of the Royal Astronomical Society, 267, 283

Argudo-Fernández, M. et al. 2015, Astronomy & Astrophysics, 578, A110

Baade, W. 1944, The Astrophysical Journal, 100, 137

Bacon, R. et al. 2010, in Ground-based and Airborne Instrumentation for Astronomy III, Vol. 7735, International Society for Optics and Photonics, 773508

Bacon, R. et al. 2001, Monthly Notices of the Royal Astronomical Society, 326, 23

Baggett, W., Baggett, S., & Anderson, K. 1998, The Astronomical Journal, 116, 1626

Bahcall, J. N., & Soneira, R. M. 1980, The Astrophysical Journal Supplement Series, 44, 73

Baillard, A. et al. 2011, Astronomy & Astrophysics, 532, A74

Balcells, M., & Quinn, P. 1990, The Astrophysical Journal, 361, 381

Baldry, I. K., Glazebrook, K., Brinkmann, J., Ivezić, Ž., Lupton, R. H., Nichol, R. C., & Szalay, A. S. 2004, The Astrophysical Journal, 600, 681

Balogh, M. L., Navarro, J. F., & Morris, S. L. 2000, The Astrophysical Journal, 540, 113

Bamford, S. P. et al. 2009, Monthly Notices of the Royal Astronomical Society, 393, 1324

Barnes, J. E., & Hernquist, L. 1996, The Astrophysical Journal, 471, 115

Barrera-Ballesteros, J. et al. 2015, Astronomy & Astrophysics, 582, A21

Barrera-Ballesteros, J. K. et al. 2020, Monthly Notices of the Royal Astronomical Society, 492, 2651

Bartko, H. et al. 2010, The Astrophysical Journal, 708, 834

Batsleer, P., & Dejonghe, H. 1995, Astronomy and Astrophysics, 294, 693

Battaglia, G., Helmi, A., Tolstoy, E., Irwin, M., Hill, V., & Jablonka, P. 2008, The Astrophysical Journal Letters, 681, L13

Begeman, K. 1989, Astronomy and Astrophysics, 223, 47

Bell, E. F., & de Jong, R. S. 2001, The Astrophysical Journal, 550, 212

Bell, E. F. et al. 2004, The Astrophysical Journal, 608, 752

Bellstedt, S. et al. 2018, Monthly Notices of the Royal Astronomical Society, 476, 4543

Bender, R., Surma, P., Doebereiner, S., Moellenhoff, C., & Madejsky, R. 1989, Astronomy and Astrophysics, 217, 35

Bershady, M. A., Verheijen, M. A., Swaters, R. A., Andersen, D. R., Westfall, K. B., & Martinsson, T. 2010a, The Astrophysical Journal, 716, 198

Bershady, M. A., Verheijen, M. A., Westfall, K. B., Andersen, D. R., Swaters, R. A., & Martinsson, T. 2010b, The Astrophysical Journal, 716, 234

Bertola, F., Buson, L., & Zeilinger, W. 1992, The Astrophysical Journal, 401, L79

Bertola, F., Pizzella, A., Persic, M., & Salucci, P. 1993, The Astrophysical Journal, 416, L45

Binney, J., Davies, R. L., & Illingworth, G. D. 1990, The Astrophysical Journal, 361, 78

Binney, J., & Mamon, G. A. 1982, Monthly Notices of the Royal Astronomical Society, 200, 361

Binney, J., & Tremaine, S. 2008, Princeton University Press, Princeton, NJ, 23, 389

Bissantz, N., Debattista, V. P., & Gerhard, O. 2004, The Astrophysical Journal Letters, 601, L155

Blanton, M. R. et al. 2017, The Astronomical Journal, 154, 28

Blanton, M. R., Kazin, E., Muna, D., Weaver, B. A., & Price-Whelan, A. 2011, The Astronomical Journal, 142, 31

Blumenthal, G. R., Faber, S., Primack, J. R., & Rees, M. J. 1984, Nature, 311, 517

Boardman, N. F. et al. 2017, Monthly Notices of the Royal Astronomical Society, 471, 4005

——. 2016, Monthly Notices of the Royal Astronomical Society, 460, 3029

Bosma, A. 1981, The Astronomical Journal, 86, 1825

Brammer, G. et al. 2009, The Astrophysical Journal Letters, 706, L173

Breddels, M. A., Helmi, A., van den Bosch, R., van de Ven, G., & Battaglia, G. 2013, Monthly Notices of the Royal Astronomical Society, 433, 3173

Bruzual, A., et al. 1983, The Astrophysical Journal, 273, 105

Bruzual, G., & Charlot, S. 2003, Monthly Notices of the Royal Astronomical Society, 344, 1000

Bryant, J. et al. 2019, Monthly Notices of the Royal Astronomical Society, 483, 458

——. 2015, Monthly Notices of the Royal Astronomical Society, 447, 2857

Bundy, K. et al. 2014, The Astrophysical Journal, 798, 7

Cappellari, M. 2002, Monthly Notices of the Royal Astronomical Society, 333, 400

——. 2008, Monthly Notices of the Royal Astronomical Society, 390, 71

Cappellari, M. et al. 2006, Monthly Notices of the Royal Astronomical Society, 366, 1126

Cappellari, M., & Copin, Y. 2003, Monthly Notices of the Royal Astronomical Society, 342, 345

Cappellari, M., & Emsellem, E. 2004, Publications of the Astronomical Society of the Pacific, 116, 138

Cappellari, M. et al. 2007, Monthly Notices of the Royal Astronomical Society, 379, 418

——. 2011, Monthly Notices of the Royal Astronomical Society, 413, 813

——. 2012, Nature, 484, 485

——. 2013a, Monthly Notices of the Royal Astronomical Society, 432, 1862

——. 2015, The Astrophysical Journal Letters, 804, L21

——. 2013b, Monthly Notices of the Royal Astronomical Society, 432, 1709

Cattaneo, A., Dekel, A., Devriendt, J., Guiderdoni, B., & Blaizot, J. 2006, Monthly Notices of the Royal Astronomical Society, 370, 1651

Cenarro, A., Gorgas, J., Vazdekis, A., Cardiel, N., & Peletier, R. 2003, Monthly Notices of the Royal Astronomical Society, 339, L12

Chabrier, G. 2003, Publications of the Astronomical Society of the Pacific, 115, 763

Chambers, K. C. et al. 2016, arXiv preprint arXiv:1612.05560

Chanamé, J., Kleyna, J., & van der Marel, R. 2008, The Astrophysical Journal, 682, 841

Cinzano, P., & van der Marel, R. P. 1994, Monthly Notices of the Royal Astronomical Society, 270, 325

Cole, S. et al. 2001, Monthly Notices of the Royal Astronomical Society, 326, 255

Colless, M. et al. 2001, Monthly Notices of the Royal Astronomical Society, 328, 1039

Conselice, C. J. 2003, The Astrophysical Journal Supplement Series, 147, 1

Copin, Y., Cretton, N., & Emsellem, E. 2004, Astronomy & Astrophysics, 415, 889

Cortés, J. R., Kenney, J. D., & Hardy, E. 2008, The Astrophysical Journal, 683, 78

Côté, P. et al. 2001, The Astrophysical Journal, 559, 828

Couture, J., & Hardy, E. 1988, The Astronomical Journal, 96, 867

Cretton, N., de Zeeuw, P. T., van der Marel, R. P., & Rix, H.-W. 1999, The Astrophysical Journal Supplement Series, 124, 383

Cretton, N., Rix, H.-W., & de Zeeuw, P. T. 2000, The Astrophysical Journal, 536, 319

Crocker, A. F., Bureau, M., Young, L. M., & Combes, F. 2011, Monthly Notices of the Royal Astronomical Society, 410, 1197

Crook, A. C., Huchra, J. P., Martimbeau, N., Masters, K. L., Jarrett, T., & Macri, L. M. 2007, The Astrophysical Journal, 655, 790

Dabringhausen, J., Kroupa, P., & Baumgardt, H. 2009, Monthly Notices of the Royal Astronomical Society, 394, 1529

Das, P., Gerhard, O., Mendez, R. H., Teodorescu, A. M., & de Lorenzi, F. 2011, Monthly Notices of the Royal Astronomical Society, 415, 1244

Davé, R. 2008, Monthly Notices of the Royal Astronomical Society, 385, 147

Davis, M., Efstathiou, G., Frenk, C. S., & White, S. D. 1985, The Astrophysical Journal, 292, 371

Davis, T. A. et al. 2011, Monthly Notices of the Royal Astronomical Society, 417, 882

Dawson, K. S. et al. 2012, The Astronomical Journal, 145, 10

de Blok, W., McGaugh, S. S., & Rubin, V. C. 2001, The Astronomical Journal, 122, 2396

de Bruyne, V., Dejonghe, H., Pizzella, A., Bernardi, M., & Zeilinger, W. 2001, The Astrophysical Journal, 546, 903

de Jong, J. T. et al. 2015, Astronomy & Astrophysics, 582, A62

de Jong, R. S. 1996, Astronomy and Astrophysics Supplement Series, 118, 557

de Lorenzi, F., Debattista, V. P., Gerhard, O., & Sambhus, N. 2007, Monthly Notices of the Royal Astronomical Society, 376, 71

de Lorenzi, F. et al. 2009, Monthly Notices of the Royal Astronomical Society, 395, 76

de Lorenzi, F., Gerhard, O., Saglia, R. P., Sambhus, N., Debattista, V. P., Pannella, M., & Méndez, R. H. 2008, Monthly Notices of the Royal Astronomical Society, 385, 1729

de Naray, R. K., McGaugh, S. S., & de Blok, W. 2008, The Astrophysical Journal, 676, 920

de Paz, A. G. et al. 2007, The Astrophysical Journal Supplement Series, 173, 185

de Vaucouleurs, G. 1953, Monthly Notices of the Royal Astronomical Society, 113, 134

——. 1959, in Astrophysik iv: Sternsysteme/astrophysics iv: Stellar systems (Springer), 275–310

de Vaucouleurs, G., de Vaucouleurs, A., Corwin, H. G., Buta, R. J., Paturel, G., & Fouqué, P. 1991, in Third Reference Catalogue of Bright Galaxies (Springer), 1–632

de Vaucouleurs, G., de Vaucouleurs, A., & Corwin, J. 1976, in Second reference catalogue of bright galaxies, Vol. 1976, p. Austin: University of Texas Press., Vol. 1976

de Vaucouleurs, G. H., de Vaucouleurs, A., & Shapley, H. 1964, University of Texas Monographs in Astronomy, Austin: University of Texas Press,| c1964

de Zeeuw, P. et al. 2002, Monthly Notices of the Royal Astronomical Society, 329, 513

Dehnen, W. 1995, Monthly Notices of the Royal Astronomical Society, 274, 919

Dehnen, W., & Gerhard, O. E. 1994, Monthly Notices of the Royal Astronomical Society, 268, 1019

Dejonghe, H. 1986, Physics reports, 133, 217

——. 1989, The Astrophysical Journal, 343, 113

Dekel, A., & Birnboim, Y. 2006, Monthly notices of the royal astronomical society, 368, 2

Dekel, A., Ceverino, D., et al. 2009, The Astrophysical Journal, 703, 785

Doi, M. et al. 2010, The Astronomical Journal, 139, 1628

Domínguez Sánchez, H., Huertas-Company, M., Bernardi, M., Tuccillo, D., & Fischer, J. 2018, Monthly Notices of the Royal Astronomical Society, 476, 3661

Drory, N. et al. 2015, The Astronomical Journal, 149, 77

Dubinski, J., & Carlberg, R. 1991, The Astrophysical Journal, 378, 496

Duckworth, C., Tojeiro, R., & Kraljic, K. 2020, Monthly Notices of the Royal Astronomical Society, 492, 1869

Eddington, A. 1916, Monthly Notices of the Royal Astronomical Society, 76, 572

Einasto, J. 1965, Trudy Astrofizicheskogo Instituta Alma-Ata, 5, 87

Elmegreen, B. G., & Elmegreen, D. M. 2005, The Astrophysical Journal, 627, 632

Emsellem, E. et al. 2011, Monthly Notices of the Royal Astronomical Society, 414, 888

——. 2007, Monthly Notices of the Royal Astronomical Society, 379, 401

——. 2004, Monthly Notices of the Royal Astronomical Society, 352, 721

Emsellem, E., Dejonghe, H., & Bacon, R. 1999, Monthly Notices of the Royal Astronomical Society, 303, 495

Emsellem, E., Monnet, G., & Bacon, R. 1994, Astronomy and Astrophysics, 285, 723

Etherington, J., & Thomas, D. 2015, Monthly Notices of the Royal Astronomical Society, 451, 660

Evans, N. 1993, Monthly Notices of the Royal Astronomical Society, 260, 191

——. 1994, Monthly Notices of the Royal Astronomical Society, 267, 333

Evans, N., & de Zeeuw, P. 1994, Monthly Notices of the Royal Astronomical Society, 271, 202

Faber, S., & Jackson, R. E. 1976, The Astrophysical Journal, 204, 668

Faber, S. et al. 2007, The Astrophysical Journal, 665, 265

Fabian, A. 2012, Annual Review of Astronomy and Astrophysics, 50, 455

Falcón-Barroso, J., Sánchez-Blázquez, P., Vazdekis, A., Ricciardelli, E., Cardiel, N., Cenarro, A., Gorgas, J., & Peletier, R. 2011, Astronomy & Astrophysics, 532, A95

Falcón-Barroso, J. et al. 2019, Astronomy & Astrophysics, 632, A59

Fischer, J., Domínguez Sánchez, H., & Bernardi, M. 2018, Monthly Notices of the Royal Astronomical Society, 483, 2057

Fisher, D. B., & Drory, N. 2008, The Astronomical Journal, 136, 773

Forestell, A. D., & Gebhardt, K. 2010, The Astrophysical Journal, 716, 370

Freeman, K. C. 1970, The Astrophysical Journal, 160, 811

Fricke, W. 1951, Astronomische Nachrichten, 280, 193

Gebhardt, K. et al. 2000, The Astronomical Journal, 119, 1157

Genzel, R. et al. 2008, The Astrophysical Journal, 687, 59

Gerhard, O., Kronawitter, A., Saglia, R., & Bender, R. 2001, The Astronomical Journal, 121, 1936

Gerhard, O. E. 1991, Monthly Notices of the Royal Astronomical Society, 250, 812

——. 1993, Monthly Notices of the Royal Astronomical Society, 265, 213

Ghigna, S., Moore, B., Governato, F., Lake, G., Quinn, T., & Stadel, J. 2000, The Astrophysical Journal, 544, 616

Giovanelli, R. et al. 2005, The astronomical journal, 130, 2598

Goddard, D. et al. 2017, Monthly Notices of the Royal Astronomical Society, 466, 4731

Graham, M. T. et al. 2018, Monthly Notices of the Royal Astronomical Society, 477, 4711

Gravet, R. et al. 2015, The Astrophysical Journal Supplement Series, 221, 8

Grillo, C. 2012, The Astrophysical Journal Letters, 747, L15

Grogin, N. A. et al. 2011, The Astrophysical Journal Supplement Series, 197, 35

Gunawardhana, M. L. et al. 2011, Monthly Notices of the Royal Astronomical Society, 415, 1647

Gunn, J. E., & Gott III, J. R. 1972, The Astrophysical Journal, 176, 1

Gunn, J. E. et al. 2006, The Astronomical Journal, 131, 2332

Hart, R. E. et al. 2016, Monthly Notices of the Royal Astronomical Society, 461, 3663

Hernquist, L., & Barnes, J. E. 1991, Nature, 354, 210

Hess, K., Falcon-Barroso, J., Ascasibar, Y., Perez-Martin, I., Serra, P., Weijmans, A., & Team, W.-A. 2020, AAS, 459

Hill, G. J. et al. 2008, in Ground-based and Airborne Instrumentation for Astronomy II, Vol. 7014, International Society for Optics and Photonics, 701470

Hopkins, P. F. et al. 2010, The Astrophysical Journal, 715, 202

Hopkins, P. F., Kereš, D., Oñorbe, J., Faucher-Giguère, C.-A., Quataert, E., Murray, N., & Bullock, J. S. 2014, Monthly Notices of the Royal Astronomical Society, 445, 581

Hubble, E. 1936, Realm of the Nebulae, by EP Hubble. New Haven: Yale University Press, 1936. ISBN 9780300025002

Hubble, E. P. 1926, The Astrophysical Journal, 64

Huchra, J., Davis, M., Latham, D., & Tonry, J. 1983, The Astrophysical Journal Supplement Series, 52, 89

Huchra, J. P. et al. 2012, The Astrophysical Journal Supplement Series, 199, 26

Hui, X., & Ford, H. 1993, in Symposium-International Astronomical Union, Vol. 155, Cambridge University Press, 533–540

Hunt, J. A., & Kawata, D. 2013, Monthly Notices of the Royal Astronomical Society, 430, 1928

Hunter, C. 1975, The Astronomical Journal, 80, 783

Hunter, C., & Qian, E. 1993, Monthly Notices of the Royal Astronomical Society, 262, 401

Jarvis, B., & Freeman, K. 1985, The Astrophysical Journal, 295, 314

Jeans, J. 1915, Monthly Notices of the Royal Astronomical Society, 76, 70

Jeans, J. H. 1919, Philosophical Transactions of the Royal Society of London. Series A, Containing Papers of a Mathematical or Physical Character, 218, 157

——. 1922, Monthly Notices of the Royal Astronomical Society, 82, 122

Jin, Y., Zhu, L., Long, R., Mao, S., Wang, L., & van de Ven, G. 2019, Monthly Notices of the Royal Astronomical Society, 491, 1690

Kannappan, S., & Fabricant, D. 2001, The Astronomical Journal, 121, 140

Kent, S. 1984, The Astrophysical Journal Supplement Series, 56, 105

Kent, S. M. 1985, The Astrophysical Journal Supplement Series, 59, 115

Kim, D.-W., Jura, M., Guhathakurta, P., Knapp, G., & van Gorkom, J. 1988, The Astrophysical Journal, 330, 684

Kimm, T. et al. 2009, Monthly Notices of the Royal Astronomical Society, 394, 1131

Klypin, A., Kravtsov, A. V., Bullock, J. S., & Primack, J. R. 2001, The Astrophysical Journal, 554, 903

Koribalski, B. 2002, in Seeing Through the Dust: The Detection of HI and the Exploration of the ISM in Galaxies, Vol. 276, 72

Kormendy, J. 1977, The Astrophysical Journal, 217, 406

Kormendy, J., & Bender, R. 1996, The Astrophysical Journal Letters, 464, L119

Kormendy, J., Fisher, D. B., Cornell, M. E., & Bender, R. 2009, The Astrophysical Journal Supplement Series, 182, 216

Kormendy, J., & Illingworth, G. 1982, The Astrophysical Journal, 256, 460

Kormendy, J., & Kennicutt Jr, R. C. 2004, Annu. Rev. Astron. Astrophys., 42, 603

Krajnovic, D., Cappellari, M., de Zeeuw, P. T., & Copin, Y. 2006, Monthly Notices of the Royal Astronomical Society, 366, 787

Krajnović, D., Cappellari, M., Emsellem, E., McDermid, R. M., & de Zeeuw, P. T. 2005, Monthly Notices of the Royal Astronomical Society, 357, 1113

Kregel, M., van der Kruit, P. C., & de Grijs, R. 2002, Monthly Notices of the Royal Astronomical Society, 334, 646

Kroupa, P. 2001, Monthly Notices of the Royal Astronomical Society, 322, 231

Kuijken, K. 1995, The Astrophysical Journal, 446, 194

Kuijken, K., & Dubinski, J. 1995, Monthly Notices of the Royal Astronomical Society, 277, 1341

Kuijken, K., Fisher, D., & Merrifield, M. R. 1996, Monthly Notices of the Royal Astronomical Society, 283, 543

La Barbera, F. et al. 2019, Monthly Notices of the Royal Astronomical Society, 489, 4090

Larson, R., Tinsley, B., & Caldwell, C. N. 1980, The Astrophysical Journal, 237, 692

Leroy, A. K. et al. 2009, The Astronomical Journal, 137, 4670

Leroy, A. K., Walter, F., Brinks, E., Bigiel, F., de Blok, W., Madore, B., & Thornley, M. 2008, The astronomical journal, 136, 2782

Leung, G. Y. et al. 2018, Monthly Notices of the Royal Astronomical Society, 477, 254

Li, H. et al. 2017, The Astrophysical Journal, 838, 77

Li, H., Li, R., Mao, S., Xu, D., Long, R., & Emsellem, E. 2016, Monthly Notices of the Royal Astronomical Society, 455, 3680

Li, Z., Han, Z., & Zhang, F. 2007, Astronomy & Astrophysics, 464, 853

Lintott, C. J. et al. 2008, Monthly Notices of the Royal Astronomical Society, 389, 1179

Long, R., & Mao, S. 2010, Monthly Notices of the Royal Astronomical Society, 405, 301

——. 2012, Monthly Notices of the Royal Astronomical Society, 421, 2580

López-Sanjuan, C. et al. 2012, Astronomy & Astrophysics, 548, A7

Lynden-Bell, D. 1962, Monthly Notices of the Royal Astronomical Society, 123, 447

Magorrian, J. 2014, Monthly Notices of the Royal Astronomical Society, 437, 2230

——. 2019, Monthly Notices of the Royal Astronomical Society, 484, 1166

Magorrian, J., & Binney, J. 1994, Monthly Notices of the Royal Astronomical Society, 271, 949

Maia, M. A., Machado, R. S., & Willmer, C. N. 2003, The Astronomical Journal, 126, 1750

Mamon, G. A., Biviano, A., & Boué, G. 2013, Monthly Notices of the Royal Astronomical Society, 429, 3079

Maraston, C. 2005, Monthly Notices of the Royal Astronomical Society, 362, 799

Maraston, C., & Strömbäck, G. 2011, Monthly Notices of the Royal Astronomical Society, 418, 2785

Martig, M., Bournaud, F., Teyssier, R., & Dekel, A. 2009, The Astrophysical Journal, 707, 250

Martin, D. C. et al. 2007, The Astrophysical Journal Supplement Series, 173, 342

Martín-Navarro, I., Barbera, F. L., Vazdekis, A., Falcón-Barroso, J., & Ferreras, I. 2015a, Monthly Notices of the Royal Astronomical Society, 447, 1033

Martín-Navarro, I. et al. 2015b, The Astrophysical Journal Letters, 806, L31

Martinsson, T. P., Verheijen, M. A., Westfall, K. B., Bershady, M. A., Andersen, D. R., & Swaters, R. A. 2013, Astronomy & Astrophysics, 557, A131

Marzke, R., Huchra, J., & Geller, M. 1994, The Astrophysical Journal, 428, 43

Masters, K. L. et al. 2010, Monthly Notices of the Royal Astronomical Society, 405, 783

——. 2011, Monthly Notices of the Royal Astronomical Society, 411, 2026

Mayer, L., Mastropietro, C., Wadsley, J., Stadel, J., & Moore, B. 2006, Monthly Notices of the Royal Astronomical Society, 369, 1021

McCarthy, I. G., Frenk, C. S., Font, A. S., Lacey, C. G., Bower, R. G., Mitchell, N. L., Balogh, M. L., & Theuns, T. 2008, Monthly Notices of the Royal Astronomical Society, 383, 593

McGaugh, S. S., & Schombert, J. M. 2014, The Astronomical Journal, 148, 77

Méndez-Abreu, J. et al. 2017, Astronomy & Astrophysics, 598, A32

Merrifield, M. R., & Kent, S. M. 1990, The Astronomical Journal, 99, 1548

Merritt, D. 1985, The Astronomical Journal, 90, 1027

Merritt, D., & Fridman, T. 1996, The Astrophysical Journal, 460, 136

Merritt, D., Graham, A. W., Moore, B., Diemand, J., & Terzić, B. 2006, The Astronomical Journal, 132, 2685

Merritt, D., & Saha, P. 1993, The Astrophysical Journal, 409, 75

Mihos, J. C., & Hernquist, L. 1994a, The Astrophysical Journal, 425, L13

——. 1994b, The Astrophysical Journal, 431, L9

——. 1996, The Astrophysical Journal, 464, 641

Mitzkus, M., Cappellari, M., & Walcher, C. J. 2016, Monthly Notices of the Royal Astronomical Society, stw2677

Mobasher, B. et al. 2015, The Astrophysical Journal, 808, 101

Monnet, G., Bacon, R., & Emsellem, E. 1992, Astronomy and Astrophysics, 253, 366

Moore, B. 1994, Nature, 370, 629

Moore, B., Lake, G., & Katz, N. 1998, The Astrophysical Journal, 495, 139

Moore, B., Quinn, T., Governato, F., Stadel, J., & Lake, G. 1999, Monthly Notices of the Royal Astronomical Society, 310, 1147

Morgan, W. 1958, Publications of the Astronomical Society of the Pacific, 70, 364

Morgan, W., & Osterbrock, D. 1969, The Astronomical Journal, 74, 515

Morganti, L., Gerhard, O., Coccato, L., Martinez-Valpuesta, I., & Arnaboldi, M. 2013, Monthly Notices of the Royal Astronomical Society, 431, 3570

Morganti, R. et al. 2006, Monthly Notices of the Royal Astronomical Society, 371, 157

Morganti, R., Sadler, E., Oosterloo, T., Pizzella, A., & Bertola, F. 1997, The Astronomical Journal, 113, 937

Napolitano, N. et al. 2007, Proceedings of the International Astronomical Union, 3, 289

——. 2011, Monthly Notices of the Royal Astronomical Society, 411, 2035

——. 2009, Monthly Notices of the Royal Astronomical Society, 393, 329

Napolitano, N. R., Pota, V., Romanowsky, A. J., Forbes, D. A., Brodie, J. P., & Foster, C. 2014, Monthly Notices of the Royal Astronomical Society, 439, 659

Navarro, J. F., Frenk, C. S., & White, S. D. 1996, The Astrophysical Journal, 462, 563

——. 1997, The Astrophysical Journal, 490, 493

Navarro, J. F. et al. 2004, Monthly Notices of the Royal Astronomical Society, 349, 1039

Neistein, E., Maoz, D., Rix, H.-W., & Tonry, J. L. 1999, The Astronomical Journal, 117, 2666

Nelson, D. et al. 2019, Computational Astrophysics and Cosmology, 6, 2

Newman, A. B., Ellis, R. S., & Treu, T. 2015, The Astrophysical Journal, 814, 26

Newman, A. B., Treu, T., Ellis, R. S., & Sand, D. J. 2013, The Astrophysical Journal, 765, 25

Noordermeer, E., Merrifield, M., & Aragón-Salamanca, A. 2008, Monthly Notices of the Royal Astronomical Society, 388, 1381

Noordermeer, E., van der Hulst, J., Sancisi, R., Swaters, R., & van Albada, T. 2007, Monthly Notices of the Royal Astronomical Society, 376, 1513

Noordermeer, E., van der Hulst, T., Sancisi, R., & Swaters, R. 2004, in Symposium-International Astronomical Union, Vol. 220, Cambridge University Press, 287–292

Norberg, P. et al. 2001, Monthly Notices of the Royal Astronomical Society, 328, 64

Norris, M. A. et al. 2012, Monthly Notices of the Royal Astronomical Society, 421, 1485

Oldham, L., & Auger, M. 2016, Monthly Notices of the Royal Astronomical Society, 457, 421

——. 2017, Monthly Notices of the Royal Astronomical Society, 474, 4169

Oldham, L. J., & Auger, M. W. 2018, Monthly Notices of the Royal Astronomical Society, 476, 133

Oort, J. 1926, The Observatory, 49, 302

Oosterloo, T. et al. 2010, Monthly Notices of the Royal Astronomical Society, 409, 500

Oosterloo, T. A., Morganti, R., Sadler, E. M., van der Hulst, T., & Serra, P. 2007, Astronomy & Astrophysics, 465, 787

Osipkov, L. 1979, Pisma v Astronomicheskii Zhurnal, 5, 77

Peng, Y., Maiolino, R., & Cochrane, R. 2015, Nature, 521, 192

Peng, Y.-j., Lilly, S. J., Renzini, A., & Carollo, M. 2012, The Astrophysical Journal, 757, 4

Peth, M. A. et al. 2016, Monthly Notices of the Royal Astronomical Society, 458, 963

Pichon, C., & Thiébaut, E. 1998, Monthly Notices of the Royal Astronomical Society, 301, 419

Poci, A., Cappellari, M., & McDermid, R. M. 2017, Monthly Notices of the Royal Astronomical Society, 467, 1397

Qian, E., de Zeeuw, P., van der Marel, R., & Hunter, C. 1995, Monthly Notices of the Royal Astronomical Society, 274, 602

Renzini, A., & Voli, M. 1981, Astronomy and Astrophysics, 94, 175

Richstone, D., & Tremaine, S. 1984, The Astrophysical Journal, 286, 27

Rix, H.-W., de Zeeuw, P. T., Cretton, N., van der Marel, R. P., & Carollo, C. M. 1997, The Astrophysical Journal, 488, 702

Rodionov, S., & Athanassoula, E. 2011, Monthly Notices of the Royal Astronomical Society, 410, 111

Rodionov, S., Athanassoula, E., & Sotnikova, N. Y. 2009, Monthly Notices of the Royal Astronomical Society, 392, 904

Rodriguez-Gomez, V. et al. 2016, Monthly Notices of the Royal Astronomical Society, 458, 2371

Rogstad, D., & Shostak, G. 1972, The Astrophysical Journal, 176, 315

Roškar, R., Debattista, V. P., Brooks, A. M., Quinn, T. R., Brook, C. B., Governato, F., Dalcanton, J. J., & Wadsley, J. 2010, Monthly Notices of the Royal Astronomical Society, 408, 783

Rowley, G. 1988, The Astrophysical Journal, 331, 124

Rubin, V. C., Burstein, D., Ford Jr, W. K., & Thonnard, N. 1985, The Astrophysical Journal, 289, 81

Rubin, V. C., Ford Jr, W. K., & Thonnard, N. 1980, The Astrophysical Journal, 238, 471

Rubin, V. C., Thonnard, N., & Ford Jr, W. 1978, The Astrophysical Journal, 225, L107

Saburova, A. S., Chilingarian, I. V., Katkov, I. Y., Egorov, O. V., Kasparova, A. V., Khoperskov, S. A., Uklein, R. I., & Vozyakova, O. V. 2018, Monthly Notices of the Royal Astronomical Society, 481, 3534

Sadler, E. M., Oosterloo, T. A., Morganti, R., & Karakas, A. 2000, The Astronomical Journal, 119, 1180

Salim, S. et al. 2007, The Astrophysical Journal Supplement Series, 173, 267

Salpeter, E. E. 1955, The Astrophysical Journal, 121, 161

Sánchez, S. et al. 2012, Astronomy & Astrophysics, 538, A8

——. 2016a, Revista mexicana de astronomía y astrofísica, 52, 171

——. 2016b, Revista mexicana de astronomía y astrofísica, 52, 21

Sanchez-Blazquez, P. et al. 2006, Monthly Notices of the Royal Astronomical Society, 371, 703

Santini, P. et al. 2012, Astronomy & Astrophysics, 538, A33

Satoh, C. 1980, Publications of the Astronomical Society of Japan, 32, 41

Sault, R. J., Teuben, P. J., & Wright, M. C. 1995, in Astronomical Data Analysis Software and Systems IV, Vol. 77, 433

Scarlata, C. et al. 2007, The Astrophysical Journal Supplement Series, 172, 406

Schawinski, K. et al. 2009, Monthly Notices of the Royal Astronomical Society, 396, 818

Schawinski, K., Thomas, D., Sarzi, M., Maraston, C., Kaviraj, S., Joo, S.-J., Yi, S. K., & Silk, J. 2007, Monthly Notices of the Royal Astronomical Society, 382, 1415

Schawinski, K. et al. 2014, Monthly Notices of the Royal Astronomical Society, 440, 889

Schaye, J. et al. 2015, Monthly Notices of the Royal Astronomical Society, 446, 521

Schechter, P. 1980, The Astronomical Journal, 85, 801

Schechter, P. L., & Gunn, J. E. 1979, The Astrophysical Journal, 229, 472

Schreiber, N. F. et al. 2006, The Astrophysical Journal, 645, 1062

Schwarzschild, M. 1979, The Astrophysical Journal, 232, 236

——. 1993, The Astrophysical Journal, 409, 563

Schweizer, F. 1982, The Astrophysical Journal, 252, 455

Sellwood, J. 2014, Reviews of Modern Physics, 86, 1

Serra, P. et al. 2012, Monthly Notices of the Royal Astronomical Society, 422, 1835

Sérsic, J. L. 1968, Cordoba, Argentina: Observatorio Astronomico, 1968, 1

Shaw, M. 1993, Astronomy and Astrophysics, 280, 33

Shier, L., & Fischer, J. 1998, The astrophysical journal, 497, 163

Simard, L., Mendel, J. T., Patton, D. R., Ellison, S. L., & McConnachie, A. W. 2011, The Astrophysical Journal Supplement Series, 196, 11

Simon, J. D., Bolatto, A. D., Leroy, A., & Blitz, L. 2003, The Astrophysical Journal, 596, 957

Siopis, C., & Kandrup, H. E. 2000, Monthly Notices of the Royal Astronomical Society, 319, 43

Skibba, R. A. et al. 2009, Monthly Notices of the Royal Astronomical Society, 399, 966

Smee, S. A. et al. 2013, The Astronomical Journal, 146, 32

Sonnenfeld, A., Treu, T., Gavazzi, R., Marshall, P. J., Auger, M. W., Suyu, S. H., Koopmans, L. V., & Bolton, A. S. 2012, The Astrophysical Journal, 752, 163

Sonnenfeld, A., Treu, T., Marshall, P. J., Suyu, S. H., Gavazzi, R., Auger, M. W., & Nipoti, C. 2015, The Astrophysical Journal, 800, 94

Speagle, J. S., Steinhardt, C. L., Capak, P. L., & Silverman, J. D. 2014, The Astrophysical Journal Supplement Series, 214, 15

Spekkens, K., Giovanelli, R., & Haynes, M. P. 2005, The Astronomical Journal, 129, 2119

Spergel, D. N. et al. 2003, The Astrophysical Journal Supplement Series, 148, 175

Stadel, J., Potter, D., Moore, B., Diemand, J., Madau, P., Zemp, M., Kuhlen, M., & Quilis, V. 2009, Monthly Notices of the Royal Astronomical Society: Letters, 398, L21

Starkenburg, T. K., Sales, L. V., Genel, S., Manzano-King, C., Canalizo, G., & Hernquist, L. 2019, The Astrophysical Journal, 878, 143

Statler, T. S. 1987, in Structure and Dynamics of Elliptical Galaxies (Springer), 487–488

Stoehr, F. 2006, Monthly Notices of the Royal Astronomical Society, 365, 147

Strateva, I. et al. 2001, The Astronomical Journal, 122, 1861

Swaters, R., Madore, B., van den Bosch, F. C., & Balcells, M. 2003, The Astrophysical Journal, 583, 732

Syer, D., & Tremaine, S. 1996, Monthly Notices of the Royal Astronomical Society, 282, 223

Taranu, D. et al. 2017, The Astrophysical Journal, 850, 70

Taylor, J. E., & Navarro, J. F. 2001, The Astrophysical Journal, 563, 483

Thomas, J. et al. 2011, Monthly Notices of the Royal Astronomical Society, 415, 545

Tinsley, B. M. 1972, Astronomy and Astrophysics, 20, 383

Tinsley, B. M., & Gunn, J. E. 1976, The Astrophysical Journal, 203, 52

Toomre, A. 1964, The Astrophysical Journal, 139, 1217

Toomre, A. 1977, in Evolution of Galaxies and Stellar Populations, 401

——. 1982, The Astrophysical Journal, 259, 535

Toomre, A., & Toomre, J. 1972, The Astrophysical Journal, 178, 623

Tortora, C., Napolitano, N., Cardone, V., Capaccioli, M., Jetzer, P., & Molinaro, R. 2010, Monthly Notices of the Royal Astronomical Society, 407, 144

Tortora, C., Napolitano, N., Romanowsky, A. J., Capaccioli, M., & Covone, G. 2009, Monthly Notices of the Royal Astronomical Society, 396, 1132

Tremaine, S. et al. 2002, The Astrophysical Journal, 574, 740

Tremblay, B., Merritt, D., & Williams, T. 1995, The Astrophysical Journal, 443, L5

Tsukui, T. 2019, in ALMA2019: Science Results and Cross-Facility Synergies, 40

Valluri, M., Merritt, D., & Emsellem, E. 2004, The Astrophysical Journal, 602, 66

van Albada, T. S., Bahcall, J. N., Begeman, K., & Sancisi, R. 1985, The Astrophysical Journal, 295, 305

van de Sande, J. et al. 2017, The Astrophysical Journal, 835, 104

van de Voort, F., Davis, T. A., Kereš, D., Quataert, E., Faucher-Giguere, C.-A., & Hopkins, P. F. 2015, Monthly Notices of the Royal Astronomical Society, 451, 3269

van den Bosch, F. C., Robertson, B. E., Dalcanton, J. J., & de Blok, W. 2000, The Astronomical Journal, 119, 1579

van den Bosch, R., van de Ven, G., Verolme, E., Cappellari, M., & de Zeeuw, P. 2008, Monthly Notices of the Royal Astronomical Society, 385, 647

van den Bosch, R. C., & van de Ven, G. 2009, Monthly Notices of the Royal Astronomical Society, 398, 1117

van der Hulst, J., van Albada, T., & Sancisi, R. 2001, in Gas and Galaxy Evolution, Vol. 240, 451

van der Kruit, P., & Freeman, K. 2011, Annual Review of Astronomy and Astrophysics, 49, 301

van der Marel, R. P. 1991, Monthly Notices of the Royal Astronomical Society, 253, 710

van der Marel, R. P., Binney, J., & Davies, R. L. 1990, Monthly Notices of the Royal Astronomical Society, 245, 582

van der Marel, R. P., Franx, M., et al. 1993, Astrophysical Journal, 407, 525

van Dokkum, P. G. 2005, The Astronomical Journal, 130, 2647

——. 2008, The Astrophysical Journal, 674, 29

van Dokkum, P. G., & Conroy, C. 2010, Nature, 468, 940

Vasiliev, E. 2013, Monthly Notices of the Royal Astronomical Society, 434, 3174

Vasiliev, E., & Athanassoula, E. 2015, Monthly Notices of the Royal Astronomical Society, 450, 2842

Vasiliev, E., & Valluri, M. 2020, The Astrophysical Journal, 889, 39

Vikram, V., Wadadekar, Y., Kembhavi, A. K., & Vijayagovindan, G. 2010, Monthly Notices of the Royal Astronomical Society, 409, 1379

Vogeley, M. S., Park, C., Geller, M. J., & Huchra, J. P. 1992, The Astrophysical Journal, 391, L5

Vogt, N. P., Forbes, D. A., Phillips, A. C., Gronwall, C., Faber, S., Illingworth, G. D., & Koo, D. C. 1996, The Astrophysical Journal Letters, 465, L15

Wake, D. A. et al. 2017, The Astronomical Journal, 154, 86

Walcher, C. et al. 2014, Astronomy & Astrophysics, 569, A1

Walker, M. G., & Penarrubia, J. 2011, The Astrophysical Journal, 742, 20

Walter, F., Brinks, E., de Blok, W., Bigiel, F., Kennicutt Jr, R. C., Thornley, M. D., & Leroy, A. 2008, The Astronomical Journal, 136, 2563

Warmels, R. 1988, Astronomy and Astrophysics Supplement Series, 72, 19

Wasserman, A. et al. 2018, The Astrophysical Journal, 863, 130

Weijmans, A.-M., Krajnović, D., van de Ven, G., Oosterloo, T. A., Morganti, R., & de Zeeuw, P. 2008, Monthly Notices of the Royal Astronomical Society, 383, 1343

Westfall, K. B., Bershady, M. A., Verheijen, M. A., Andersen, D. R., Martinsson, T. P., Swaters, R. A., & Schechtman-Rook, A. 2011, The Astrophysical Journal, 742, 18

Westfall, K. B. et al. 2019, The Astronomical Journal, 158, 231

Widrow, L. M., & Dubinski, J. 2005, The Astrophysical Journal, 631, 838

Widrow, L. M., Pym, B., & Dubinski, J. 2008, The Astrophysical Journal, 679, 1239

Wilkinson, M., Kleyna, J., Evans, N., & Gilmore, G. 2002, Monthly Notices of the Royal Astronomical Society, 330, 778

Willett, K. W. et al. 2013, Monthly Notices of the Royal Astronomical Society, 435, 2835

Williams, M. J., Bureau, M., & Cappellari, M. 2010, Monthly Notices of the Royal Astronomical Society, 409, 1330

Willmer, C. N. et al. 2006, The Astrophysical Journal, 647, 853

Yang, M., Zhu, L., Weijmans, A.-M., van de Ven, G., Boardman, N., Morganti, R., & Oosterloo, T. 2020, Monthly Notices of the Royal Astronomical Society, 491, 4221

Young, L. 2002, The Astronomical Journal, 124, 788

Young, L. M., Bureau, M., & Cappellari, M. 2008, The Astrophysical Journal, 676, 317

Yurin, D., & Springel, V. 2014, Monthly Notices of the Royal Astronomical Society, 444, 62

Zhang, C. et al. 2019, The Astrophysical Journal Letters, 884, L52

Zhao, H. 1996, Monthly Notices of the Royal Astronomical Society, 278, 488

Zhu, L. et al. 2014, The Astrophysical Journal, 792, 59

——. 2016, Monthly Notices of the Royal Astronomical Society, 462, 4001

——. 2020, Monthly Notices of the Royal Astronomical Society

Zhu, L., van de Ven, G., Méndez-Abreu, J., & Obreja, A. 2018a, Monthly Notices of the Royal Astronomical Society, 479, 945

Zhu, L. et al. 2018b, Nature Astronomy, 2, 233

——. 2018c, Monthly Notices of the Royal Astronomical Society, 473, 3000

Zou, H. et al. 2017, The Astronomical Journal, 153, 276

Zwicky, F. 1933, Helvetica Physica Acta, 6, 110